Physik-Department

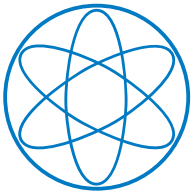

Search for the Higgs Boson in the Process pp → Hqq, H → WW with the ATLAS Detector

Dissertation
von
Steffen Kaiser

München
Januar 2010

Max-Planck-Institut für Physik
(Werner-Heisenberg-Institut)

TECHNISCHE UNIVERSITÄT MÜNCHEN

Max-Planck-Institut für Physik
(Werner-Heisenberg-Institut)

Search for the Higgs Boson in the Process $pp \rightarrow Hqq$, $H \rightarrow WW$ with the ATLAS Detector

Steffen Kaiser

Vollständiger Abdruck der von der Fakultät für Physik der Technischen Universität München zur Erlangung des akademischen Grades eines

Doktors der Naturwissenschaften (Dr. rer. nat.)

genehmigten Dissertation.

Vorsitzender: Univ.-Prof. Dr. A. Ibarra
Prüfer der Dissertation:
1. Priv.-Doz. Dr. H. Kroha
2. Univ.-Prof. Dr. L. Oberauer

Die Dissertation wurde am 11.01.2010 bei der Technischen Universität München eingereicht und durch die Fakultät für Physik am 18.02.2010 angenommen.

Abstract

The subject of this thesis is the evaluation of the discovery potential of the ATLAS experiment at the Large Hadron Collider (LHC) for the Standard Model Higgs boson in vector-boson fusion production in proton-proton collisions with subsequent decay into two W bosons. This decay channel is one of the most promising for the discovery of the Higgs boson since it has the largest branching fraction for Higgs boson masses above 160 GeV.
At the LHC design luminosity of $10^{34}\,\mathrm{cm}^{-2}\,\mathrm{s}^{-1}$, each triggered physics event will be overlaid by 22 additional inelastic pp interactions which deteriorate the discovery potential for the Higgs boson. The impact of these pile-up events on the discovery potential at an instantaneous luminosity of $10^{32}\ \mathrm{cm}^{-2}\,\mathrm{s}^{-1}$ has been studied. Methods have been developed to suppress the pile-up effects on observable quantities by association of final-state particles to the primary interaction vertex exploiting tracking information.
Simulated data samples for a center-of-mass energy of 10 TeV have been used in order to estimate the achievable exclusion limits and signal significances for an integrated luminosity of $1\,\mathrm{fb}^{-1}$. Taking into account theoretical and experimental systematic uncertainties, the Standard Model Higgs boson production via vector-boson fusion can be excluded at 95% confidence level for Higgs boson masses between 160 and 180 GeV. The best discovery potential with a significance of $2.7\,\sigma$ is expected for a Higgs boson mass of 165 GeV.
For the reconstruction of physics processes such as W- and Z-boson decays into muons, a very good muon momentum resolution is necessary which requires precise alignment of the ATLAS muon detectors. In the context of this thesis, a χ^2 minimization algorithm for the track-based alignment of the muon spectrometer has been developed and implemented in the ATLAS software.

Contents

Chapter 1

Introduction

For several decades particle physicists have been striving for a complete theory describing the elementary particles in nature and the fundamental interactions between them. Although not a final theory, the Standard Model of particle physics successfully describes the known elementary particles and three of the four interactions between them: the strong, weak and electromagnetic interactions. It has successfully been validated by high precision measurements to correctly describe these three interactions at the energies currently accessible by experiments. However, one fundamental pillar remains experimentally unverified: the origin of particle masses. Within the Standard Model, particle masses are generated by the electroweak symmetry breaking mechanism which entails a new particle, namely the Higgs boson. Since its prediction in 1964, particle physicists have been eagerly striving for a discovery of the Higgs boson at particle accelerators such as the Large Electron Positron (LEP) collider at CERN[1] and the Tevatron at Fermilab. While the allowed mass range has been constrained, the Higgs boson remains the last undiscovered particle in the Standard Model. Chapter 2 provides a short introduction to the Standard Model of particle physics and the theoretical background this thesis is based on.

In the year 2000, LEP was decommissioned in order to allow for the construction of its successor, the Large Hadron Collider (LHC). Providing proton-proton collisions at a yet unrivaled center-of-mass energy of 14 TeV and a design luminosity of up to 10^{34} $\mathrm{cm}^{-2}\,\mathrm{s}^{-1}$, the LHC will open a new era in particle physics. It will allow for long anticipated discoveries and precision measurements of processes within and beyond the Standard Model. After many years of development and construction, operation of the LHC has started providing the first proton-proton collisions at a center-of-mass energy of 900 GeV at the interaction regions of the two general-purpose experiments, ATLAS and CMS. The design and the physics goals of the ATLAS experiment are discussed in Chapter 3.

During the first year of operation with pp collisions, ATLAS will mainly focus on the understanding and the calibration of all detector subsystems as well as on the measurement of high cross section Standard Model processes in the new energy regime which also helps to validate the performance and the reliability of the reconstruction algorithms for observable objects such as electrons, muons and jets.

For the measurement of the masses and cross sections of Z and W bosons subsequently decaying into muons as well as for the search for the Higgs boson in ZZ/WW decays a

[1] CERN - **C**onseil **E**uropéene pour la **R**echerche **N**ucléaire

good muon momentum resolution is of particular importance. Muons are reconstructed based on measurements provided by high-precision tracking chambers, mainly Monitored Drift Tube (MDT) chambers, in the ATLAS muon spectrometer which have to be precisely aligned with respect to each other. In Chapter 4 an algorithm is introduced which allows for the relative position reconstruction (alignment) of the MDT chambers during ATLAS data taking using reconstructed muons in a global χ^2 fit.
In this thesis, the discovery potential of the Higgs boson production via vector-boson fusion with subsequent Higgs boson decays into two W bosons is evaluated. Due to its large branching fraction, the decay into two W bosons is one of the most promising decay channels for a discovery of the Higgs boson. In particular at initially low integrated luminosities, it provides an unrivaled opportunity for setting exclusion limits on the Higgs boson production cross section. While suppressed by one order of magnitude with respect to the Higgs boson production via gluon fusion, the topology of the vector-boson fusion production process provides efficient background suppression by means of two characteristic jets in the forward regions of the detector. The background contributions and event selection criteria for this process are discussed in Chapter 5.
At the LHC design luminosity of $10^{34}\,\mathrm{cm}^{-2}\,\mathrm{s}^{-1}$, on average 23 inelastic proton-proton collisions will take place at each bunch crossing. Thus, each interesting physics event will be superimposed by 22 additional inelastic pp interactions which will deteriorate the discovery potential of the Higgs boson. As presented in Chapter 6, in particular the increased activity in the calorimeter as well as jets originating from additional inelastic pp interactions have a significant impact on the selection of jets originating from the vector-boson fusion production of the Higgs boson. However, tracking and vertexing information allows for the association of jets to the primary interaction. Two different approaches are studied, first, the reconstruction of jets based solely on inner detector tracks originating from the primary interaction vertex and, second, the association of calorimeter jets to tracks from the primary vertex.
In Chapter 7, the theoretical and experimental systematic uncertainties are evaluated and the achievable discovery potential and exclusion limits for the Higgs boson are estimated using simulated ATLAS data corresponding to an integrated luminosity of $1\,\mathrm{fb}^{-1}$ and a pp center-of-mass energy of 10 TeV.
Finally, a summary of the results of this thesis and prospects for future developments are given in Chapter 8.

Chapter 2

The Higgs Boson in the Standard Model

This chapter gives an introduction to the Standard Model of particle physics and provides the theoretical background for this thesis. The brief review of the Standard Model and the Higgs mechanism in Section 2.1 is based on References [1,2]. The following sections present the current limits on the mass of the Higgs boson as well as an overview of the Standard Model Higgs production mechanisms and decay channels in proton-proton collisions at the LHC. A short introduction to the phenomenology of proton-proton collisions is given in Section 2.4.

2.1 The Standard Model of Particle Physics

The Standard Model (SM) of particle physics successfully describes the known elementary particles and three of the four fundamental interactions between them: the strong, the weak and the electromagnetic interaction which are mediated by gauge bosons[1] (see Tables 2.1 and 2.2).

A unified electroweak gauge theory has been developed in the 1960's by Glashow [3], Weinberg [4] and Salam [5] and is therefore referred to as GWS theory. It is based on the $SU(2)_L \times U(1)_Y$ gauge symmetry group of the weak isospin and the weak hypercharge. Quantum Chromodynamics (QCD), the theory of the strong interaction between the colored quarks mediated by gluons is described the $SU(3)_C$ gauge group. Both theories together provide a complete description of the three fundamental forces between point-like fermions by means of a $SU(3)_C \times SU(2)_L \times U(1)_Y$ gauge field theory: the Standard Model of particle physics. The SM has been thoroughly validated in high-precision measurements to correctly describe the strong and electroweak interactions at the energies currently accessible by experiments.

[1] The fourth force, gravitation, is not described by the Standard Model. It is assumed to be too weak to play a significant role on the scale of elementary particle physics. Furthermore, a description in the frame of a consistent quantum field theory did not succeed yet.

Force	Relative strength	Mediator
Strong	1	Gluon (g_1, …, g_8)
Electromagnetic	10^{-2}	Photon (γ)
Weak	10^{-13}	$W^{\pm}$, Z
Gravitational	10^{-38}	–

Table 2.1: The fundamental interactions and the corresponding mediators (gauge bosons) in the Standard Model.

	Generation 1	2	3	Electric charge [e]
Leptons	ν_e	ν_μ	ν_τ	0
	e	μ	τ	-1
Quarks	u_i	c_i	t_i	$+2/3$
	d_i	s_i	b_i	$-1/3$

Table 2.2: The three generations of fermions. The quark index denotes the colors: i = **r**ed, **b**lue, **g**reen.

2.1.1 Quantum Chromodynamics

Quantum Chromodynamics, the theory of the strong interaction between quarks is based on color charges and described by the $SU(3)_C$ gauge symmetry. Interactions between the colored quarks are mediated by eight massless gauge bosons, the gluons. Carrying color charge themselves, gluons self-interact with each other via 3-gluon and 4-gluon vertices. The specific structure of the $SU(3)_C$ gauge symmetry entails two important implications, *asymptotic freedom* and *confinement*.

The strong coupling constant α_s is a function of the energy scale Q of the process[2]. $\alpha_s(Q^2)$ decreases with increasing energy scale and asymptotically vanishes for $Q^2 \to \infty$ which is referred to as asymptotic freedom. Hence, at large momentum transfer or short distances, the strong interaction becomes weak and quarks can be considered as almost free objects which allows for quantitative predictions by means of perturbation theory.

In contrast, at low energy scales and large distances, α_s increases and the perturbative approach to QCD calculations is no longer applicable. This characteristic results in the non-existence of unbound colored objects, called confinement. Increasing the distance between two color-charged objects leads to a linear increase in binding energy and finally to the creation of quark-antiquark pairs from the vacuum. These quark pairs are grouped together with the initial partons in color-neutral bound states, the hadrons, which are observable. This process is known as *hadronization*.

2.1.2 The Electroweak Interaction

The theory of electroweak interactions between fermions mediated by vector bosons is described by a $SU(2)_L \times U(1)_Y$ gauge symmetry. It comprises one $U(1)_Y$ gauge field B_μ and three $SU(2)_L$ gauge fields W^i_μ. B_μ couples to both the left- and right-handed components of the fermion fields, ψ_L and ψ_R, while the W^i_μ gauge fields only couple to the left-handed components. The left-handed projections of the fermion fields form weak isospin doublets,

$$\psi_L = \begin{pmatrix} \nu_l \\ l^- \end{pmatrix}_L, \begin{pmatrix} q_u \\ q_d \end{pmatrix}_L \tag{2.1}$$

[2]The energy scale Q of the process is defined by the momentum transfer q of the interacting particles according to $Q^2 = |q^2|$.

with $l = e, \mu, \tau$; $q_u = u, c, t$ and $q_d = d, s, b$; whereas the right-handed projections form $SU(2)_L$ singlets:

$$\psi_R = l_R,\, q_{uR},\, q_{dR}. \tag{2.2}$$

The gauge invariant Lagrangian of the electroweak theory can be written as sum of a gauge field and a fermion term:

$$\mathcal{L}_{EW} = \mathcal{L}_G + \mathcal{L}_F, \tag{2.3}$$

which will be introduced in the following. The gauge field term of the Lagrangian reads

$$\mathcal{L}_G = -\frac{1}{4} W^i_{\mu\nu} W_i^{\mu\nu} - \frac{1}{4} B_{\mu\nu} B^{\mu\nu} \tag{2.4}$$

with the field strengths defined by

$$W^i_{\mu\nu} = \partial_\mu W^i_\nu - \partial_\nu W^i_\mu + g\epsilon^{ijk} W^j_\mu W^k_\nu \quad \text{and} \tag{2.5}$$

$$B_{\mu\nu} = \partial_\mu B_\nu - \partial_\nu B_\mu, \tag{2.6}$$

where g denotes the weak $SU(2)_L$ coupling constant. Linear combinations of the four gauge fields B_μ and W^i_μ represent the observable weak gauge bosons γ, Z and $W^\pm$:

$$\begin{pmatrix} A_\mu \\ Z_\mu \end{pmatrix} = \begin{pmatrix} \cos\theta_W & \sin\theta_W \\ -\sin\theta_W & \cos\theta_W \end{pmatrix} \begin{pmatrix} B_\mu \\ W^3_\mu \end{pmatrix} \quad \text{and} \tag{2.7}$$

$$W^\pm_\mu = \frac{1}{\sqrt{2}} W^1_\mu \pm i W^2_\mu. \tag{2.8}$$

Here, the weak mixing angle θ_W can be expressed by the $U(1)_Y$ and $SU(2)_L$ coupling constants g' and g according to $\cos\theta_W = g/\sqrt{g^2 + g'^2}$.
Interactions between fermions and the gauge fields are described by the Lagrangian

$$\mathcal{L}_F = i\bar{\psi}_L \gamma^\mu D_{\mu L} \psi_L + i\bar{\psi}_R \gamma^\mu D_{\mu R} \psi_R \tag{2.9}$$

with the local gauge invariance of the theory being ensured by the covariant derivatives

$$D_{\mu L}\psi_L = \left(\partial_\mu + ig\frac{\sigma_i}{2} W^i_\mu + ig'\frac{Y_L}{2} B_\mu\right)\psi_L \quad \text{and} \tag{2.10}$$

$$D_{\mu R}\psi_R = \left(\partial_\mu + ig'\frac{Y_R}{2} B_\mu\right)\psi_R, \tag{2.11}$$

where σ_i represents the Pauli spin matrices for the weak isospin and Y the weak hypercharge.
In contrast to experimental observations, fermions and gauge bosons have to be massless for the Lagrangian to obey $SU(2)_L \times U(1)_Y$ local gauge symmetry.

2.1.3 The Higgs Mechanism

The mechanism of electroweak symmetry breaking introduced in 1964 by Higgs [6] and others [7, 8] overcomes the restriction to massless states in the Lagrangian. Massive

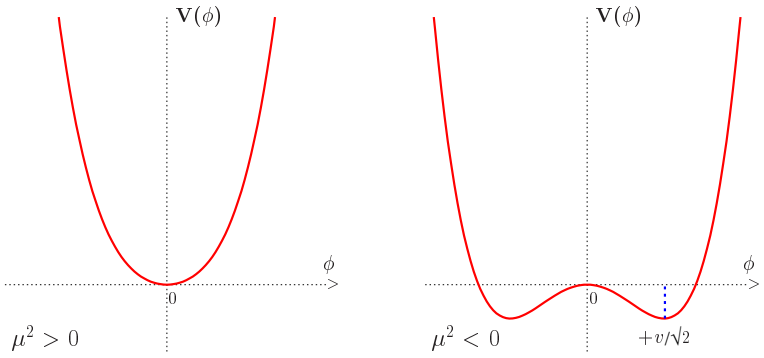

Figure 2.1: The Higgs potential $V(\phi)$ for $\mu^2 > 0$ (left) and $\mu^2 < 0$ (right) [1].

fermions and gauge bosons are incorporated by introducing a doublet of complex scalar fields:

$$\phi = \begin{pmatrix} \phi^+ \\ \phi^0 \end{pmatrix} = \frac{1}{\sqrt{2}} \begin{pmatrix} \phi_1 - i\phi_2 \\ \phi_3 - i\phi_4 \end{pmatrix} \tag{2.12}$$

with a potential

$$V(\phi) = \mu^2 \phi^\dagger \phi + \lambda (\phi^\dagger \phi)^2, \tag{2.13}$$

where μ denotes the mass parameter and λ the strength of the self-coupling of ϕ. The scalar field ϕ is integrated in the Lagrangian of the electroweak theory (Equation 2.3) by adding a term

$$\mathcal{L}_H = (D^\mu \phi)^\dagger (D_\mu \phi) - V(\phi), \tag{2.14}$$

which is invariant under $SU(2)_L \times U(1)_Y$ transformation.

$$D_\mu \phi = \left(\partial_\mu + ig \frac{\sigma_i}{2} W_\mu^i + ig' \frac{Y_\phi}{2} B_\mu \right) \phi \tag{2.15}$$

represents the covariant derivative with the weak hypercharge $Y_\phi = 1$.
The shape of the potential $V(\phi)$ is visualized in Figure 2.1 for $\mu^2 > 0$ and $\mu^2 < 0$. For $\mu^2 > 0$ the minimum of the potential is at $\phi_0 = 0$. In case of $\mu^2 < 0$, the minimum of the potential is obtained for configurations satisfying

$$|\phi_0^2| = -\frac{\mu^2}{2\lambda} \equiv \frac{v^2}{2} \tag{2.16}$$

with the vacuum expectation value v deviating from 0. Choosing an arbitrary ground state such as

$$\phi_0 = \frac{1}{\sqrt{2}} \begin{pmatrix} 0 \\ v \end{pmatrix} \tag{2.17}$$

breaks the $SU(2)_L$ symmetry while the Lagrangian remains invariant under $SU(2)_L \times U(1)_Y$ transformations which is called *spontaneous symmetry breaking* in analogy to phase transitions in condensed matter physics. Excitations of the scalar field are parametrized as

$$\phi = \frac{1}{\sqrt{2}} \begin{pmatrix} 0 \\ v + H \end{pmatrix} \tag{2.18}$$

with H denoting the scalar Higgs field which represents the physical Higgs boson. Inserting Equations 2.18, 2.7 and 2.8 in the Lagrangian $\mathcal{L}_H$ in Equation 2.14 results in

$$\mathcal{L}_H = \frac{1}{2}\partial^\mu H \partial_\mu H + \frac{g^2 v^2}{8}\left(W_\mu^+ W^{+\mu} + W_\mu^- W^{-\mu}\right) + \frac{g^2 v^2}{8\cos^2\theta_W} Z_\mu Z^\mu - V(\phi), \tag{2.19}$$

which contains mass terms for the Z and $W^\pm$ bosons with the mass given by

$$m_W = \cos\theta_W m_Z = \frac{gv}{2}, \tag{2.20}$$

while the photon remains massless, $m_A = 0$.
Fermion masses are generated by introducing additional terms in the Lagrangian describing the Yukawa coupling of the fermions to the scalar field ϕ. For instance, for the first generation leptons the corresponding Yukawa term assumes the form

$$\mathcal{L}_Y = -g_e\left[(\bar{\nu}_e, \bar{e})_L \phi e_R + \bar{e}_R \phi^\dagger \begin{pmatrix}\nu_e \\ e\end{pmatrix}_L\right] = -m_e \bar{e} e - \frac{g_e}{\sqrt{2}}\bar{e} e H \tag{2.21}$$

with g_e denoting the Yukawa coupling constant of electrons and $m_e = g_e v/\sqrt{2}$. In general, the fermion masses are given by

$$m_f = \frac{g_f v}{\sqrt{2}}. \tag{2.22}$$

By inserting Equation 2.18 in the definition of the Higgs potential $V(\phi)$, the following expression for the Higgs boson mass can be derived:

$$m_H = \sqrt{-2\mu^2} = \sqrt{2\lambda}\, v, \tag{2.23}$$

which, like the self-coupling parameter λ is a free parameter of the theory. The vacuum expectation value v can be determined with the help of Equation 2.20 from the measurement of the Fermi constant G_F via the muon life time according to $v = (\sqrt{2}G_F)^{-1/2} = 246\,\text{GeV}$. Hence, the masses of fermions and gauge bosons are incorporated into the theory of the electroweak interaction by means of spontaneous electroweak symmetry breaking:

$$SU(2)_L \times U(1)_Y \xrightarrow{SSB} U(1)_Q, \tag{2.24}$$

which introduces a new physical particle: the Higgs boson.
The coupling strengths of the Higgs boson to the fermions and bosons are proportional to the masses of the particles participating in the interaction. While the fermion and boson masses have been measured experimentally, predictions of the production cross section and decay branching ratios of the Higgs boson are not possible due its unknown mass. The Higgs boson is the only particle in the Standard Model which has not been discovered yet. However, its mass range is restricted theoretically and experimentally as discussed in Section 2.2.

2.1.4 Problems and Extensions of the Standard Model

The Standard Model of particle physics is very successful in describing experimental data at the highest precision. Up to now, no contradictions to its predictions could be experimentally established. However, the Standard Model is unlikely to be the final theory of

elementary particles due to several limitations. One of these limitations is the necessary *fine tuning* of the Higgs boson mass. The current experimental data indicates the Higgs boson mass at the electroweak scale ($\sim 100\,\text{GeV}$). In the Standard Model, quadratically diverging radiative corrections drive the natural value of m_H to the largest possible scale, the Planck scale at $10^{19}\,\text{GeV}$. These divergences have to be compensated with unnaturally high accuracy to keep m_H at the electroweak scale which is referred to as fine tuning of the Higgs boson mass.
Different theoretical extensions of the Standard Model exist which account for its limitations such as the fine tuning problem. For instance, Supersymmetry (SUSY) [9, 10] provides an elegant extension which allows for the cancellation of the diverging radiative corrections. Supersymmetry predicts a superpartner for each fundamental fermion and boson with a spin different by 1/2. In addition, electroweak symmetry breaking in the minimal supersymmetric extension of the Standard Model (MSSM) predicts three neutral (h, H, A) and two charged ($H^{\pm}$) Higgs particles. So far, no experimental evidence for Supersymmetry or any other theory beyond the Standard Model has been found, but further insight is expected from measurements by the LHC experiments.

2.2 Limits on the Higgs Boson Mass

Although the mass of the Higgs boson cannot be predicted by the Standard Model, the allowed range can be restricted by consistency considerations. Furthermore, electroweak precision measurements and direct Higgs boson searches provide constraints on the Higgs boson mass range.

2.2.1 Theoretical Limits

Theoretical limits on the mass of the Higgs boson can be derived depending on the energy scale Λ up to which the Standard Model is valid and no new particles and interactions appear [1, 11]. The value of Λ is unknown up to now, though it is restricted by the Planck scale ($\Lambda \leq M_{Planck} = 10^{19}\,\text{GeV}$), which is the energy scale at which gravitational effects become sizable and can no longer be neglected compared to the other interactions. Hence, at the latest for energies on the order of M_{Planck} the Standard Model has to be extended or replaced by a theory which incorporates gravitation.
Limits on m_H can be derived requiring finite positive values for the self-coupling parameter λ of the Higgs field (Equation 2.13). The self-coupling parameter $\lambda(Q)$ increases with the energy scale Q. Hence, requiring finite values $\lambda(Q)$ for $Q \leq \Lambda$ allows for setting an upper bound on m_H referred to as *triviality bound*.
A lower limit on the mass of the Higgs boson and an improved upper limit is obtained by requiring *vacuum stability*, i. e. the potential $V(\phi)$ to be bound from below which corresponds to imposing $\lambda > 0$. Requiring $\lambda(Q) > 0$ for $Q \leq \Lambda$ results in the lower and upper band in Figure 2.2.
Measuring m_H therefore gives hints on the validity scale Λ of the Standard Model. For values $\Lambda \sim M_{Planck}$ the Higgs boson mass is restricted to the narrow range

$$130\,\text{GeV} \lesssim m_H \lesssim 180\,\text{GeV}, \tag{2.25}$$

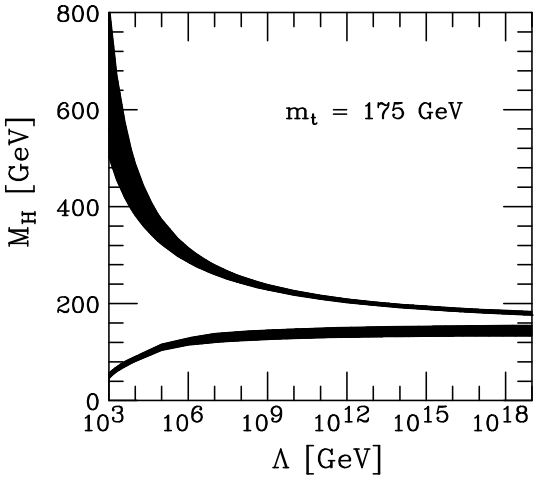

Figure 2.2: Theoretical limits on the Higgs boson mass depending on the energy scale Λ up to which the Standard Model is valid [11]. The limits have been derived assuming a top-quark mass of $m_t = (175 \pm 6)\,\text{GeV}$ and a strong coupling constant of $\alpha_s(m_Z) = 0.118 \pm 0.002$. The shaded bands represent the theoretical uncertainties on the calculated limits and enclose the allowed range of the Higgs boson mass.

whereas for $\Lambda = 1\,\text{TeV}$ the mass of the Higgs boson is allowed in the range

$$55\,\text{GeV} \lesssim m_H \lesssim 600\,\text{GeV}. \tag{2.26}$$

2.2.2 Experimental Limits

The mass range of the Higgs boson is indirectly restricted by precision measurements of Standard Model parameters at experiments at the Large Electron Positron Collider (LEP), the Stanford Linear Collider (SLC) and at the Tevatron, which have reached a precision which allows for probing radiative corrections including such involving the Higgs boson. Figure 2.3 shows the results from a combined fit of the Standard Model prediction to the electroweak precision measurements with the Higgs boson mass as a free parameter [12]. The most constraining measurements are the measurements of the Z boson mass and decay width in $e^+e^- \to Z \to f\bar{f}$ processes at LEP as well as measurements of the W boson mass and decay width and of the mass of the top quark by the Tevatron experiments. According to the fit, the most probable Higgs boson mass is $m_H = 84^{+34}_{-26}\,\text{GeV}$ assuming $m_t = 172.5 \pm 1.2\,\text{GeV}$. Taking into account the lower limit on m_H from direct Higgs searches at LEP (see below) an upper limit of $m_H \leq 185\,\text{GeV}$ at 95% confidence level (CL) is obtained.

The Higgs boson mass range can be further restricted by direct searches of the LEP and Tevatron experiments. At LEP, the Higgs boson was searched for at center-of-mass energies up to $\sqrt{s} = 209\,\text{GeV}$ via the $e^+e^- \to Z^* \to HZ$ Higgsstrahlung production mechanism. A lower limit of $m_H > 114.4\,\text{GeV}$ at 95% CL was obtained [13]. The current results of the Higgs boson searches by the Tevatron experiments DØ and CDF are based on data samples corresponding to integrated luminosities of up to $4.2\,\text{fb}^{-1}$ recorded in $p\bar{p}$ collisions at $\sqrt{s} = 1.96\,\text{TeV}$. The combination of searches for the Higgs boson via

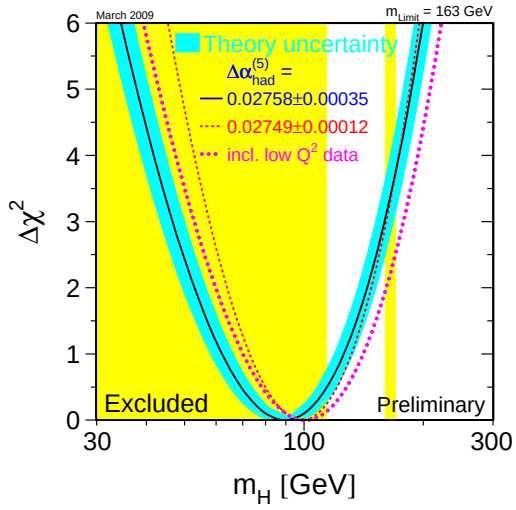

Figure 2.3: $\Delta\chi^2 = \chi^2 - \chi^2_{min}$ of the combined fit to electroweak precision measurements as a function of the Higgs boson mass m_H [12]. The blue/shaded band indicates the theoretical uncertainties due to unknown higher order corrections. The vertical yellow/shaded bands represent the regions excluded at 95% CL by direct Higgs boson searches in experiments at LEP and Tevatron.

gluon fusion production with Higgs decays into two W bosons and via the production in association with W/Z bosons or a $t\bar{t}$ pair with subsequent Higgs decays into $b\bar{b}$ pairs allows for an exclusion of Higgs boson masses between 160 GeV and 170 GeV at 95% CL [14].

2.3 The Higgs Boson at the LHC

At the LHC, pp collisions at a center-of-mass energy of $\sqrt{s} = 14$ TeV allow for a discovery of the Higgs boson over a broad mass range of up to $m_H = 1$ TeV. The Higgs boson will be searched for in various production processes and decay channels which will be briefly introduced in the following.

2.3.1 Higgs Boson Production Mechanisms

The Higgs boson can be produced by several mechanisms. The Feynman diagrams of the four dominant production processes at the LHC, gluon fusion, vector-boson fusion, Higgsstrahlung of vector bosons and the associated production with a top-quark pair, are shown in Figure 2.4. The corresponding cross sections are shown in Figure 2.5 as a function of m_H for a center-of-mass energy of $\sqrt{s} = 14$ TeV. Over the whole mass range accessible by the LHC, the gluon fusion is the dominant production mechanism due to the strong coupling of the Higgs boson to the top quark and the larger phase space compared to the associated production with top quarks. The cross section of the vector-boson fusion production is about an order of magnitude smaller in the low Higgs-mass range and reaches the same order at large masses. However, the vector-boson fusion production

mechanism allows for an efficient suppression of background processes by means of the two characteristic highly energetic jets in the forward regions of the detector spanning a rapidity gap with suppressed jet activity which provides a competitive discovery potential even at low m_H.
The two remaining production mechanisms have significantly lower cross sections but allow for a measurement of the Higgs boson in specific decay channels. For instance, in the $H \to b\bar{b}$ decay channel the two additional top quarks in the associated production allow for trigger and a better background suppression.

2.3.2 Higgs Boson Decay Channels

In the Standard Model, the Higgs boson decays predominantly into fermion and gauge boson pairs. The Feynman diagrams of the dominant Higgs decay channels in the Standard Model are displayed in Figure 2.6. Since the coupling strength of the Higgs boson is directly proportional to the masses of the particles involved, the decay into the heaviest particles allowed by phase space dominates for a given Higgs mass. This is shown in Figure 2.7 which depicts the branching fractions of the different Higgs boson decay channels as a function of m_H. In the low mass range, decays into $\tau^+\tau^-$ and $b\bar{b}$ pairs constitute the largest contribution. At larger masses ($m_H \gtrsim 2m_W, 2m_Z$), Higgs boson decays into WW and ZZ pairs are kinematically allowed and thus dominant. Gluons and photons are massless particles and therefore do not couple directly to the Higgs boson. Decays of the Higgs boson into photon pairs are mediated by charged fermion and W boson loops whereas decays into gluon pairs are only mediated by quark loops with the top quark exchange being the dominant contribution.

2.4 Phenomenology of Proton-Proton Collisions

Higgs boson production in pp interactions occurs at high momentum transfer. In this case, the production cross section can be calculated in the parton model. Assuming a and b to be constituents of the protons A and B, the hadronic process

$$A + B \to c + X, \tag{2.27}$$

where c represents for instance the Higgs boson and X the hadronic remnants of the interaction, can be related to the parton subprocess:

$$a + b \to c. \tag{2.28}$$

The cross section of the parton subprocess $\sigma_{a+b\to c}$ can be calculated in the Standard Model and translated into the hadronic cross section $\sigma_{A+B\to c+X}$ according to:

$$d\sigma_{A+B\to c+X} = \sum_{a,b} \int_0^1 dx_a \int_0^1 dx_b f_A^a(x_a, Q^2) f_B^b(x_b, Q^2) d\sigma_{a+b\to c} \tag{2.29}$$

where the sum extends over all partonic subprocesses which contribute to the production of c. f_A^a and f_B^b denote the *parton distribution functions* (PDFs) evaluated at the scale

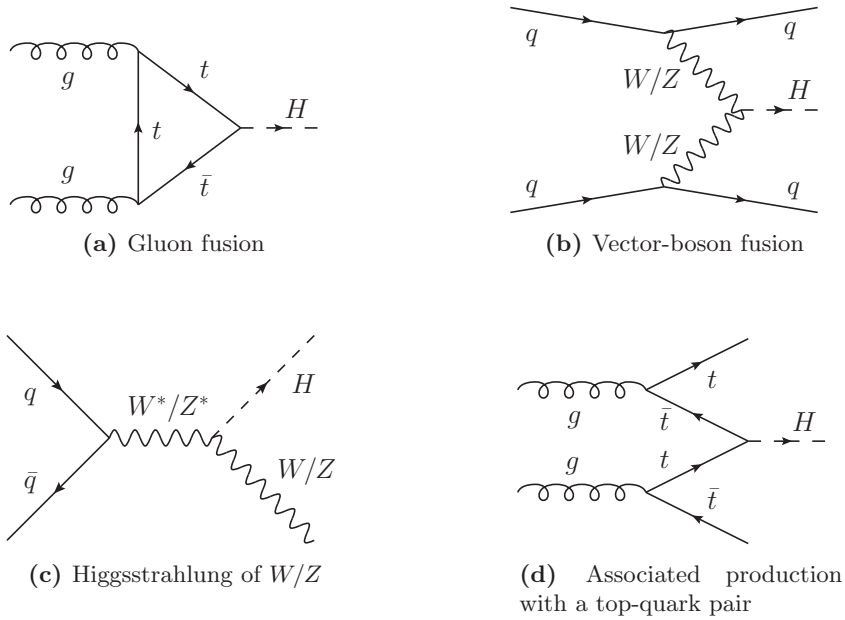

(a) Gluon fusion

(b) Vector-boson fusion

(c) Higgsstrahlung of W/Z

(d) Associated production with a top-quark pair

Figure 2.4: Tree-level Feynman diagrams of the dominant production processes of a Standard Model Higgs boson in pp collisions at the LHC.

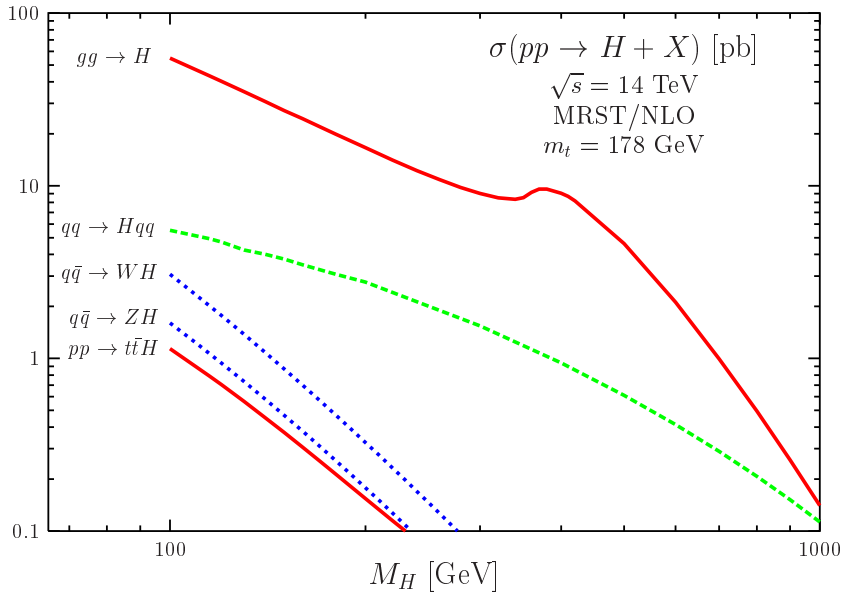

Figure 2.5: Production cross sections of the Standard Model Higgs boson as a function of the Higgs boson mass for a LHC center-of-mass energy of $\sqrt{s} = 14\,\text{TeV}$ [1].

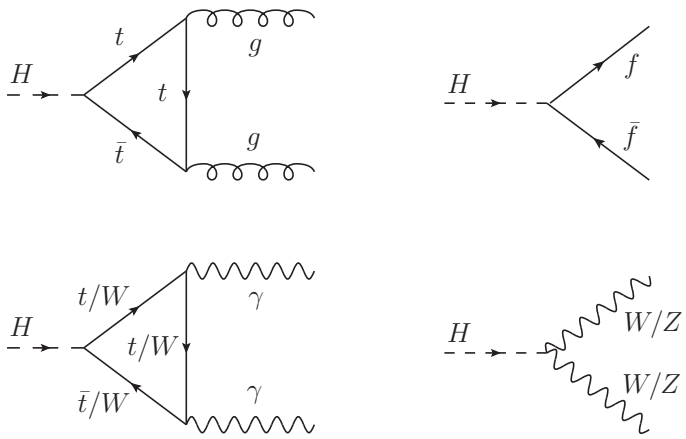

Figure 2.6: Tree-level Feynman diagrams of the dominant Higgs boson decay channels in the Standard Model.

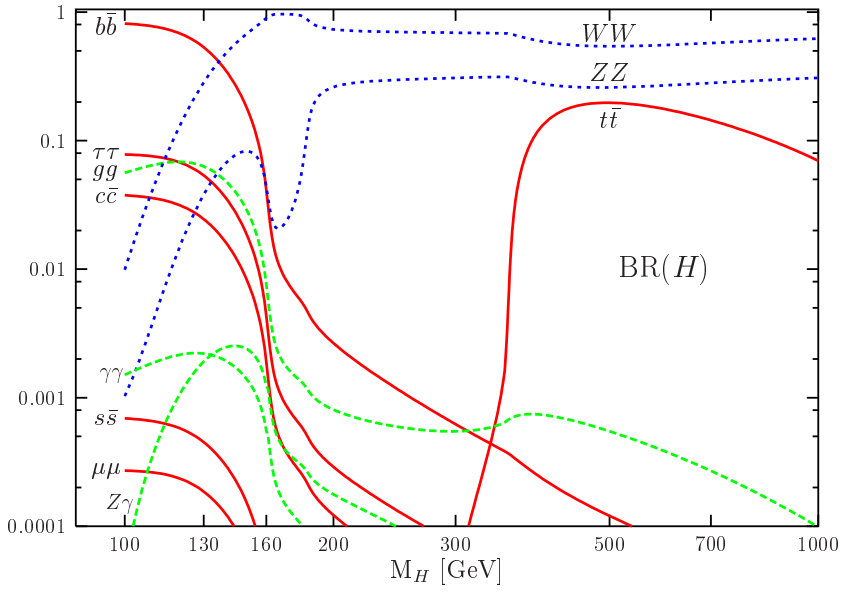

Figure 2.7: Branching ratios of the Standard Model Higgs boson as a function of the Higgs boson mass [1].

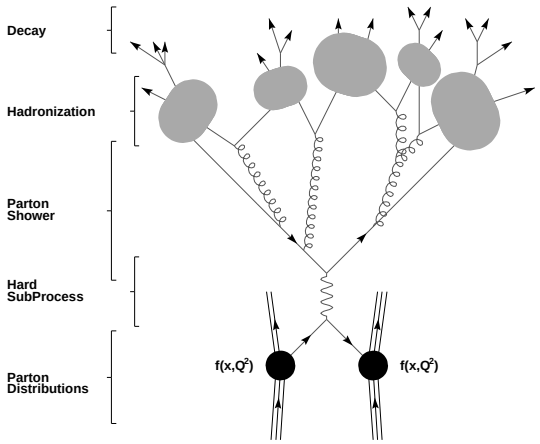

Figure 2.8: Phenomenological model of a hard proton-proton interaction [16]. The time progresses from the bottom of the graphic to the top.

Q^2 of the process which give the probability to encounter a parton a with the momentum fraction x_a within its parent proton A.

This approach of separating the interaction in a short-distance hard-scattering part which can be calculated by perturbation theory and a long-distance part represented by the PDFs is called *factorization* and the scale Q^2 is referred to as factorization scale. The PDFs cannot be calculated from first principles but have to be measured, for instance in deep inelastic scattering experiments [15].

Up to now, hard parton processes have been calculated in leading order or, in some cases, in next-to-leading order perturbation theory. Higher order corrections and non-perturbative hadronic fragmentation effects are taken into account by the so-called *parton-shower* method as shown in Figure 2.8, which illustrates for example the production of a Z boson in pp collisions with subsequent decay into a quark-antiquark pair. Since the quarks carry color charge, they radiate gluons which themselves create new $q\bar{q}$ pairs resulting in a cascade of partons. Such parton showers also originate from the initial state partons which is not shown in the figure for simplicity. The resulting colored partons are then grouped together into color-singlet hadrons, in a process called *hadronization* for which several phenomenological models exist such as the Lund string or the cluster fragmentation models [16].

All contributions to the final state in a pp interaction not originating from the hard process are referred to as *underlying event*. This includes initial state and final state radiation, ISR and FSR, as well as interactions of the proton remnants which, due to their color charges, are color-connected to the hard process. Furthermore, since protons are composed of multiple partons, several parton scattering processes can take place in one pp interaction.

In addition, at the high LHC luminosities, several inelastic pp collisions will take place per bunch crossing which are called pile-up events. Due to the large cross section, these processes are predominantly soft interactions which are discussed in more detail in Section 6.1.

The non-perturbative effects mentioned above, the hadronization and the description of the parton shower and the underlying event, are represented by phenomenological models

which have to be tuned on data in order to allow for a reliable modeling of the physics process. Up to now, these models are tuned on data from the UA5 and CDF experiments at center-of-mass energies of up to $\sqrt{s} = 1.8\,\text{TeV}$ and extrapolations to LHC energies of 14 TeV are employed. This entails large uncertainties due to different models predicting largely different cross sections [17, 18]. Hence in order to obtain a reliable description of the physics processes, these models have to be tuned on LHC data at the respective center-of-mass energy.

Chapter 3

The ATLAS Experiment at the Large Hadron Collider

Since its prediction in 1964, the Higgs boson has become one of the holy grails in particle physics. Physicists have been eagerly striving for its discovery for several decades at particle accelerators like the Tevatron at Fermilab and the Large Electron Positron (LEP) collider at CERN. While the former is still in operation, LEP was decommissioned in the year 2000 after eleven years of data taking in order to allow for the construction of its successor, the Large Hadron Collider (LHC) [19] which is depicted in Figure 3.1. For LEP as electron-positron collider, the attainable center-of-mass energy was limited by synchrotron radiation accompanying circulating charged particles. Since for accelerated particles with mass m the total radiated power is proportional to $1/m^4$, this limitation can be overcome by accelerating protons and antiprotons. These are brought into collision at the Tevatron at a center-of-mass energy of 1.96 TeV. In comparison to protons, the production and acceleration of a large number of antiprotons is technically much more demanding. Therefore, at the LHC two counter-rotating beams of protons are accelerated up to energies of 7 TeV providing a yet unrivaled center-of-mass energy of 14 TeV. Superconducting dipole magnets, providing a magnetic field strength of 8.33 T, are employed to keep the proton beams on the circular track of 26.7 km circumference in the former LEP tunnel.

Four different experiments are installed at the four interaction points covering a broad range of experimental studies. The two general-purpose detectors, ATLAS (A Toroidal LHC ApparatuS) [20] and CMS (Compact Muon Solenoid) [21] will provide information on long anticipated new phenomena and precision measurements of Standard Model processes as explained in Section 3.1. The LHCb (Large Hadron Collider beauty) experiment is designed to study B-meson physics and to explore CP-violation in B decays at high precision [22]. In addition to protons, the LHC will also accelerate and collide heavy ions. ALICE (A Large Ion Collider Experiment) [23] is dedicated to the study of heavy ion collisions and of the quark-gluon plasma, a state consisting of free quarks and gluons. During the startup phase, the LHC will operate only at a center-of-mass energy of $\sqrt{s} = 7\,\text{TeV}$ to allow for safe commissioning of the accelerator. Subsequently, the center-of-mass energy will be increased up to the design value of $\sqrt{s} = 14\,\text{TeV}$. At the beginning, the LHC will also operate at relatively low instantaneous luminosities of $\mathcal{L} = 10^{30} - 10^{32}\ \text{cm}^{-2}\,\text{s}^{-1}$,

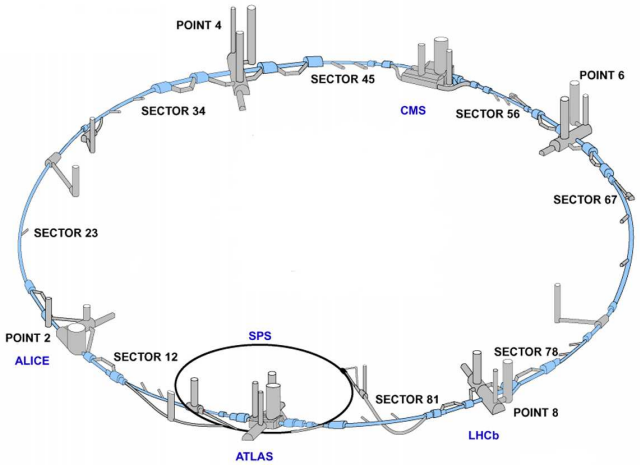

Figure 3.1: Schematic layout of the LHC at CERN.

with the luminosity being defined by beam parameters such as the number of particles per bunch N_b, the number of bunches per beam n_b and the revolution frequency f_{rev} as $\mathcal{L} \propto N_b^2 n_b f_{rev}$. The event rate of a physics process is then given by:

$$\frac{dN}{dt} = \mathcal{L} \cdot \sigma(\sqrt{s}) \tag{3.1}$$

with σ denoting the cross section of the physics process at the proton-proton center-of-mass energy $\sqrt{s}$. After this initial phase, the luminosity will first be increased to $\mathcal{L} = 10^{33}\,\mathrm{cm}^{-2}\,\mathrm{s}^{-1}$ before the LHC will finally reach its design luminosity of $10^{34}\,\mathrm{cm}^{-2}\,\mathrm{s}^{-1}$ which corresponds to an integrated luminosity of approximately $100\,\mathrm{fb}^{-1}$ per year. To achieve the design luminosity, 2835 bunches of 10^{11} protons are accelerated in each direction leading to bunch crossings every 25 ns at the interaction points. In this case, on average 23 inelastic proton-proton collisions will take place at each bunch crossing. Thus, each interesting physics event will be overlaid on average by 22 so-called pile-up events. This high interaction rate and the therefore very high particle production rate impose an unprecedented technical challenge on all the experiments.

3.1 The ATLAS Detector

ATLAS (A Toroidal LHC ApparatuS) is one of the two general-purpose detectors at the LHC designed to study a broad spectrum of physics processes. The detector design is largely driven by an optimal discovery potential for the Higgs boson. However, proton-proton collisions at the LHC allow for the exploration of various other Standard Model processes and, furthermore, of phenomena beyond the Standard Model.

- **Precision measurements:** Already at low integrated luminosities, precise measurements of the W- and Z-boson masses and production cross sections are possible

and allow for the calibration and for performance measurements of all detector components.

- **Top physics:** The top quark has been discovered by the experiments at the Tevatron in 1995 [24, 25]. The expected top-quark production cross section at the LHC surpasses the one at Tevatron by two orders of magnitude allowing for very precise measurements of its mass, production cross section and decay branching ratios.
- **Higgs physics:** The LHC experiments provide access to a mass range up to 1 TeV for searches for the Higgs boson in the Standard Model and beyond and will therefore provide insight into the question of the origin of the particle masses.
- **Supersymmetry:** Supersymmetry (SUSY) [9,10] is a extensively studied extension of the Standard Model which has not been observed yet experimentally. The Minimal Supersymmetric Standard Model (MSSM) is the most favored supersymmetric extension of the Standard Model. Discovery of SUSY is already possible with an integrated luminosity of $1\,\mathrm{fb}^{-1}$ for favorable combinations of model parameters [26], because of relatively large production cross sections and the clear signature of large missing energy in the detector due to the lightest supersymmetric particle (LSP), which is stable and weakly interacting, escaping detection.
- **Beyond the Standard Model:** Besides Supersymmetry, signatures of various other new physics processes beyond the Standard Model will be searched for by the LHC experiments. New phenomena discoverable by ATLAS are, for instance, new heavy gauge bosons W' and Z' with masses up to $\sim 6\,\mathrm{TeV}$, rare decays of heavy quarks and leptons as well as mini black holes and other consequences of extra spatial dimensions.

Figure 3.2 shows the production cross sections of the most important Standard Model processes. The search for rare processes with very low cross sections such as the Higgs boson production or processes predicted by theories beyond the Standard Model is hampered by several orders of magnitude more frequent processes such as b- and top-quark, QCD jet or W- and Z-boson production. While being interesting subjects of high precision Standard Model measurements themselves, these processes constitute large backgrounds to the search for rare processes.
The high particle rates at the LHC are very demanding for the detector design and construction requiring fast and radiation-hard detector technologies and electronics, very precise tracking and momentum measurement, large calorimeter coverage with precise jet and missing transverse energy measurement as well as a very selective trigger system which has to provide strong reduction of the event rate while efficiently selecting interesting physics events.
A schematic view of the ATLAS detector is shown in Figure 3.3. It consists of three major subsystems which are arranged cylindrically around the beam pipe. The design performances of the different subsystems are listed in Table 3.1. Based on References [20, 28], they will be described in more detail in the following sections. From the inside to the outside the main detector systems provide:

- **Inner Detector (ID):** Tracking as well as momentum and charge measurement of charged particles,

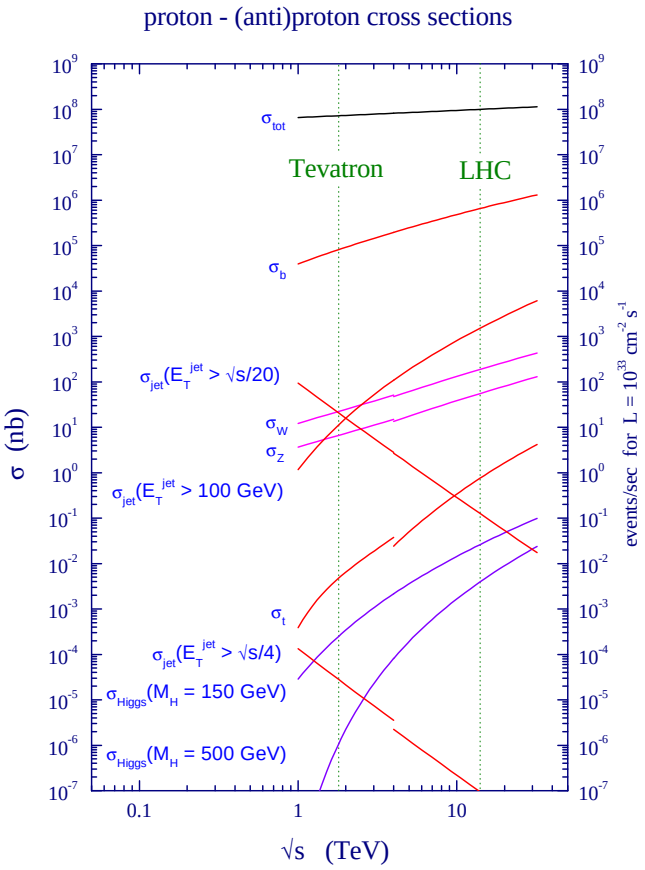

Figure 3.2: Production cross sections and event rates for the dominant processes in proton-(anti)proton collisions as a function of the center-of-mass energy $\sqrt{s}$ at a luminosity of $10^{33}\ \mathrm{cm}^{-2}\,\mathrm{s}^{-1}$ [27]. The discontinuities in the curves at $\sqrt{s} = 4\,\mathrm{TeV}$ are due to the different colliding particles: $p\bar{p}$ at the Tevatron and pp at the LHC.

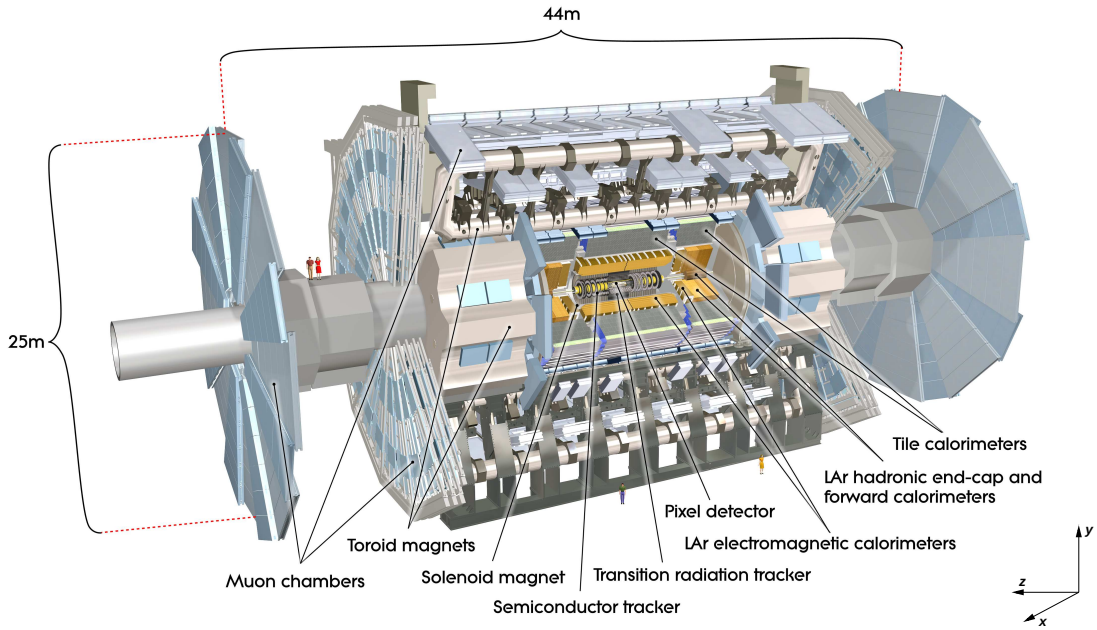

Figure 3.3: Cut-away view of the ATLAS detector.

Detector component	Required resolution	$\lvert\eta\rvert$ coverage
Inner detector	$\sigma_{p_T}/p_T = 0.05\% \, p_T \oplus 1\%$	≤ 2.5
EM calorimeter	$\sigma_E/E = 10\%/\sqrt{E} \oplus 3\%$	≤ 3.2
Hadron calorimeter		
Barrel and end-cap	$\sigma_E/E = 50\%/\sqrt{E} \oplus 3\%$	≤ 3.2
Forward region	$\sigma_E/E = 100\%/\sqrt{E} \oplus 10\%$	$3.1 < \lvert\eta\rvert < 4.9$
Muon spectrometer	$\sigma_{p_T}/p_T = 10\%$ at $p_T = 1\,\text{TeV}$	≤ 2.7

Table 3.1: Design performance of the ATLAS detector subsystems [20]. The energy E and transverse momentum p_T are given in GeV.

- **Calorimeter System (CS):** Identification and energy measurement of electrons, photons and hadron jets,
- **Muon Spectrometer (MS):** Identification, tracking as well as stand-alone momentum and charge measurement of muons.

Each subdetector consists of three parts: a cylindrically shaped barrel part and two end-caps enclosing the barrel on both sides.

3.1.1 The Coordinate System

The origin of the ATLAS coordinate system is located at the nominal interaction point (IP). The x-axis points from the origin towards the center of the LHC ring while the y-axis points upwards. The z-axis is pointing along the beam axis with the orientation chosen such that the coordinate system is right-handed as shown in Figure 3.3. The A-side of the detector is defined as the hemisphere with $z > 0$ whereas $z < 0$ defines the C-side.

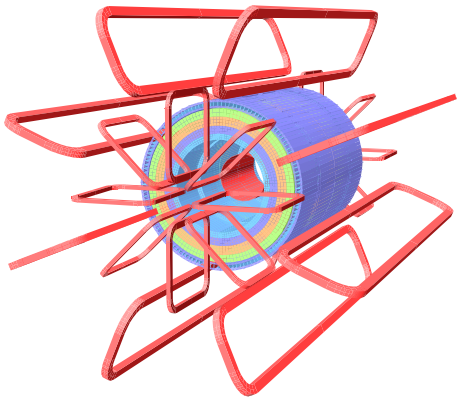

Figure 3.4: Sketch of the ATLAS magnet system with the central solenoid and the three toroids.

The azimuthal angle ϕ is the angle in the x-y plane with respect to the positive x-axis whereas the polar angle θ is defined with respect to the positive z-axis. An important variable in high-energy physics at hadron colliders is the so-called *rapidity*:

$$y = \frac{1}{2} \ln \frac{E - p_z}{E + p_z} \tag{3.2}$$

which is invariant under Lorentz transformations along the z-axis. In the limit of small masses it simplifies to the frequently used *pseudo-rapidity*:

$$\eta = -\ln \tan \frac{\theta}{2}. \tag{3.3}$$

ϕ and η are the commonly used coordinates for physics objects in ATLAS with the distance ΔR in the η-ϕ-space defined as:

$$\Delta R = \sqrt{\Delta\eta^2 + \Delta\phi^2}. \tag{3.4}$$

In proton-proton collisions, the momentum of the incoming partons is unknown. The momentum components in x- and y-direction can, however, be assumed to be zero. Thus, the center-of-mass system of the interaction is not known and quantities defined in the transverse (x-y) plane to the z-axis, are of particular importance. Transverse variables used throughout this work are for instance, the transverse momentum p_{T}, the transverse energy E_{T} and the missing transverse energy $E_{\mathrm{T}}^{\mathrm{miss}}$.

3.1.2 The Magnet System

The magnetic field, essential to measure particle momenta, is provided by a superconducting magnet system shown in Figure 3.4.
The inner tracking detector is surrounded by the central superconducting solenoid which is operated at a temperature of 4.5 K and generates a 2 T solenoidal magnetic field at a nominal operating current of approximately 7.7 kA. The solenoid coil extends 5.8 m in length and 2.6 m in diameter. Since it is placed between the tracking detector and the electromagnetic calorimeter, the design of the central solenoid has to minimize the amount

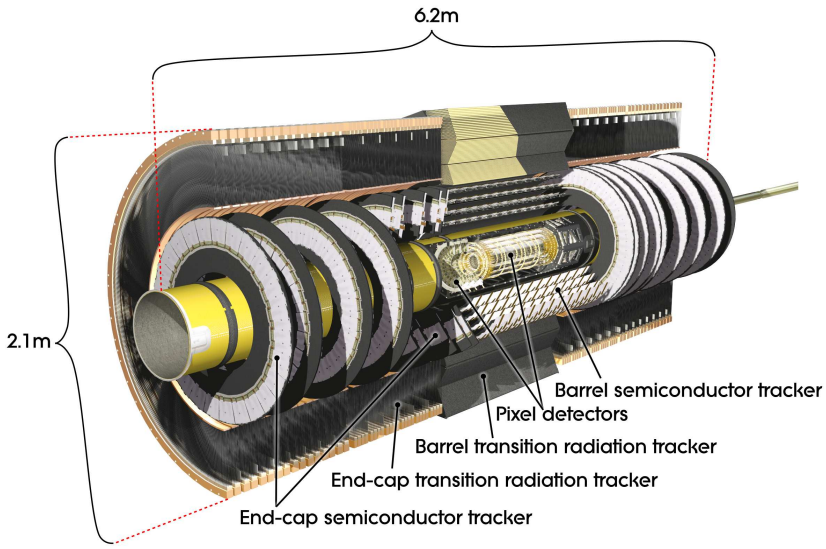

Figure 3.5: Cut-away view of the ATLAS inner detector.

of material in order to allow for a precise energy measurement of particles reaching the calorimeter. Therefore, the solenoid shares one vacuum vessel with the electromagnetic calorimeter exploiting its iron absorbers as return yoke.
The magnetic field for the muon spectrometer is provided by three large air-core toroid magnets (25 m long in the barrel and 5 m long in the two end-caps), each of them consisting of eight coils arranged symmetrically around the beam axis. The two end-cap toroids are placed in the forward regions of the detector inside the barrel toroid. While for each of the end-cap toroids all eight magnet coils are housed in the same vacuum vessel, each of the barrel toroid coils is housed in an individual cryostat. All three toroids are operated at a nominal current of 20.5 kA. The barrel toroid provides a magnetic field strength between 0.2 T and 2.5 T in the region $|\eta| < 1.4$ whereas the end-cap toroids provide a field of $0.2 - 3.5$ T in the region $1.6 < |\eta| < 1.7$. In the transition region $1.4 < |\eta| < 1.6$ where the magnetic fields overlap, the field strength is lower. An air core magnet system has been chosen in order to minimize material the muons have to traverse and hence the multiple scattering which deteriorates the muon momentum resolution.

3.1.3 The Inner Detector

At the LHC design luminosity of $10^{34}\,\mathrm{cm}^{-2}\,\mathrm{s}^{-1}$, every 25 ns approximately 1000 tracks will emerge from the collision point within $|\eta| < 2.5$ creating a large track density in the detector. Fast and highly granular detectors are used to provide precise momentum measurement of charged particles as well as accurate reconstruction of secondary vertices close to the beam pipe. This is achieved by semiconductor pixel and strip tracking detectors (SCT) which cover the region $|\eta| < 2.5$ and are surrounded by the Transition Radiation Tracker (TRT) as shown in Figure 3.5. The silicon pixel detector, the innermost part, provides an intrinsic resolution of 10 μm in the transverse and of 115 μm in the longitudinal direction. It is arranged in three concentric cylindrical layers in the barrel part and

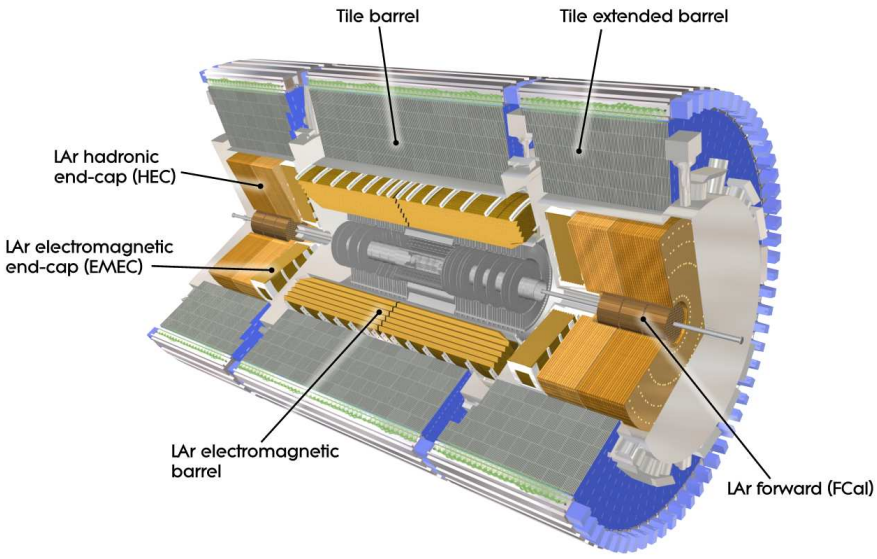

Figure 3.6: Cut-away view of the ATLAS calorimeter system.

four discs in each end-cap. The pixel detector is enclosed by four SCT barrel layers and two times nine end-cap discs providing a position resolution of 17 μm in the transverse direction and of 580 μm in the longitudinal direction, respectively. The high granularity entails a large number of readout channels, 80.4 million channels in the pixel detector and 6.3 million channels in the SCT. The outermost part of the inner detector, the TRT, covers a region of $|\eta| < 2.0$ and consists of 4 mm diameter kapton straw tubes with 30 μm thick tungsten-rhenium anode wires and a $Xe/CO_2/O_2$ gas mixture. It provides typically 36 hits per track with an intrinsic resolution per straw of 130 μm in the R-ϕ plane.

3.1.4 The Calorimeter System

The ATLAS calorimeter system shown in Figure 3.6 consists of the electromagnetic calorimeter (ECAL) followed by the hadron calorimeter (HCAL). Both calorimeters are sampling calorimeters constructed of alternating layers of an active medium and of passive absorber material in order to measure the energy of absorbed particles.
The electromagnetic calorimeter identifies electrons and photons and precisely measures their energies. It comprehends a barrel part covering the region $|\eta| < 1.5$ and two end-cap calorimeters (EMEC, $1.4 < |\eta| < 3.2$) all using liquid argon (LAr) as the active medium and lead as the absorber material arranged in accordion-like shape in order to achieve homogeneous ϕ-coverage.
The hadron calorimeter comprises a tile calorimeter and two liquid argon end-cap calorimeters (HEC). The tile calorimeter consists of a barrel part ($|\eta| < 1.0$) and two extended barrels ($0.8 < |\eta| < 1.7$) employing steel as absorber and scintillating tiles as active material. Radially, the tile calorimeter extends from an inner radius of 2.28 m to an outer radius of 4.25 m. Because the irradiation doses are too high for scintillators in the end-cap region, liquid argon is used there as active material and copper as absorber. The end-

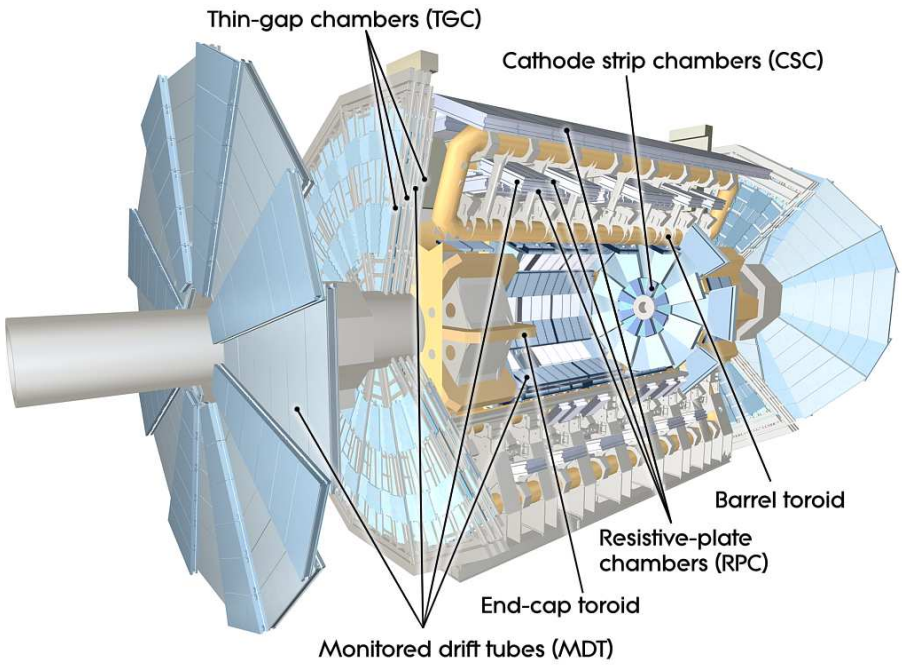

Figure 3.7: Cut-away view of the ATLAS muon spectrometer.

cap calorimeter is composed of two independent wheels per end-cap, each built from 32 wedge-shaped modules, following behind the EMECs and sharing the same cryostats.
In the region $3.1 < |\eta| < 4.9$, LAr Forward Calorimeters are integrated in the end-cap cryostats, each consisting of an electromagnetic module (FCAL1) and two hadronic modules (FCAL2 and 3) using copper and tungsten as absorber material, respectively.
The total thickness of the calorimeter system is more than 22 radiation lengths (X_0) and approximately ten hadronic interaction lengths, which is required to achieve good containment for electromagnetic and hadronic showers with limited punch-through into the muon spectrometer. The thickness and the large η coverage (up to $|\eta| = 4.9$) of the calorimeter system provides accurate $E_{\mathrm{T}}^{\mathrm{miss}}$ measurement and high energy resolution for highly energetic jets.

3.1.5 The Muon Spectrometer

The layout of the muon spectrometer is shown in Figure 3.7. The purpose of this outermost subdetector is to provide a precise muon momentum measurement based on the magnetic deflection of muon tracks in the magnetic field generated by the three air-core toroids (Section 3.1.2). The muon spectrometer is instrumented with dedicated Trigger Chambers, Resistive Plate Chambers (RPC) in the barrel region and Thin Gap Chambers (TGC) in the end-cap region. Monitored Drift Tube (MDT) chambers and Cathode Strip Chambers (CSC) serve as high precision tracking chambers in the barrel and the end-cap regions, respectively. The muon chambers in the barrel region are arranged in three cylindrical layers around the beam axis whereas the chambers in the end-cap regions are installed in four planes perpendicular to the beam axis.

The design based on air-core toroids has been chosen to minimize multiple scattering and thus, to allow for a stand-alone measurement of the muon momentum and direction. However, in order to achieve higher precision and efficiency, in particular for low-p_{T} muons, also inner detector and calorimeter measurements are exploited in the muon reconstruction.
Since the alignment of the muon spectrometer is a major subject of this thesis, Section 3.2 provides a more detailed description of the design and the instrumentation of the ATLAS muon spectrometer.

3.1.6 Trigger and Data Acquisition

The high luminosity of the LHC imposes an enormous technical challenge on the trigger and data acquisition system in order to reduce the event rate by efficiently selecting and recording interesting physics events. With an average event size of approximately 1.3 Mbyte, the ATLAS computing system is capable of handling a final event rate of 200 Hz which has to be met by the output of the trigger system.
The trigger selection proceeds in three consecutive levels, L1, L2 and the event filter, each level refining the trigger decision of the previous one. The first level (L1) is completely hardware based and uses only a limited amount of detector information to provide a trigger decision in less than 2.5 μs. It exploits trigger information provided by the muon spectrometer and the calorimeters at a reduced granularity. The selection criteria and thresholds are chosen to select events with high-p_{T} muons, electrons, photons, jets and hadronically decaying τ-leptons as well as large missing and total transverse energy. The selected events with their associated Regions-of-Interest (RoI), i. e. the regions in the detector where interesting patterns have been identified, are passed to the second trigger level (L2) at a rate of 75 kHz. The L2 selection criteria have been chosen such that the event rate is reduced to 3.5 kHz at an event processing time of 40 ms. The selection is based on the detector information at full granularity and precision within the RoIs ($\sim 2\%$ of the data). The full detector information for events selected by the L2 trigger is collected by the event builder and passed to the event filter (EF). This third step of the event selection is entirely software based and is running on a dedicated computer farm. Offline event reconstruction algorithms are employed and the final trigger decision is provided at an event processing time on the order of four seconds and at a final event rate of 200 Hz. Events selected by the trigger system are recorded on mass-storage devices for further processing and physics analyses. One year of ATLAS data taking at the LHC amounts to a data volume of approximately 1 Pbyte. The data volume recorded by all experiments at the LHC cannot be stored and processed by one local computing center alone. Therefore, after initial processing at CERN, the recorded data is distributed to many computing centers outside CERN which together form the LHC Computing Grid (LCG), a worldwide computing framework [29, 30].

3.2 The ATLAS Muon Spectrometer

The muon spectrometer is designed to detect muons with transverse momenta larger than 3 GeV and to measure muon transverse momenta with a resolution of better than 3-4% in the range of 10 GeV $< p_{\mathrm{T}} <$ 500 GeV and of better than 10% for transverse momenta up

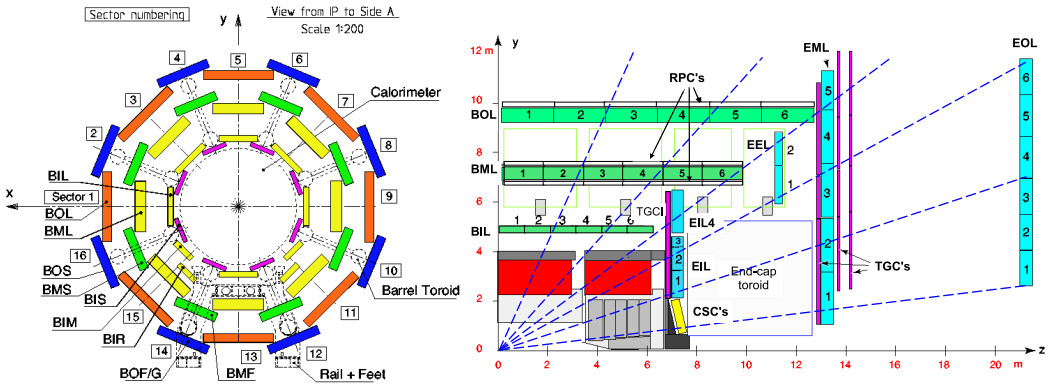

Figure 3.8: Cross section of the muon spectrometer in the x-y plane perpendicular to the beam pipe (left) and in the y-z plane (one quadrant) which is the bending plane of the muons (right).

Type	Function	Chamber resolution			Measurements/track		Number of
		z/R	ϕ	Time	Barrel	End-cap	chambers
MDT	tracking	35 μm (z)	-	-	20	20	1150
CSC	tracking	40 μm (R)	5 mm	7 ns	-	4	32
RPC	trigger	10 mm (z)	10 mm	1.5 ns	6	-	606
TGC	trigger	2-6 mm (R)	3-7 mm	4 ns	-	9	3588

Table 3.2: Performance of the four subsystems of the muon spectrometer [20].

to 1 TeV. These strong requirements on the precision are imposed by the ATLAS physics goals.

The trajectories of muons are determined by measurements in three consecutive layers of precision tracking chambers. As shown in Figure 3.8, the tracking chambers are installed in the barrel on and between the toroid coils in three layers at radii of approximately 5 m, 7.5 m and 10 m. In the end-cap regions, the chambers are arranged in wheels perpendicular to the beam axis at distances of 7.4 m, 10.8 m, 14 m and 21.5 m. In ϕ the muon spectrometer can be subdivided into 16 sectors with alternating small and large chambers. In both η-hemispheres of the barrel, each layer consists of six chambers which extend up to pseudo-rapidities of $|\eta| = 1$. Table 3.2 summarizes the different chamber types employed in the ATLAS muon spectrometer and the spatial resolution they provide. The following sections provide a more detailed description of the four different chamber types.

3.2.1 Precision Tracking Chambers

The precision measurements of the track coordinates are provided by Monitored Drift Tube (MDT) chambers over most of the η-range and by Cathode Strip Chambers (CSC) in the innermost layer of the very forward region ($2.0 < |\eta| < 2.7$), since in this region the particle counting rates exceed the limit of a safe operation of the MDT chambers of 500 Hz/cm^2. The MDT chambers will be described in detail in Section 3.2.3.

CSCs are multi-wire proportional chambers with a cathode strip readout. They are filled with an Ar/CO_2 (80/20) gas mixture with 40 ns maximum drift time and can be safely operated up to counting rates of 1700 Hz/cm^2. Each CSC layer comprises eight small and

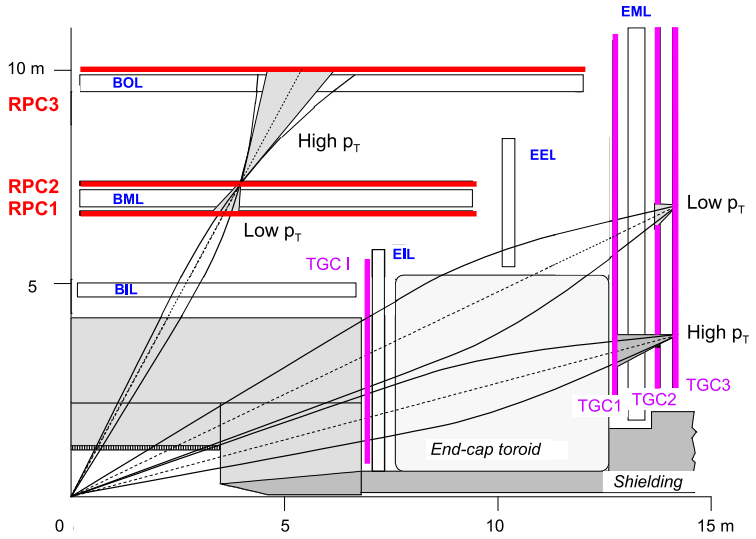

Figure 3.9: Schematic view of the muon trigger system.

eight large chambers. The CSCs provide a position resolution in the bending plane of 60 μm.

3.2.2 Trigger Chambers

The trigger chambers have to provide fast information on the transverse momentum of muon tracks traversing the muon spectrometer to be used in the L1 trigger logic. In addition, they have to provide bunch-crossing identification and a measurement of the second coordinate perpendicular to the bending plane of the muon track which both cannot be provided by the MDT chambers. The muon trigger system covers the full ϕ-range and the pseudo-rapidity range up to $|\eta| = 2.4$.

Muon momenta corresponding to a given p_{T} are strongly increasing with η and the end-cap trigger layers are located outside the magnetic field (see Figure 3.9). Furthermore, the background rates in the end-cap regions excel the ones in the barrel on average by a factor ten. Hence, in order to obtain a constant p_{T}-resolution over the covered η-range, different detector technologies and granularities have to be employed depending on the location of the chamber. Resistive Plate Chambers (RPC) are used in the barrel region ($|\eta| < 1.05$) and Thin Gap Chambers (TGC) in the end-cap regions ($1.05 < |\eta| < 2.4$).

Figure 3.9 shows the schematic layout of the muon trigger system. The barrel trigger system consists of three layers of RPCs located below and above the middle MDT layer (RPC1 and RPC2) and above (below) the outer MDT layer in the large (small) sectors (RPC3). In the end-cap regions, three TGC planes provide trigger information. One in front (TGC1) and two behind (TGC2 and TGC3) the second MDT wheel. The TGCI layer only provides the measurement of the second coordinate for the inner end-cap MDT layer. The trigger is generated by coincidence patterns which correspond to certain curvatures of the tracks and are used as a criterion that the track passes a certain p_{T} threshold. A measure of the curvature, i. e. the deviation of the track from straightness, is the difference

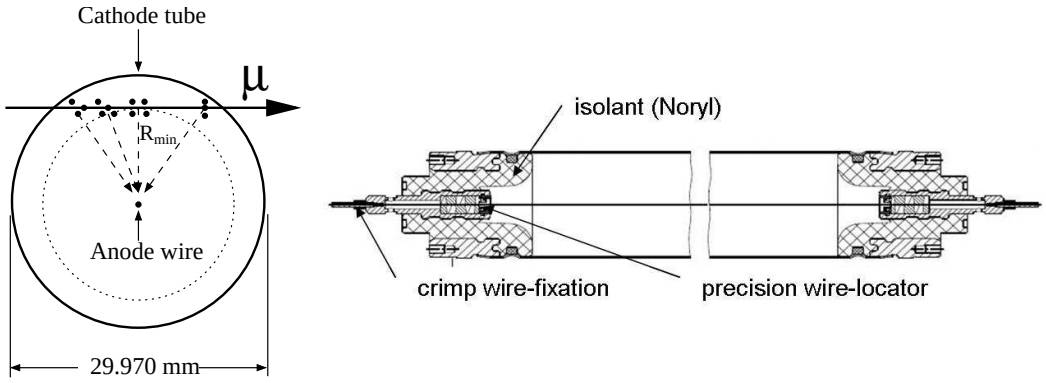

Figure 3.10: Radial (left) and longitudinal (right) cross sections of a MDT tube.

of the slope of the track segment between two trigger chambers and the slope of the straight line from the interaction point to a hit on the track in the reference (pivot) plane which is the RPC2 plane in the barrel and the TGC3 plane in the end-caps. For example in the barrel, for the low (high)-p_{T} trigger the slope of the track segment between hits in the RPC2 and RPC1 (RPC3) plane is compared to the slope of the straight line between the interaction point and the hit in the RPC2 plane.
An RPC consists of two parallel resistive bakelite plates spanning a 2 mm wide gas gap filled with a $C_2H_2F_4$/Iso-C_4H_{10}/SF_6 (94.7/5/0.3) gas mixture. Avalanches form along the ionizing track in the high electric field of 4.9 kV/mm between the plates. The corresponding signal with a width of about 5 ns at the operating voltage of 9.8 kV is read out by two orthogonal layers of pick-up strips. An RPC chamber is composed of two adjacent detector layers (gas volumes).
TGCs are multi-wire proportional chambers where the wire-pitch distance of 1.8 mm is larger than the wire-cathode distance of 1.4 mm, in contrast to the CSCs. The TGCs are filled with a 55/45 CO_2 and n-C_5H_{12} (n-pentane) gas mixture and are operated at 2900 V. The trigger information is provided by signals from the anode wires oriented parallel to the MDT tubes together with the orthogonally oriented cathode readout strips which also provide the measurement of the second coordinate.

3.2.3 The Monitored Drift Tube Chambers

1150 MDT chambers cover a total detector area of 5500 m^2 serving as the main precision tracking chambers in the muon spectrometer. The basic detector elements of the MDT chambers are aluminum drift tubes with an outer diameter of 29.97 mm and a wall thickness of 400 μm. A gold-plated tungsten-rhenium sense wire with a diameter of 50 μm is centered at the tube ends by cylindrical endplugs which provide a positioning accuracy of the wire with respect to an external reference on the endplugs of below 10 μm (see Figure 3.10). The tubes are filled with an Ar/CO_2 (97/3) gas mixture at a pressure of 3 bar. A high voltage of 3080 V is applied between wire and tube wall creating a radial electric field.
A muon traversing the tube ionizes the detector gas leading to stochastically distributed charge clusters along the track. The positively charged ions drift towards the tube wall

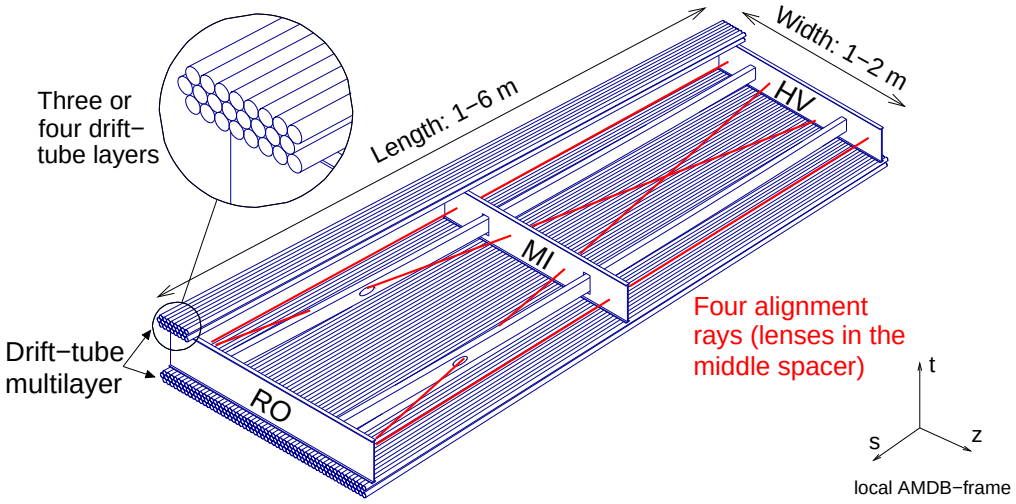

Figure 3.11: Layout of a barrel MDT chamber. End-cap MDT chambers have a trapezoidal instead of a rectangular shape.

whereas the electrons drift to the anode wire. In a region up to a radius of 150 μm around the wire, the accelerated electrons cause secondary ionizations leading to avalanche charge multiplication with an amplification factor (gas gain) of $2 \cdot 10^4$. Due to this very short drift distance of the secondary electrons, the electron signal induced on the anode wire is very short and cannot be detected by the read-out electronics. Only the current signal induced by the secondary ions drifting from the avalanche region to the tube wall is measured.

The time difference between the rising edge of the induced signal and the bunch-crossing time, after corrections for the muon flight time and the signal propagation time in the wire, corresponds to the time the primary electrons needed to reach the anode wire, the so-called *drift time*. The drift time is then translated into the *drift radius* r, the distance of closest approach between the muon trajectory and the anode wire, by employing the space-to-drift time relationship $r(t)$. Hence, the position resolution of the drift tubes depends on the accuracy in the determination of the time offsets (t_0) and of the $r(t)$-relationship of the drift tubes. The latter depends on the operation conditions, e. g. gas temperature and pressure, magnetic field strength and background counting rate. The $r(t)$-relationship is therefore determined in regular time intervals (typically 24 hours) by means of an autocalibration procedure exploiting muon tracks detected in the MDT chambers [31].

MDT chambers are composed of two multilayers of drift tubes mounted on an aluminum support frame as shown in Figure 3.11 for a typical barrel chamber. In the middle and outer barrel chambers a multilayer comprises three tube layers whereas the multilayers in the inner barrel chambers are built up from four tube layers in order to cope with the higher particle rates.

Only very accurate knowledge of the wire position inside a chamber allows for a muon reconstruction with the required accuracy. Chamber deformations caused, for example, by thermal expansion or temperature gradients can lead to a degradation of the muon momentum resolution. This necessitates the continuous monitoring of chamber deformations by means of optical imaging systems. These optical in-plane alignment systems comprehend diagonal and longitudinal light rays where the image of a mask illuminated by an

infrared LED at one end of the chamber is projected by a lens onto a CMOS pixel sensor at the opposite end (see Figure 4.3). Deformations of the chamber lead to shifts of the mask pattern on the sensor which are measured with a few μm precision.

Chamber Naming Convention

The naming convention of the MDT chambers describes their location in the muon spectrometer. For instance, the location of the chamber with the name BMS2A04 is identified according to the following scheme:

- The leading letter 'B' identifies chambers in the barrel part of the muon spectrometer while chambers in the end-caps have the leading letter 'E'.
- The spectrometer comprises three layers of muon chambers, the inner (I), middle (M) and outer (O) layer.
- As shown in Figure 3.8, the muon spectrometer is subdivided in 16 azimuthal sectors with alternating sectors of small (S) and large chambers (L). The last number in the chamber name denotes the sector number. Even numbers refer to small and odd numbers to large sectors.
- Each sector comprises at least 12 chambers per layer in beam direction divided into the A- and C-hemisphere of the detector (Figure 3.8). The label of the detector hemisphere is preceded by the chamber number (η-index) starting from the center of the detector ($\eta = 0$) in both hemispheres.

Hence, the chamber BMS2A04 is a small barrel chamber at the second position on the A-side of the detector, in the middle layer of sector 4.

Local Chamber Coordinate System

In addition to the global coordinate system introduced in Section 3.1.1, a local coordinate system is defined for each MDT chamber which is employed for the alignment of MDT chambers described in Chapter 4. The local chamber coordinate system, also referred to as local-AMDB[1] system, is depicted in Figure 3.11. It is a right-handed coordinate system with the s-axis oriented in tube direction. The local z-axis corresponds to the precision coordinate perpendicular to the tube axis in the chamber plane. In the barrel part of the muon spectrometer, the direction and orientation of the local z-axis agrees with the global z-axis. The local t-axis is oriented perpendicular to the chamber plane away from the interaction point. The origin of the local coordinate system lies in the middle of the chamber along the s-axis at the chamber edge closest to the interaction point along the z- and t-axes.

Chapter 4 provides a more detailed description of the muon track reconstruction and the measures taken in order to achieve the required momentum resolution.

[1] AMDB - **A**TLAS **M**uon **D**ata **B**ase

Chapter 4

Alignment of the ATLAS Muon Spectrometer

The ATLAS muon spectrometer is designed to measure muon transverse momenta with a resolution of better than 3%-4% in the range of $10\,\text{GeV} < p_\text{T} < 500\,\text{GeV}$ and of better than 10% for transverse momenta up to 1 TeV [32] driven by the ATLAS physics goals described in Chapter 3. This imposes stringent requirements on the calibration and alignment accuracy of the precision tracking chambers.

This chapter details the measures taken in order to achieve the required alignment accuracy of the MDT chambers. The alignment strategy for the ATLAS muon spectrometer, described in Section 4.1, is based on an optical alignment system complemented by alignment algorithms exploiting muon tracks. In Section 4.2, an alignment algorithm is introduced which is based on a global χ^2 fit employing curved muon tracks during ATLAS data taking. The application of this approach to chambers without full optical alignment in the barrel muon spectrometer is described in Section 4.3. Section 4.4 gives prospects for future developments necessary in order to achieve the required alignment accuracy for all MDT chambers in the barrel muon spectrometer.

4.1 Alignment Strategy

The alignment of the muon spectrometer is mainly based on an optical alignment system. However, since part of the MDT chambers is not fully connected to the optical alignment system and therefore cannot be accurately aligned with the optical system alone, track-based alignment is necessary in addition in order to achieve the required alignment precision for all MDT chambers in the muon spectrometer. Furthermore, track-based alignment provides independent information about the chamber positions during data taking. This section describes the reconstruction of muons in the muon spectrometer, the requirements on the alignment precision as well as the optical alignment system and the role of track-based alignment methods. The discussion concentrates on the barrel part of the muon spectrometer.

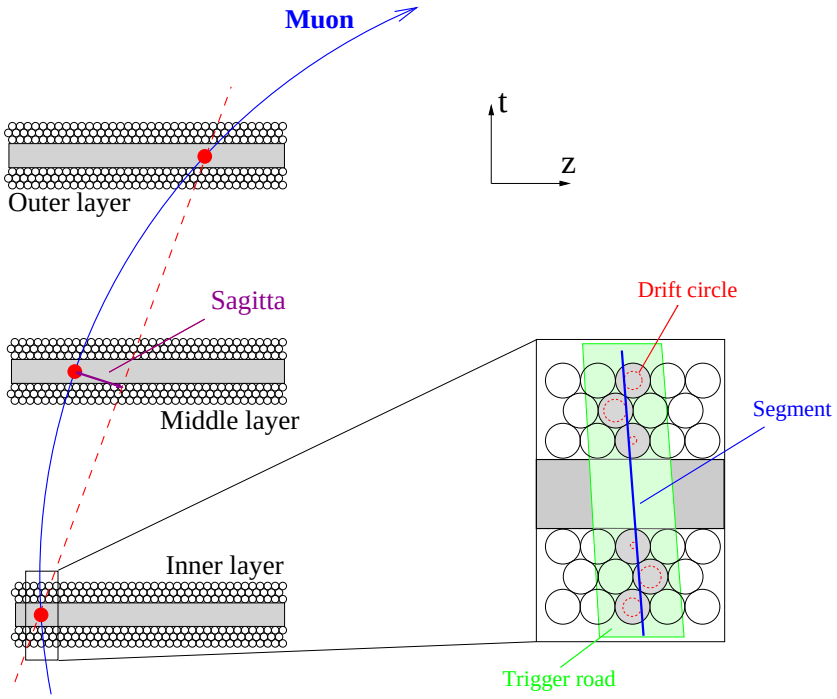

Figure 4.1: Illustration of the track sagitta measurement in the barrel muon spectrometer [33].

4.1.1 Muon Reconstruction and Alignment Requirements

Muons are reconstructed in the muon spectrometer mainly based on the precision track measurements in the MDT chambers. The coordinate perpendicular to the bending plane along the drift tubes is measured by the trigger chambers. A measurement in a drift tube yields a drift radius to which the muon track is tangential. Based on the individual tube measurements within one chamber, straight muon track segments are reconstructed. The trajectory of the muon is determined by combining the track segments of the three consecutive layers of precision tracking chambers.
In the barrel region of the muon spectrometer, the sagitta s serves as a measure for the momentum of the muon track. The sagitta is the deviation of the muon trajectory from a straight line connecting the track points in the inner and outer tracking chambers in the bending plane of the magnetic field B (see Figure 4.1). For a homogeneous magnetic field, the dependence of the momentum p on the sagitta is given by [34]:

$$p = \frac{0.3BL^2}{8s} \text{ [GeV, T, m]}, \tag{4.1}$$

with L denoting the distance between the track points in the inner and outer chambers. Hence, a required p_{T} resolution of better than 10% translates into a minimum required accuracy of the sagitta measurement of $\Delta s = 50\,\mu$m for a muon transverse momentum of 1 TeV corresponding to $s = 500\,\mu$m. Figure 4.2 shows the expected momentum resolution depending on the transverse momentum of the muon. In the low p_{T} region, the

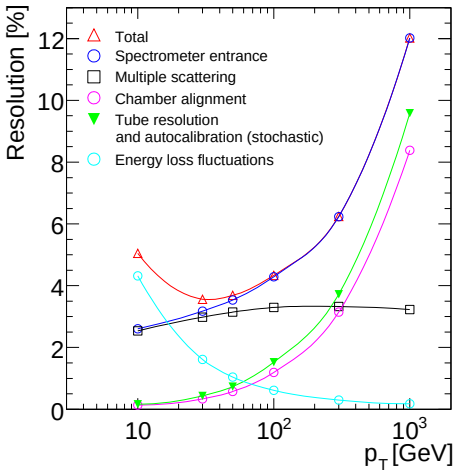

Figure 4.2: Contributions to the muon momentum resolution in the ATLAS muon spectrometer as a function of the transverse momentum for $|\eta| < 1.5$. The contribution of the chamber alignment assumes an uncertainty of 30 μm on the sagitta measurement [32].

contributions from multiple scattering in the muon chambers and support structures and from energy loss fluctuations in the calorimeter are dominant, which can be improved by combining inner detector and muon spectrometer measurements. For high-p_{T} muons, the spatial resolution of the MDT chambers including the calibration accuracy and the alignment precision become the dominant contributions to the momentum resolution.
In order to fulfill the requirement of a sagitta resolution of better than 50 μm, the MDT chambers need to have a spatial resolution of better than 35 μm. Furthermore, the sagitta error due to uncertainties in the *relative* positions of the muon chambers traversed by the track has to be less than 30 μm. The *absolute* position of the MDT chambers in the ATLAS coordinate system has to be known less precisely (at the level of 1 mm), mainly for a precise measurement of the magnetic field by the sensors mounted on the chambers, for pattern recognition in the high background environment at the LHC design luminosity and for the alignment with respect to the inner detector and the interaction point.

4.1.2 The Optical Alignment System

The optical alignment system in the barrel muon spectrometer [20, 35] is based on optical three-point straightness monitors, the RasNiK[1] sensors (see Figure 4.3). Various alignment subsystems constrain different degrees of freedom.

The In-plane Alignment System

As discussed in Section 3.2.3, MDT chambers are equipped with an in-plane alignment system which monitors chamber deformations with an accuracy of better than 5 μm.

[1] RasNiK - **R**ed **a**lignment **s**ystem of **NIK**HEF

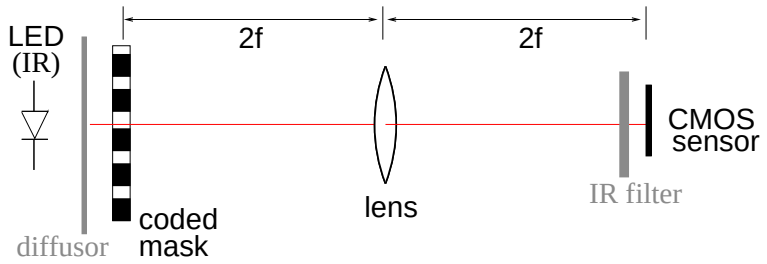

Figure 4.3: Principle of a RasNiK sensor consisting of a coded mask illuminated by an infrared LED, a lens and a CMOS image sensor. Relative changes of position of the three components lead to a shift of the mask pattern projected onto the CMOS sensor and can thus be measured with a precision of a few μm.

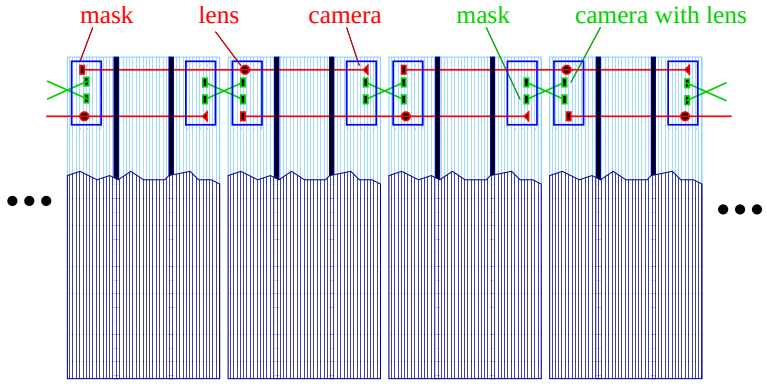

Figure 4.4: Layout of the proximity (green) and axial (red) sensor connections between adjacent chambers within one sector.

The Praxial Alignment System

Relative positions of adjacent chambers within one sector and layer are monitored by the praxial (proximity and axial) alignment system. As shown in Figure 4.4, the proximity sensors are mounted at the corner of the chambers creating two diagonal optical connections between neighboring chambers. The axial alignment system establishes optical connections parallel to the global z-axis on either side of the chambers monitoring the planarity of a chamber layer. The praxial system measures the relative positions and orientations of two adjacent chambers with accuracies of better than 10 μm and 30 μrad, respectively.

The Projective Alignment System

In order to accurately measure the momentum of a muon, the relative positions of the chambers traversed by the track have to be precisely known. The chambers in the muon spectrometer are arranged such that the chambers traversed by the muon form triplets with a projective geometry with respect to the nominal interaction point.
The projective alignment system is the central part of the optical alignment system since it interconnects the chambers in the inner, middle and outer layer with each other (Figure 4.5). The relative positions of chambers in the three layers are determined with an

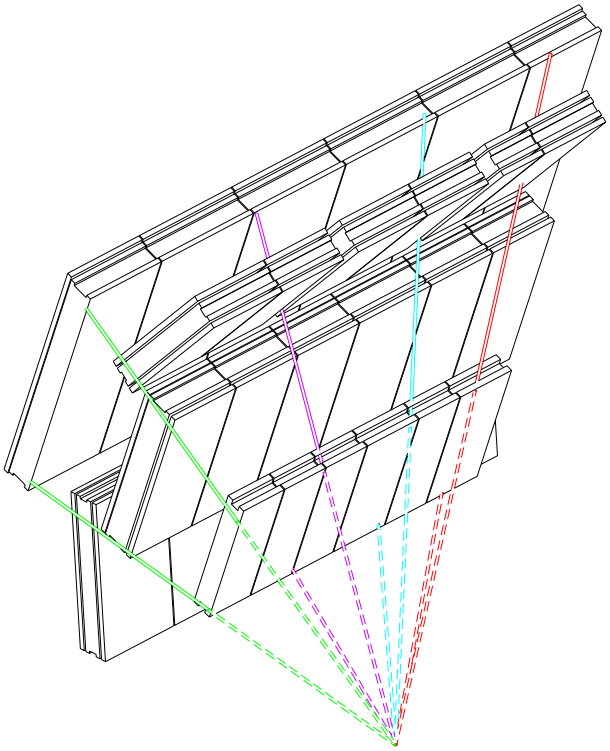

Figure 4.5: Layout of the projective alignment connections between the three chamber layers in the large barrel sectors.

accuracy of about 30 μm.
Due to geometric constraints, the chambers in the small sectors are not equipped with projective alignment sensors. Instead, their positions are monitored with respect to the adjacent large chamber layers by so-called chamber-to-chamber connections (CCC) with an accuracy on the order of 50 μm. The small chambers have to be aligned in addition with muon tracks traversing the overlap regions between the small and the precisely monitored large chambers in order to achieve the required alignment accuracy.

The Reference Alignment System

The optical alignment systems described precisely measure the relative positions of chambers with respect to each other. The absolute chamber positions in the ATLAS coordinate system have to be known less precisely, with an accuracy of about 1 mm. This is achieved by the reference alignment system which establishes optical connections between the chambers and the toroid coils. This allows for the determination of the absolute chamber positions and defines an absolute length scale with an accuracy of about 400 μm.

The End-cap Alignment System

The location of the cryostat of the end-cap toroid magnet between the inner and outer MDT end-cap wheels does not allow for a sufficient number of projective optical connections between the individual chambers. This problem is solved by employing a grid of eight precision alignment bars per MDT wheel relative to which the chamber positions are measured by optical connections. The straightness and thermal elongation of the aluminum bars are monitored by internal RasNiK and temperature sensors. The alignment bars within each wheel and in different wheels are optically connected which allows for a precise determination of the relative positions of all MDT chambers in the different end-cap wheels. No additional track-based alignment is required.

4.1.3 Track-Based Alignment

In addition to the optical alignment system, track-based alignment procedures are necessary to achieve the required alignment precision for all MDT chambers in the barrel muon spectrometer.

Calibration of the Optical Alignment System with Straight Tracks

In order to precisely determine the chamber positions and orientations, the optical sensors have to be mounted on the chambers with a precision of about 20 μm with respect to the MDT wires. Measurements of the platform positions using an X-ray tomograph have shown that a significant fraction of the sensors ($\sim$20%) does not meet this requirement with deviations of up to 500 μm [35]. Since, in contrast to the end-cap chambers, not all sensor positions for the barrel chambers could be measured, their calibration with tracks is indispensable. For this purpose, straight tracks from cosmic muons with the toroidal magnetic field switched off are used. Since not all chambers can be aligned with cosmic muons with the required accuracy, run periods without toroidal magnet field are foreseen at the beginning of the LHC operation in order to acquire sufficient statistics of straight

muon tracks to calibrate the optical sensors of all barrel MDT chambers with the required accuracy.

Overlap Alignment of Optically Insufficiently Monitored Chambers

Some barrel MDT chambers cannot be optically monitored with the required precision. For instance, the small barrel chambers are not equipped with a projective alignment system and, therefore, the optical alignment precision for these chambers is only on the order of 100 μm. Furthermore, certain chambers are not monitored by the optical alignment system at all. These chambers have to be aligned during ATLAS data taking with curved tracks traversing the overlap regions with chambers which are optically precisely aligned.

Barrel – End-cap Alignment

There is no optical connection between the barrel and the end-cap part of the ATLAS muon spectrometer. In order to obtain an optimal precision in the transition region, both parts have to be aligned with respect to each other exploiting overlap tracks traversing MDT chambers in the barrel as well as in the end-cap region.

Muon Spectrometer – Inner Detector Alignment

In order to achieve a good momentum resolution for muon tracks reconstructed in the inner detector (ID) and the muon spectrometer (MS), their relative position has to be known with a precision of about 1 mm. Since there is no optical connection, the MS-ID alignment has to be performed with muon tracks.

Several methods have been investigated in order to fulfill all the demands on the track-based alignment. In the context of this thesis, a global χ^2 minimization algorithm has been developed for the alignment of the MDT chambers and applied to the alignment of the small barrel chambers with respect to the neighboring, precisely optically aligned large chambers. During ATLAS data taking, the chamber positions will be constantly remeasured (about every 15 minutes) by the optical system. Muon tracks are then reconstructed taking into account the optical alignment corrections to the relative chamber positions. During the initial phase, alignment algorithms using curved tracks will only serve as additional verification of the optical alignment corrections. Later on, with sufficient statistics of reconstructed muons, track-based alignment corrections to the optically monitored chamber positions will be derived on a daily basis. These corrections will then be taken into account in the subsequent reprocessing of the recorded data.

4.1.4 The Muon Calibration Stream

The maximum rate of muon triggers after the event filter is 40 Hz. However, a dedicated muon calibration stream is extracted at the second trigger level (L2) with an acquisition rate of about 1 kHz. This allows for a daily calibration of the $r(t)$-relationship and at the same time for the track-based alignment of the muon spectrometer with about $30 \cdot 10^6$ muon tracks per day which corresponds roughly to 75,000 tracks per chamber triplet [37].

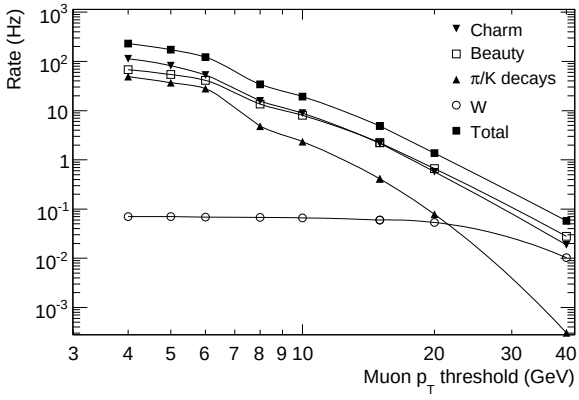

Figure 4.6: Expected muon trigger rates from different sources after the event filter at an initial instantaneous luminosity of 10^{31} cm^{-2} s^{-1} as a function of the transverse momentum threshold [36].

The expected muon trigger rates after the event filter are shown in Figure 4.6 for different p_{T} thresholds at low instantaneous luminosities of 10^{31} cm^{-2} s^{-1}. An exponential decrease of the trigger rate with increasing threshold is visible. At low luminosities, muon transverse momenta above 6 GeV will be required for the calibration stream. Hence, the calibration stream will predominantly comprise muons with transverse momenta of about 6 GeV. At increasing instantaneous luminosities, this threshold will be increased up to $p_{\mathrm{T}} = 20$ GeV in order to keep the calibration stream at a constant acquisition rate sufficient for the required calibration and alignment accuracy.

4.2 The Global χ^2 Alignment Algorithm

In the context of this thesis, a global χ^2 minimization algorithm for the alignment of the muon spectrometer has been developed. This method is successfully used for the alignment of the ATLAS inner detector. This section gives a brief description of the alignment software framework as well as an introduction to the global χ^2 method.

4.2.1 The Alignment Software Framework

Several algorithms have been developed within different tracking software frameworks in order to fulfill the demands on the track-based alignment of the MDT chambers including the alignment with straight [38] and curved tracks [33, 39] as well as the alignment of the muon spectrometer with respect to the inner detector. Also for the alignment of the inner detector, different methods are used such as the global χ^2 method [40, 41], the local χ^2 method [42, 43] and a so-called robust alignment approach [44].
To unify the efforts, a new alignment software framework has been developed into which the different alignment algorithms can be integrated. The generic structure of this framework allows for the individual and the combined alignment of the different subdetectors. Furthermore, it allows for the combination of detectors to alignable units. For instance, MDT chambers can be aligned individually with respect to each other or they can be

grouped together into larger units, for instance the barrel and end-cap parts of the muon spectrometer. The barrel – end-cap as well as the MS-ID alignment can be implemented in this way.

4.2.2 The Global χ^2 Method

The global χ^2 alignment algorithm [40, 41] is based on the minimization of the following χ^2 function:

$$\chi^2 = \sum_{tracks} \boldsymbol{r}^T V^{-1} \boldsymbol{r} \tag{4.2}$$

with $\boldsymbol{r} = \boldsymbol{r}(\boldsymbol{a}, \boldsymbol{\pi})$ denoting the vector of residuals of all hits on the track and V being the covariance matrix of these residual measurements. $\boldsymbol{r}(\boldsymbol{a}, \boldsymbol{\pi})$ depends on the track parameters[2] $\boldsymbol{\pi}$ as well as on the vector of alignment parameters $\boldsymbol{a}$ (see Section 4.2.4) of all MDT chambers which have hits associated to one of the tracks.
The aim is to minimize the χ^2 function with respect to the alignment parameters. Therefore, the minimum is required to fulfill

$$\frac{d\chi^2}{d\boldsymbol{a}} = 2 \sum_{tracks} \frac{d\boldsymbol{r}^T}{d\boldsymbol{a}} V^{-1} \boldsymbol{r} = 0. \tag{4.3}$$

In order to solve this equation, a Taylor expansion of the residuals around the initial alignment parameters $\boldsymbol{a}_0$ is employed:

$$\boldsymbol{r} \approx \boldsymbol{r}_0 + \frac{d\boldsymbol{r}}{d\boldsymbol{a}_0} \delta\boldsymbol{a} \tag{4.4}$$

with $\frac{d}{d\boldsymbol{a}_0}$ denoting the derivative with respect to $\boldsymbol{a}$ evaluated at $\boldsymbol{a} = \boldsymbol{a}_0$. Only terms up to the first order in $\delta\boldsymbol{a} = (\boldsymbol{a} - \boldsymbol{a}_0)$ are used in the expansion assuming that higher-order terms are negligible. Thus, the following solution for the alignment parameters is obtained:

$$\delta\boldsymbol{a} = -\left(\sum_{tracks} \frac{d\boldsymbol{r}^T}{d\boldsymbol{a}_0} V^{-1} \frac{d\boldsymbol{r}}{d\boldsymbol{a}_0} \right)^{-1} \times \sum_{tracks} \frac{d\boldsymbol{r}^T}{d\boldsymbol{a}_0} V^{-1} \boldsymbol{r}_0. \tag{4.5}$$

A derivation of Equation 4.5 is provided in References [40, 41]. $\frac{d\boldsymbol{r}}{d\boldsymbol{a}}$ represents the total derivative of the residuals $\boldsymbol{r}(\boldsymbol{a}, \boldsymbol{\pi})$ with respect to the alignment parameters which can be written by means of the partial derivatives as:

$$\frac{d\boldsymbol{r}}{d\boldsymbol{a}} = \frac{\partial\boldsymbol{r}}{\partial\boldsymbol{a}} + \frac{\partial\boldsymbol{r}}{\partial\boldsymbol{\pi}} \frac{\partial\boldsymbol{\pi}}{\partial\boldsymbol{a}}. \tag{4.6}$$

This total derivative of the vector of residuals can either be determined numerically or by means of an analytical calculation of the partial derivatives. While for the alignment of the inner detector analytical derivatives are employed, the derivatives are derived numerically for the muon spectrometer because of the rather non-uniform field of the toroid magnets.

[2] Straight tracks for $B = 0$ are described by four parameters whereas curved tracks for $B \neq 0$ are described by five parameters (see Section 6.3.1).

Equation 4.5 is a set of n coupled linear equations, where n is the number of alignment degrees-of-freedom. In the global χ^2 approach, this equation is solved by inverting the $n \times n$ matrix. However, this matrix can become very large and the inversion a considerable effort, in particular for the alignment of the inner detector due to the large number of modules to be aligned. Therefore, as an approximation in the local χ^2 approach, the matrix is broken up into small independent matrices, one for each detector module [42, 43]. The correlations between the alignment parameters of the different detector modules are taken into account by iteration of the χ^2 fit.

4.2.3 Determination of Derivatives

The derivation of the alignment parameters by means of minimizing the global χ^2 function defined in Equation 4.2 requires the determination of the total derivative of the vector of residuals with respect to the vector of alignment parameters (Equation 4.5). The total derivative with respect to the alignment parameter a_i is determined numerically by displacing the particular chamber by a small distance Δa_i in the description of the detector geometry and subsequently refitting the muon track. To first order, the derivatives are given by the difference ratio:

$$\frac{d\boldsymbol{r}}{da_i} = \frac{\boldsymbol{r}(a_i + \Delta a_i) - \boldsymbol{r}(a_i - \Delta a_i)}{2\Delta a_i}. \tag{4.7}$$

However, this linear approximation is not sufficient. Hence, the derivatives are obtained by displacing the chamber in two steps in each direction and fitting a second order polynomial to the resulting five residuals per hit including the initial chamber position.

4.2.4 Definition of Alignment Parameters

The alignment parameters of MDT chambers, i. e. the translation and rotation of the chamber with respect to its nominal position, are defined in the local chamber coordinate system described in Section 3.2.3. Since the MDT chambers are insensitive to hit positions along the sense wires, translations of MDT chambers along the s-axis are currently not taken into account in the track-based alignment algorithms. Hence, five alignment parameters per chamber are considered, two translations (z, t) and three rotations ($\alpha(s)$, $\beta(z)$, $\gamma(t)$), assuming that the chamber deformations have been corrected for using the in-plane alignment system.

4.3 Small Barrel Chamber Alignment

Different algorithms have already been developed and tested for the initial calibration of the optical alignment system with straight tracks [38] as well as for the alignment of the muon spectrometer with respect to the inner detector. In contrast, only preliminary feasibility studies of the alignment of MDT chambers with curved tracks have been performed [33, 39]. Since the alignment with curved tracks is essential for MDT chambers which are only equipped with a partial set of optical sensors, this section is devoted to the evaluation of the performance of the global χ^2 alignment algorithm for the alignment of the small barrel chambers with curved tracks.

p_T [GeV]	Muons per chamber triplet
1000	25,000
100	15,000
20	75,000
6	75,000

Table 4.1: Single-muon Monte Carlo data samples used for the alignment studies presented in this chapter. The number of muons per chamber triplet in the samples with transverse momenta of 20 and 6 GeV correspond to the statistics expected per day in the calibration stream. While the sample for $p_T = 20$ GeV contains only muons with a transverse momentum of 20 GeV, the sample for $p_T = 6$ GeV comprises a mixture of 6, 10 and 20 GeV muons (100:10:1).

The large barrel chamber positions can be assumed to be monitored with sufficient accuracy by the optical alignment system. Hence, the small chambers can be aligned with respect to the adjacent large chambers on both sides in ϕ exploiting tracks traversing the overlap regions between small and large chambers.

Up to now, large sectors are assumed to be perfectly aligned internally. In addition, the relative positions of large sectors with respect to each other are assumed to be precisely known. Possible misalignments of large MDT chambers will be taken into account in the future.

4.3.1 Monte Carlo Samples

The alignment monitoring of the small chambers with curved tracks is required to be performed on a daily basis exploiting muon tracks provided by the muon calibration stream. The achievable accuracy of the global χ^2 algorithm is estimated using single-muon Monte Carlo data samples corresponding to the number of muon tracks expected in the calibration stream per day, i. e. about 75,000 tracks per chamber triplet (see Table 4.1).

The increasing effect of multiple scattering with decreasing track momentum imposes an enormous challenge on the alignment with curved tracks at the transverse momentum threshold of $p_T = 6$ GeV. Therefore, the alignment algorithm is first tested exploiting simulated muon tracks with $p_T = 100$ GeV before the performance is evaluated for tracks with transverse momenta of 20 and 6 GeV corresponding to the p_T thresholds employed for the calibration stream for different instantaneous luminosities. Muons with transverse momenta of 1 TeV are used for the validation of the resulting alignment parameters. The Monte Carlo samples used for the performance studies for the 20 GeV threshold of the calibration stream only contain muons with $p_T = 20$ GeV while a mixture of 6, 10, and 20 GeV muons in the ratio 100:10:1 as expected in the calibration stream has been used for the studies for the 6 GeV threshold. It should be noted that the energy loss of muons in the calorimeter system amounts to about 3 GeV. Thus, in particular low momentum muons have significantly decreased transverse momenta at the entrance of the muon spectrometer compared to the values at the interaction point.

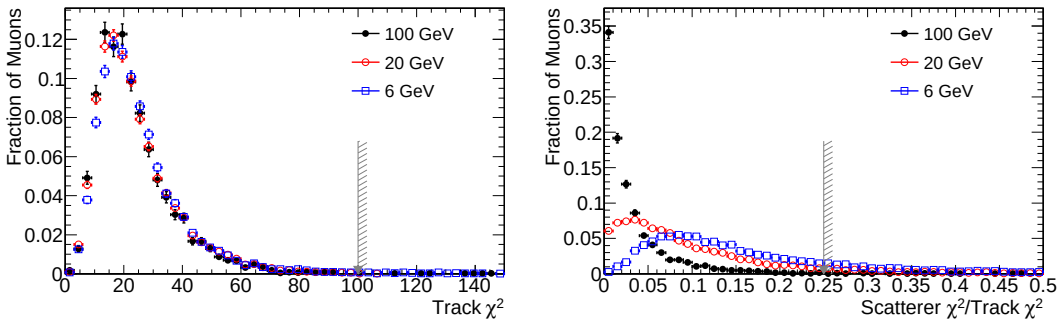

Figure 4.7: Distributions of the χ^2 values of the muon track fit (left) and the contribution of multiple scattering (right) for different muon transverse momenta. The gray arrows indicate the cut values.

4.3.2 Track Selection

The reconstruction of muon tracks employed for the alignment of the MDT chambers is solely based on measurements in the muon spectrometer, i. e. additional information provided by the inner detector and the calorimeter is not taken into account. These so-called stand-alone muons are reconstructed by the Moore algorithm [45] using the standard ATLAS global χ^2 track fitter [46]. Multiple scattering effects occurring for muons traversing the detector material are incorporated in the track fit by means of so-called scattering angles accounting for deflections of the trajectory.
Figure 4.7 shows the χ^2 distributions of the muon track fit for different transverse momenta. A track χ^2 value below 100 is required in order to reject tracks of poor quality. Since the scattering χ^2 is directly calculated based on the scattering angles[3], the ratio of the scattering χ^2 and the total track χ^2 value is a measure of the influence of multiple scattering on the track reconstruction. As expected, for muons with a transverse momentum of 100 GeV only a minor effect is observed. The effect of multiple scattering increases significantly with decreasing transverse momentum. In order to reject tracks with large multiple scattering effects, the contribution of multiple scattering to the total track χ^2 is required to be below 0.25 for the performance studies for muon transverse momenta of 20 and 6 GeV entailing track selection efficiencies of about 92.5% and 82.9%, respectively.
The small chambers in the barrel muon spectrometer are mounted on the toroid coils (Figure 4.8), therefore, the impact of multiple scattering is more pronounced for tracks traversing a small chamber triplet in comparison to large chamber triplets. This is visualized in Figure 4.9 which shows the ratio of the scattering χ^2 to the total track χ^2 for all tracks traversing a small chamber triplet in comparison to tracks which pass the overlap regions between the small and the adjacent large chamber triplets. Tracks are considered to pass the overlap region if they have at least one hit in a small and an adjacent large MDT chamber. Since they do not traverse the toroid coils, a lower multiple scattering contribution is observed for overlap tracks in comparison to all tracks passing the small chamber triplet. Only about 25% of the muon tracks passing a small chamber triplet also

[3] The contribution of each scattering center to the χ^2 of the track with polar angle θ is given by $\Delta\chi^2 = \left(\frac{\Delta\phi \sin\theta}{\sigma(\Delta\phi)\sin\theta}\right)^2 + \left(\frac{\Delta\theta}{\sigma(\Delta\theta)}\right)^2$ for the scattering angles $\Delta\phi$ and $\Delta\theta$.

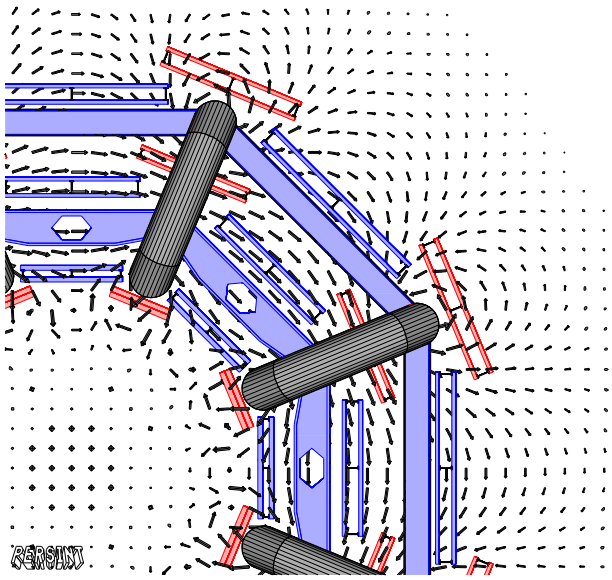

Figure 4.8: Cross section of a barrel muon spectrometer quadrant. Small MDT chambers (red) are mounted on the toroid coils while large chambers (blue) are located between two adjacent coils. The gray arrows indicate the magnetic field lines.

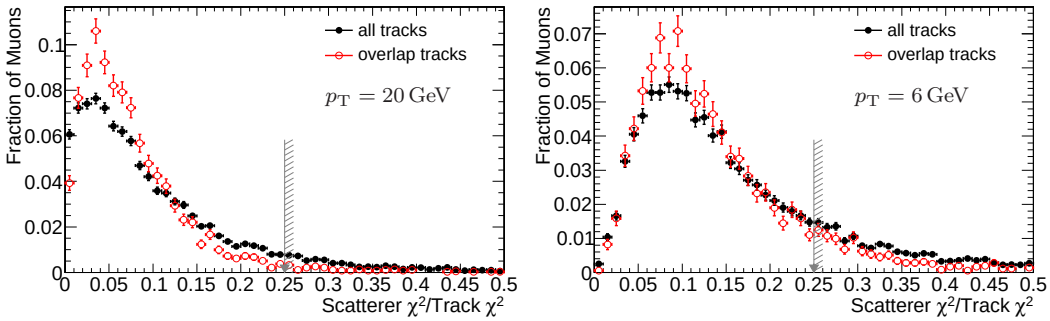

Figure 4.9: Distributions of the contribution of multiple scattering to the total track χ^2 for all tracks passing a small MDT chamber triplet and for tracks which pass the overlap regions between the small and the adjacent large chamber triplets. The distributions are shown for muons with transverse momenta of 20 GeV (left) and 6 GeV (right). The gray arrows indicate the cut value.

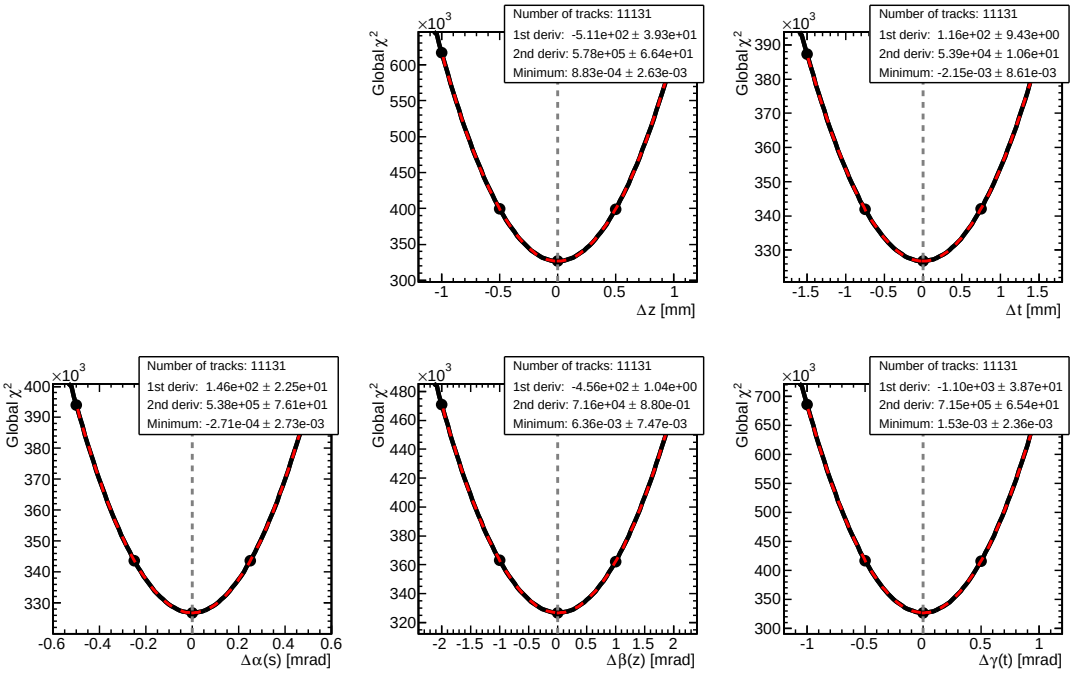

Figure 4.10: Derivatives of the global χ^2 function with respect to the alignment parameters for chamber BMS2A04 at its nominal position $\boldsymbol{a} = (0, 0, 0, 0, 0)$. The derivatives are determined for muon tracks with a transverse momentum of 100 GeV. The black dots represent the χ^2 values corresponding to the different chamber displacements fitted by the black parabola while the red parabola is determined from the first and second derivatives of the χ^2 function (see text).

traverse at least one large chamber. Thus, it has to be studied if the decreased contribution of multiple scattering processes for overlap tracks outweighs the significant loss of statistics.

4.3.3 Alignment with 100 GeV Muon Tracks

Due to the low curvature and the small contribution of multiple scattering, muon tracks with $p_{\mathrm{T}} = 100\,\mathrm{GeV}$ provide an excellent possibility for a first study of the reliability of the alignment algorithm. The accuracy of the determination of the derivatives and of the alignment parameters is evaluated with about 15,000 muon tracks traversing a small chamber triplet.

Figure 4.10 shows the derivatives of the global χ^2 function with respect to the alignment parameters for the case that all chambers are at their nominal positions. The black dots represent the χ^2 values corresponding to the displaced chamber positions used for the determination of the derivatives and are fitted by a second order polynomial (black parabola). The red parabola is determined from the first and second derivatives of the χ^2

function at the minimum:

$$\frac{d\chi^2}{da_i} = 2\sum_{tracks}\frac{d\boldsymbol{r}^T}{da_{i0}}V^{-1}\boldsymbol{r}, \tag{4.8}$$

$$\frac{d^2\chi^2}{da_i^2} = 2\sum_{tracks}\left(\frac{d\boldsymbol{r}^T}{da_{i0}}V^{-1}\frac{d\boldsymbol{r}}{da_{i0}} + \boldsymbol{r}^T V^{-1}\frac{d^2\boldsymbol{r}}{da_{i0}^2}\right) \tag{4.9}$$

$$\approx 2\sum_{tracks}\frac{d\boldsymbol{r}^T}{da_{i0}}V^{-1}\frac{d\boldsymbol{r}}{da_{i0}}, \tag{4.10}$$

where the second term in Equation 4.9 has been neglected. Figure 4.10 demonstrates that the minima of the functions agree with the nominal chamber position and the determination of the total derivatives described in Section 4.2.3 proves to be consistent.
The evolution of the alignment parameters for the chamber triplet studied is shown in Figure 4.11 for consecutive iterations of the alignment procedure after starting at the nominal or randomly displaced chamber positions. For both cases, the final corrected positions of the three chambers agree and are within errors consistent with the nominal positions. The uncertainties on the alignment parameters in the linear approximation are derived from the second derivatives of the global χ^2 according to:

$$\sigma(a_i) = \sqrt{\frac{2}{d^2\chi^2/da_i^2}}. \tag{4.11}$$

4.3.4 Alignment Performance with the Calibration Stream

In this section, the performance of the small chamber alignment is tested with data samples equivalent to the statistics of muons of the calibration data stream expected during one day which is about 75,000 muon tracks per chamber triplet. Two different transverse momentum thresholds are studied: 20 and 6 GeV.

Calibration Stream with 20 GeV Threshold

The evolution of the alignment parameters for consecutive iterations of the alignment procedure is shown in Figure 4.12 starting at the nominal chamber positions. No convergence of the alignment parameters to the nominal chamber positions is observed when all tracks traversing the chamber triplet are taken into account. The situation is improved when tracks passing through the overlap regions between the small and the adjacent large chamber triplets are selected entailing reduced multiple scattering effects. Due to correlations between the translational alignment parameters Δz and Δt, small deviations from the nominal positions of about 27 μm and 60 μm, respectively, are observed for the inner chamber. These correlations are related to the low sensitivity of projective tracks to misalignments in track direction which do not change the χ^2 of the track fit and are referred to as weak modes of the alignment procedure. However, due to the projective nature of these misalignments, the resulting chamber positions only correspond to a relative displacement of 27 μm in sagitta direction for an average track. As can be seen in Figure 4.13, the resulting alignment parameters when starting at misaligned chamber

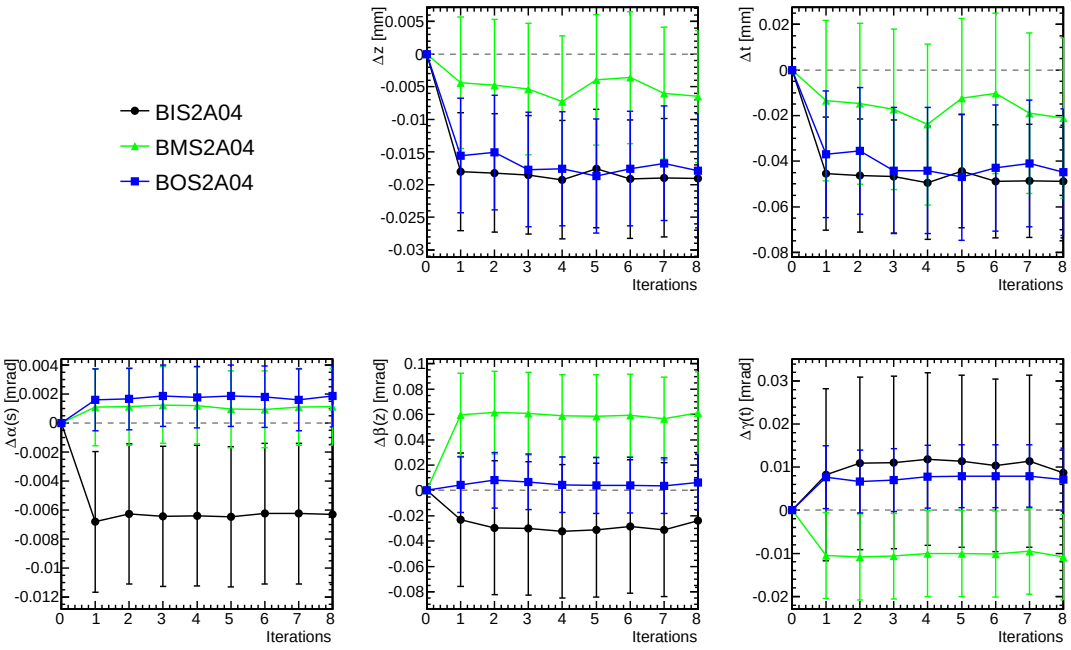

(a) Starting from nominal chamber positions.

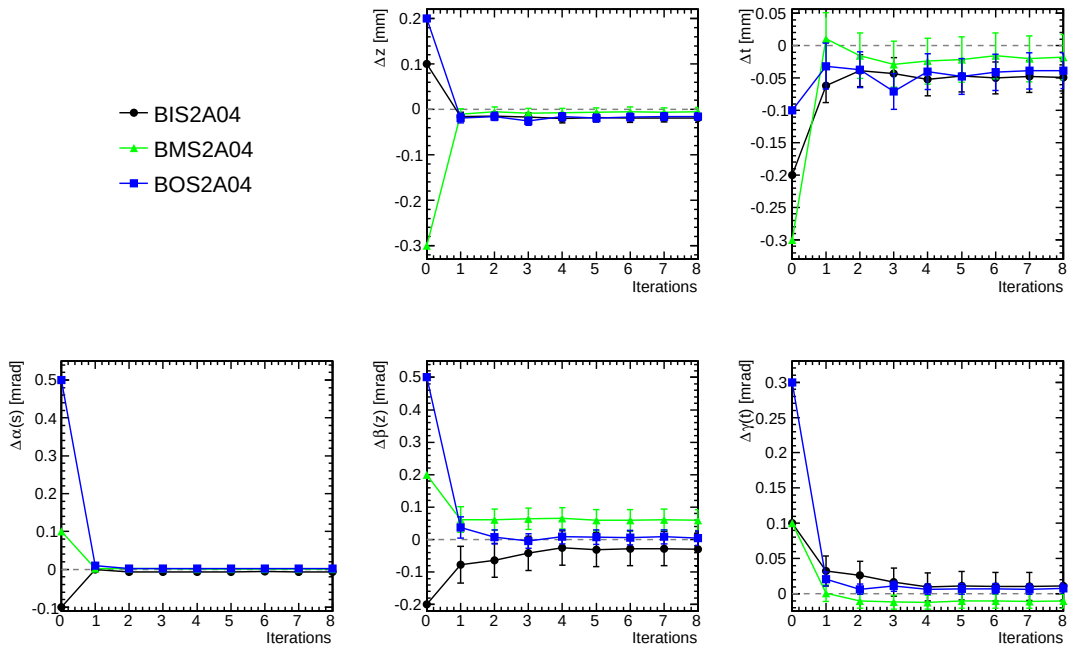

(b) Starting from misaligned chamber positions.

Figure 4.11: Evolution of the alignment parameters of a small chamber triplet for consecutive iterations of the alignment procedure for muon tracks with a transverse momentum of 100 GeV.

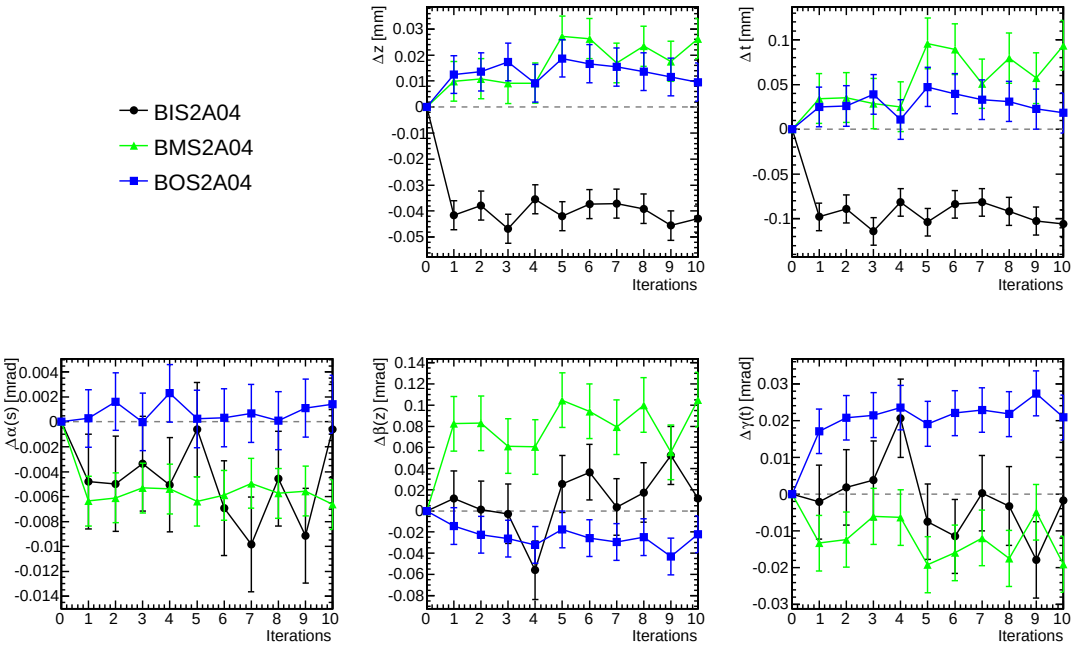

(a) All tracks.

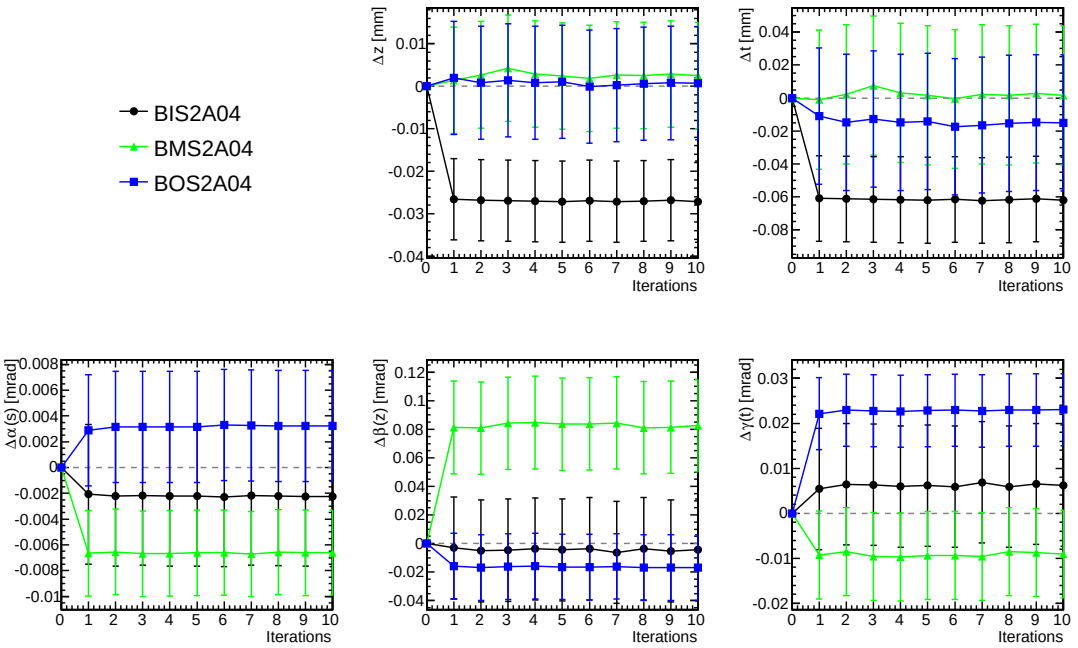

(b) Overlap tracks.

Figure 4.12: Evolution of the alignment parameters of a small chamber triplet for consecutive iterations of the alignment procedure starting at the nominal chamber positions for muon tracks with a transverse momentum of 20 GeV. The evolution of the alignment parameters is shown for all tracks traversing the small chamber triplet (a) and for tracks which pass through the overlap regions between the small and the adjacent large chamber triplets (b).

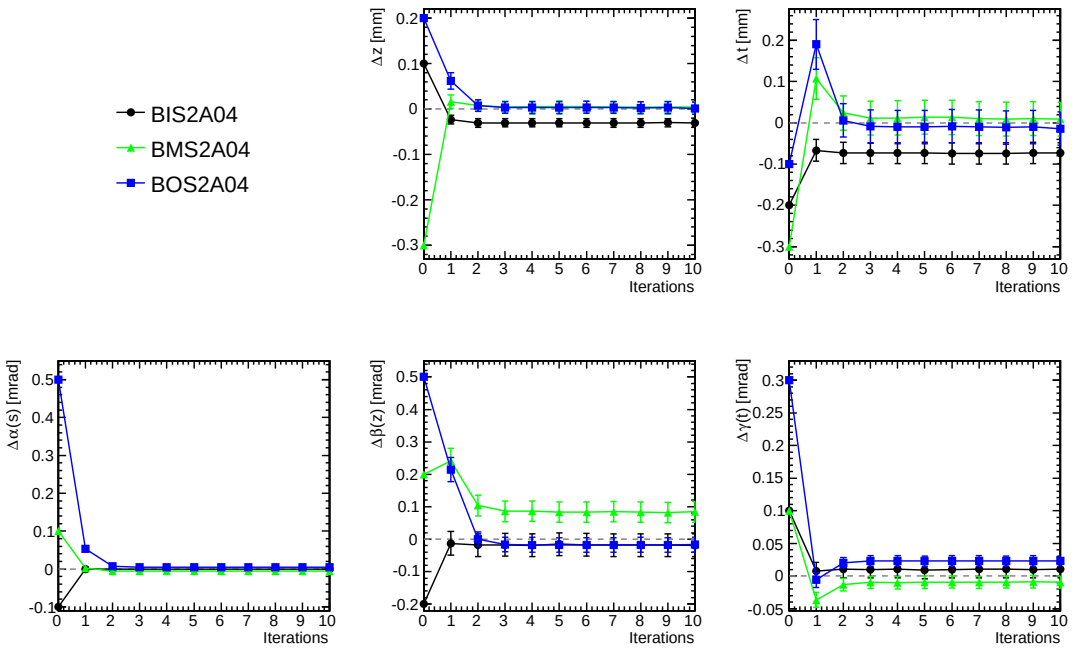

Figure 4.13: Evolution of the alignment parameters of a small chamber triplet for consecutive iterations of the alignment procedure starting at misaligned chamber positions for muon tracks with a transverse momentum of 20 GeV. The evolution of the alignment parameters is shown for tracks which pass through the overlap regions between the small and the adjacent large chamber triplets.

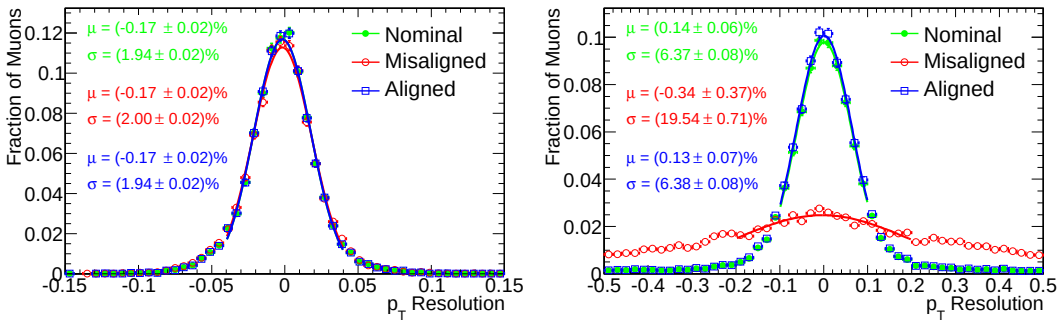

Figure 4.14: Transverse momentum resolution for the nominal and misaligned (see Figure 4.13) chamber positions as well as after the track-based overlap alignment with 20 GeV muon tracks. The resolutions are shown for 20 GeV (left) and 1 TeV muon tracks (right).

positions are compatible with the ones obtained when starting at the nominal chamber positions.

Figure 4.14 shows the transverse momentum resolution for the nominal and misaligned chamber positions as well as after the alignment with overlap tracks. The p_{T} resolution is defined as:

$$\frac{\Delta p_{\mathrm{T}}}{p_{\mathrm{T}}} = \frac{1/p_{\mathrm{T}}(\text{Reco muon}) - 1/p_{\mathrm{T}}(\text{Truth muon})}{1/p_{\mathrm{T}}(\text{Truth muon})}. \tag{4.12}$$

Since the p_{T} resolution for low momentum tracks is dominated by multiple scattering effects and energy loss fluctuations (see Figure 4.2), only a minor impact of chamber misalignment effects is visible for 20 GeV muons. In contrast, for high-p_{T} muons the spatial resolution and alignment of the MDT chambers are the dominant contributions to the transverse momentum resolution. Therefore, Figure 4.14 also shows the significant impact of the same chamber misalignment on the p_{T} resolution of muon tracks with a transverse momentum of 1 TeV whereas only a minor degradation of the resolution is observed after the track-based alignment. Although small deviations from the nominal chamber positions result from the alignment with 20 GeV muon tracks, only a minor impact on the sagitta and the transverse momentum resolution is observed due to the projective nature of the remaining misalignments.

The alignment parameters obtained for the individual alignment of all chamber triplets within one sector and for the combined alignment of all MDT chambers within this sector are depicted in Figure 4.15. For the individual alignment of the chamber triplets only small deviations from the nominal positions are observed except for the last triplet (η-index = 6) for which somewhat larger deviations are obtained. In contrast, significant deviations are obtained for the combined alignment of all small chambers within one sector. In particular, the displacements with respect to the nominal chamber positions increase with increasing η-index. In case of the individual alignment of chamber triplets, additional constraints of the alignment parameters are provided by tracks also traversing chambers in the same sector which are fixed at their nominal positions. These constraints are not present when simultaneously aligning all 18 chambers in the sector. The large discrepancies between the resulting alignment parameters for the simultaneous alignment of all 18 chambers and the nominal chamber positions originate from strong correlations, for instance between the

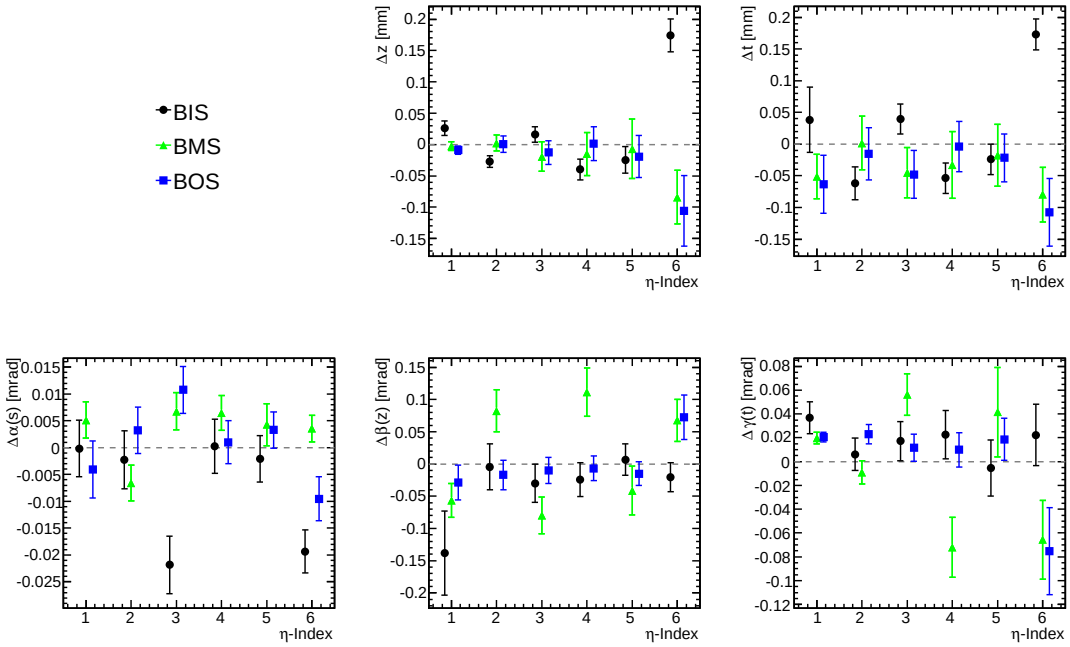

(a) Individual alignment of the chamber triplets.

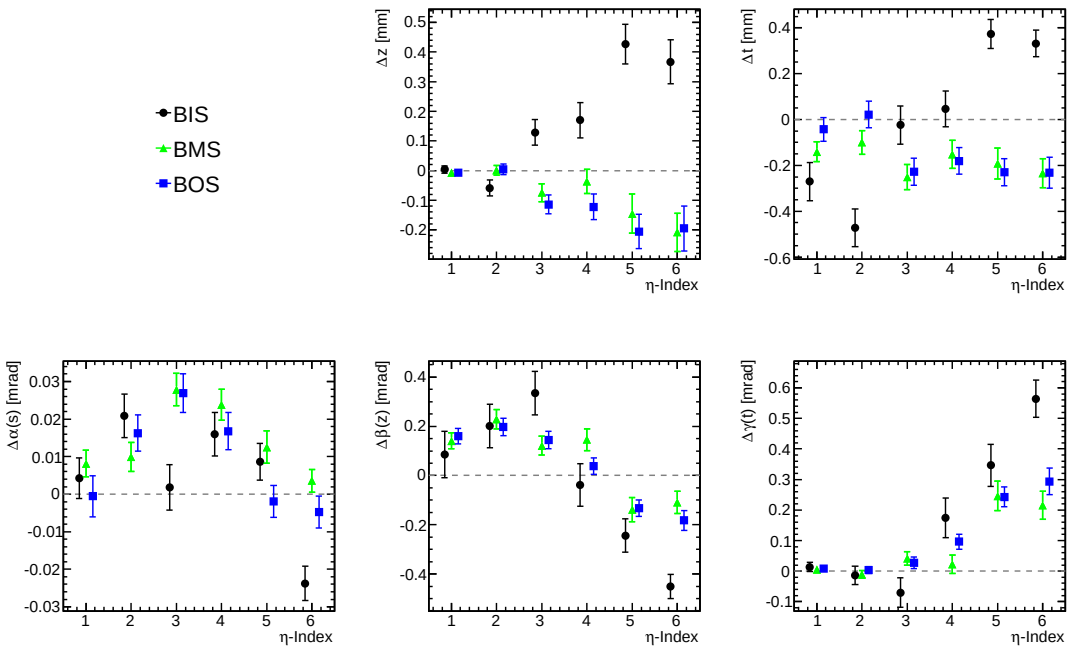

(b) Combined alignment of the chamber triplets.

Figure 4.15: Alignment parameters of the different chamber triplets within a small barrel sector (sector 4) for the individual alignment of the chamber triplets (a) and the combined alignment of all chambers within this sector (b) with 20 GeV overlap tracks.

translational alignment parameters along the z and t-axis. While muon tracks with a large angular spread are needed to resolve these correlations, chambers in adjacent triplets of a sector are only interconnected by tracks within a small angular range. The angular spread decreases with increasing η-index leading to large chamber displacements, in particular at large η-indices. However, adjacent chambers within one sector are connected by proximity and axial optical sensors with an accuracy of better than 10 μm and 30 μrad. Exploiting this information provided by the optical alignment system will help to constrain the weak alignment modes. Since optical constraints could not be implemented in the alignment software framework within the time frame of this thesis, these studies will be performed in the future.

Calibration Stream with 6 GeV Threshold

At low instantaneous luminosities, a trigger threshold of $p_{\mathrm{T}} = 6\,\mathrm{GeV}$ will be used for the calibration stream. The increased effect of multiple scattering for low momentum tracks significantly decreases the performance of the track-based alignment. In particular, instabilities are observed in the determination of the derivatives by means of refitting the muon tracks for displaced chamber positions. These instabilities degrade the reliability and accuracy of the alignment algorithm. The evolution of the alignment parameters for consecutive iterations of the alignment procedure is shown in Figure 4.16 for all tracks passing the small chamber triplet starting at the nominal chamber positions. Employing only overlap tracks does not result in an improvement of the alignment parameters due to the significantly decreased number of tracks in the overlap regions. Since scattering effects can be misinterpreted as chamber misalignments, large track statistics are required in order to reliably determine the alignment parameters at low transverse momenta.
The resulting alignment parameters differ significantly from the nominal chamber positions. In particular, large displacements of 120 μm and 300 μm along the z- and t-axis, respectively, are obtained for the inner chamber. For an average track, these deviations translate into a relative displacement of 165 μm in sagitta direction.
For low momentum muons, the insensitivity to projective misalignments in track direction apparently has increased impact on the alignment parameters. More detailed studies are necessary in order to improve the performance of the alignment algorithm for low momentum tracks. In addition to a refined track reconstruction and selection, information from the optical alignment system is needed to constrain the weak modes of the track-based alignment.
However, as shown in Figure 4.17, the remaining misalignments have only small impact on the transverse momentum resolution for 1 TeV muon tracks since the chamber displacements are essentially in track direction.

4.4 Conclusions

The requirement of a muon transverse momentum resolution of better than 10% for transverse momenta up to 1 TeV imposes an enormous challenge on the alignment of MDT chambers, the major precision tracking chambers in the muon spectrometer. The optical alignment system is designed to guarantee the alignment with sufficient accuracy for a

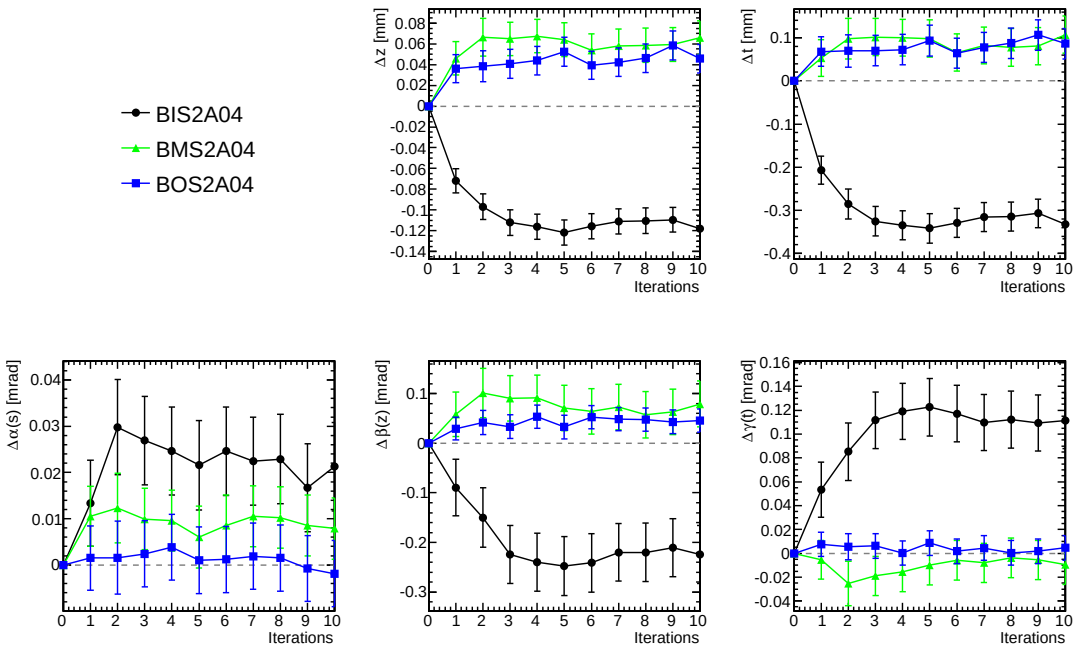

Figure 4.16: Evolution of the alignment parameters for consecutive iterations of the alignment procedure starting at the nominal chamber positions for muon tracks with a transverse momentum of 6 GeV. The evolution of the alignment parameters is shown for all tracks traversing the small chamber triplet.

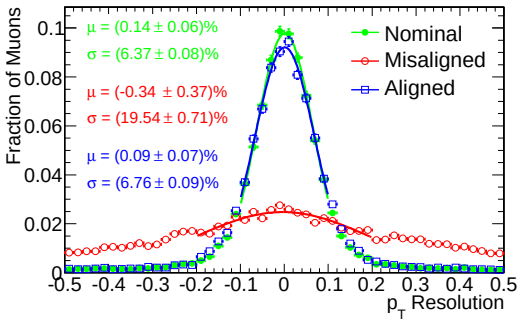

Figure 4.17: Transverse momentum resolution for 1 TeV muon tracks for the nominal and misaligned chamber positions as well as after the track-based alignment with 6 GeV muon tracks.

large fraction of MDT chambers. However, track-based alignment procedures are needed for several tasks, in particular for the alignment of chambers which are only equipped with a partial set of optical sensors. For instance, the alignment with curved muon tracks is indispensable for the small chambers in the barrel part of the muon spectrometer.
A new generic framework has been developed to provide a common flexible foundation which allows for the implementation of the different alignment algorithms as well as for the individual and combined alignment of the different subsystems of the ATLAS detector.
In this chapter, the performance of the global χ^2 minimization method has been studied for the alignment of the small barrel chambers with respect to the adjacent optically precisely aligned large chambers. Since the alignment of the small chambers has to be performed with muon tracks provided by a dedicated muon calibration stream, the alignment algorithm has been validated with Monte Carlo data samples equivalent to one day of data taking at trigger p_{T} thresholds of 20 GeV and 6 GeV, respectively. While a good performance is observed for muons with transverse momenta of 20 GeV, the alignment with 6 GeV muon tracks is deteriorated by increased multiple scattering effects. Further improvements of the alignment with low-p_{T} tracks are necessary, for instance for the reliable determination of the numerical derivatives of the χ^2 function.
Individual chamber triplets can been aligned with sufficient accuracy with 20 GeV muon tracks while for the combined alignment of all chambers in a sector significant deviations from the nominal chamber positions are observed. These deviations are mainly caused by the low sensitivity of the alignment with projective tracks from the interaction point to particular displacements which do not change the track χ^2, for example chamber displacements along the track direction. This can be solved, for instance, by exploiting information provided by the optical alignment sensors to constrain such weak modes of the track-based alignment.
So far, the large sectors used as a reference for the alignment of the small chambers have been assumed to be perfectly aligned internally and with respect to each other. However, the eventual objective of the introduced alignment approach is to align all MDT chambers in the barrel part of the muon spectrometer simultaneously with respect to one large sector. Since large sectors are internally monitored with sufficient precision by the optical alignment system, the chambers within each large sector will be combined to one alignable unit whereas each small chamber will be treated as an individual module.

Chapter 5

The Search for the Higgs Boson

In the analysis presented in this thesis, the achievable exclusion limits and the discovery potential are evaluated for the Standard Model Higgs boson in vector-boson fusion production with subsequent decay into two W bosons. The decay into two W bosons is one of the most promising decay channels for a discovery of the Higgs boson since it exhibits the dominant branching fraction for Higgs boson masses above 160 GeV. In particular during the early data taking phase with relatively low integrated luminosity, it provides an unrivaled opportunity to set exclusion limits on the Higgs production cross section. In comparison to Higgs boson production via gluon fusion (GF), the cross section for the production through vector-boson fusion (VBF) is suppressed by one order of magnitude and therefore entails a lower discovery potential at low integrated luminosities. However, the topology of this production mechanism allows for an efficient suppression of background contributions by means of two characteristic jets in the forward regions of the detector, which provides improved sensitivity compared to the gluon fusion production at large integrated luminosities. The exclusion limit and the discovery potential for the Higgs boson are estimated for $1\,\mathrm{fb}^{-1}$ of proton-proton collision data recorded by the ATLAS detector at a center-of-mass energy of $\sqrt{s} = 10\,\mathrm{TeV}$, which corresponds to about one year of data taking at the LHC at an instantaneous luminosity of $10^{32}\ \mathrm{cm}^{-2}\,\mathrm{s}^{-1}$. In this analysis, a cut-based separation of signal and background events is employed and the impact of the presence of pile-up on the Higgs boson discovery potential is studied in detail.

This chapter is organized as follows. The topologies of the signal and background processes are introduced in Sections 5.1 and 5.2. In Section 5.3, the Monte Carlo samples used are specified. The reconstruction of physics objects is described in Section 5.4 whereas the event selection criteria employed in order to suppress the various background processes are discussed in Section 5.5. In Section 5.6, the event selection efficiencies and the different background contributions are summarized. A Higgs boson mass of $m_H = 170\,\mathrm{GeV}$ is used as a benchmark in this chapter and a comparison of the event selection efficiencies for different m_H is presented in Section 5.6.3.

The influence of pile-up events originating from additional inelastic pp interactions in each bunch crossing is studied in Chapter 6. Different methods exploiting tracking and vertexing information are introduced in order to minimize the degradation of the discovery potential in the presence of pile-up. The systematic uncertainties, the prospects for setting exclusion limits on the Higgs production cross section as well as the discovery potential

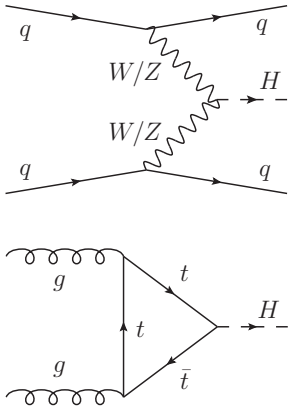

Figure 5.1: Tree-level Feynman diagrams of the Higgs boson production mechanisms studied, vector-boson fusion (top) and gluon fusion (bottom).

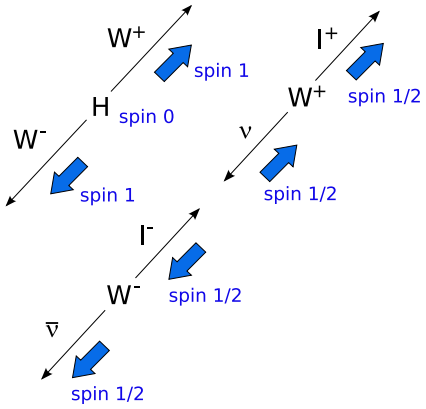

Figure 5.2: Illustration of the spin correlation in $H \rightarrow WW \rightarrow l\nu l\nu$ decays. For Higgs masses close to the threshold $m_H \approx 2m_W$, the W bosons are produced virtually at rest and the two charged leptons tend to be emitted into the same direction.

W^- decay mode	Branching ratio [%]
$e^-\nu$	10.75 ± 0.13
$\mu^-\nu$	10.57 ± 0.15
$\tau^-\nu$	11.25 ± 0.20
hadrons	67.60 ± 0.27

Table 5.1: W-boson decay modes and the corresponding branching ratios [47].

for different mass values of the Standard Model Higgs boson are discussed in Chapter 7.

5.1 Signal Event Topology

The signature of Higgs production by vector-boson fusion is characterized by two jets in the forward regions of the detector, the so-called tagging jets which arise from the remnants of the quarks emitting the vector bosons (Figure 5.1). In the central region of the detector, between the two tagging jets, very low activity apart from the Higgs decay products is expected due to the absence of color exchange between the quarks from different protons participating in the vector-boson fusion process. This allows for an efficient suppression of background processes. The gluon fusion process contributes significantly to the search for the Higgs boson in the WW decay channel with two additional jets, since its cross section surpasses the one of the vector-boson fusion process by an order of magnitude and jets from the underlying event, initial and final state radiation, or additional inelastic pp interactions can be misidentified as tagging jets.
In this thesis, the discovery potential for the Higgs boson in decays into two W bosons is studied. This is the dominant Standard Model Higgs decay channel for $m_H > 160\,\text{GeV}$ (see Figure 2.7). The branching ratios for the subsequent W-boson decays are summarized in Table 5.1. Although the W boson decays dominantly into hadrons, these decay modes

are not taken into account in this analysis since the discovery potential in hadronic final states suffers from a large background contribution of QCD multi-jet processes, in particular at low Higgs masses. Furthermore, hadronic W decay channels require a very good understanding of the jet reconstruction and calibration performance. Therefore, a search for the Higgs boson in hadronic W decay channels is not feasible in the initial data taking phase. In comparison to $W \to e\nu/\mu\nu$ decays, the contribution from W bosons decaying into τ leptons is negligible since the branching fraction in leptonic τ decays only amounts to $(35.21 \pm 0.07)\%$ [47] and the leptons originating from the τ decays have significantly lower transverse momenta in comparison to leptons from direct W boson decays. Hence, only W boson decays into electrons and muons are considered corresponding to a total branching ratio of 21.3%.
For Higgs boson masses close to the threshold $m_H \approx 2m_W$ ($m_W = 80.40 \pm 0.03\,\text{GeV}$ [47]), decays in two W bosons which further decay leptonically can be separated from the background by employing spin correlations between the two W bosons as illustrated in Figure 5.2. In the center-of-mass system of the Higgs boson, the W bosons are produced virtually at rest for $m_H \approx 2m_W$. The Higgs boson is a scalar particle with spin 0, hence, the spins of the two W bosons are directed opposite to each other. Being a left-handed particle, the neutrino is emitted opposite to the spin direction of the W^+ while the right-handed antineutrino is emitted in the direction of the W^- spin. Thus, the two charged leptons originating from the W boson decays tend to be emitted into the same direction, opposite to the direction of the two neutrinos, and are expected to be reconstructed within a small ΔR region of the detector. This signature diminishes for Higgs masses significantly above the threshold $m_H \approx 2m_W$.
The mass of the Higgs boson cannot be reconstructed in $H \to WW \to l\nu l\nu$ decays since the longitudinal components of the neutrino four-momenta in beam direction cannot be measured and their individual contributions to the missing transverse energy cannot be separated from each other. Therefore, only the transverse mass

$$m_\text{T} = \sqrt{\left(E_\text{T}^{ll} + E_\text{T}^{\nu\nu}\right)^2 - \left(\boldsymbol{p}_\text{T}^{ll} + \boldsymbol{p}_\text{T}^\text{miss}\right)^2} \tag{5.1}$$

of the lepton-neutrino system can be reconstructed with the di-lepton and di-neutrino energies defined as:

$$E_\text{T}^{ll} = \sqrt{\left(p_\text{T}^{ll}\right)^2 + {m_{ll}}^2}, \tag{5.2}$$

$$E_\text{T}^{\nu\nu} = \sqrt{\left(p_\text{T}^\text{miss}\right)^2 + m_{\nu\nu}^2}. \tag{5.3}$$

Different approximations of $m_{\nu\nu}$ and m_{ll} can be employed leading to various definitions of the transverse mass with different advantages.

- $\boldsymbol{m_\text{T}^{ll\nu}}$ [48] denotes the transverse mass under the assumption of negligible di-lepton masses m_{ll} and $m_{\nu\nu}$ at high lepton momenta. This leads to the approximations $E_\text{T}^{ll} \approx p_\text{T}^{ll}$ and $E_\text{T}^\text{miss} \approx p_\text{T}^\text{miss}$ and thus, to the following expression for the transverse mass:

$$m_\text{T}^{ll\nu} = \sqrt{2p_\text{T}^{ll}p_\text{T}^\text{miss} - 2\boldsymbol{p}_\text{T}^{ll}\boldsymbol{p}_\text{T}^\text{miss}} \tag{5.4}$$

$$= \sqrt{2p_\text{T}^{ll}p_\text{T}^\text{miss}(1 - \cos\Delta\phi)} \tag{5.5}$$

with $\Delta\phi$ being the angle between the di-lepton transverse momentum vector and the $p_{\mathrm{T}}^{\mathrm{miss}}$ vector.

- $\boldsymbol{m_{\mathrm{T}}^{\mathrm{approx}}}$ [48] was used for the definition of the Higgs mass search window and the estimation of discovery potential in previous studies of this decay channel [49]. It employs the approximation $m_{\nu\nu} \approx m_{ll}$ which is valid for Higgs masses at the threshold $m_H \approx 2m_W$ where the W bosons are produced virtually at rest in the Higgs boson center-of-mass system. With this approximation, the definition of $E_{\mathrm{T}}^{\nu\nu}$ in Equation 5.3 is replaced by:

$$E_{\mathrm{T}}^{\nu\nu} = \sqrt{\left(p_{\mathrm{T}}^{\mathrm{miss}}\right)^2 + {m_{ll}}^2}. \tag{5.6}$$

- $\boldsymbol{m_{\mathrm{T}}^{0}}$ [50] was only recently introduced and denotes the transverse mass with the assumption $m_{\nu\nu} \approx 0$ under which Equation 5.3 results in:

$$E_{\mathrm{T}}^{\nu\nu} = p_{\mathrm{T}}^{\mathrm{miss}}. \tag{5.7}$$

  This definition of the transverse mass has the advantage of providing a lower bound on the Higgs boson mass (which is not the case for $m_{\mathrm{T}}^{\mathrm{approx}}$). It is therefore used for the estimation of the discovery potential.

A comparison of the distributions of the different transverse mass definitions is shown in Section 5.5. Throughout this thesis the notation $\boldsymbol{m_{\mathrm{T}}} \equiv \boldsymbol{m_{\mathrm{T}}^{0}}$ is used.

5.2 Background Processes

Every process with at least two jets and two highly energetic leptons in the final state constitutes a potential background to the search for $H \to WW$ decays in vector-boson fusion production. The most important background processes are introduced in the following. The respective Feynman diagrams are shown in Figure 5.3. Unless stated otherwise, the cross sections are taken from Reference [51] and have been calculated at next-to-leading order with the MCFM program[1] [52] for pp collisions at $\sqrt{s} = 10\,\mathrm{TeV}$.

- $t\bar{t}$ background:
  The dominant background is $t\bar{t}$ pair production (Figure 5.3a) due to the large cross section of 395.6 pb. Top quarks decay almost exclusively into a W boson and a b quark. If the jets originating from the b quarks are misidentified as jets from light quarks this process contains the same reconstructed objects in the final state as the signal process. Hence, efficient identification of b-jets is of particular importance for the rejection of the $t\bar{t}$ background.

- Wt background:
  The single top production in the Wt channel has a cross section of 18.3 pb. Except

[1] The calculations employ the CTEQ6M parton distribution functions [15] and the following parameter definitions: $G_F = 1.16639 \times 10^{-5}\,\mathrm{GeV}^{-2}$, $m_W = 80.41\,\mathrm{GeV}$, $m_Z = 91.187\,\mathrm{GeV}$, $m_c = 1.4\,\mathrm{GeV}$, $m_b = 4.6\,\mathrm{GeV}$ and $m_t = 172\,\mathrm{GeV}$.

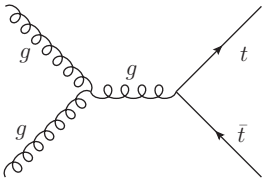

(a) $t\bar{t}$ production.

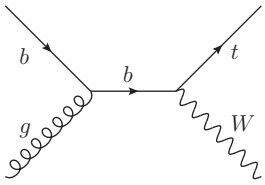

(b) Wt production.

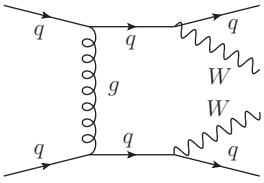

(c) QCD WW + jets production.

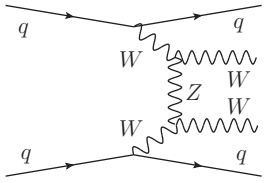

(d) EW WW + jets production.

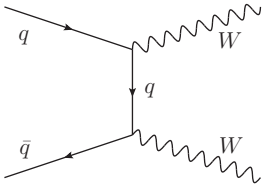

(e) $q\bar{q} \to WW$ production.

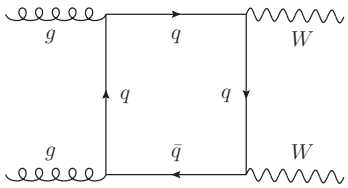

(f) $gg \to WW$ production.

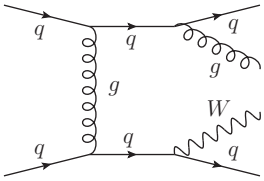

(g) W + jets production.

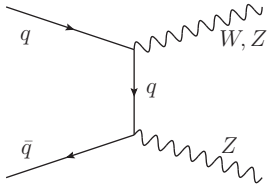

(h) ZZ, WZ production.

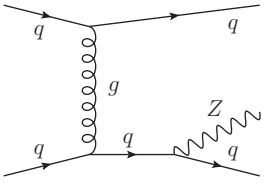

(i) QCD Z + jets production.

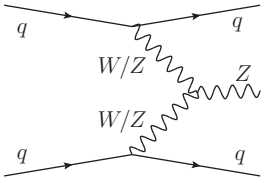

(j) EW Z + jets production.

Figure 5.3: Tree-level Feynman diagrams for the dominant background processes.

for a second b-jet, the final state contains the same particles as the $t\bar{t}$ process (Figure 5.3b). Since additional jets from initial or final state radiation, the underlying event or additional inelastic pp interactions can be misidentified as tagging jets, also the Wt process is a potential background.

- WW background:
  Obviously, WW production in the presence of additional jets in the final state constitutes an important background contribution (Figures 5.3c and 5.3d). The total cross section for $qq/qg \rightarrow WW$ production (Figure 5.3e) amounts to 73.1 pb. Although suppressed proportional to α_s^2, the gluon induced WW production mediated by quark loops (Figure 5.3f) also constitutes a significant background contribution due to the smaller opening angle between the two leptons entailing an enhancement by the signal selection cuts with respect to the quark-antiquark production [53]. The total cross section for $gg \rightarrow WW$ production amounts to 2.8 pb calculated with the GG2WW program [53].

- W + jets background:
  The cross section for inclusive W production (Figure 5.3g) is with $132.2 \cdot 10^3$ pb several orders of magnitudes larger than the one for the signal or the $t\bar{t}$ process. It constitutes a potential background if an additional jet is misidentified as a lepton. Therefore, a low and accurately measured misidentification rate of jets as leptons is necessary in order to suppress and reliably estimate the W + jets background.

- Z + jets background:
  $Z \rightarrow \tau\tau \rightarrow l\nu\nu l\nu\nu$ decays with additional jets contain the same particles in the final state as the signal process. Because of inaccurate $E_{\mathrm{T}}^{\mathrm{miss}}$ reconstruction, in particular during the initial data taking phase, also $Z \rightarrow ee/\mu\mu$ decays can contribute. Feynman diagrams for the electroweak and QCD Z + jets production are shown in Figures 5.3j and 5.3i, respectively.

- WZ, ZZ background:
  In the case of one vector boson decaying leptonically and the other one hadronically or additional jets misidentified as the tagging jets, also di-boson production (Figure 5.3h) constitutes a potential background.

- $c\bar{c}$, $b\bar{b}$ and QCD multi-jet background:
  These processes have cross sections above 10^8 pb and can be a background contribution due to the misidentification of jets as leptons or leptons originating from c- or b-hadron decays. These background processes can be very efficiently suppressed by the requirement of two isolated leptons and missing transverse energy. Due to the large production cross section and very strong suppression, the remaining small background rate cannot be determined by Monte Carlo simulation and is assumed to be negligible.

5.3 Monte Carlo Simulation

This analysis is based on Monte Carlo simulated signal and background data samples which have been centrally produced with the ATLAS software framework Athena, release

14.2.25. The details of the Monte Carlo data samples such as the cross sections of the processes, the numbers of generated events and the corresponding integrated luminosities are summarized in Tables 5.2 and 5.3. Further details on all the background samples studied are provided in Tables A.1-A.5 in Appendix A.
The simulation of physics processes in proton-proton collisions starts with the simulation of the hard scattering process followed by parton showering and the hadronization. Subsequently, the particle interactions with matter and the detector response are simulated for the stable particles emerging from the event. In addition to the primary hard interaction also the underlying event, i. e. interactions between the proton-remnants are simulated. The Monte Carlo samples used for the studies presented in this chapter do not take into account pile-up effects due to additional inelastic pp collisions. However, these effects have been accounted for in the simulation of the samples used for the studies presented in Chapter 6.
Various Monte Carlo generators have been employed for the simulation of the hard interaction, each specifically suited for the generation of a particular process. The vector-boson fusion and gluon fusion Higgs data samples have been simulated with the MC@NLO [55] and Herwig [56] generators, respectively. Most of the Z/W+jets background samples have been generated with ALPGEN [57] while the MC@NLO and AcerMC [58] event generators have been used for the simulation of the top-quark backgrounds. The different generators use the Herwig or Pythia programs [59] for the simulation of the parton showering, the hadronization as well as the underlying event. Herwig uses the Jimmy [60] generator for the simulation of the underlying event.
Except for MC@NLO, which is a next-to-leading order generator for QCD processes, all generators employ leading order calculations and K-factors are used to scale the simulated leading-order cross sections to the corresponding theoretical next-to-leading order cross section. The K-factors are obtained from the MCFM program (see previous section).
In order to increase the number of simulated events of specific background processes in the interesting phase space region, event filters have been applied after the generator level. Thus, events can already be rejected before entering the CPU time-consuming detector simulation. For the generation of the $t\bar{t}$ background samples a lepton filter has been applied rejecting events which do not contain on generator level at least one lepton with $p_{\mathrm{T}} \geq 1\,\mathrm{GeV}$ in the whole η range.

5.3.1 Simulation of the Detector Response

For a reliable Monte Carlo modeling of the real data a detailed and realistic simulation of the detector response is important. Two approaches of simulating the interaction of particles with matter and the detector response are employed, both based on the GEANT4 toolkit [61].
The standard simulation uses a detailed description of the detector geometry and of the propagation of the particles through the detector material and has been thoroughly validated with test-beam data. It is, however, very time-consuming. The time needed for this *full simulation* of one event is typically several minutes with the simulation of the calorimeter being the most time-consuming part.
Therefore, a *fast simulation* with a reduced level of detail in the simulation of the detector response, denoted as ATLFAST II [62], has been developed. This approach employs

Process	Cross section [fb]	Events	Integrated luminosity [fb^{-1}]
GF $H \to WW$ (MC@NLO):			
$m_H = 120\,\text{GeV}$	126.1	178 200	1412.8
$m_H = 130\,\text{GeV}$	235.3	168 920	718.0
$m_H = 140\,\text{GeV}$	343.5	178 710	520.2
$m_H = 150\,\text{GeV}$	423.7	4 500	10.6
$m_H = 160\,\text{GeV}$	494.1	4 540	9.2
$m_H = 165\,\text{GeV}$	496.5	58 660	118.1
$m_H = 170\,\text{GeV}$	471.0	58 570	124.4
$m_H = 180\,\text{GeV}$	408.6	4 510	11.0
$m_H = 190\,\text{GeV}$	306.0	4 500	14.7
$m_H = 200\,\text{GeV}$	262.8	36 190	137.7
VBF $H \to WW$ (Herwig):			
$m_H = 120\,\text{GeV}$	15.3	5000	326.8
$m_H = 130\,\text{GeV}$	30.1	29940	993.2
$m_H = 140\,\text{GeV}$	46.7	5000	107.0
$m_H = 150\,\text{GeV}$	60.6	5000	82.5
$m_H = 160\,\text{GeV}$	74.8	5000	66.8
$m_H = 165\,\text{GeV}$	76.7	28740	374.6
$m_H = 170\,\text{GeV}$	74.0	39960	539.7
$m_H = 180\,\text{GeV}$	66.6	5000	75.1
$m_H = 190\,\text{GeV}$	51.2	5000	97.6
$m_H = 200\,\text{GeV}$	45.1	39930	884.4

Table 5.2: Overview of the signal Monte Carlo samples used in this analysis which are only taking into account $W \to e/\mu\,\nu$ decays. The next-to-leading order cross sections are given as quoted in Reference [51] multiplied by the leptonic W branching fraction. The numbers of simulated events and the corresponding integrated luminosities are also given. The production cross sections of the gluon fusion and vector-boson fusion processes have been calculated with the HIGLU and VV2H programs, respectively, while the Higgs decay branching ratio has been obtained from the HDECAY program [54].

Process	Subdecays/ event filter	Generator	Cross section [pb]	Integrated luminosity [fb^{-1}]
$t\bar{t}$	$W_1 \to e/\mu/\tau\,\nu$	MC@NLO	217.6	6.75
$t\bar{t}$ (fast sim.)	$W_1 \to e/\mu/\tau\,\nu$	MC@NLO	217.6	16.9
Wt	$W \to e/\mu/\tau\,\nu$	AcerMC	3.01	14.96
$qq \to WW$	$W \to e/\mu/\tau\,\nu$	MC@NLO	7.76	20.0
$gg \to WW$	$W \to e/\mu/\tau\,\nu$	GG2WW	0.28	320.0
W + jets	$W \to e/\mu/\tau\,\nu$	Alpgen	$48.9 \cdot 10^3$	0.9
$Z \to \ell\ell$ + jets	–	Alpgen	$2.9 \cdot 10^3$	2.5
$Z \to \tau\tau$ + jets	–	Alpgen	$1.4 \cdot 10^3$	2.5
WZ	$Z \to ee/\mu\mu/\tau\tau$	MC@NLO	2.42	~ 200
ZZ	$Z \to ee/\mu\mu/\tau\tau$	MC@NLO	0.36	~ 500

Table 5.3: Overview of the background Monte Carlo samples used in this analysis. The next-to-leading order production cross sections including the decay branching fractions are given together with the event generators employed, the cross sections and the corresponding integrated luminosities. In the case of the $t\bar{t}$ sample, the cross section also includes the single lepton filter efficiency of 55%. Further details on the background Monte Carlo samples are provided in Appendix A.

the full simulation of the propagation of all particles through the inner detector and of muons through the whole detector. The simulation of the interactions of particles (except muons) in the calorimeter is based on a parameterization of the showers provided by the FastCaloSim [63] package. The calorimeter response is parameterized exploiting average shower properties while neglecting fluctuations and avoiding the simulation of the individual particle propagation, interaction and shower development. The time needed for the fast simulation of one event is reduced by a factor of ten compared to the full detector simulation.
Due to its large cross section, the $t\bar{t}$ process is one of the dominant background processes for the search for the Higgs boson in vector-boson fusion production. Large numbers of simulated events are necessary in order to reliably estimate its contribution. Hence, $t\bar{t}$ Monte Carlo samples simulated with ATLFAST II are used in this study while all other processes have been simulated with the full detector simulation. In the following section, the reconstruction performance of physics objects in full and fast detector simulation is compared. A detailed comparison of the event selection efficiencies is provided in Section 5.6.1.

5.4 Reconstruction of Physics Objects

This section provides an overview of the reconstruction, the detector performance and the preselection criteria applied for the physics objects used in this analysis. A more detailed review can be found in References [20, 32]. The reconstruction efficiencies and misidentification rates for electrons, muons and jets are calculated with respect to generated or

truth objects. An object is classified as correctly reconstructed and identified if it has a matching truth object of the same type within a certain ΔR cone. For electrons and muons a cone size of $\Delta R = 0.1$ is used whereas reconstructed jets are matched to truth jets within a cone of $\Delta R = 0.3$.
The reconstruction efficiency represents the fraction of truth objects which have a matching reconstructed object within the defined cone:

$$\text{Efficiency} = \frac{N(\text{Reconstructed objects with a matching truth object})}{N(\text{Truth objects})}.$$

The misidentification rate is defined as the fraction of reconstructed objects which have not correctly been identified, i. e. which cannot be matched to a truth object of the same type:

$$\text{Misid. rate} = \frac{N(\text{Reconstructed objects without a matching truth object})}{N(\text{Reconstructed objects})}.$$

5.4.1 Electron Reconstruction

The electron reconstruction is based on clusters in the electromagnetic calorimeter which are formed by spatially grouped calorimeter cells with significant energy deposition. In order to reject calorimeter clusters corresponding to photons, tracking information is exploited: the clusters are required to match with a track and not to overlap in solid angle with a photon conversion reconstructed in the inner detector.
The electrons are required to pass *medium* cuts [64] according to the selection criteria described in the following. The lateral and longitudinal shower shape in the electromagnetic calorimeter as well as the fraction of the electron energy deposited in the hadron calorimeter are used in order to suppress misidentified jets. In addition, the matching track is required to have at least one hit in the pixel detector and in total at least nine hits in the pixel and SCT detectors as well as a transverse impact parameter of $|d_0| < 1\,\text{mm}$ with respect to the reconstructed primary vertex.
On top of this selection, several additional cuts are imposed in order to reduce the misidentification rate of jets as electrons. Only electrons within $|\eta| < 2.5$ with transverse momenta above 15 GeV and a transverse impact parameter significance of $|d_0|/\sigma(d_0) < 10$ are retained. In addition, the electrons are required to be isolated, i. e. the energy deposited in a $\Delta R = 0.3$ cone around the electron shower is required to be below 10 GeV and to be less than 20% of the transverse momentum of the electron. The sum of transverse momenta of tracks in a cone of $\Delta R = 0.3$ around the electron is required to be below 10 GeV and to be less than 10% of the transverse momentum of the electron. Only tracks originating from the same reconstructed vertex as the electron are considered.
In the transition regions between the barrel and end-cap regions of the calorimeter ($1.37 < |\eta| < 1.52$) the misidentification rate of jets as electrons is significantly larger compared to other detector regions. Therefore, electrons in these regions are rejected. The p_T distributions of electrons in the signal and background processes and the electron reconstruction efficiency as a function of p_T and η are shown in Figures 5.4 and 5.5, respectively. The decreasing reconstruction efficiency at high transverse momentum in $H \to WW$ events originates from requiring the electrons to be isolated. In contrast to $t\bar{t}$ events, the two

leptons in $H \to WW$ events are emitted in a small ΔR region of the detector, due to spin correlations between the two W bosons. This can lead to increased deposited energies and a larger number of tracks in the isolation cone around the electron and, thus, to the electrons not being isolated. However, only a small fraction of electrons has transverse momenta above $p_{\mathrm{T}} = 90\,\mathrm{GeV}$, for which a decreased reconstruction efficiency is observed. Hence, no significant impact on the discovery potential is expected.

5.4.2 Muon Reconstruction

In ATLAS, muons are reconstructed with a comparable performance by two different algorithms, STACO [65] and MUID [66], which both exploit the information provided by all detector subsystems. Muons are reconstructed in the muon spectrometer and extrapolated to the interaction point taking into account the energy loss in the calorimeter system. Within the acceptance of the inner detector ($|\eta| < 2.5$) the reconstructed segments of the muon trajectory in the inner detector and muon spectrometer are combined in order to achieve optimal momentum resolution. For muons with high transverse momenta, the momentum resolution is dominated by the muon spectrometer measurement while at lower transverse momenta the resolution is dominated by measurements in the inner detector. For transverse momenta below 100 GeV, a transverse momentum resolution of 2-3% is achieved by combining the inner detector and muon spectrometer measurements. Further details regarding the muon reconstruction in the muon spectrometer are provided in Section 4.1.1.
In this analysis, muons reconstructed by the STACO algorithm within $|\eta| < 2.5$, with transverse momenta above 15 GeV and with a transverse impact parameter significance of $|d_0|/\sigma(d_0) < 10$ are employed. In addition, calorimeter and track isolation requirements are imposed. The energy deposited in a cone with radius $\Delta R = 0.3$ around the muon is required to be below 10 GeV and to be less than 20% of the transverse momentum of the muon. The sum of transverse momenta of tracks originating from the same reconstructed vertex in a cone of the same size is required to be below 10 GeV and to be less than 10% of the muon transverse momentum.
The muon p_{T} distributions in signal and background events are shown in Figure 5.4. In Figure 5.5, the reconstruction efficiency of muons is shown as a function of p_{T} and η for signal and $t\bar{t}$ events. The reconstruction inefficiencies are caused by gaps in the acceptance of the muon spectrometer at $|\eta| = 0$ due to service connections and in the barrel–end-cap transition region at $|\eta| \cong 1.2$. As for electrons, the decreasing muon reconstruction efficiency at high transverse momentum in $H \to WW$ events originates from requiring the muons to be isolated.

5.4.3 Jet Reconstruction

Jets are reconstructed from topological clusters in the calorimeter comprising neighboring calorimeter cells grouped in η and ϕ around a seed cell [67]. Several jet reconstruction algorithms are available in the ATLAS software framework. This study employs a seeded, fixed-size cone algorithm [68,69] with a cone size of $R_{\mathrm{cone}} = 0.4$ which is discussed in more detail in Section 6.4.1. The reconstructed jet energies are calibrated by means of a cell signal weighting method referred to as H1-weighting [70].

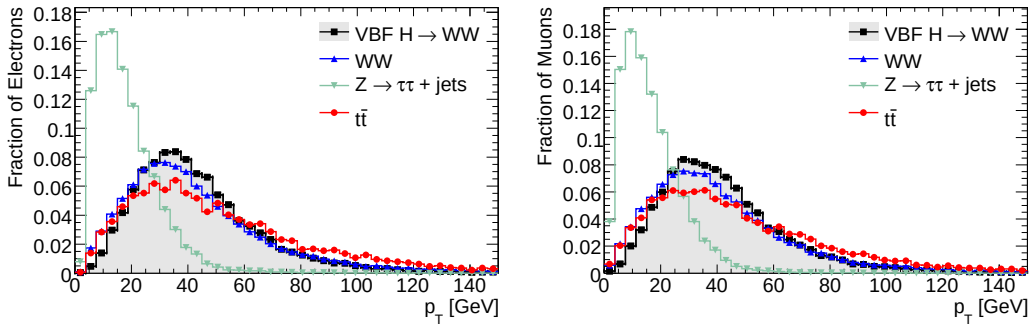

Figure 5.4: Transverse momentum distributions of electrons (left) and muons (right) for vector-boson fusion $H \rightarrow WW$ events and different background processes.

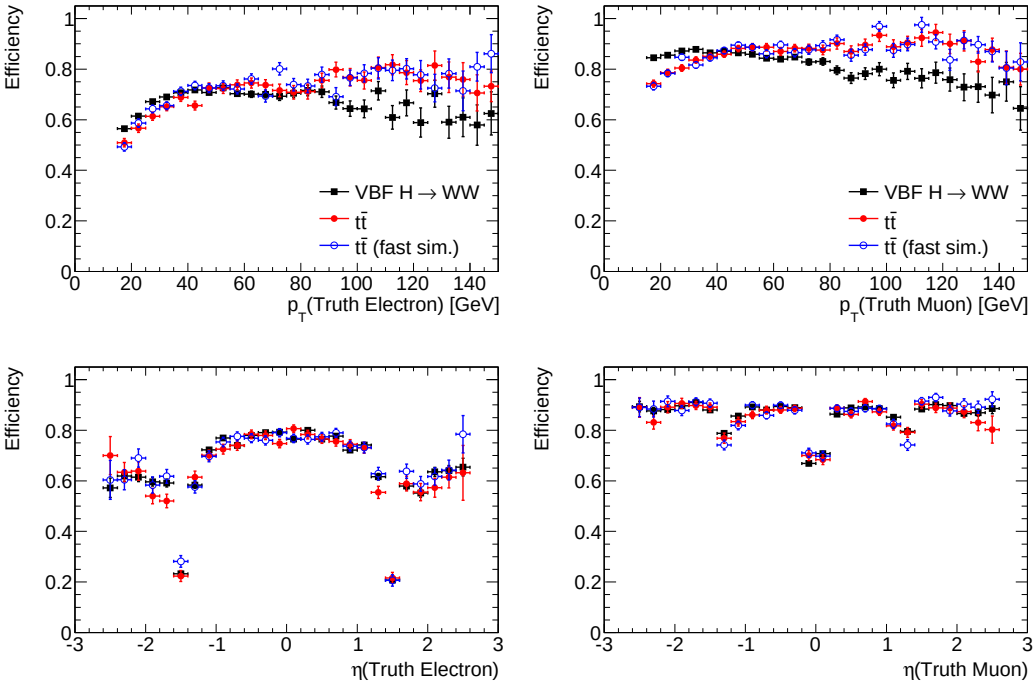

Figure 5.5: Electron (left) and muon (right) reconstruction efficiencies for vector-boson fusion $H \rightarrow WW$ and $t\bar{t}$ background events from full and fast detector simulation.

	VBF $H \to WW$	$t\bar{t}$	$t\bar{t}$ (fast sim.)
Efficiency:			
Electron:	67.88 ± 0.26	67.33 ± 0.40	68.60 ± 0.40
Muon:	85.23 ± 0.19	84.64 ± 0.31	84.83 ± 0.31
Jet:	99.04 ± 0.04	98.11 ± 0.03	98.31 ± 0.03
Misidentification rate:			
Electron:	0.18 ± 0.03	0.72 ± 0.09	0.47 ± 0.07
Muon:	0.03 ± 0.01	0.13 ± 0.03	0.15 ± 0.04
Jet:	12.10 ± 0.11	5.21 ± 0.05	5.20 ± 0.05

Table 5.4: Reconstruction efficiencies and misidentification rates [%] for electrons, muons and jets. A good agreement between the values for $t\bar{t}$ events with fast and full detector simulation is observed. Only the misidentification rate for electrons is slightly underestimated in the present version of ATLFAST II.

Since the jet reconstruction is solely based on calorimeter objects, energy depositions by electrons and photons are also reconstructed by the jet reconstruction algorithm. Therefore, jet candidates which overlap within a cone of $\Delta R = 0.4$ with a reconstructed electron with $p_{\mathrm{T}} > 10\,\mathrm{GeV}$ are rejected[2]. Also, jets with a distance below $\Delta R = 0.4$ to a reconstructed muon are discarded. The same procedure is applied on truth level, i. e. truth jets which overlap with a truth lepton are rejected. The distributions of the transverse momentum and the pseudo-rapidity of jets are displayed in Figure 5.6. Jets originating from the vector-boson fusion production are predominantly reconstructed in the forward regions of the detector at large $|\eta|$ whereas jets from the background processes are concentrated in the central region of the detector. As shown in Figure 5.7 and Table 5.4, comparable jet reconstruction efficiencies of about 98% are observed for the signal and the $t\bar{t}$ processes. The large differences between the misidentification rates in signal and $t\bar{t}$ events in the region $|\eta| < 2.5$ are caused by electrons which are not reconstructed and identified by the electron reconstruction algorithm. Thus, the corresponding jets are not rejected on reconstruction level while they are on truth level. Due to the larger jet multiplicities in $t\bar{t}$ events, a lower impact is observed compared to $H \to WW$ events.
Recently, it has been shown that other jet reconstruction algorithms such as the anti-k_T [71] or SISCone [72] algorithms show a better reconstruction performance compared to the standard cone algorithm and will in fact be the first algorithms to be studied with early data. However, these new algorithms could not be considered in this study since the data samples employed only contain jets reconstructed by the cone algorithm.

5.5 Event Selection Criteria

After the events have passed the trigger selection, several variables are employed in order to separate signal from background processes. Two groups of variables suppress background selecting the leptons originating from $H \to WW$ decays and the tagging jets, respectively.

[2]Since none of the involved signal and background processes comprise photons in the final state at tree-level, a photon overlap removal is not necessary.

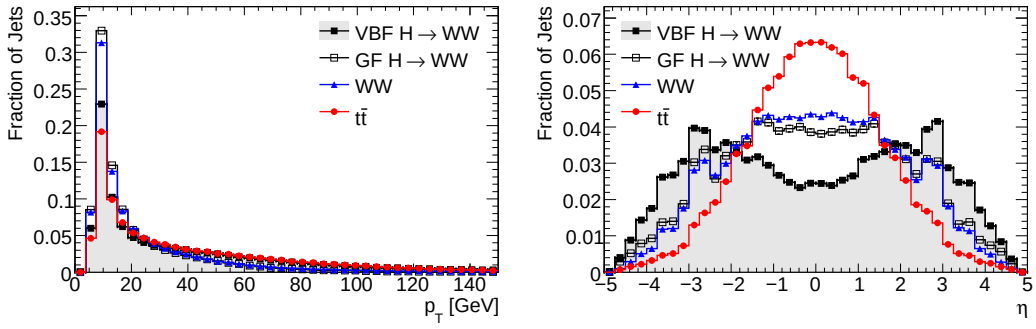

Figure 5.6: Distributions of the transverse momentum (left) and the pseudo-rapidity (right) of jets for $H \rightarrow WW$ (VBF = vector-boson fusion, GF = gluon fusion) events and different background processes.

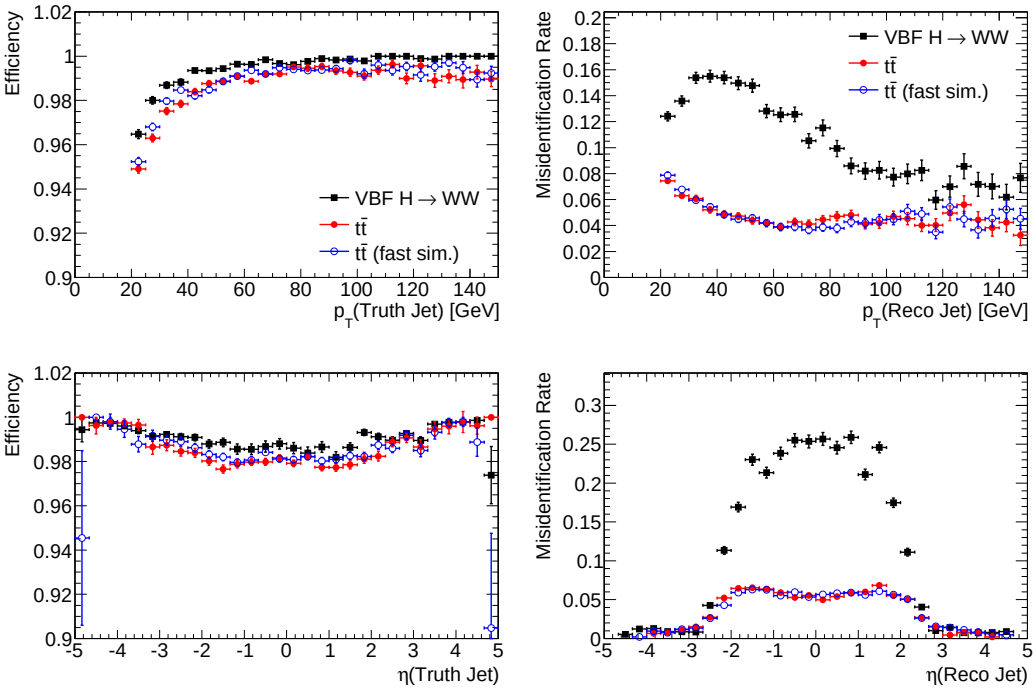

Figure 5.7: Jet reconstruction efficiencies and misidentification rates for vector-boson fusion $H \rightarrow WW$ and $t\bar{t}$ background events from full and fast detector simulation.

Trigger	Electron	Muon	Combined
L1	90.0 ± 0.1	62.6 ± 0.2	98.4 ± 0.1
L2	76.1 ± 0.2	97.1 ± 0.1	95.7 ± 0.1
EF	87.5 ± 0.2	97.5 ± 0.1	96.5 ± 0.1
Total	60.0 ± 0.2	59.2 ± 0.2	90.9 ± 0.1

Table 5.5: Event selection efficiencies [%] of the different electron (e10_medium) and muon (mu10) trigger levels and their combination for vector-boson fusion $H \rightarrow WW$ events.

This analysis studies the discovery potential of the Higgs boson with early data corresponding to $1\,\text{fb}^{-1}$, for which relatively large statistical and systematic uncertainties are expected. The cut values applied on the selection variables have mostly been determined in the framework of the ATLAS $H \rightarrow WW$ working group [73] based on the studies presented in Reference [49]. Since previous analyses focused on the estimation of the discovery potential at $10\,\text{fb}^{-1}$, several cuts had to be adjusted for optimal performance at $1\,\text{fb}^{-1}$.

5.5.1 Trigger

As stated in Section 3.1.6, the ATLAS trigger selection proceeds in trigger chains consisting of three consecutive levels: level 1, level 2 (L1, L2) and the event filter (EF). In this analysis, two single-lepton trigger chains are employed, denoted as `e10_medium` and `mu10`, requiring electrons or muons with transverse energy or momentum above 10 GeV. The selection efficiencies of the three trigger levels are shown in Figure 5.8. The trigger efficiency for electrons is almost 100%, independent of η and ϕ. In contrast, for muons an efficiency of about 90% is observed which exhibits a modulation in ϕ corresponding to the eight-fold symmetry of the muon spectrometer. Efficiency losses of the L1 muon trigger in η and ϕ are due to regions of the muon spectrometer not covered by trigger chambers because of spatial constraints. Table 5.5 gives the event selection efficiencies for $H \rightarrow WW \rightarrow ll$ events for the two trigger chains and for their combination.

5.5.2 Selection of the Higgs Decay Products

This section gives an overview of the discriminating variables related to the Higgs decay products whereas the following section introduces the tagging jet selection criteria.

Number of Leptons

In Figure 5.9, the number of reconstructed leptons per event in signal and background is shown. Only events with exactly two reconstructed leptons with $p_{\text{T}} > 15\,\text{GeV}$ are retained. The large fraction of signal events with less then two leptons is caused by the reconstruction inefficiencies for electrons and muons.

Furthermore, the two leptons are required to carry opposite charges which rejects backgrounds such as the W + jets process in which a jet is misidentified as a lepton.

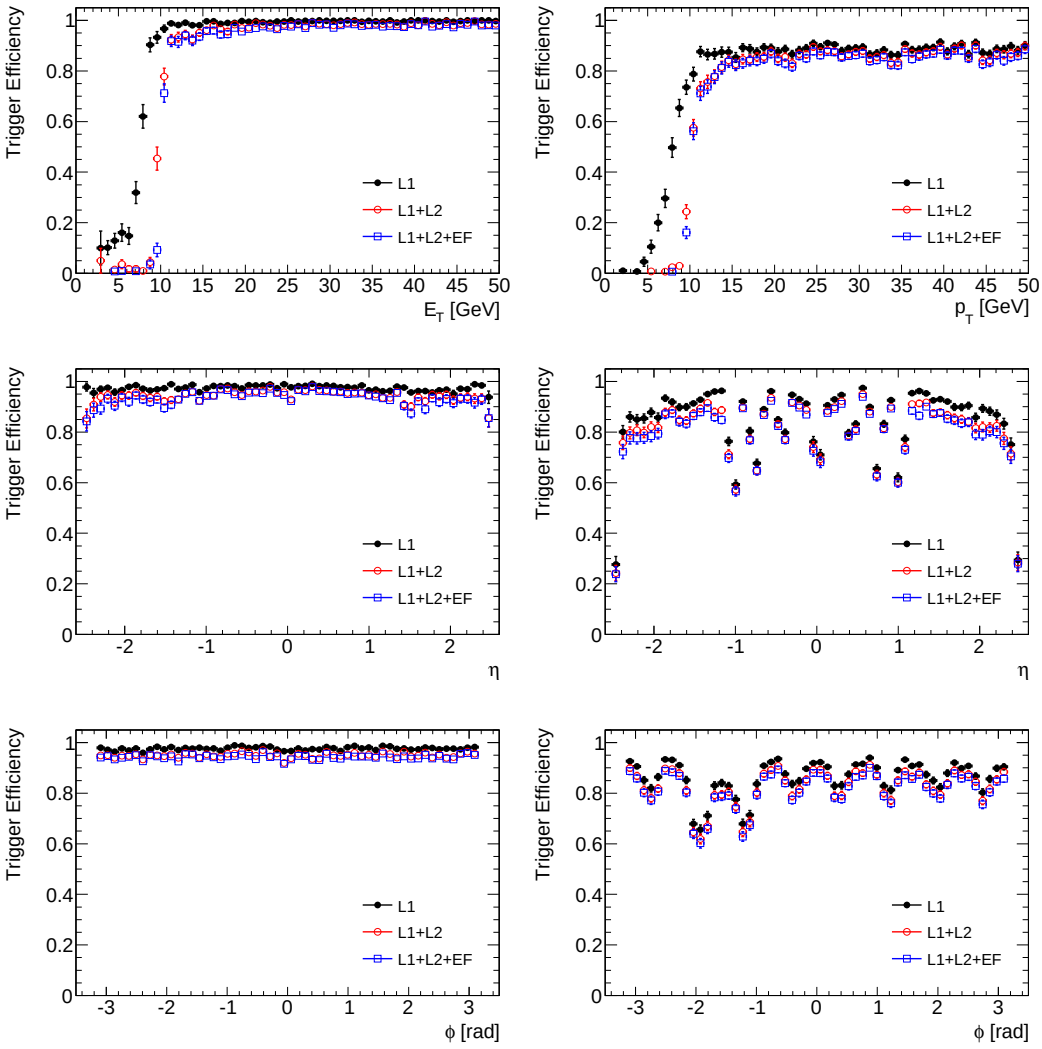

Figure 5.8: Efficiencies of the electron (left) and muon (right), e10_medium and mu10, trigger chains as a function of E_{T} (p_{T}), η and ϕ of the leptons determined by the offline reconstruction algorithms for vector-boson fusion $H \rightarrow WW$ events.

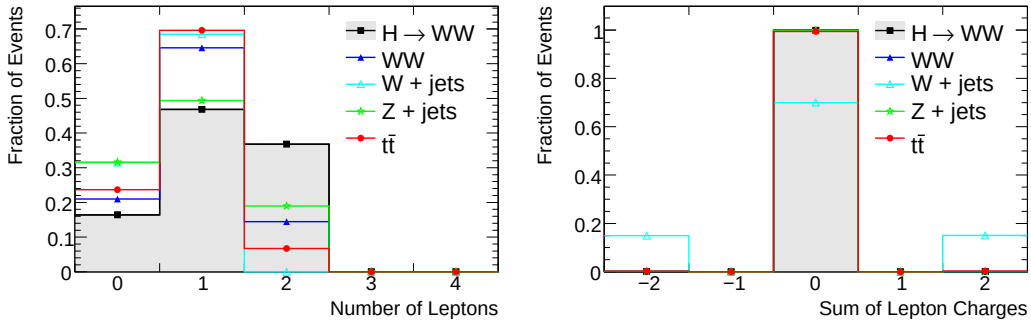

Figure 5.9: Number of reconstructed leptons (electrons and muons) in signal and background events (left) and the sum of the charges of the two selected leptons (right). Only events which contain exactly two oppositely charged leptons are retained in the analysis.

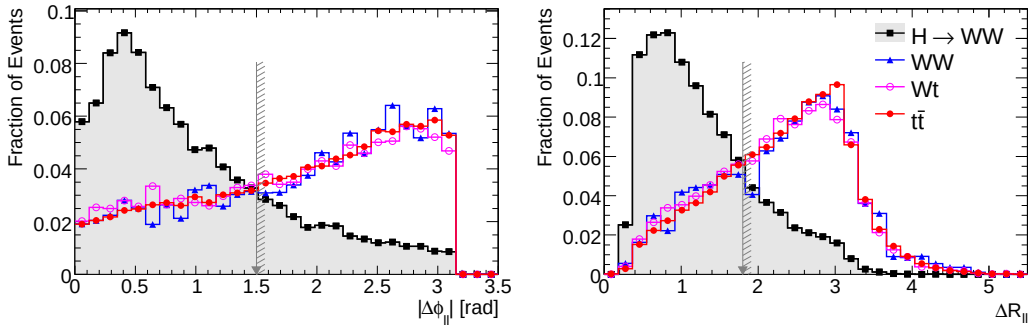

Figure 5.10: Distributions of the azimuthal angle $\Delta\phi_{ll}$ (left) and the distance $\Delta R_{\ell\ell}$ (right) between the two leptons. The gray arrows indicate the cut values. In addition, the leptons have been required to have a minimal distance of $\Delta R = 0.3$ between each other in order to avoid double reconstruction.

Lepton Kinematics

As stated in Section 5.1, in $H \to WW \to l\nu l\nu$ decays the two leptons tend to be emitted in the same direction due to the spin correlation between the two W bosons. Thus, background contributions can efficiently be suppressed by requiring a small distance in ϕ ($|\Delta\phi_{ll}| < 1.3$ rad) and η-ϕ ($\Delta R_{\ell\ell} < 1.8$) between the two leptons. The corresponding distributions are shown in Figure 5.10.
The invariant mass of the lepton-pair m_{ll} is used in order to suppress leptons originating from Z bosons. As shown in Figure 5.11, requiring $m_{ll} < 70\,\text{GeV}$ provides a very good rejection against $Z \to \ell\ell$ events. In addition, a cut of $m_{ll} > 15\,\text{GeV}$ is applied in order to reject contributions from $b\bar{b}$ events.

Missing Transverse Energy $E_{\mathrm{T}}^{\mathrm{miss}}$

The presence of the two neutrinos from $W \to l\nu$ decays in the signal process leads to a significant amount of missing transverse energy. In contrast, apart from detector effects, the missing transverse energy should vanish for background processes without neutrinos.

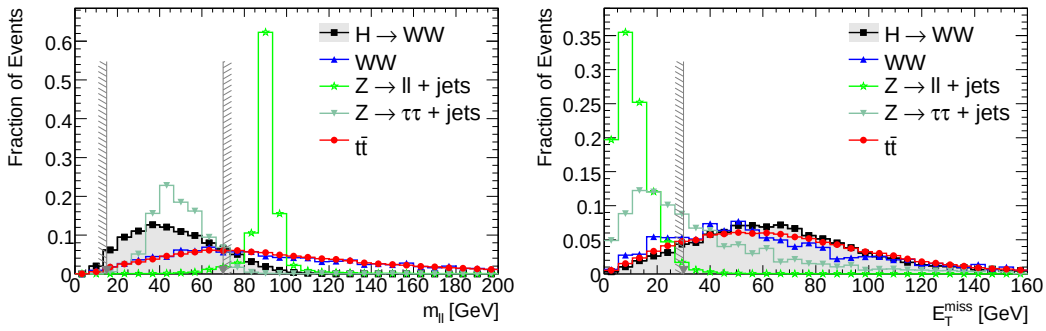

Figure 5.11: Distributions of the di-lepton invariant mass m_{ll} (left) and the missing transverse energy (right). The gray arrows indicate the cut values.

Therefore, these processes can efficiently be suppressed by requiring a minimum missing transverse energy in the event. The missing transverse energy is calculated as the vectorial sum of the transverse calorimeter cell energies and the transverse momenta of muons which have an associated track in the inner detector [74]. Here, the muon transverse momenta are reconstructed in the muon spectrometer alone taking into account the energy loss in front of and within the calorimeter. Figure 5.11 shows that a cut of $E_{\mathrm{T}}^{\mathrm{miss}} > 30\,\mathrm{GeV}$ allows for an efficient suppression of the $Z \to \ell\ell$ and $Z \to \tau\tau$ background.

$Z \to \tau\tau$ Veto

Assuming that the two leptons and the missing transverse energy are originating from $Z \to \tau\tau \to l\nu\nu l\nu\nu$ decays, the invariant mass $m_{\tau\tau}$ of the τ-pair can be reconstructed by means of the collinear approximation and is used to identify and suppress $Z \to \tau\tau$ events. Due to the large Lorentz boost of the τ leptons, the τ decay products can be assumed to be emitted parallel to the τ direction as depicted in Figure 5.12. With this assumption, the contribution of the neutrinos from each τ lepton decay to the total missing transverse energy can be determined.
The fractions of the τ momenta in the transverse plane carried by the visible τ-lepton decay products, χ_1 and χ_2, are defined by:

$$\boldsymbol{p}_T^{\tau_1} + \boldsymbol{p}_T^{\tau_2} = \frac{\boldsymbol{p}_T^1}{\chi_1} + \frac{\boldsymbol{p}_T^2}{\chi_2} = \boldsymbol{p}_T^1 + \boldsymbol{p}_T^2 + \boldsymbol{E}_T^{\mathrm{miss}} \tag{5.8}$$

with $\boldsymbol{p}_T^{\tau_1(\tau_2)}$ and $\boldsymbol{p}_T^{1(2)}$ representing the transverse momenta of the τ-leptons and of the visible τ-decay products, respectively. χ_1 and χ_2 can be calculated from this equation according to

$$\begin{aligned} \chi_1 &= \frac{p_{\mathrm{x}}^1 p_{\mathrm{y}}^2 - p_{\mathrm{y}}^1 p_{\mathrm{x}}^2}{p_{\mathrm{y}}^2 (p_{\mathrm{x}}^1 + E_{\mathrm{x}}^{\mathrm{miss}}) - p_{\mathrm{x}}^2 (p_{\mathrm{y}}^1 + E_{\mathrm{y}}^{\mathrm{miss}})} \\ \chi_2 &= \frac{p_{\mathrm{x}}^1 p_{\mathrm{y}}^2 - p_{\mathrm{y}}^1 p_{\mathrm{x}}^2}{p_{\mathrm{x}}^1 (p_{\mathrm{y}}^2 + E_{\mathrm{y}}^{\mathrm{miss}}) - p_{\mathrm{y}}^1 (p_{\mathrm{x}}^2 + E_{\mathrm{x}}^{\mathrm{miss}})}. \end{aligned} \tag{5.9}$$

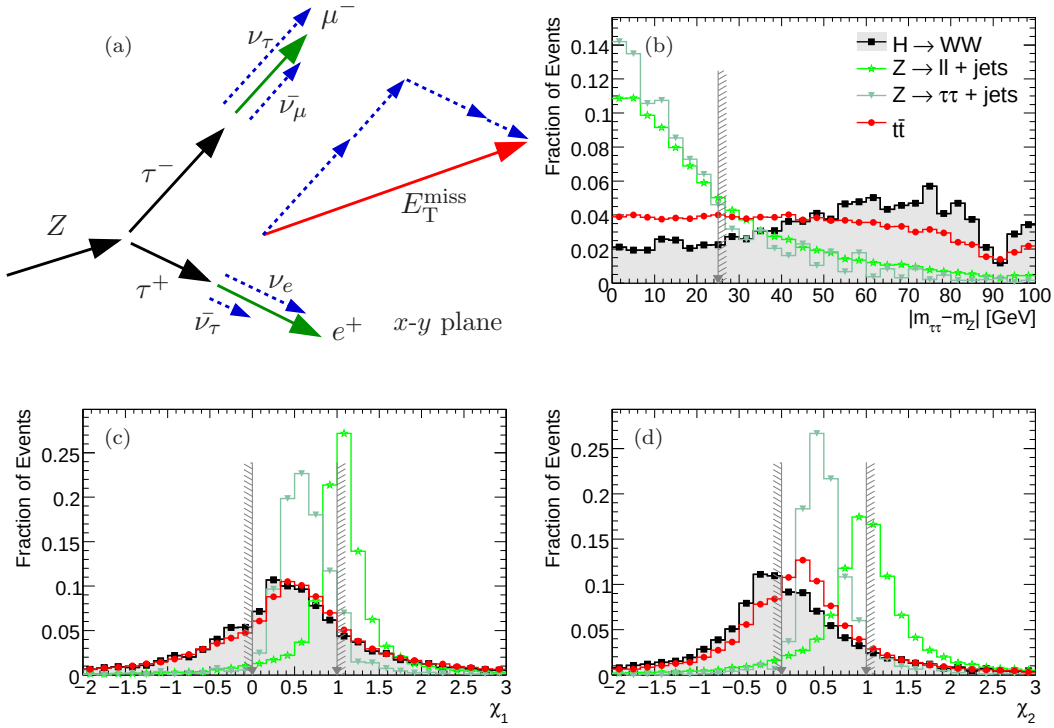

Figure 5.12: The principle of the collinear approximation in $Z \to \tau\tau$ events [75] is shown in (a). Due to the Lorentz boost of the τ leptons, the τ-decay products can be assumed to be emitted in the flight direction of the τ leptons. Thus, the individual contributions of the neutrinos to the missing transverse energy can be estimated which allows for the calculation of the τ momenta and of the invariant mass $m_{\tau\tau}$ of the τ-pair. The distributions of $m_{\tau\tau}$ and of the visible τ momentum fractions χ_1 and χ_2 are shown in (b)-(d). The gray arrows indicate the cuts against $Z \to \tau\tau$ events.

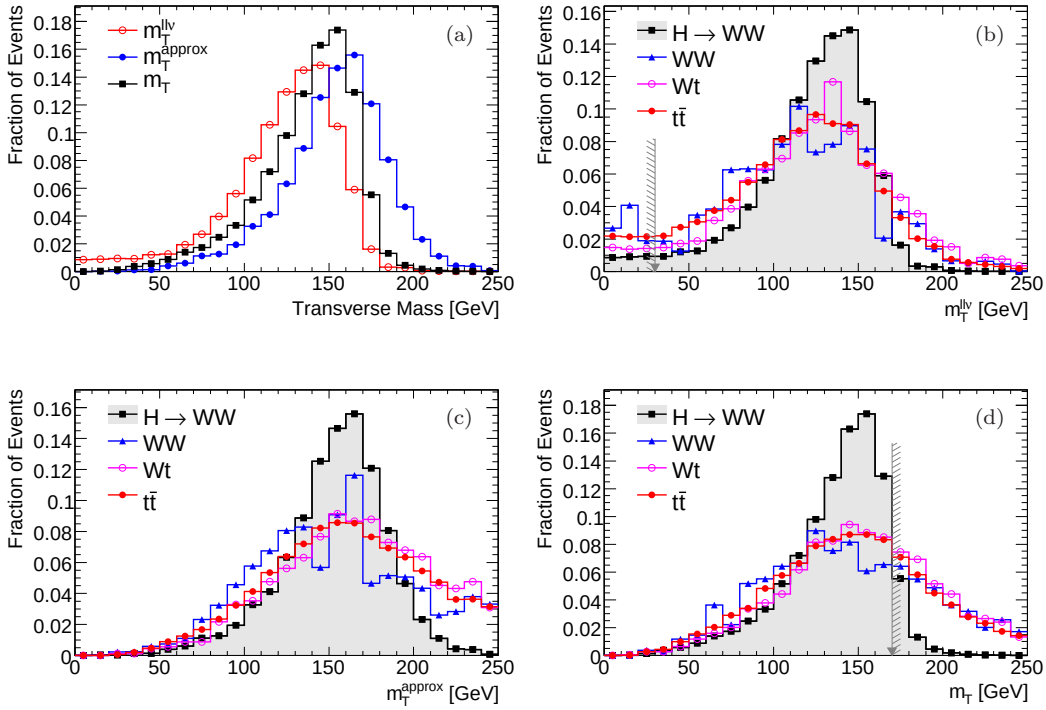

Figure 5.13: Distributions of the different Higgs transverse mass definitions for signal events with $m_H = 170\,\text{GeV}$ (a) and the comparison to the most dominant background processes in (b)-(d). The gray arrows indicate the cut values applied on $m_{\text{T}}^{ll\nu}$ and m_{T}.

Hence, the momenta of the τ leptons and the invariant mass of the τ-pair can be determined. A more detailed description of the collinear approximation and the derivation of Equation 5.9 is provided in Reference [75].
As shown in Figure 5.12, the momentum fractions χ_1 and χ_2 in $Z \to \tau\tau$ decays have physical values between 0 and 1 in contrast to the signal process. Therefore, events simultaneously fulfilling $\chi_1 > 0$, $\chi_2 > 0$ and $|m_{\tau\tau} - m_Z| < 25\,\text{GeV}$ are rejected which allows for a good separation between signal and $Z \to \tau\tau$ events.

Transverse Mass

In Figure 5.13, the distributions of the different Higgs transverse mass definitions introduced in Section 5.1 are compared for vector-boson fusion $H \to WW$ events with a Higgs boson mass of $m_H = 170\,\text{GeV}$ and the dominant background processes.
The distribution of $m_{\text{T}}^{ll\nu}$ is shifted towards lower values with respect to the other definitions of the transverse mass since it is defined under the assumption of vanishing di-lepton masses, $m_{ll} \approx 0$ (see Equation 5.6). This shift is even more pronounced for the background distributions. Therefore, a cut $m_{\text{T}}^{ll\nu} > 30\,\text{GeV}$ is used in order to reject background contributions at very low masses.
For the signal process, m_{T} and $m_{\text{T}}^{ll\nu}$ show, in contrast to $m_{\text{T}}^{\text{approx}}$, a characteristic edge at the Higgs boson mass ($m_H = 170\,\text{GeV}$), providing a lower bound on m_H apart from

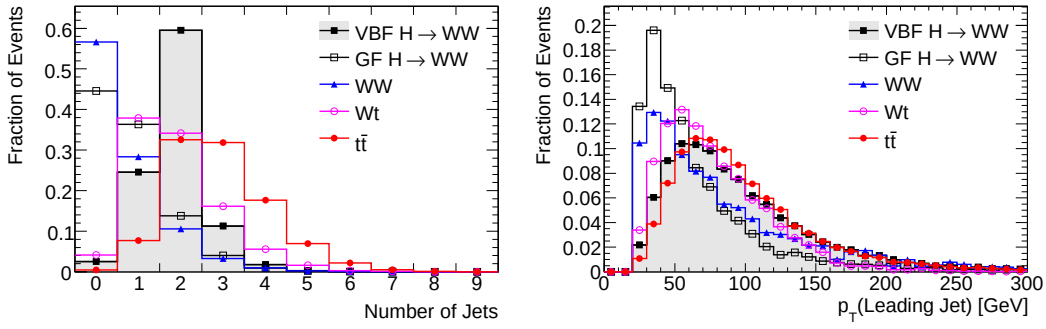

Figure 5.14: Number of jets with transverse momenta above 20 GeV within $|\eta| < 4.8$ (left) and the transverse momentum distribution of the leading jet (right). Only events which contain at least two jets are retained in this analysis. In addition, for the leading jet a transverse momentum above 40 GeV is required.

detector resolution effects. m_{T} is used for the definition of the Higgs mass search window and a cut of $m_{\mathrm{T}} < m_H$ is applied in order to reject backgrounds at high masses[3].

5.5.3 Tagging Jet Selection

Tagging Jet Candidates

The topology of the vector-boson fusion production process is exploited by requiring at least two jets with $p_{\mathrm{T}} > 20$ GeV within $|\eta| < 4.8$ in the event. The number of reconstructed jets per event is shown in Figure 5.14. The two jets with the highest transverse momentum are classified as the tagging jets and are required to lie in opposite hemispheres of the detector. The highest momentum (leading) jet is required to have a transverse momentum above 40 GeV.

Tagging Jet Kinematics

In contrast to all background processes, the jets from vector-boson fusion tend to be emitted into the forward detector regions and thus span a large rapidity gap as shown in Figure 5.15. This characteristic signature is exploited by requiring the jets to be well separated in η ($|\Delta\eta_{jj}| > 3.8$). In addition, jets from the vector-boson fusion production tend to have high energies in contrast to jets originating from QCD processes. Therefore, for the selection of vector-boson fusion events usually a cut on the invariant mass of the jet pair m_{jj} is applied (e. g. $m_{jj} > 500$ GeV). However, due to the high background rejection of the selection cuts applied, this analysis suffers from rather low Monte Carlo background statistics and from a low number of expected background events. Therefore, the cut on m_{jj} is omitted here which allows for a background prediction with significantly reduced Monte Carlo statistical error. As shown in Figure 5.15, for example, a cut of $m_{jj} > 500$ GeV also rejects a large fraction of vector-boson fusion and gluon fusion $H \rightarrow WW$ signal events. The cut on m_{jj} can be omitted without decreasing the signal significance. It is assumed

[3] With early collision data, the discovery potential for the Higgs boson will be probed individually for each assumed value of m_H.

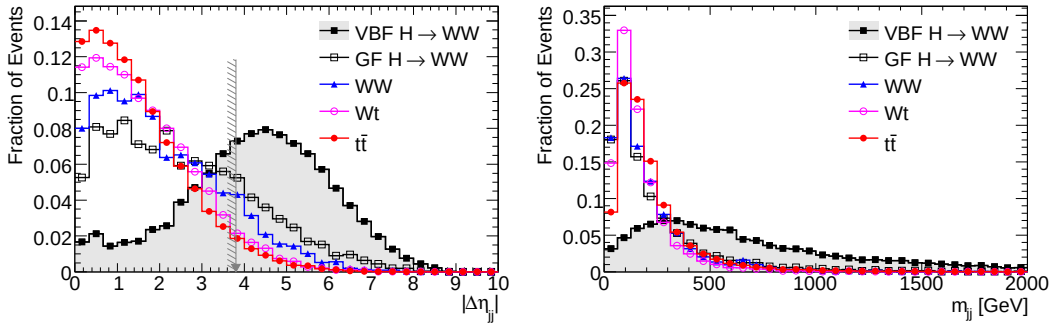

Figure 5.15: Distributions of the pseudo-rapidity distance $\Delta\eta_{jj}$ between the two tagging jets (left) and the invariant di-jet mass m_{jj} (right). The gray arrow indicates the cut value applied on $\Delta\eta_{jj}$.

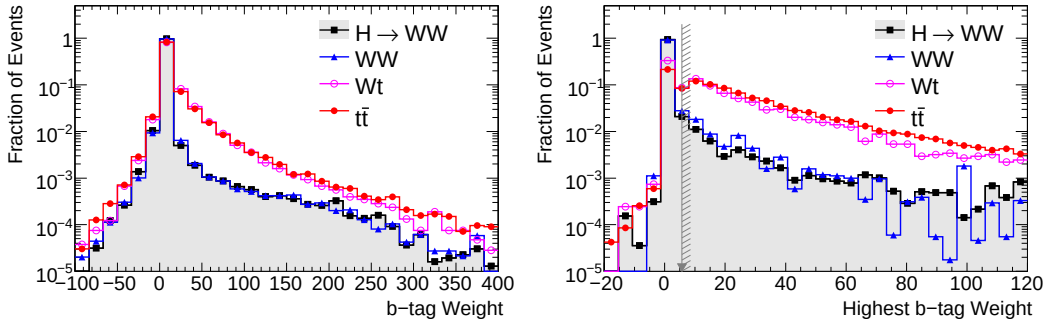

Figure 5.16: b-tag weight distribution for all jets in an event (left) and for the jets with the highest b-tag weight in the event (right). The gray arrow indicates the cut value.

that the contribution from QCD multi-jet processes can still be sufficiently suppressed by the cut on the missing transverse energy as well as by the lepton and the other tagging jet selection criteria.

b-jet Veto

Top quarks decay almost exclusively into a W boson and a b quark while no b-jets are present in the signal process. Therefore, $t\bar{t}$ events can efficiently be rejected by vetoing b-jets.
Since b hadrons have a relatively long lifetime of $\tau \sim 1.5\,\text{ps}$ their decay vertex is displaced from the primary interaction vertex on average by a few millimeters. Therefore, tracks emerging from the hadronization of b quarks tend to have a large transverse impact parameter with respect to the primary vertex and can usually be associated to a common secondary vertex. Thus, jets can be identified as initiated by a b quark if they contain tracks originating from a displaced vertex. Several algorithms for b-jet identification exist in the ATLAS reconstruction software. In this study, the SV0 b-tagger is employed which identifies b-jets by means of the signed decay length significance of the secondary vertex [76]. Figure 5.16 shows the distribution of b-tag weights used for the classification

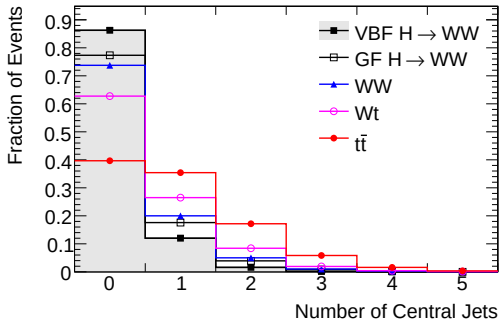

Figure 5.17: Number of additional central jets within $|\eta| < 3.0$. Only events without additional central jets are retained in this analysis.

of b-jets for all jets in the event as well as for the jets with the highest b-tag weight. A jet is classified as b-jet by having a b-tag weight above 5.71.
The b-jet identification efficiency and light-jet rejection depend on the performance of the track and secondary vertex reconstruction and, thus, on the alignment accuracy of the inner detector which will not yet be perfect for the early data taking. The SV0 tagger has been chosen since it is one of the first b-tagging algorithms to be studied with early data.

Central Jet Veto

Due to the absence of color exchange between the partons participating in the vector-boson fusion process, jet activity in the central region of the detector is suppressed. Thus, a veto is applied on events which contain jets with $p_{\mathrm{T}} > 20\,\mathrm{GeV}$ within $|\eta| < 3.0$ in addition to the tagging jets. As shown in Figure 5.17, this central jet veto provides a particularly good rejection against the top-quark background processes. A more detailed study of the central jet veto performance, in particular of its sensitivity to pile-up is given in Section 6.8.

Transverse Momentum Balance

The transverse momentum of the incoming partons essentially vanishes. Thus, in the vector-boson fusion $H \rightarrow WW$ process the total transverse momentum of the Higgs decay products and the tagging jets vanishes provided there are no additional jets present in the final state. Hence, a cut is applied on the total transverse momentum $p_{\mathrm{T}}^{\mathrm{tot}} < 30\,\mathrm{GeV}$ of the decay products and tagging jets:

$$\boldsymbol{p}_{\mathrm{T}}^{\mathrm{tot}} = \boldsymbol{p}_{\mathrm{T}}^{j1} + \boldsymbol{p}_{\mathrm{T}}^{j2} + \boldsymbol{p}_{\mathrm{T}}^{\ell 1} + \boldsymbol{p}_{\mathrm{T}}^{\ell 2} + \boldsymbol{p}_{\mathrm{T}}^{\mathrm{miss}}, \tag{5.10}$$

where $j1, j2$ and $l1, l2$ denote the two tagging jets and leptons, respectively. As shown in Figure 5.18, the distribution of the total transverse momentum depends on the number of additional central jets. Hence, the central jet veto and the cut on the transverse momentum balance are strongly correlated. While the central jet veto has the advantage of not depending on the missing transverse energy, the transverse momentum balance is more robust against additional central jets originating from pile-up events. The impact of the presence pile-up on both selection criteria is studied in Chapter 6.

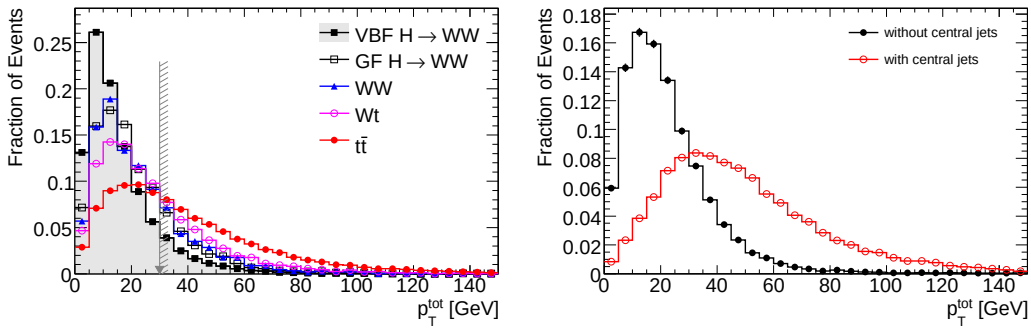

Figure 5.18: Distributions of the total transverse momentum $p_{\mathrm{T}}^{\mathrm{tot}}$ defined in Equation 5.10 for the signal and the dominant background processes (left) and for $t\bar{t}$ events without and with additional central jets (right). The gray arrow indicates the cut value.

5.6 Event Selection Efficiencies

5.6.1 Comparison of Full and Fast Simulation

Due to the large cross section, sufficiently large Monte Carlo event statistics for the $t\bar{t}$ background can only be produced with the fast detector simulation. This section provides a comparison between the $t\bar{t}$ event selection efficiencies in the full and the fast simulation. In the ATLFAST II version used, the simulation of the trigger was not yet included. Thus, the trigger selection has been emulated by requiring at least one reconstructed lepton with $p_{\mathrm{T}} > 10\,\mathrm{GeV}$ in the event selection. Due to regions of the muon spectrometer not covered by trigger chambers, the average trigger efficiency for muons is only about 90% over almost the whole p_{T} range while a trigger efficiency of almost 100% is observed for electrons as shown in Figure 5.8. This is taken into account by randomly rejecting 10% of the muons passing the trigger condition in events from the fast simulation. As shown in Table 5.6, a slightly higher trigger selection efficiency is observed in the fast simulation compared to the full simulation. This is due to leptons with transverse momenta just above the trigger threshold of 10 GeV where the trigger efficiency is steeply rising before it reaches a plateau at about 15 GeV, an effect not taken into account by the simple p_{T} cut. Very good agreement between the event selection efficiencies is observed after requiring two leptons with $p_{\mathrm{T}} > 15\,\mathrm{GeV}$, since for these transverse momenta the trigger efficiencies for electrons and muons have reached the plateau and the differences between full and fast simulation vanish.

As shown in Table 5.6, for most of the event selection criteria good agreement between full and fast simulation is observed. The differences in the selection efficiencies of the cut on the transverse momentum balance $p_{\mathrm{T}}^{\mathrm{tot}}$ are due to the low statistics of $t\bar{t}$ events from the full simulation at this stage of the event selection. The fast simulation is validated for the latter cuts in the event selection by omitting cuts which exploit kinematic relations of the leptons. As shown in Table 5.7, also for the cut on the transverse momentum balance and the b-jet veto good agreement between fast and full simulation is observed.

As shown in Figure 5.19, good agreement is observed between fast and full simulation for the distributions of the most important discriminating variables. Solely for the missing

	Full sim.	Fast sim.
Cross section	217 600	217 600
Trigger	137 800 ± 87	138 800 ± 55
$N(e+\mu)=2$	9 976 ± 38	9 968 ± 24
Lepton charge	9 920 ± 37	9 910 ± 24
$E_T^{miss} > 30\,\text{GeV}$	8 500 ± 35	8 424 ± 22
$m_{ll} = [15, 70]\,\text{GeV}$	2 730 ± 20	2 738 ± 13
$m_{\text{T}}^{ll\nu} > 30\,\text{GeV}$	2 427 ± 19	2 439 ± 12
$Z \to \tau\tau$ veto	2 342 ± 19	2 355 ± 12
$\lvert\Delta\phi_{ll}\rvert < 1.5$	1 585 ± 15	1 610 ± 10
$\Delta R_{\ell\ell} < 1.8$	1 462 ± 15	1 491 ± 9
$m_{\text{T}} < 170\,\text{GeV}$	1 213 ± 13	1 241 ± 9
$N(\text{jets}) \geq 2$	1 129 ± 13	1 154 ± 8
$p_T(\text{jet1}) > 40\,\text{GeV}$	1 083 ± 13	1 107 ± 8
$\eta_{j1} \times \eta_{j2} < 0$	460.6 ± 8.3	469.4 ± 5.2
$\lvert\Delta\eta_{jj}\rvert > 3.8$	42.67 ± 2.51	44.27 ± 1.62
Central jet veto	10.67 ± 1.26	10.64 ± 0.79
$p_{\text{T}}^{\text{tot}} < 30\,\text{GeV}$	6.07 ± 0.95	7.57 ± 0.67
b-jet veto	1.93 ± 0.53	2.72 ± 0.40

(a) Cross section times efficiency [fb].

Full sim.	Fast sim.
100	100
63.3 ± 0.1	63.8 ± 0.1
7.2 ± 0.1	7.2 ± 0.1
99.4 ± 0.1	99.4 ± 0.1
85.7 ± 0.1	85.0 ± 0.1
32.1 ± 0.2	32.5 ± 0.1
88.9 ± 0.2	89.1 ± 0.1
96.5 ± 0.1	96.5 ± 0.1
67.7 ± 0.4	68.4 ± 0.2
92.2 ± 0.3	92.7 ± 0.2
83.0 ± 0.4	83.2 ± 0.2
93.1 ± 0.3	93.0 ± 0.2
95.9 ± 0.2	96.0 ± 0.1
42.5 ± 0.6	42.4 ± 0.4
9.3 ± 0.5	9.4 ± 0.3
25.0 ± 2.6	24.0 ± 1.6
56.9 ± 5.8	71.1 ± 3.4
31.7 ± 7.3	35.9 ± 4.2

(b) Relative selection efficiencies [%].

Table 5.6: Evolution of the cross section times selection efficiency and the relative selection efficiencies for the cuts in this analysis for $t\bar{t}$ events from full and fast detector simulation.

	Full sim.	Fast sim.
Cross section	217 600	217 600
Trigger	137 800 ± 87	138 800 ± 55
$N(e+\mu) \geq 2$	9 982 ± 38	9 974 ± 24
Lepton charge	9 926 ± 37	9 915 ± 24
$N(\text{jets}) \geq 2$	9 115 ± 36	9 124 ± 23
$p_T(\text{jet1}) > 40\,\text{GeV}$	8 668 ± 35	8 660 ± 22
$\eta_{j1} \times \eta_{j2} < 0$	3 924 ± 24	3 878 ± 15
$\lvert\Delta\eta_{jj}\rvert > 3.8$	403.1 ± 7.7	401.4 ± 4.9
Central jet veto	97.63 ± 3.80	97.77 ± 2.40
$p_{\text{T}}^{\text{tot}} < 30\,\text{GeV}$	64.15 ± 3.08	65.97 ± 1.97
b-jet veto	26.82 ± 1.99	29.56 ± 1.32

(a) Cross section times efficiency [fb].

Full sim.	Fast sim.
100	100
63.3 ± 0.1	63.8 ± 0.1
7.2 ± 0.1	7.2 ± 0.1
99.4 ± 0.1	99.4 ± 0.1
91.8 ± 0.1	92.0 ± 0.1
95.1 ± 0.1	94.9 ± 0.1
45.3 ± 0.2	44.8 ± 0.1
10.3 ± 0.2	10.4 ± 0.1
24.2 ± 0.8	24.4 ± 0.5
65.7 ± 1.8	67.5 ± 1.2
41.8 ± 2.4	44.8 ± 1.5

(b) Relative selection efficiencies [%].

Table 5.7: Evolution of the cross section times selection efficiency and the relative selection efficiencies for $t\bar{t}$ events from full and fast detector simulation omitting cuts on the kinematics of the decay leptons.

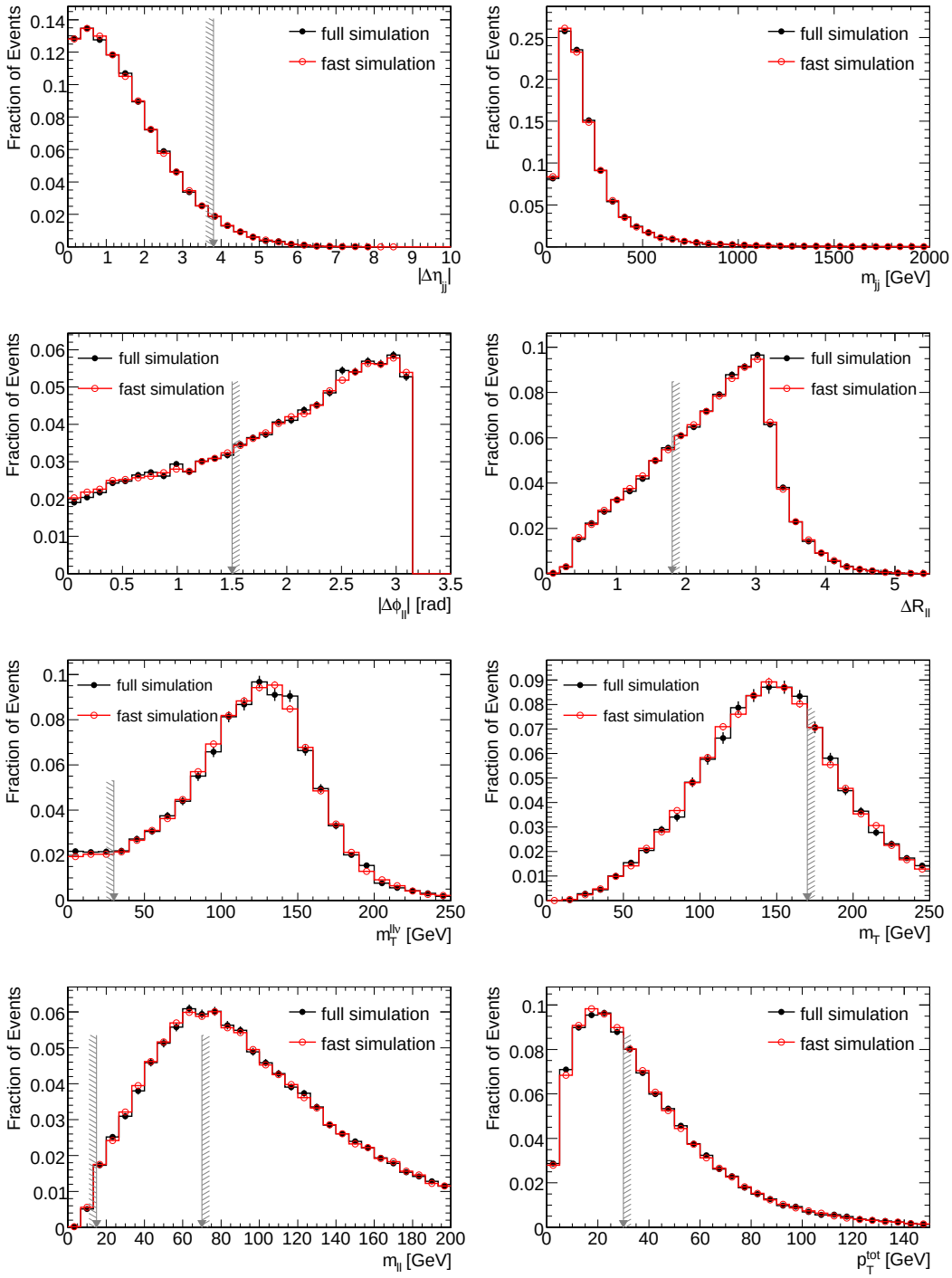

Figure 5.19: Distributions of some of the most important discriminating variables for $t\bar{t}$ events from full and fast detector simulation. The gray arrows indicate the cut values.

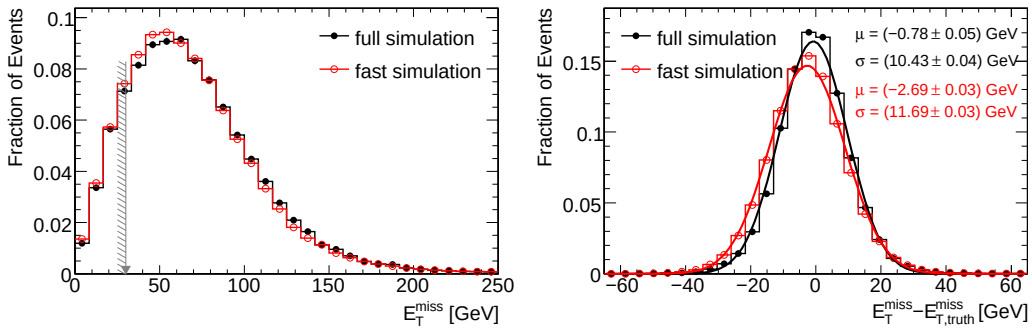

Figure 5.20: The distribution of the missing transverse energy (left) and of its resolution (right) for $t\bar{t}$ events from full and fast detector simulation. The gray arrow indicates the cut value.

transverse energy shown in Figure 5.20 a small shift towards lower values is observed in the fast simulation compared to the full simulation, which has only a minor impact on the selection efficiency of the $E_{\mathrm{T}}^{\mathrm{miss}}$ cut.
To conclude, within statistical uncertainties good agreement between the selection efficiencies for $t\bar{t}$ events produced by full and fast simulation is observed. Hence, the fast detector simulation can reliably be employed for $t\bar{t}$ events without causing additional systematic uncertainty.

5.6.2 Estimation of the Background Contributions

The evolution of the cross section times selection efficiency for the different selection cuts is shown in Figure 5.21 and Tables 5.8 and 5.9 for the signal and background processes. Particularly strong background suppression is achieved by the requirements of two isolated leptons in the event, of a minimal η-distance between the tagging jets of 3.8 and of no additional central jets. After applying the selection criteria described, 8.1 $H \to WW$ events and in total 4.5 background events are expected for an integrated luminosity of $1\,\mathrm{fb}^{-1}$. With 2.7 expected events the $t\bar{t}$ process is the most dominant background followed by the WW background for which 1.3 events are expected. A contribution of about 0.5 Wt events is expected with large uncertainty due to the low Monte Carlo statistics.
Due to the strong suppression and the low Monte Carlo statistics, a reliable estimation of the minor background contributions, in particular of $W+\mathrm{jets}$ and $Z+\mathrm{jets}$ events, is not possible (see Table 5.9). In these cases, the cut efficiencies have to be determined by means of a factorization of the selection criteria.
Table A.7 in Appendix A shows the selection efficiencies for $Z+\mathrm{jets}$ events omitting cuts on the kinematic relations between the leptons such as the $Z \to \tau\tau$ veto, and the cuts on $m_{\mathrm{T}}^{ll\nu}$, m_{ll} and on the angular distance between the leptons. Multiplying the cross section times selection efficiency of $Z+\mathrm{jets}$ events, after requiring at least two jets in the event ($N(\mathrm{jets}) \geq 2$), by the efficiencies of the subsequent selection criteria quoted in Table A.7 results in expected cross sections of (0.06 ± 0.02) fb for $Z \to \ell\ell + \mathrm{jets}$ and of (0.03 ± 0.02) fb for $Z \to \tau\tau + \mathrm{jets}$ events.
For the $W+\mathrm{jets}$ background, the available Monte Carlo statistics only corresponds to

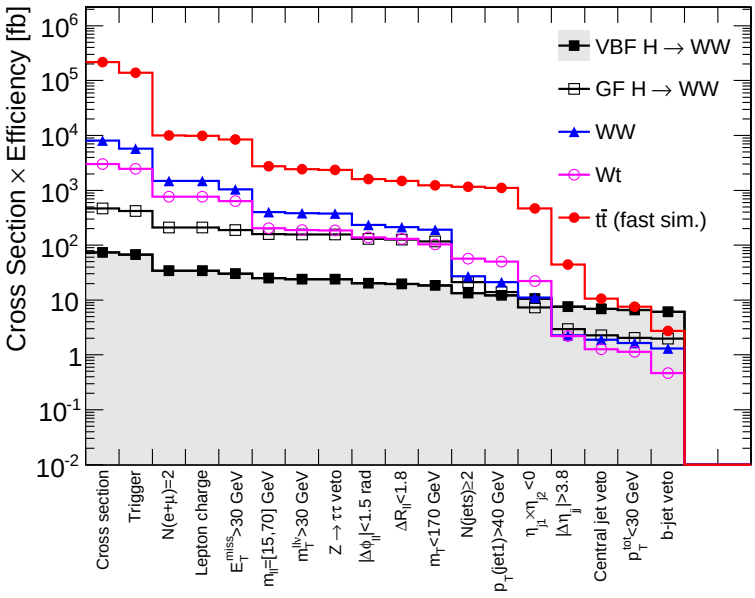

Figure 5.21: Evolution of the cross section times selection efficiency for the signal and the dominant background processes.

	VBF $H \to WW$	GF $H \to WW$	WW	Wt	$t\bar{t}$ (fast sim.)
Cross section	74.04	471.0	8 039	3 006	217 600
Trigger	67.29 ± 0.11	421.0 ± 0.6	$5\,743 \pm 9$	$2\,455 \pm 6$	$138\,800 \pm 54$
$N(e+\mu) = 2$	34.15 ± 0.18	209.9 ± 1.0	$1\,491 \pm 9$	764.9 ± 6.2	$9\,968 \pm 24$
Lepton charge	34.08 ± 0.18	209.6 ± 1.0	$1\,487 \pm 9$	762.5 ± 6.2	$9\,910 \pm 24$
$E_T^{miss} > 30$ GeV	30.30 ± 0.18	188.5 ± 1.0	$1\,038 \pm 9$	632.7 ± 5.8	$8\,424 \pm 22$
$m_{ll} = [15, 70]$ GeV	25.28 ± 0.18	158.6 ± 0.9	403.8 ± 6.0	204.2 ± 3.6	$2\,738 \pm 13$
$m_{\mathrm{T}}^{ll\nu} > 30$ GeV	24.17 ± 0.17	156.6 ± 0.9	384.0 ± 5.9	189.5 ± 3.4	$2\,440 \pm 12$
$Z \to \tau\tau$ veto	23.87 ± 0.17	156.0 ± 0.9	379.6 ± 5.9	184.7 ± 3.4	$2\,355 \pm 12$
$\lvert\Delta\phi_{ll}\rvert < 1.5$	20.30 ± 0.17	131.4 ± 0.9	234.3 ± 4.7	138.6 ± 3.0	$1\,610 \pm 10$
$\Delta R_{\ell\ell} < 1.8$	19.76 ± 0.16	126.7 ± 0.9	214.2 ± 4.5	130.1 ± 2.9	$1\,492 \pm 9$
$m_{\mathrm{T}} < 170$ GeV	18.38 ± 0.16	117.5 ± 0.8	191.3 ± 4.3	102.8 ± 2.6	$1\,241 \pm 9$
$N(\text{jets}) \geq 2$	13.32 ± 0.14	21.29 ± 0.40	27.10 ± 1.55	56.74 ± 1.93	$1\,154 \pm 8$
$p_T(\text{jet1}) > 40$ GeV	12.23 ± 0.14	13.91 ± 0.33	21.29 ± 1.35	50.12 ± 1.81	$1\,107 \pm 8$
$\eta_{j1} \times \eta_{j2} < 0$	10.54 ± 0.13	7.29 ± 0.24	11.14 ± 1.02	22.19 ± 1.21	469.4 ± 5.3
$\lvert\Delta\eta_{jj}\rvert > 3.8$	7.56 ± 0.11	2.98 ± 0.15	2.26 ± 0.43	2.21 ± 0.38	44.27 ± 1.62
Central jet veto	6.85 ± 0.11	2.27 ± 0.13	1.88 ± 0.41	1.27 ± 0.29	10.64 ± 0.79
$p_{\mathrm{T}}^{\mathrm{tot}} < 30$ GeV	6.55 ± 0.11	2.03 ± 0.13	1.66 ± 0.40	1.14 ± 0.28	7.57 ± 0.67
b-jet veto	6.13 ± 0.10	1.98 ± 0.13	1.31 ± 0.31	0.47 ± 0.18	2.72 ± 0.40

Table 5.8: Evolution of the cross section times selection efficiency [fb] for the signal and the dominant background processes. The values for the WW process are for the combination of the two production processes $qq \to WW$ and $gg \to WW$, which after all selection cuts have cross sections of (0.95 ± 0.31) fb and (0.35 ± 0.03) fb, respectively.

	WZ/ZZ	$W+$jets	$Z \to \ell\ell+$jets	$Z \to \tau\tau+$jets
Cross section	2 778	48 855 000	2 965 000	1 489 000
Trigger	$2\,353 \pm 6.11$	$18\,797\,000 \pm 9\,300$	$2\,241\,000 \pm 1\,500$	$279\,700 \pm 920$
$N(e+\mu)=2$	$1\,022 \pm 8.59$	$1\,497 \pm 103$	$915\,300 \pm 1\,540$	$8\,230 \pm 174$
Lepton charge	944.6 ± 8.56	$1\,047 \pm 86$	$913\,400 \pm 1\,540$	$8\,206 \pm 174$
$E_T^{miss} > 30$ GeV	278.0 ± 2.43	622.4 ± 64.4	$2\,412 \pm 71$	777.1 ± 41.6
$m_{ll} = [15, 70]$ GeV	20.35 ± 0.59	359.4 ± 50.9	80.41 ± 14.36	752.5 ± 40.7
$m_{\mathrm{T}}^{ll\nu} > 30$ GeV	18.16 ± 0.57	355.0 ± 50.9	59.46 ± 11.41	185.4 ± 22.0
$Z \to \tau\tau$ veto	17.53 ± 0.56	350.7 ± 50.8	42.19 ± 8.83	73.68 ± 15.08
$\lvert\Delta\phi_{ll}\rvert < 1.5$	11.13 ± 0.48	163.5 ± 32.9	18.73 ± 2.79	2.00 ± 0.89
$\Delta R_{\ell\ell} < 1.8$	10.21 ± 0.46	144.4 ± 31.1	17.03 ± 2.66	2.00 ± 0.89
$m_{\mathrm{T}} < 170$ GeV	9.16 ± 0.44	143.3 ± 31.1	10.41 ± 2.08	2.00 ± 0.89
$N(\text{jets}) \geq 2$	2.92 ± 0.32	19.30 ± 4.68	9.11 ± 1.94	1.59 ± 0.79
$p_T(\text{jet1}) > 40$ GeV	2.58 ± 0.31	11.46 ± 3.62	7.88 ± 1.81	1.59 ± 0.79
$\eta_{j1} \times \eta_{j2} < 0$	1.26 ± 0.27	4.61 ± 2.30	2.40 ± 0.98	0.79 ± 0.56
$\lvert\Delta\eta_{jj}\rvert > 3.8$	0.31 ± 0.07	1.16 ± 1.16	0.38 ± 0.38	–
Central jet veto	0.23 ± 0.06	1.16 ± 1.16	–	–
$p_{\mathrm{T}}^{\mathrm{tot}} < 30$ GeV	0.11 ± 0.04	–	–	–
b-jet veto	0.11 ± 0.04	–	–	–

Table 5.9: Evolution of the cross section times selection efficiency [fb] for the minor background contributions. The dash "–" indicates that no Monte Carlo events remain after the respective cut. Because of the low Monte Carlo statistics available for the $W+$jets and $Z+$jets processes, the corresponding background contributions are estimated assuming factorization of the selection criteria (see text).

an integrated luminosity of about $0.9\,\mathrm{fb}^{-1}$ (Table 5.3) hampering the estimation of its contribution. Table A.8 shows the selection efficiencies for $W+$jets events omitting cuts on the kinematic relations between the leptons. As for $Z \to \ell\ell+$jets events, the cross section times selection efficiency after requiring at least two jets in the event ($N(\text{jets}) \geq 2$) quoted in Table 5.9 is multiplied by the efficiencies of the subsequent selection criteria quoted in Table A.8. This results in an expected cross section of (0.18 ± 0.18) fb for the $W+$jets background. Hence, the total cross section for the minor background contributions listed in Table 5.9 expected after applying all selection criteria amounts to approximately (0.37 ± 0.19) fb.

In contrast to the other background processes, $W+$jets events only constitute a background contribution if jets are misidentified as leptons. Hence, the contribution of $W+$jets processes strongly depends on the misidentification rate of jets as leptons, in particular electrons, which can only reliably be estimated from real data. Therefore, the studies with Monte Carlo data only serve as a first indication of the size of the $W+$jets contribution until the lepton misidentification rates have been measured in the data. Different methods for the estimation of the $W+$jets background from real data are currently under development and will be briefly summarized in Section 7.2.3.

5.6.3 Different Higgs Boson Masses

This study evaluates the discovery potential of the Standard Model Higgs boson in the mass range $120\,\mathrm{GeV} < m_H < 200\,\mathrm{GeV}$ where the branching ratio for $H \to WW$ decays is maximal (see Figure 2.7). The cut values introduced above have been specifically optimized

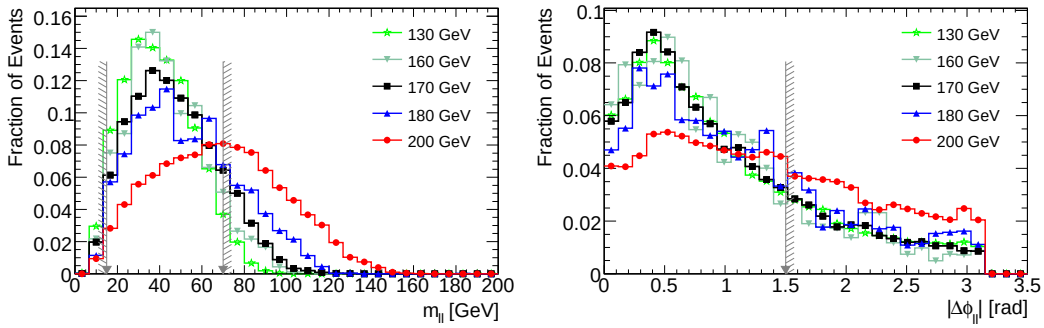

Figure 5.22: Distributions of the invariant mass of the lepton pair (left) and of the azimuthal angle between the two leptons (right) for different Higgs boson masses. The gray arrows indicate the cut values.

for a Higgs boson mass of $m_H = 170\,\text{GeV}$. Variables related to the lepton kinematics like the invariant mass of the lepton-pair m_{ll} and the azimuthal angle between the leptons $\Delta\phi_{ll}$, however, exhibit a dependence on m_H as shown in Figure 5.22. For Higgs boson masses significantly larger than the threshold $m_H \approx 2m_W$, the characteristic signature of a small angular distance between the leptons vanishes since the spin correlation between the two W bosons is only observable if the W bosons are produced nearly at rest in the Higgs boson center-of-mass frame. Although entailing a non-optimal signal selection at large m_H, the cut values $\Delta\phi_{ll} < 1.5$ and $m_{ll} < 70\,\text{GeV}$ chosen for $m_H = 170\,\text{GeV}$ are retained also for larger Higgs boson masses since they allow for an efficient background suppression. For instance, loosening the cut value on m_{ll} would increase the contribution from $Z \to ll$ and $Z \to \tau\tau$ background processes as can be seen in Figure 5.11.
The only Higgs mass dependent cut is the one on the transverse mass of the Higgs boson, $m_\text{T} < m_H$. The distributions of the transverse mass and of the numbers of signal and background events expected for different Higgs boson masses are displayed in Figure 5.23. Furthermore, Table 5.10 summarizes the cross sections of the signal and background processes after applying all selection criteria for different m_H. The dependence of the minor background contributions listed in Table 5.9 on the transverse mass of the Higgs boson has not been studied and is assumed to be the same as for the dominant background processes.

The following chapter provides a study of the impact of pile-up on the event selection efficiencies for the vector-boson fusion $H \to WW$ process and the $t\bar{t}$ background which is the dominant background contribution over the whole mass range. The theoretical and experimental systematic uncertainties are discussed in Chapter 7 together with the expected exclusion limits and discovery potential for different mass values of the Standard Model Higgs boson.

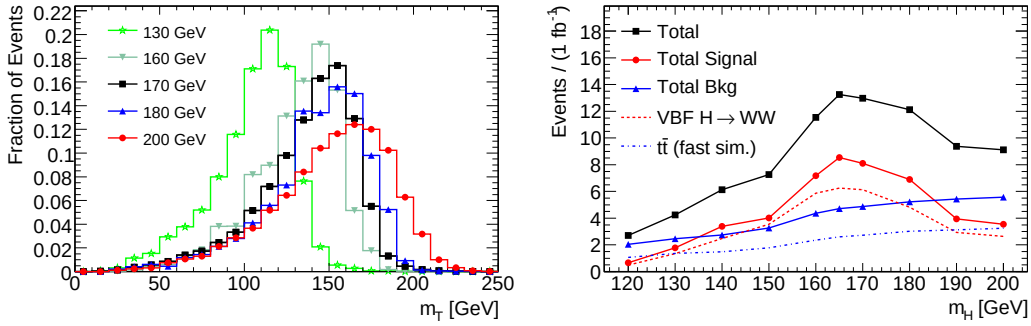

Figure 5.23: Distributions of the transverse mass of the Higgs boson in $H \to WW$ events (left) and the expected number of events for the signal and background processes after applying all event selection criteria (right). The distribution labeled with 'Total Signal' comprises events from the gluon fusion and the vector-boson fusion Higgs boson production while the 'Total Bkg' distribution contains the contributions from the WW, Wt, $t\bar{t}$ and the minor background processes.

m_H [GeV]	VBF $H \to WW$	GF $H \to WW$	WW	Wt	$t\bar{t}$ (fast sim.)	Minor backgrounds
120	0.48 ± 0.04	0.17 ± 0.01	0.56 ± 0.15	0.27 ± 0.13	1.06 ± 0.25	0.16 ± 0.08
130	1.34 ± 0.04	0.43 ± 0.02	0.58 ± 0.15	0.33 ± 0.15	1.36 ± 0.28	0.19 ± 0.09
140	2.48 ± 0.15	0.91 ± 0.04	0.71 ± 0.17	0.33 ± 0.15	1.48 ± 0.30	0.21 ± 0.11
150	3.54 ± 0.20	0.47 ± 0.21	0.90 ± 0.19	0.33 ± 0.15	1.77 ± 0.32	0.25 ± 0.13
160	5.87 ± 0.28	1.30 ± 0.38	1.20 ± 0.30	0.47 ± 0.18	2.36 ± 0.37	0.34 ± 0.17
165	6.25 ± 0.12	2.29 ± 0.14	1.28 ± 0.31	0.47 ± 0.18	2.60 ± 0.39	0.36 ± 0.18
170	6.13 ± 0.10	1.98 ± 0.13	1.31 ± 0.31	0.47 ± 0.18	2.72 ± 0.40	0.37 ± 0.19
180	4.82 ± 0.24	2.08 ± 0.43	1.34 ± 0.31	0.47 ± 0.18	3.01 ± 0.42	0.40 ± 0.20
190	2.93 ± 0.17	1.02 ± 0.26	1.35 ± 0.31	0.53 ± 0.19	3.13 ± 0.43	0.42 ± 0.21
200	2.63 ± 0.05	0.91 ± 0.08	1.36 ± 0.31	0.53 ± 0.19	3.25 ± 0.44	0.43 ± 0.22

Table 5.10: Cross section times selection efficiency [fb] after applying all event selection criteria for the signal and background processes and for different Higgs boson masses m_H.

Chapter 6

Impact of Pile-up on the Analysis

At the LHC design luminosity of $\mathcal{L} = 10^{34}\,\mathrm{cm}^{-2}\,\mathrm{s}^{-1}$, on average 23 inelastic proton-proton collisions, varying according to a Poisson distribution, will take place at each bunch crossing. Thus, each interesting physics event reconstructed in the ATLAS detector will be superimposed by 22 additional inelastic pp interactions, so-called pile-up events. Depending on the LHC beam parameters, even at lower luminosities a significant number of inelastic collisions per bunch crossing is expected. Hence, the identification and precise reconstruction of the primary interaction vertex as well as the association of the reconstructed objects to this vertex is of particular importance for all physics studies.

In this chapter, the impact of the presence of pile-up on the search for the Higgs boson with a mass of $m_H = 170\,\mathrm{GeV}$ is studied. For this purpose, only the vector-boson fusion production of the Higgs boson with subsequent decay into two W bosons and $t\bar{t}$ production, the dominant background, are considered. For other backgrounds, Monte Carlo data samples with pile-up do not exist. In contrast to the previous chapter, Higgs production via gluon fusion is not considered here.

The total cross-section of pp interactions at the LHC is dominated by QCD processes with low-energy jets. Pile-up events are thus expected to deteriorate the jet reconstruction in hard-scattering events. In particular, the performance of the central jet veto, which efficiently suppresses $t\bar{t}$ background, is expected to degrade due to additional jets originating from minimum bias events. This can be avoided by exploiting tracking and vertexing information in order to associate jets to the primary interaction vertex and to reject jets from additional inelastic pp interactions. Two different approaches are investigated. Track jets reconstructed solely from inner detector tracks originating from the primary interaction vertex have been developed in the context of this thesis. For comparison, the association of calorimeter jets to tracks from the primary vertex is studied for different levels of pile-up.

This chapter is organized as follows. The first section explains the Monte Carlo samples which are used to study the impact of pile-up on the event selection in Section 6.2. The ATLAS track and vertex reconstruction and its utilization for jet reconstruction is described in Sections 6.3 and 6.4. Sections 6.5 and 6.6 discuss the performance of the two approaches for pile-up jet rejection while the impact of the amount of pile-up is studied in Section 6.7. Finally, the impact of the methods on the central jet veto in the vector-boson fusion $H \to WW$ analysis is discussed in Section 6.8. The prospects for measuring the track jet performance with collision data are given in Section 6.9.

6.1 Monte Carlo Simulation

6.1.1 Simulation of Pile-up

Pile-up at high instantaneous luminosities in the ATLAS detector has several origins. First, due to the large number of protons per bunch, at each bunch crossing multiple inelastic *pp* interactions overlay the interesting physics processes selected by the trigger system. In addition, the electronic signals are integrated over several bunch crossing. The first source of pile-up is referred to as *in-time* and the latter as *out-of-time* pile-up. The out-of-time pile-up to be considered depends on the time between bunch crossings and on the electronic integration times which differ for the different detector subsystems. Additional inelastic *pp* interactions, predominantly minimum bias events, are simulated by Pythia and overlaid onto the simulated hard-scattering events. The total proton-proton cross section can be subdivided into an elastic and an inelastic contribution with the inelastic contribution comprising single diffractive, double diffractive and non-diffractive processes:

$$\sigma_{tot} = \sigma_{elas} + \sigma_{sd} + \sigma_{dd} + \sigma_{nd}.$$

The term *minimum bias* interaction usually refers to non-single diffractive processes $\sigma_{nsd} = \sigma_{tot} - \sigma_{elas} - \sigma_{sd}$ selected by triggers based on forward-backward coincidences in former hadron-collider experiments (see, for instance, References [77, 78]). However, in the simulation of minimum bias events employed in this analysis, all inelastic processes are taken into account [79].
Furthermore, so-called cavern background from thermalized neutrons and low-energy photons escaping the calorimeter has an impact on the performance of the muon spectrometer and has to be taken into account. Since an accurate prediction of cavern background rates is not possible, safety factors are used in the simulation covering the uncertainty in the predicted rates.

6.1.2 Monte Carlo Samples

This study is based on Monte Carlo data samples which have been produced with the Athena software release 14.2.25. The Monte Carlo samples used are listed in Table 6.1. Two levels of pile-up are considered corresponding to instantaneous luminosities of $\mathcal{L} = 10^{32}\ \mathrm{cm}^{-2}\,\mathrm{s}^{-1}$ and $10^{33}\ \mathrm{cm}^{-2}\,\mathrm{s}^{-1}$, and 4.1 and 6.9 collisions per bunch crossing, respectively. Further details of the pile-up conditions are specified in Table 6.2. Monte Carlo data for the signal process is only available for a pile-up level corresponding to an instantaneous luminosity of $10^{32}\ \mathrm{cm}^{-2}\,\mathrm{s}^{-1}$ which is used as benchmark scenario in the following. A cross check of the jet reconstruction performance in $t\bar{t}$ events at a luminosity of $10^{33}\ \mathrm{cm}^{-2}\,\mathrm{s}^{-1}$ is presented in Section 6.7.

6.2 Impact of Pile-up on the Event Selection

Pile-up from additional minimum bias interactions and cavern background imposes additional challenges on the particle reconstruction in all detector subsystems due to higher noise level, degraded resolutions and increased fake rates. In this section, the impact of

Process	Generator	Cross section [fb]	Events	Integrated luminosity [fb^{-1}]	Instantan. luminosity [cm^{-2} s^{-1}]	Reco. tag
VBF $H \to WW$	Herwig	65.65	40 000	609.3	–	r635
	Herwig	65.65	40 000	609.3	10^{32}	r642
$t\bar{t}$	MC@NLO	$374 \cdot 10^3$	1 470 000	3.93	–	r635
	MC@NLO	$374 \cdot 10^3$	1 500 000	4.02	10^{32}	r642
	MC@NLO	$374 \cdot 10^3$	450 000	1.21	10^{33}	r641
Min. Bias	Pythia	$5.2 \cdot 10^5$	50 000	$9.6 \cdot 10^{-5}$	–	r635

Table 6.1: Monte Carlo data samples used for the studies presented in this chapter. The $H \to WW$ data sample is simulated assuming a Higgs-boson mass of $m_H = 170\,\text{GeV}$. The reconstruction tags in the last column correspond to sets of parameters defining the pile-up conditions explained in Table 6.2.

Reconstruction tag	r635	r642	r641
$\mathcal{L}$ [cm^{-2} s^{-1}]	–	10^{32}	10^{33}
Bunch spacing [ns]	–	450	75
Cavern background SF	–	2	5
Collisions per BC	1	4.1	6.9

Table 6.2: The different pile-up conditions considered in this study. The reconstruction tag defines the instantaneous luminosity, the bunch spacing and the safety factor (SF) for the cavern background. The pile-up level corresponding to a luminosity of 10^{32} cm^{-2} s^{-1} and 4.1 proton-proton collisions per bunch crossing (BC) is used as benchmark scenario in this study. The reconstruction tag 'r635' represents data samples simulated without pile-up.

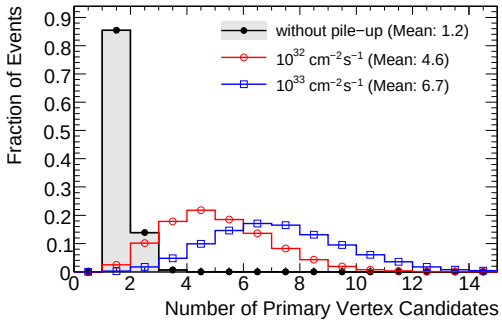

Figure 6.1: Number of reconstructed primary vertex candidates in $t\bar{t}$ events for different levels of pile-up. The instantaneous luminosity $\mathcal{L} = 10^{32}\ \mathrm{cm}^{-2}\,\mathrm{s}^{-1}$ is used as benchmark scenario for the pile-up studies.

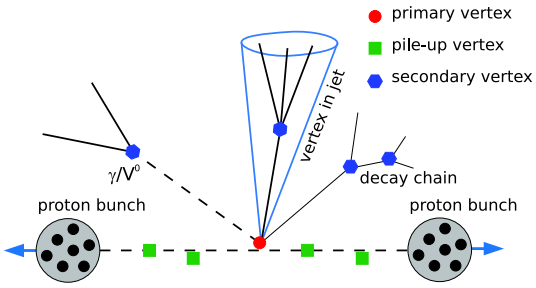

Figure 6.2: Vertex topologies in pp collisions at the LHC [80]. The primary vertex and additional pile-up vertices are reconstructed by the primary vertex reconstruction algorithms and are referred to as primary vertex candidates.

pile-up corresponding to an instantaneous luminosity of $10^{32}\ \mathrm{cm}^{-2}\,\mathrm{s}^{-1}$ on the event selection in the vector-boson fusion $H \to WW$ analysis is presented. Figure 6.1 shows the number of reconstructed vertices per bunch crossing for $t\bar{t}$ events and different pile-up scenarios. At a luminosity of $\mathcal{L} = 10^{32}\ \mathrm{cm}^{-2}\,\mathrm{s}^{-1}$, on average 4.6 vertices are reconstructed per event.

The event selection efficiencies for the cuts described in the previous chapter are shown in Figure 6.3 and Table 6.3 for vector-boson fusion $H \to WW$ and $t\bar{t}$ events without and with pile-up. Since this section focuses on the vector-boson fusion production of the Higgs boson, a cut on the invariant mass of the tagging jet pair of $m_{jj} > 500\,\mathrm{GeV}$ is included in the event selection in contrast to the previous chapter where it is omitted (see Section 5.5.3). It has been verified that the influence of pile-up on the event selection efficiency is the same without and with cut on m_{jj}. The presence of pile-up has only minor impact on the efficiencies of the lepton selection criteria. Only the efficiency of the requirement of exactly two reconstructed leptons shows a small sensitivity to pile-up. As shown in Figure 6.4, the number of reconstructed muons per event is independent of pile-up whereas a small dependence is visible in the fraction of reconstructed electrons. As can be seen in Table 6.4, this is at least partly caused by the difference in the efficiency of the calorimeter isolation criteria (see Section 5.4) which is due to the increased activity in the calorimeter in the presence of pile-up.

No impact on the sum of the track transverse momenta in a cone of $\Delta R = 0.3$ around the electron is observed since only tracks originating from the same vertex as the electron are taken into account.

The low $t\bar{t}$ Monte Carlo statistics after all selection cuts does not allow for statistically significant conclusions on the dependence of the jet selection criteria on the presence of pile-up. Therefore, the cuts exploiting kinematic relations of the leptons are omitted in order to test the impact of pile-up on the efficiency of the jet selection criteria. Figure 6.5 and Table 6.6 show the relative event selection efficiencies of the jet selection cuts without cuts on the lepton kinematics.

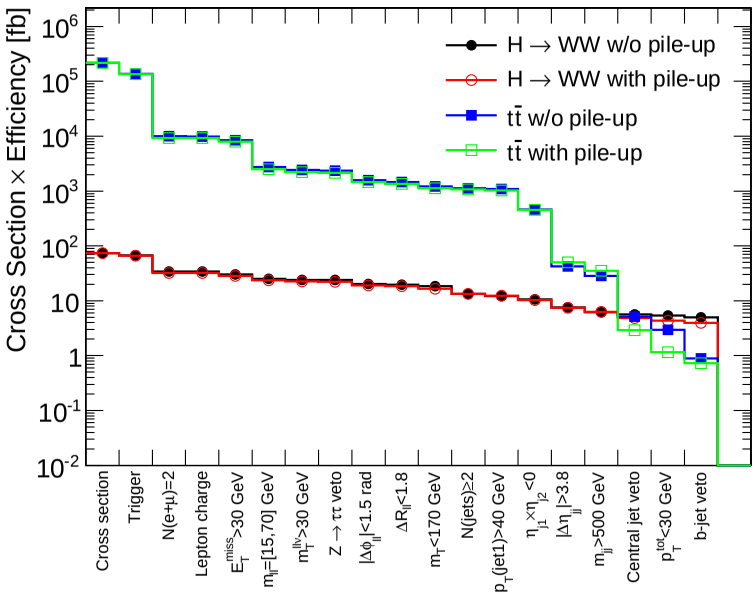

(a) Cross section times efficiency.

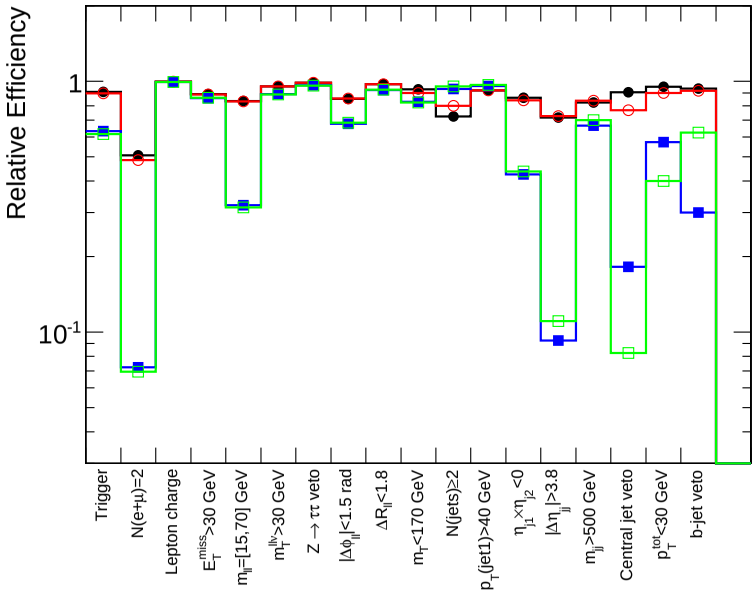

(b) Relative selection efficiencies.

Figure 6.3: Evolution of the cross section times selection efficiency and the relative selection efficiencies for the cuts applied in this analysis without and with pile-up.

	$H \to WW$		$t\bar{t}$	
	without pile-up	with pile-up	without pile-up	with pile-up
Cross section	74.04	74.04	217 600	217 600
Trigger	67.29 ± 0.11	66.25 ± 0.11	$137\,800 \pm 87$	$134\,000 \pm 86$
$N(e+\mu) = 2$	34.15 ± 0.18	32.16 ± 0.18	$9\,976 \pm 38$	$9\,332 \pm 36$
Lepton charge	34.08 ± 0.18	32.11 ± 0.18	$9\,920 \pm 37$	$9\,283 \pm 36$
$E_T^{miss} > 30\,\text{GeV}$	30.30 ± 0.18	28.51 ± 0.18	$8\,500 \pm 35$	$7\,995 \pm 33$
$m_{ll} = [15, 70]\,\text{GeV}$	25.28 ± 0.18	23.71 ± 0.17	$2\,730 \pm 20$	$2\,512 \pm 19$
$m_{\text{T}}^{ll\nu} > 30\,\text{GeV}$	24.17 ± 0.17	22.65 ± 0.17	$2\,427 \pm 19$	$2\,225 \pm 18$
$Z \to \tau\tau$ veto	23.87 ± 0.17	22.34 ± 0.17	$2\,342 \pm 19$	$2\,142 \pm 18$
$\lvert\Delta\phi_{ll}\rvert < 1.5$	20.30 ± 0.17	19.08 ± 0.16	$1\,585 \pm 15$	$1\,467 \pm 15$
$\Delta R_{\ell\ell} < 1.8$	19.76 ± 0.16	18.60 ± 0.16	$1\,462 \pm 15$	$1\,360 \pm 14$
$m_{\text{T}} < 170\,\text{GeV}$	18.38 ± 0.16	16.71 ± 0.15	$1\,213 \pm 13$	$1\,120 \pm 13$
$N(\text{jets}) \geq 2$	13.32 ± 0.14	13.35 ± 0.14	$1\,129 \pm 13$	$1\,068 \pm 12$
$p_T(\text{jet1}) > 40\,\text{GeV}$	12.23 ± 0.14	12.29 ± 0.14	$1\,083 \pm 13$	$1\,034 \pm 12$
$\eta_{j1} \times \eta_{j2} < 0$	10.54 ± 0.13	10.32 ± 0.13	460.6 ± 8.3	451.7 ± 8.1
$\lvert\Delta\eta_{jj}\rvert > 3.8$	7.56 ± 0.11	7.49 ± 0.11	42.67 ± 2.51	49.93 ± 2.69
$m_{jj} > 500\,\text{GeV}$	6.23 ± 0.10	6.27 ± 0.10	28.45 ± 2.05	35.02 ± 2.25
Central jet veto	5.64 ± 0.10	4.81 ± 0.09	5.19 ± 0.88	2.89 ± 0.65
$p_{\text{T}}^{\text{tot}} < 30\,\text{GeV}$	5.37 ± 0.10	4.31 ± 0.09	2.96 ± 0.66	1.16 ± 0.41
b-jet veto	5.02 ± 0.09	3.95 ± 0.08	0.89 ± 0.36	0.72 ± 0.32

(a) Cross section times efficiency [fb].

Trigger	90.9 ± 0.1	89.5 ± 0.2	63.3 ± 0.1	61.6 ± 0.1
$N(e+\mu) = 2$	50.8 ± 0.3	48.5 ± 0.3	7.2 ± 0.1	7.0 ± 0.1
Lepton charge	99.8 ± 0.1	99.8 ± 0.1	99.4 ± 0.1	99.5 ± 0.1
$E_T^{miss} > 30\,\text{GeV}$	88.9 ± 0.2	88.8 ± 0.2	85.7 ± 0.1	86.1 ± 0.1
$m_{ll} = [15, 70]\,\text{GeV}$	83.4 ± 0.3	83.2 ± 0.3	32.1 ± 0.2	31.4 ± 0.2
$m_{\text{T}}^{ll\nu} > 30\,\text{GeV}$	95.6 ± 0.2	95.6 ± 0.2	88.9 ± 0.2	88.6 ± 0.2
$Z \to \tau\tau$ veto	98.7 ± 0.1	98.6 ± 0.1	96.5 ± 0.1	96.3 ± 0.2
$\lvert\Delta\phi_{ll}\rvert < 1.5$	85.0 ± 0.3	85.4 ± 0.3	67.7 ± 0.4	68.5 ± 0.4
$\Delta R_{\ell\ell} < 1.8$	97.4 ± 0.2	97.5 ± 0.2	92.2 ± 0.3	92.7 ± 0.3
$m_{\text{T}} < 170\,\text{GeV}$	93.0 ± 0.2	89.8 ± 0.3	83.0 ± 0.4	82.4 ± 0.4
$N(\text{jets}) \geq 2$	72.4 ± 0.4	79.9 ± 0.4	93.1 ± 0.3	95.4 ± 0.2
$p_T(\text{jet1}) > 40\,\text{GeV}$	91.9 ± 0.3	92.1 ± 0.3	95.9 ± 0.2	96.8 ± 0.2
$\eta_{j1} \times \eta_{j2} < 0$	86.2 ± 0.4	83.9 ± 0.5	42.5 ± 0.6	43.7 ± 0.6
$\lvert\Delta\eta_{jj}\rvert > 3.8$	71.7 ± 0.6	72.6 ± 0.6	9.3 ± 0.5	11.1 ± 0.6
$m_{jj} > 500\,\text{GeV}$	82.4 ± 0.6	83.7 ± 0.6	66.7 ± 2.8	70.1 ± 2.5
Central jet veto	90.6 ± 0.5	76.6 ± 0.7	18.2 ± 2.8	8.3 ± 1.8
$p_{\text{T}}^{\text{tot}} < 30\,\text{GeV}$	95.2 ± 0.4	89.7 ± 0.6	57.1 ± 8.4	40.0 ± 11.0
b-jet veto	93.5 ± 0.5	91.6 ± 0.6	30.0 ± 10.2	62.5 ± 17.1
total	6.8 ± 0.1	5.3 ± 0.1	$(0.4 \pm 0.2) \cdot 10^{-3}$	$(0.3 \pm 0.1) \cdot 10^{-3}$

(b) Relative selection efficiencies [%].

Table 6.3: Evolution of the cross section times selection efficiency and the relative selection efficiencies for the cuts applied in this analysis without and with pile-up.

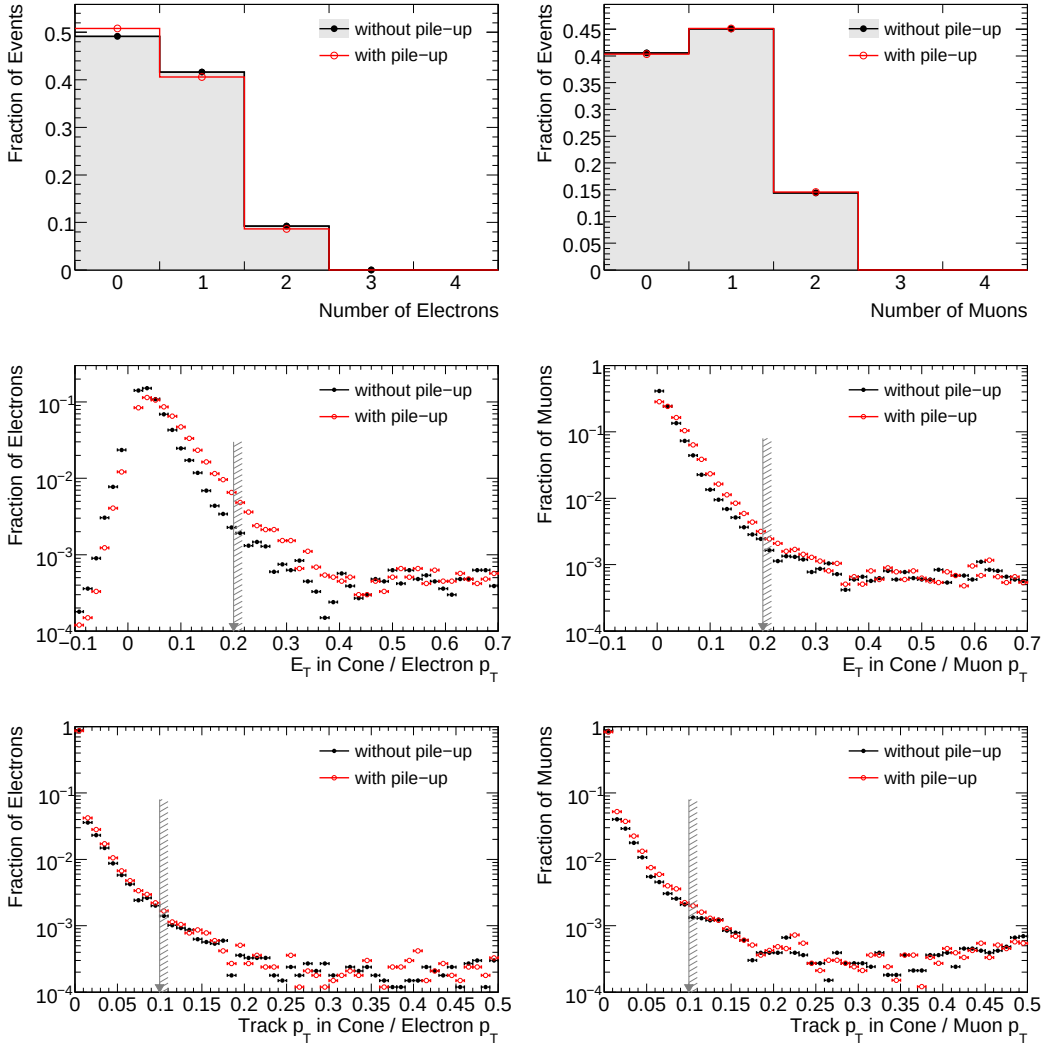

Figure 6.4: Number of reconstructed electrons and muons per event (top) and the calorimeter (middle) and track (bottom) isolation variables for electrons and muons. The distributions are shown for $H \to WW$ events without and with pile-up. The gray arrows indicate the isolation requirements.

	$H \to WW$		$t\bar{t}$	
	without pile-up	with pile-up	without pile-up	with pile-up
Without isol.	71.51 ± 0.25	69.19 ± 0.25	73.20 ± 0.38	70.87 ± 0.39
Calo isol.	95.87 ± 0.49	93.82 ± 0.51	93.36 ± 0.73	90.67 ± 0.76
Track isol.	98.96 ± 0.52	98.84 ± 0.57	98.52 ± 0.82	98.45 ± 0.90
Total	67.84 ± 0.26	64.16 ± 0.26	67.33 ± 0.40	63.25 ± 0.41

Table 6.4: Efficiencies [%] of the electron reconstruction and isolation requirements for $H \to WW$ and $t\bar{t}$ events without and with pile-up.

	$H \to WW$		$t\bar{t}$	
	without pile-up	with pile-up	without pile-up	with pile-up
Without isol.	92.43 ± 0.14	92.36 ± 0.14	92.81 ± 0.22	92.62 ± 0.22
Calo isol.	94.68 ± 0.24	94.21 ± 0.25	93.57 ± 0.38	93.15 ± 0.39
Track isol.	97.37 ± 0.30	97.25 ± 0.30	97.47 ± 0.48	97.51 ± 0.49
Total	85.22 ± 0.19	84.62 ± 0.20	84.64 ± 0.31	84.13 ± 0.31

Table 6.5: Efficiencies [%] of the muon reconstruction and isolation requirements for $H \to WW$ and $t\bar{t}$ events without and with pile-up.

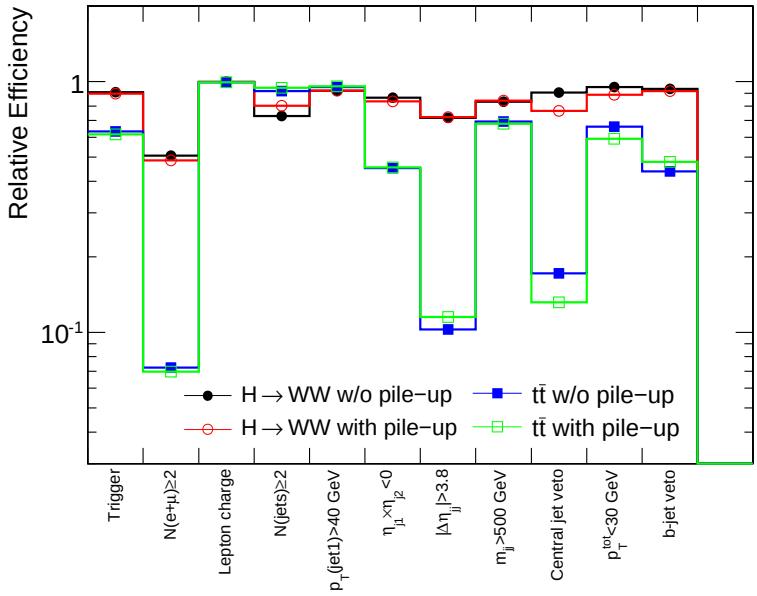

Figure 6.5: Relative selection efficiencies for events without and with pile-up omitting cuts on the kinematic relations of the leptons.

	$H \to WW$		$t\bar{t}$	
	without pile-up	with pile-up	without pile-up	with pile-up
Cross section	74.04	74.04	217 600	217 600
Trigger	67.29 ± 0.11	66.25 ± 0.11	$137\,800 \pm 87$	$134\,000 \pm 86$
$N(e+\mu) \geq 2$	34.17 ± 0.18	32.17 ± 0.18	$9\,982 \pm 38$	$9\,338 \pm 36$
Lepton charge	34.10 ± 0.18	32.11 ± 0.18	$9\,926 \pm 37$	$9\,288 \pm 36$
$N(\text{jets}) \geq 2$	24.86 ± 0.17	25.77 ± 0.18	$9\,115 \pm 36$	$8\,768 \pm 35$
$p_T(\text{jet1}) > 40\,\text{GeV}$	22.85 ± 0.17	23.67 ± 0.17	$8\,668 \pm 35$	$8\,388 \pm 34$
$\eta_{j1} \times \eta_{j2} < 0$	19.70 ± 0.16	19.76 ± 0.16	$3\,924 \pm 24$	$3\,818 \pm 23$
$\lvert\Delta\eta_{jj}\rvert > 3.8$	14.11 ± 0.15	14.29 ± 0.15	403.1 ± 7.7	439.8 ± 8.0
$m_{jj} > 500\,\text{GeV}$	11.76 ± 0.14	12.01 ± 0.14	279.3 ± 6.4	299.0 ± 6.6
Central jet veto	10.64 ± 0.13	9.17 ± 0.12	48.00 ± 2.67	39.37 ± 2.39
$p_{\text{T}}^{\text{tot}} < 30\,\text{GeV}$	10.12 ± 0.13	8.13 ± 0.12	31.70 ± 2.17	23.30 ± 1.84
b-jet veto	9.47 ± 0.12	7.45 ± 0.11	13.93 ± 1.44	11.14 ± 1.27

(a) Cross section times efficiency [fb].

Trigger	90.9 ± 0.1	89.5 ± 0.2	63.3 ± 0.1	61.6 ± 0.1
$N(e+\mu) \geq 2$	50.8 ± 0.3	48.6 ± 0.3	7.2 ± 0.1	7.0 ± 0.1
Lepton charge	99.8 ± 0.1	99.8 ± 0.1	99.4 ± 0.1	99.5 ± 0.1
$N(\text{jets}) \geq 2$	72.9 ± 0.3	80.2 ± 0.3	91.8 ± 0.1	94.4 ± 0.1
$p_T(\text{jet1}) > 40\,\text{GeV}$	91.9 ± 0.2	91.9 ± 0.2	95.1 ± 0.1	95.7 ± 0.1
$\eta_{j1} \times \eta_{j2} < 0$	86.2 ± 0.3	83.5 ± 0.3	45.3 ± 0.2	45.5 ± 0.2
$\lvert\Delta\eta_{jj}\rvert > 3.8$	71.7 ± 0.4	72.3 ± 0.4	10.3 ± 0.2	11.5 ± 0.2
$m_{jj} > 500\,\text{GeV}$	83.3 ± 0.4	84.1 ± 0.4	69.3 ± 0.9	68.0 ± 0.8
Central jet veto	90.5 ± 0.4	76.3 ± 0.5	17.2 ± 0.9	13.2 ± 0.7
$p_{\text{T}}^{\text{tot}} < 30\,\text{GeV}$	95.1 ± 0.3	88.7 ± 0.5	66.0 ± 2.6	59.2 ± 3.0
b-jet veto	93.7 ± 0.3	91.6 ± 0.4	43.9 ± 3.4	47.8 ± 3.9
total	12.8 ± 0.2	10.1 ± 0.2	$(6.4 \pm 0.7) \cdot 10^{-3}$	$(5.1 \pm 0.6) \cdot 10^{-3}$

(b) Relative selection efficiencies [%].

Table 6.6: Evolution of the cross section times selection efficiency and the relative selection efficiencies for $H \to WW$ events with $m_H = 170\,\text{GeV}$ and the $t\bar{t}$ background without and with pile-up omitting cuts on the kinematic relations of the leptons. The level of pile-up corresponds to an instantaneous luminosity of $10^{32}\ \text{cm}^{-2}\,\text{s}^{-1}$.

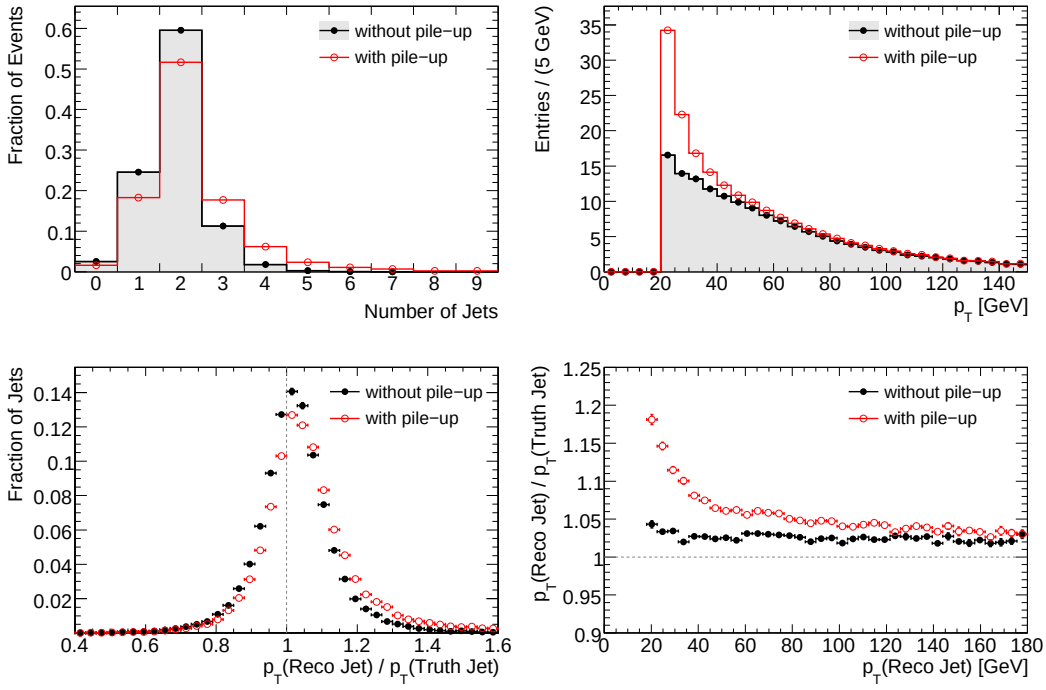

Figure 6.6: Jet multiplicity (top left) and p_{T} distribution scaled to $1\,\mathrm{fb}^{-1}$ (top right) in $H \to WW$ events without and with pile-up. The bottom plots show the distribution (left) and p_{T} dependence (right) of the ratio of the reconstructed and the true jet transverse momentum.

Minimum bias events are predominantly QCD processes involving the production of low-energy jets. Hence, the impact of pile-up is much more pronounced for the jet selection than for the lepton selection. Additional jets not originating from the primary interaction are reconstructed and the energy of jets from the hard-scattering process can be biased towards larger values due to the increased activity in the calorimeter. Both effects are visible in Figure 6.6 which shows the number of jets per event, their p_{T} spectrum as well as the ratio of the reconstructed and the true jet transverse momentum which is reconstructed only from truth particles originating from the primary interaction. The influence of pile-up on the jet multiplicity and resolution is particularly pronounced for jets with transverse momenta below 50 GeV.

After requiring the transverse momentum of the highest-energy tagging jet to be above 40 GeV and the two tagging jets to point in opposite hemispheres of the detector, the impact of pile-up on the η-distance and invariant mass of the selected tagging jets in $H \to WW$ and $t\bar{t}$ events is small as shown in Figure 6.7.

In contrast to the tagging jet selection, the central jet veto efficiency is severely influenced by the presence of pile-up due to additional jets with transverse momenta above 20 GeV within $|\eta| < 3.0$ filling the rapidity gap between the tagging jets of the vector-boson fusion process. The central jet veto is particularly powerful in suppressing the $t\bar{t}$ background dominant for the vector-boson fusion $H \to WW$ analysis. Pile-up, therefore, has significant impact on the discovery potential.

Progressing in the cut evolution, also the selection efficiency of the cut on the transverse

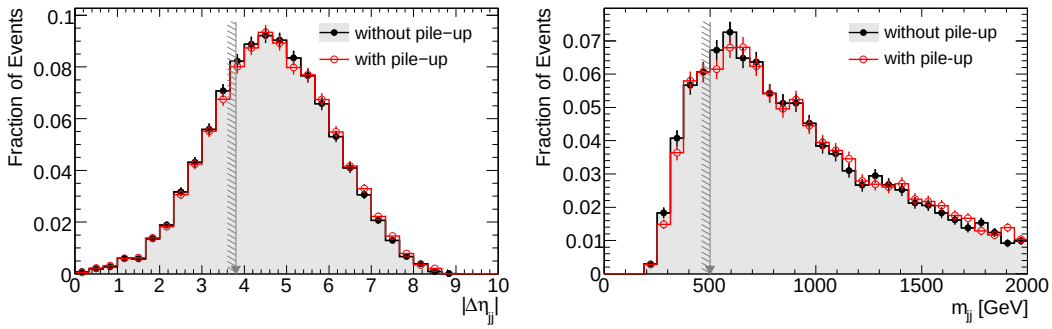

Figure 6.7: Distributions of the pseudo-rapidity distance $\Delta\eta_{jj}$ between the two tagging jets (left) and of the invariant di-jet mass m_{jj} (right) for $H \rightarrow WW$ events without and with pile-up. The gray arrows indicate the cut values.

momentum balance $p_{\mathrm{T}}^{\mathrm{tot}}$ (see Equation 5.10) differs for events without and with pile-up. As shown in Figure 6.8, the distribution of $p_{\mathrm{T}}^{\mathrm{tot}}$ is significantly affected by pile-up mainly caused by the degradation of the $E_{\mathrm{T}}^{\mathrm{miss}}$ resolution, whereas the other variables entering the calculation of $p_{\mathrm{T}}^{\mathrm{tot}}$ are robust against pile-up. While the distribution of the missing transverse energy itself, displayed in Figure 6.9, shows no dependence on pile-up, its resolution is significantly affected. The $E_{\mathrm{T}}^{\mathrm{miss}}$ resolution for $H \rightarrow WW$ events degrades from (8.2 ± 0.1) GeV to (12.8 ± 0.1) GeV in the presence of pile-up due to the increased activity and noise level in the calorimeter. Due to its large width, the distribution of the transverse missing energy is not affected by this degradation of the resolution. However, the distributions of variables calculated using the transverse missing energy such as the total transverse momentum $p_{\mathrm{T}}^{\mathrm{tot}}$ of the event or the transverse mass m_{T} of the Higgs boson are severely affected by the deteriorated $E_{\mathrm{T}}^{\mathrm{miss}}$ resolution as shown in Figure 6.8.

The relative selection efficiencies of the b-jet veto in Table 6.6 show a slight dependence on pile-up. The distributions of the highest b-tagging weight in the event are displayed in Figure 6.10 showing differences in the distributions without and with pile-up for $H \rightarrow WW$ events. Since the b-tagging algorithm classifies jets as b-jets by the association of tracks to secondary vertices, jets can gain a larger b-tag weight due to the wrong assignment of tracks from additional minimum bias vertices. Good agreement of the distributions is observed for $t\bar{t}$ events due to the better vertex reconstruction compared to $H \rightarrow WW$ events (see Section 6.3.2) and due to the fact that b-jets have larger b-tagging weights compared to misidentified jets from minimum bias interactions and, therefore, the relative effect of pile-up is smaller.

To summarize, two major effects of pile-up on the analysis have been identified. First, the degradation of the $E_{\mathrm{T}}^{\mathrm{miss}}$ resolution results in broader distributions of discriminating variables calculated using the missing transverse energy such as m_{T} and $p_{\mathrm{T}}^{\mathrm{tot}}$. Second, additional jets from minimum bias events deteriorate the performance of the central jet veto. Since the vertices of different pp interactions in one bunch crossing can reliably be reconstructed and identified in the inner detector, the impact of pile-up can be reduced by exploiting tracks originating from the primary vertex in order to associate physics objects to the vertex of the hard-scattering process. While studies of a track-based reconstruction of the missing transverse energy have been presented elsewhere [81], the following sections

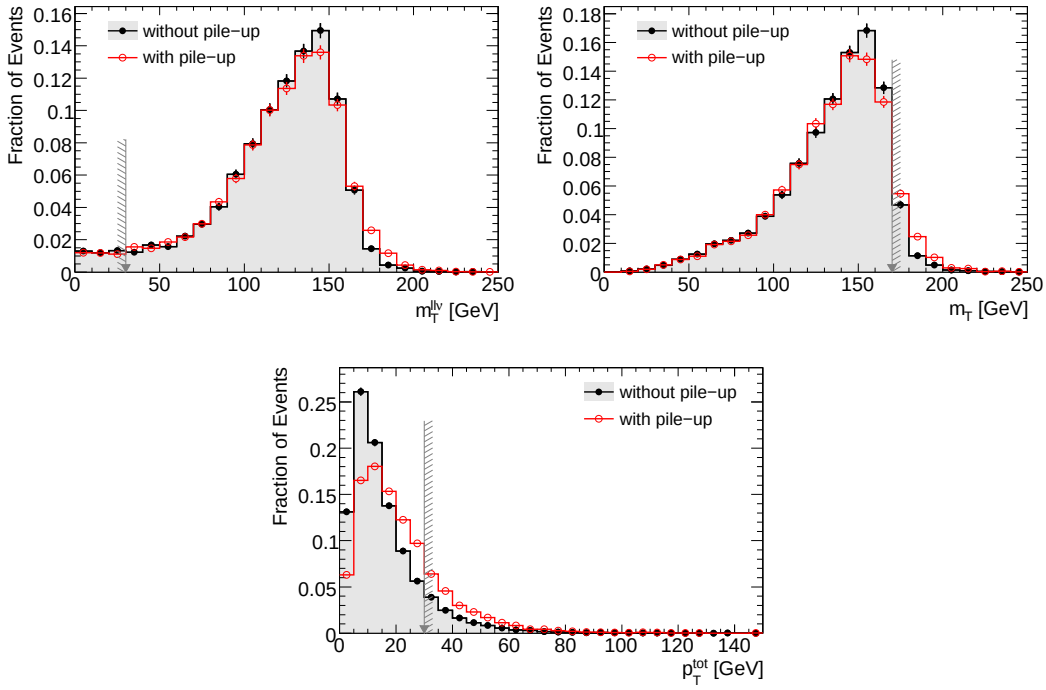

Figure 6.8: Distributions of the transverse masses $m_{\mathrm{T}}^{lll\nu}$ (left) and m_{T} (right) and of the total transverse momentum $p_{\mathrm{T}}^{\mathrm{tot}}$ (bottom) for $H \rightarrow WW$ events without and with pile-up. The gray arrows indicate the cut values.

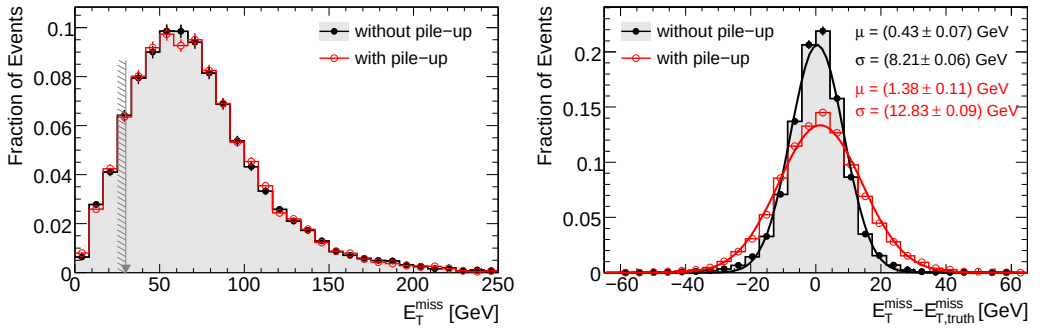

Figure 6.9: Distributions of the missing transverse energy (left) and of its resolution (right) for $H \rightarrow WW$ events without and with pile-up. The gray arrow indicates the cut value.

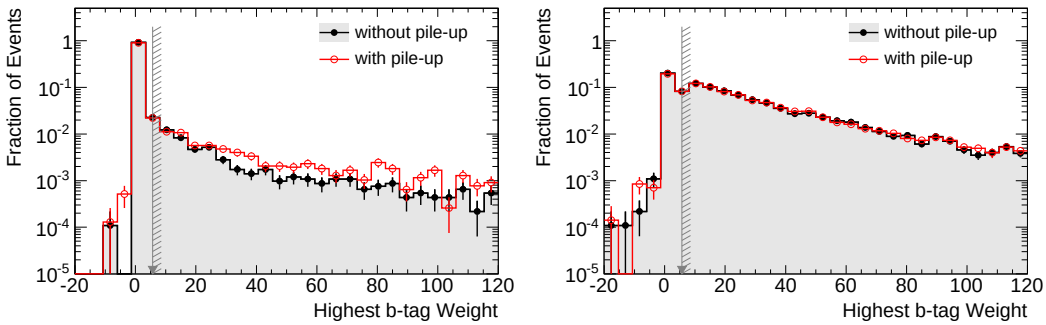

Figure 6.10: b-tag weight distributions of the jets with the highest b-tag weight in $H \rightarrow WW$ (left) and $t\bar{t}$ events (right). The gray arrows indicate the cut value.

focus on the possibilities to decrease the impact of pile-up on the central jet veto by associating jets to the primary interaction vertex.

6.3 Track and Vertex Reconstruction

6.3.1 Track Reconstruction

At a luminosity of $10^{34}\,\mathrm{cm}^{-2}\,\mathrm{s}^{-1}$ every 25 ns approximately 1000 tracks are produced in the interaction region within $|\eta| < 2.5$ imposing a major challenge on the track reconstruction in the inner detector.

Prior to the track reconstruction, the raw data information from the pixel and SCT detectors is converted into hit clusters and subsequently into space points and the TRT drift time information is transformed into drift circles. The track reconstruction [82] first selects track seeds from a combination of space-points in the pixel detector and in the first SCT layer. These seeds are then extended through the SCT into the TRT and refitted with the full information of the three tracking detector subsystems [46]. Only tracks with transverse momenta above $p_{\mathrm{T}} = 0.5\,\mathrm{GeV}$ are reconstructed by the standard tracking algorithms due to the high curvature and the increased multiple scattering of lower momentum tracks. Fake tracks are rejected by applying quality cuts, for instance on the minimum number of clusters associated to the track and the maximum number of clusters shared between different tracks.

As sketched in Figure 6.11, tracks are described by five track parameters defined with respect to the origin of the ATLAS coordinate system: the inverse transverse momentum multiplied by the charge q/p_{T}, the azimuthal angle ϕ, the polar angle $\cot\theta$, and the transverse and longitudinal impact parameters d_0 and z_0, respectively. The resolutions of the transverse momentum and of the longitudinal impact parameter are shown in Figure 6.12 as a function of $|\eta|$ for the calibrated and aligned inner detector. As displayed in Figure 6.13, the track reconstruction efficiency decreases with the transverse momentum and for $|\eta| > 1$, mostly because of the increased amount of scattering material in the inner detector traversed by the particles.

Studies have shown that the track reconstruction efficiency is only slightly affected by additional pile-up interactions [84]. However, the reconstruction of tracks inside highly

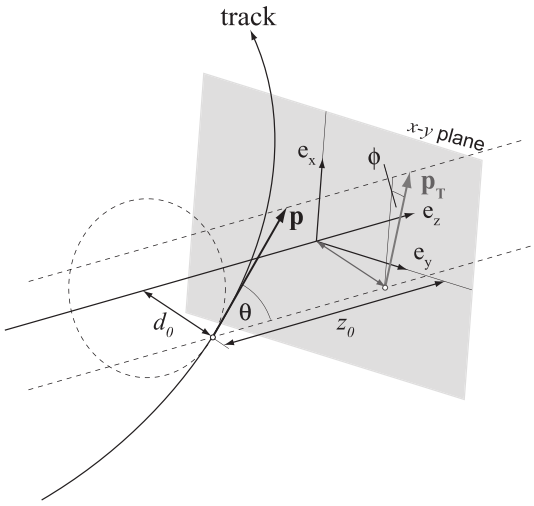

Figure 6.11: Definition of the track parameters with respect to the origin of the ATLAS coordinate system [83].

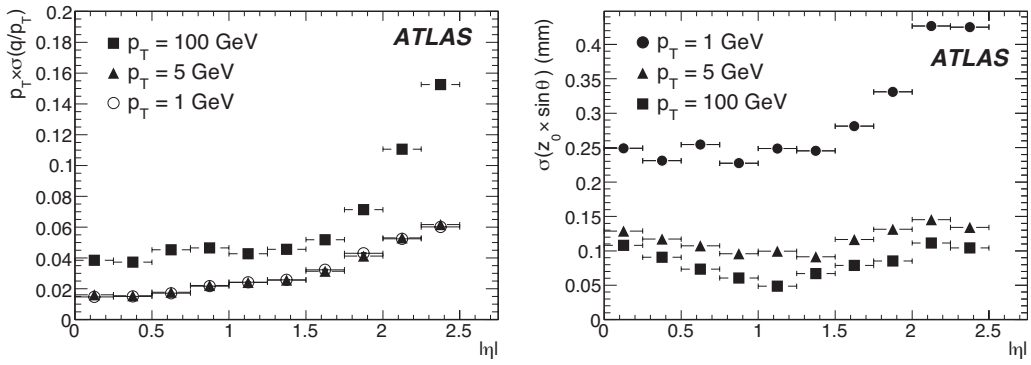

Figure 6.12: The transverse momentum resolution $p_{\mathrm{T}} \times \sigma(q/p_{\mathrm{T}})$ for muons (left) and the resolution of the modified longitudinal impact parameter $z_0 \times \sin\theta$ for charged pions (right) with different p_{T} as a function of η [82].

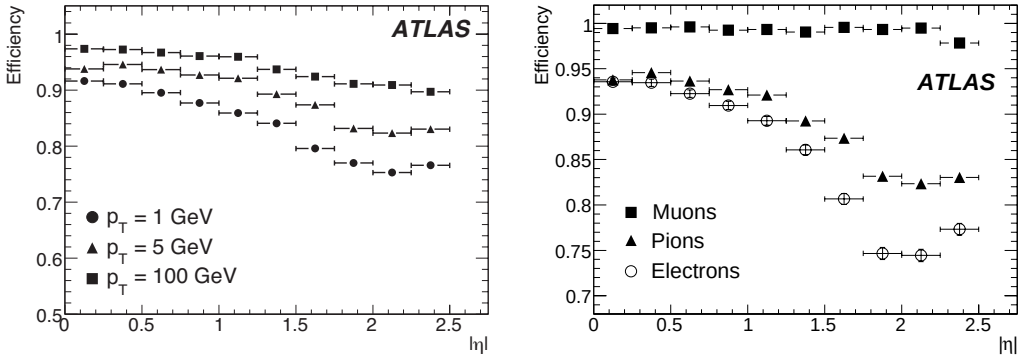

Figure 6.13: Track reconstruction efficiencies for pions with different transverse momenta (left) and for muons, pions and electrons with $p_{\mathrm{T}} = 5\,\mathrm{GeV}$ (right) as a function of η [82].

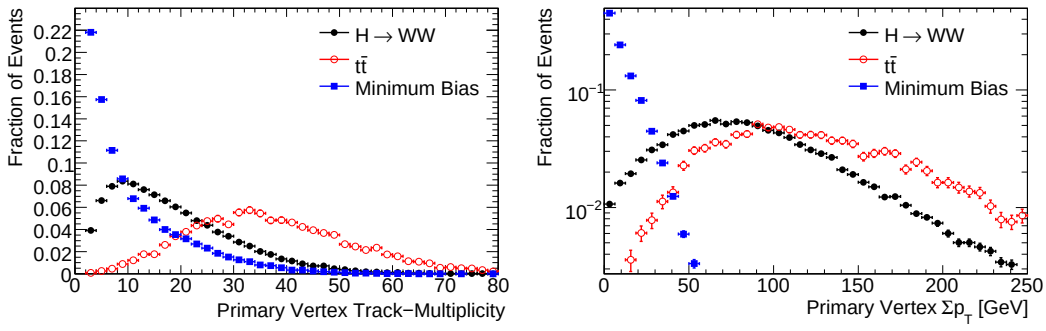

Figure 6.14: Number of tracks associated to each vertex by the vertex fitter (left) and the sum of their transverse momenta (right) for $H \to WW$, $t\bar{t}$ and minimum bias events.

energetic jets is very challenging because of the high track density [82].
The track reconstruction is followed by algorithms reconstructing the primary vertex, photon conversions and secondary vertices from b-hadron decays.

6.3.2 Primary Vertex Reconstruction and Identification

Depending on the instantaneous luminosity and the beam parameters of the LHC, interesting physics events will be superimposed by several pile-up interactions. Hence, the identification and precise reconstruction of the primary vertex is of particular importance for all physics studies.
Minimum bias interactions can usually be distinguished from the primary interaction by their lower track multiplicity and transverse momenta as shown in Figure 6.14. Furthermore, vertices of different pp interactions are usually well separated in the z-coordinate since the interaction region has an approximate Gaussian shape with transverse and longitudinal widths of $\sigma_{x,y} = 15\,\mu$m and $\sigma_z = 56\,$mm, respectively. An overview of the primary vertex reconstruction algorithms in ATLAS can be found in Reference [80].
The primary vertex and the vertices of in-time minimum bias interactions are reconstructed simultaneously by an adaptive multi-vertex fitter [85]. The vertex reconstruction starts with the formation of a primary vertex candidate including all tracks likely to originate from the interaction region. This candidate is then fitted using the adaptive fitter. Tracks which are classified as outliers in the first fit iteration are used to create a second primary vertex candidate, and in the second iteration a simultaneous fit of the two candidates is performed. Thus, the number of vertex candidates grows with each iteration where the candidates compete with each other for the assignment of tracks until a final collection of primary vertex candidates has been found. In this procedure, only vertices of pp interactions are reconstructed and no secondary vertices from b-hadron decays or photon conversions (see Figure 6.2) are considered. From all reconstructed primary vertex candidates, the primary vertex (PV) is identified as the one with the maximal $\sqrt{N}\sum_{i=1}^{N} p_{Ti}^2$ with the number N of tracks assigned to the vertex[1].

[1] In recent Athena software releases, the factor $\sqrt{N}$ has been dropped from the selection criterion and the vertex with the largest $\sum_{i=1}^{N} p_{Ti}^2$ is selected as the primary vertex since this provides an improved primary vertex selection performance.

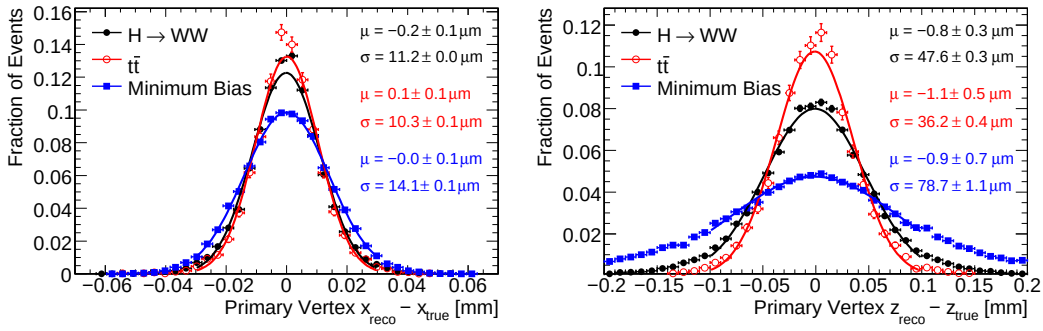

Figure 6.15: Distributions of the distance between reconstructed and true vertex position in the x- (left) and the z-coordinate (right) for vector-boson fusion $H \to WW$, $t\bar{t}$ and minimum bias events.

Process	ε_{reco}	ε_{sel}	ε_{tot}
$t\bar{t}$ without pile-up	100.00 ± 0.00	99.73 ± 0.06	99.73 ± 0.06
$t\bar{t}$ with pile-up	99.88 ± 0.02	99.18 ± 0.06	99.06 ± 0.07
$H \to WW$ without pile-up	94.85 ± 0.11	99.83 ± 0.02	94.69 ± 0.11
$H \to WW$ with pile-up	92.84 ± 0.13	96.29 ± 0.10	89.39 ± 0.15

Table 6.7: Vertex reconstruction and selection efficiencies [%] for $t\bar{t}$ and $H \to WW$ events without and with pile-up. The reconstruction efficiency ε_{reco} is the fraction of events with at least one reconstructed primary vertex candidate within $|\Delta z| < 300\,\mu$m around the true vertex. The selection efficiency ε_{sel} represents the probability that for events with at least one correctly reconstructed vertex the selected primary vertex has a distance below $|\Delta z| = 300\,\mu$m from the true vertex. The total vertex identification efficiency ε_{tot} is the product of ε_{reco} and ε_{sel}.

The vertex-position resolution is shown in Figure 6.15 for vector-boson fusion $H \to WW$, $t\bar{t}$ and minimum bias events. Gaussian fits indicate resolutions of the z vertex-coordinate of $\sigma_z = 36\,\mu$m for $t\bar{t}$ and of $\sigma_z = 48\,\mu$m for vector-boson fusion $H \to WW$ events, respectively. The worse vertex-position resolution in $H \to WW$ events can be explained by the lower number of particles originating from the primary vertex (see Figure 6.14). The lower vertex-position resolution is reflected in the lower vertex reconstruction and selection efficiencies quoted in Table 6.7. For $t\bar{t}$ events the correct primary vertex is identified in almost all events ($\varepsilon_{tot} > 99.0\%$) independently of pile-up while for $H \to WW$ events the vertex reconstruction efficiency decreases significantly in the presence of pile-up. For $H \to WW$ events with pile-up, the correct primary vertex is only found in 89.4% of the events.

The vertex reconstruction efficiency ε_{reco}, which is the main contribution to this inefficiency, can only be increased by improvements in the vertex reconstruction algorithms. The vertex selection efficiency ε_{sel} can be improved either by employing more sophisticated methods for selecting the primary vertex from all candidates, like artificial neural networks or by employing the event topology exploiting, for instance, the additional information of isolated leptons from the hard-scattering process. In Reference [86] a primary vertex selection method has been introduced achieving $\varepsilon_{sel} \approx 100\%$ for vector-boson fusion

$H \to \tau\tau \to lh$ events by reweighting the contribution of the reconstructed lepton track according to its impact parameter significance $z_0/\sigma(z_0)$ with respect to a primary vertex candidate. This method has not been employed for this study since a sufficiently high vertex selection efficiency is obtained for vector-boson fusion $H \to WW$ events containing at least two isolated leptons and two tagging jets within $|\eta| < 4.8$. This increases the vertex reconstruction and selection efficiencies for $H \to WW$ events with pile-up to $\varepsilon_{reco} = 93.8\%$ and $\varepsilon_{sel} = 98.5\%$, respectively.

The conclusion from the vertex reconstruction and identification efficiencies in Table 6.7 is that in $t\bar{t}$ events the primary vertex is efficiently reconstructed independently of pile-up while the vertex reconstruction performance in $H \to WW$ events is significantly deteriorated already for pile-up corresponding to an instantaneous luminosity of 10^{32} cm^{-2} s^{-1} due to the relatively low track multiplicity. In contrast to the vertex reconstruction efficiency, the vertex selection efficiency can be improved by exploiting event topology information. The vertex reconstruction efficiency in vector-boson fusion $H \to WW$ events is expected to degrade further with increasing level of pile-up which has to be studied and improved for data taking at higher luminosities.

6.3.3 Track – Vertex Association

For the methods exploiting inner detector tracks in order to associate jets to the primary vertex, a reliable association of tracks to the primary vertex is very important. Selecting only tracks associated to the primary vertex by the vertex fitter results in the highest insensitivity to pile-up. However, due to the tight selection of tracks for the vertex reconstruction, this is accompanied by a relatively low track selection efficiency which is not acceptable for the studies presented here. Thus, a different track-vertex association retaining more tracks is employed with the drawback of introducing more sensitivity to pile-up.

Tracks are associated to the primary vertex if the z_0 significance $|z_0|/\sigma(z_0)$ with respect to this vertex is less than 30 and if the z distance to each pile-up vertex is larger than the distance between the pile-up vertex and the primary vertex multiplied by $\sum p_{\mathrm{T}}(puv)/(\sum p_{\mathrm{T}}(puv)+\sum p_{\mathrm{T}}(pv))$ with $\sum p_{\mathrm{T}}(pv)$ and $\sum p_{\mathrm{T}}(puv)$ denoting the total transverse momentum of tracks assigned to the primary and to the pile-up vertices, respectively, by the vertex fitter [86]. Figure 6.16 shows the z_0 significance of tracks with respect to the primary vertex as well as the number of tracks associated to the primary vertex for $H \to WW$ events. Both distributions show a small sensitivity to pile-up.

6.4 Jet Reconstruction Exploiting Tracking Information

Two approaches exploiting tracking and vertexing information in order to associate jets to the primary vertex have been studied. First, so-called track jets reconstructed from inner detector tracks only are introduced and, for comparison, the performance of associating tracks from the primary vertex to calorimeter jets is evaluated.

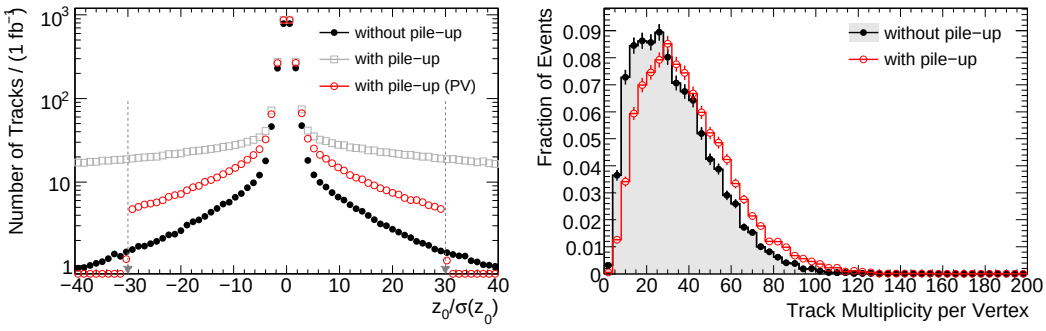

Figure 6.16: Distributions of the z_0 significance (left) and of the number of tracks associated to the primary vertex (right) for $H \to WW$ events without and with pile-up. In the left figure, the gray squares show the distribution of the z_0 significance for all tracks while the red open circles correspond only to tracks associated to the primary vertex. The gray arrows indicate the cut value of $|z_0|/\sigma(z_0) < 30$ required to associate tracks to the primary interaction vertex.

6.4.1 Track Jet Reconstruction

Track jets are reconstructed using tracking information only [87,88]. Inner detector tracks with $p_{\mathrm{T}} > 0.5\,\mathrm{GeV}$ associated to the primary vertex and with at least seven hits in the pixel and semiconductor tracker are subjected to the standard ATLAS cone jet finding algorithm [68,69] as described in the following.

1. The jet reconstruction starts from seeds, defined as inner detector tracks with transverse momenta above 2 GeV. The first jet is reconstructed based on the seed with largest transverse momentum.

2. Tracks within $\Delta R < R_{\mathrm{cone}}$ (here $R_{\mathrm{cone}} = 0.4$) around the seed track are added to the jet and the new jet axis is calculated from the 4-momenta of the tracks belonging to the jet.

3. New tracks are added or removed from the jet depending on whether they fulfill $\Delta R < R_{\mathrm{cone}}$ with respect to the new jet axis.

4. Steps 2 and 3 are repeated until a stable configuration is obtained. The reconstructed object is then added to the list of jet candidates. The tracks belonging to a particular jet candidate are not removed from the collection of tracks in order to allow for tracks to be shared by different jet candidates.

5. The procedure is repeated with the seed track with the next lower p_{T} until all seeds have been processed.

At this stage, tracks may be assigned to several track jet candidates. Therefore, splitting and merging algorithms are applied to the jet candidates in order to obtain the final collection of jets. Subsequently, reconstructed track jets are required to have a transverse momentum above 10 GeV and to contain at least three tracks. Track jets which overlap with an isolated electron or muon within a cone of $\Delta R = 0.4$ are rejected. The selection of the electrons and muons is described in Section 5.4.

The track selection criteria employed to reject fake tracks, i. e. the cuts on the transverse momentum, the number of hits on the track and the track-vertex association have been optimized for high track jet reconstruction efficiency and low misidentification rate as well as for good transverse momentum resolution (Section 6.5). Alternative track selection criteria requiring a minimum number of hits in the pixel detector or associating tracks to the primary vertex based on a cut on the z_0 distance alone resulted in a significantly worse transverse momentum resolution and have therefore been discarded.
In order to test the performance of the track jet reconstruction, truth track jets are reconstructed by applying the standard ATLAS truth-jet reconstruction algorithm to charged final-state truth particles from the primary interaction vertex without p_{T} or η restriction. It has to be emphasized that on truth level physics objects like calorimeter or track jets are reconstructed only from truth particles originating from the true primary interaction vertex.

6.4.2 Calorimeter Jet – Vertex Association

In order to associate standard calorimeter jets to the primary vertex, the primary vertex p_{T} fraction of the jet $r_{p_{\mathrm{T}}}$ is used [86,89]. It is defined as the total p_{T} of the tracks associated to the jet emerging from the primary vertex (PV) and the total p_{T} of all tracks associated to the jet:

$$r_{p_{\mathrm{T}}} = \frac{\sum p_{\mathrm{T}}(\text{tracks from PV associated to calorimeter jet})}{\sum p_{\mathrm{T}}(\text{all tracks associated to calorimeter jet})}.$$

The same track selection is applied as for the reconstruction of tracks jets, i. e. only inner detector tracks with $p_{\mathrm{T}} > 0.5\,\mathrm{GeV}$ and at least seven hits in the pixel and semiconductor tracker are used. Tracks are associated to a calorimeter jet by requiring a distance to the jet axis below $\Delta R = 0.4$. Jets with a total p_{T} of the associated tracks below 2 GeV are assigned a negative $r_{p_{\mathrm{T}}}$ value. Calorimeter jets are then tagged as originating from the primary interaction vertex by applying a cut on the primary vertex p_{T} fraction.

6.4.3 Comparison of the Methods

In principle, both approaches are capable of reducing the two major effects of pile-up on the jet reconstruction performance: the presence of additional jets originating from minimum bias events and the increased jet energy due to the higher activity in the calorimeter. Both effects are illustrated in Figure 6.17 which shows the tracks associated to calorimeter and track jets in a typical vector-boson fusion $H \to WW$ event with pile-up. While track jets are solely reconstructed based on tracks originating from the primary vertex, several tracks associated to calorimeter jets originate from additional minimum bias events and therefore result in increased jet energies and additional calorimeter jets being reconstructed in the presence of pile-up.
The track jet transverse momentum and reconstruction efficiency are expected to be independent of pile-up by construction. Nevertheless, a decreased vertex reconstruction and track-vertex association efficiency at high pile-up levels could deteriorate the track jet reconstruction performance, in particular for processes with relatively low track multiplicities like Higgs boson production (see Section 6.3.2). In events without reconstructed vertices, track jets are reconstructed from all tracks in the event.

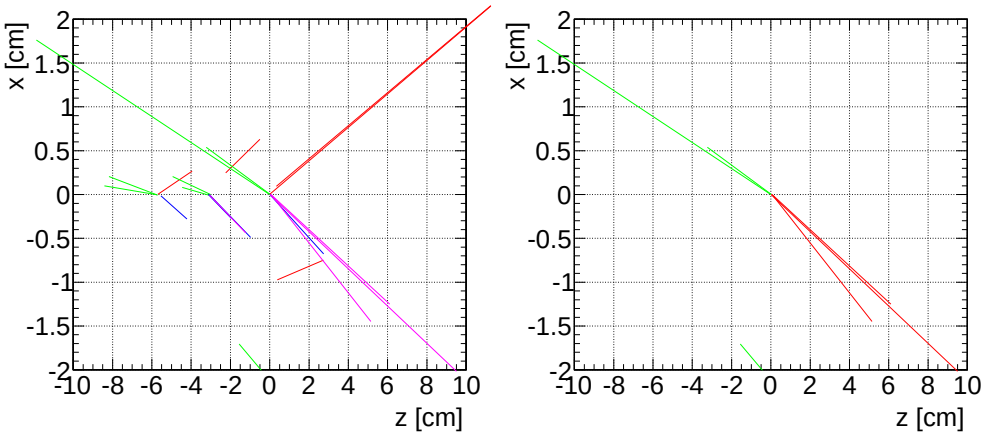

Figure 6.17: Tracks associated to calorimeter jets (left) and to track jets (right) in a vector-boson fusion $H \rightarrow WW$ event with pile-up in the x-z plane of the inner detector. Tracks of the same color are associated to the same jet. Only calorimeter jets with $p_{\mathrm{T}} > 20\,\mathrm{GeV}$ and track jets with $p_{\mathrm{T}} > 10\,\mathrm{GeV}$ are shown. Tracks are required to have transverse momenta above 1 GeV. A line with a length of 1 cm corresponds to a track with transverse momentum of 1 GeV.

In order to compare the effect of using track or calorimeter jets in the analysis, in particular on the performance of the central jet veto, the transverse momenta and reconstruction efficiencies of track jets have to be measured absolutely and relative to calorimeter jets. Since the track multiplicities of quark and gluon jets differ [90], these measurements have to take into account the origin of the jet.

In order to avoid the systematic uncertainties in the track jet transverse momentum reconstruction, either track jets or the primary vertex p_{T} fraction can be used to tag calorimeter jets to originate from the primary interaction vertex, which both require the calibration of calorimeter jets to be robust against pile-up. This can be achieved by different methods. At the Tevatron experiments DØ and CDF, methods have been developed to correct the calorimeter jet energy for contributions from additional pp interactions by subtracting a constant offset from the energy of all jets in the event, which is determined from the average calorimeter energy deposition of minimum bias events and the vertex multiplicity in the event [91]. Alternatively, the jet energy can be corrected on a jet-by-jet level by multiplication with the primary vertex p_{T} fraction which accounts for the contribution of additional minimum bias events to the transverse momentum of the jet [89].

In contrast to track jets, the cut to be applied on the primary vertex p_{T} fraction in order to reliably tag calorimeter jets to originate from the primary vertex is expected to depend on the level of pile-up (see Section 6.7). As the track jet reconstruction performance, the efficiency of the primary vertex p_{T} fraction cut will suffer from deteriorated primary vertex reconstruction and track-vertex association at high pile-up levels.

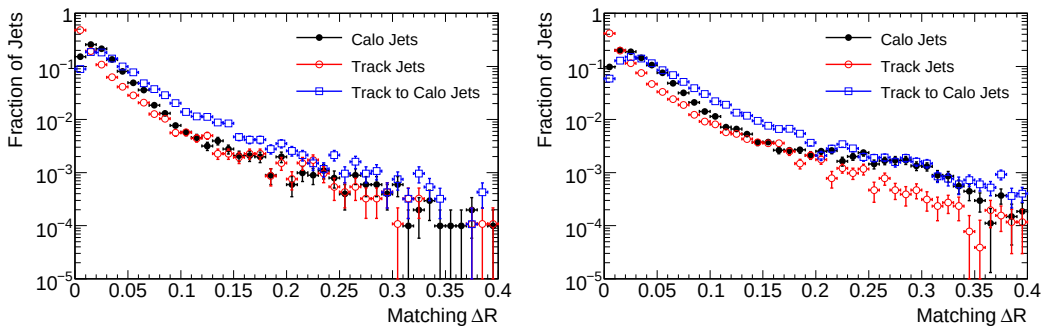

Figure 6.18: Matching distance ΔR between reconstructed track and calorimeter jets and the matching truth jets in $H \rightarrow WW$ (left) and $t\bar{t}$ events (right). In addition, the distribution of ΔR between track jets and the matching calorimeter jets is shown. $\Delta R < 0.3$ is required to match reconstructed and truth jets as well as track and calorimeter jets.

	$H \rightarrow WW$		$t\bar{t}$	
	without pile-up	with pile-up	without pile-up	with pile-up
Efficiency:				
Track jets	91.88 ± 0.13	89.24 ± 0.15	93.41 ± 0.07	93.01 ± 0.07
Calo jets	98.77 ± 0.05	98.61 ± 0.06	97.99 ± 0.04	97.79 ± 0.04
Misidentification rate:				
Track jets	17.92 ± 0.18	19.73 ± 0.19	16.75 ± 0.09	16.93 ± 0.09
Calo jets	19.74 ± 0.18	29.64 ± 0.18	5.69 ± 0.06	10.20 ± 0.08

Table 6.8: Reconstruction efficiencies and misidentification rates [%] for track and calorimeter jets within $|\eta| < 2.5$.

6.5 Track Jet Performance

This section gives an overview of the performance of the track and calorimeter jet reconstruction. In particular, the impact of pile-up on the reconstruction efficiency, misidentification rate and transverse momentum resolution is studied for the different jet definitions.

6.5.1 Efficiency and Misidentification Rate

The distribution of the distance ΔR between the reconstructed track and calorimeter jets and the matching truth jets is shown in Figure 6.18.
In Figure 6.19 the track and calorimeter jet reconstruction efficiencies and misidentification rates are shown for $H \rightarrow WW$ events without and with pile-up. The corresponding plots for tracks jets in $t\bar{t}$ events are shown in Figure B.4 in Appendix B. The efficiency is defined as the fraction of truth jets which can be matched to a reconstructed jet within $\Delta R < 0.3$ while the misidentification rate is the fraction of reconstructed jets which cannot be matched to a truth jet. The values obtained for $H \rightarrow WW$ and $t\bar{t}$ events without and with pile-up are summarized in Table 6.8.
In comparison to track jets, calorimeter jets are reconstructed with larger efficiency and

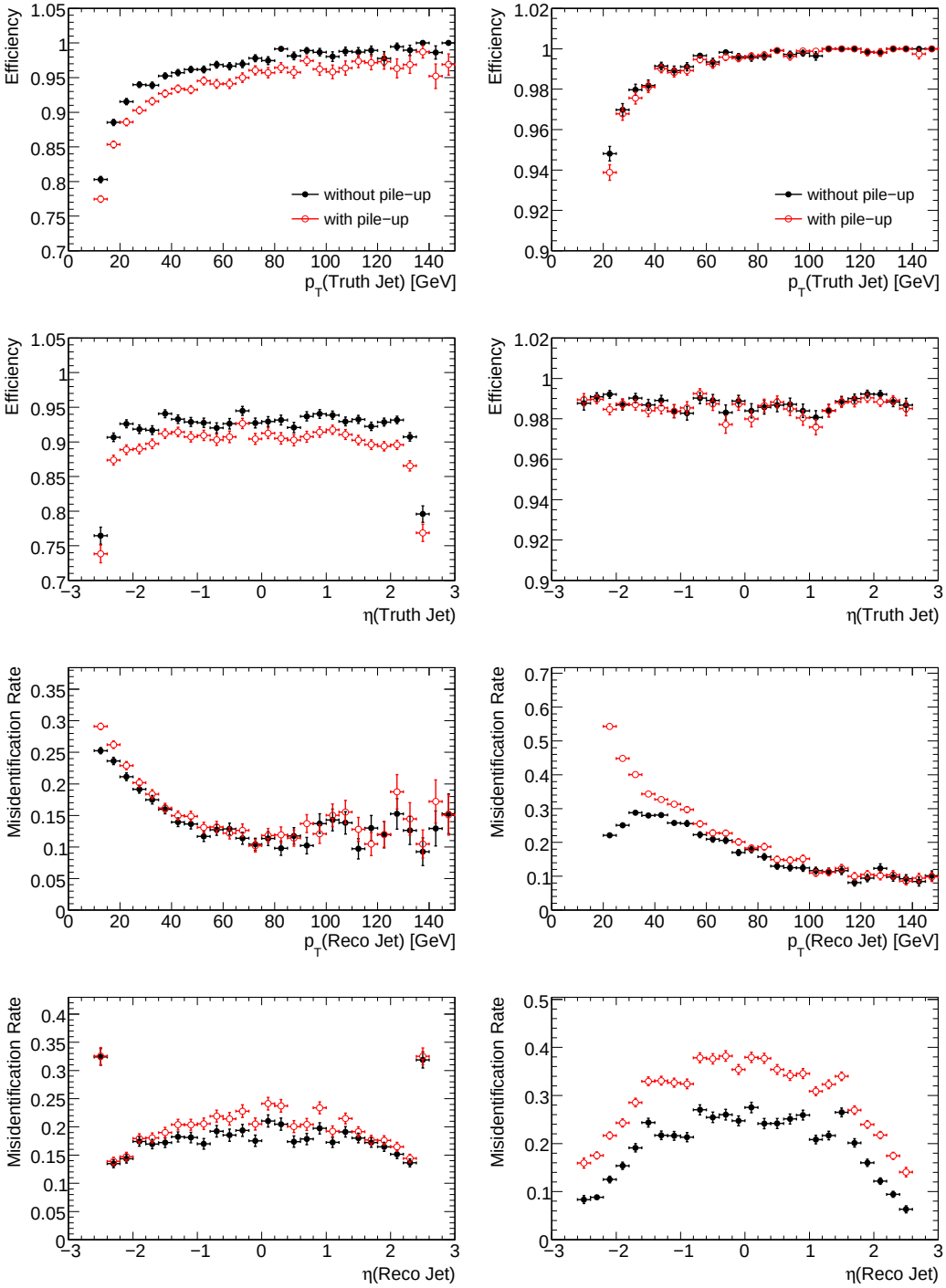

Figure 6.19: Reconstruction efficiencies and misidentification rates as a function of p_{T} and η, respectively, for track jets (left) and calorimeter jets (right) within $|\eta| < 2.5$ for $H \rightarrow WW$ events without and with pile-up.

smaller misidentification rate for events without pile-up due to the better performance of the calorimeter for low-energy clusters compared to the relatively low tracking efficiency for low-p_{T} tracks. However, in the presence of pile-up, a large number of additional low-p_{T} calorimeter jets is produced. It has to be noted that the jet misidentification rate also includes jets from pile-up events since on truth level no physics objects from pile-up interactions are reconstructed. Therefore, the misidentification rate of calorimeter jets increases significantly while the reconstruction efficiency is robust against pile-up.

The efficiency and misidentification rate of the track jets show only little sensitivity to pile-up as expected. The small differences observed between $H \to WW$ events without and with pile-up are caused by the more difficult vertex reconstruction and track-vertex association in the presence of pile-up. A rapidity independent average efficiency of 90% and a misidentification rate of about 18% are achieved for $H \to WW$ events. The reconstruction efficiency drops for track jet transverse momenta below 40 GeV because of inefficiencies in the reconstruction of low-p_{T} tracks. Efficiencies larger than 95% are obtained for high-p_{T} track jets.

The reconstruction of jets is more difficult in $H \to WW$ events compared to $t\bar{t}$ events due to the larger fraction of isolated leptons, particularly of electrons which can be misidentified as a jet (see Section 5.4.3).

6.5.2 Multiplicity

The low sensitivity of the track jet reconstruction to pile-up is also reflected in the jet multiplicities shown in Figure 6.20 for $H \to WW$ events. The corresponding distributions for $t\bar{t}$ events are shown in Figure 6.29. The additional pile-up interactions create additional low-p_{T} calorimeter jets while the multiplicities of track jets are only slightly affected by pile-up. The small differences are caused by the more difficult vertex identification and track-vertex association in the presence of pile-up. Figure 6.21 shows the track multiplicity per track jet which is insensitive to pile-up and the average track multiplicity of track jets as a function of the jet transverse momentum. The difference between the track multiplicities of track jets in $H \to WW$ and $t\bar{t}$ events arises from the different origin of the jets. Jets in the vector-boson fusion signal process are predominantly due to light quarks from the colliding protons while in $t\bar{t}$ events a large fraction of jets originates from the hadronization of b-quarks.

As shown in Figure 6.22, the track jet multiplicity as a function of the number of reconstructed primary vertex candidates is robust against pile-up. After applying a cut on the transverse momentum of $p_{\mathrm{T}} > 20\,\mathrm{GeV}$, also the calorimeter jet multiplicity shows only a small sensitivity to pile-up for events with less than six primary vertex candidates. For events with more reconstructed vertices the impact of pile-up increases significantly.

As can be seen in Figures 6.20 and 6.22, for high transverse momenta above $30 - 35\,\mathrm{GeV}$ the effect of pile-up on the calorimeter jet multiplicity becomes small. However, a high p_{T} cutoff will decrease the performance of the central jet veto and will have to depend on the level of pile-up. Therefore, employing track jets or a cut on the primary vertex p_{T} fraction allows for more efficient rejection of pile-up jets.

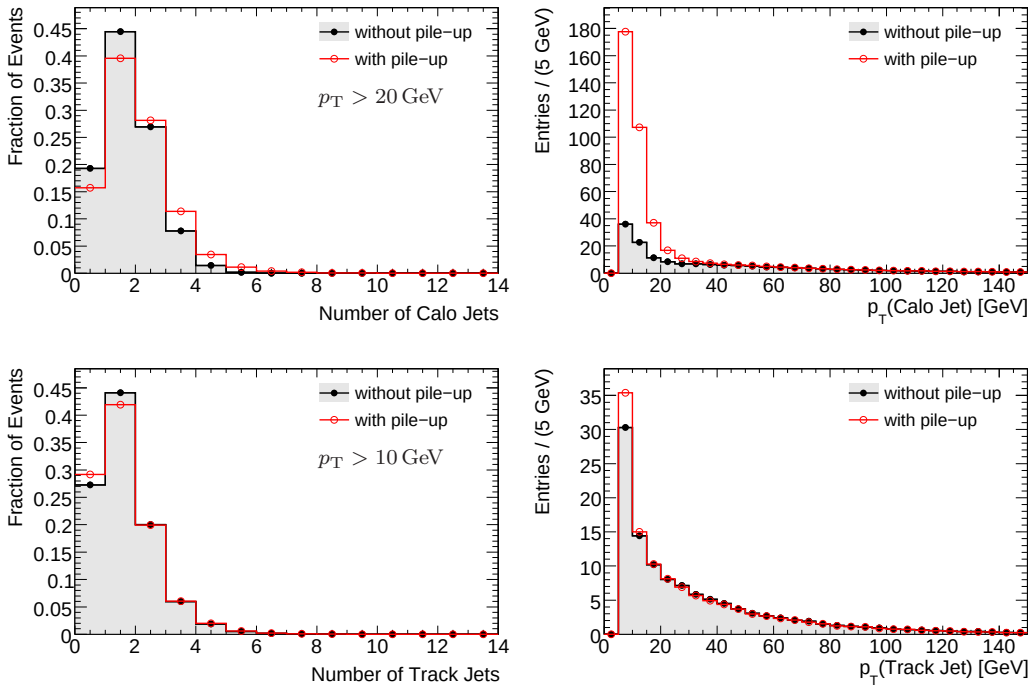

Figure 6.20: Comparison of the jet multiplicities (left) and the p_T distributions (right) of calorimeter jets (top) and of track jets (bottom) within $|\eta| < 2.5$ in $H \rightarrow WW$ events without and with pile-up. The p_T distributions are scaled to $1\,\text{fb}^{-1}$.

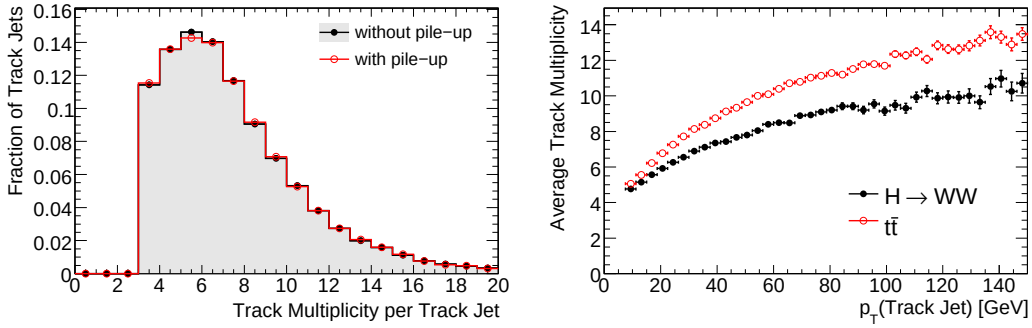

Figure 6.21: Track multiplicity per track jet for $H \rightarrow WW$ events (left) and the average track multiplicity as a function of the track jet transverse momentum for $H \rightarrow WW$ and $t\bar{t}$ events (right).

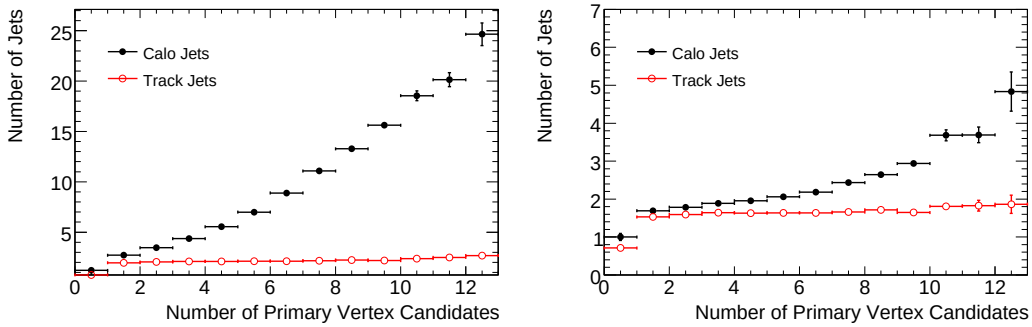

Figure 6.22: Multiplicities of track and calorimeter jets without p_{T} cut (left) and for track jets with $p_{\mathrm{T}} > 10\,\mathrm{GeV}$ and calorimeter jets with $p_{\mathrm{T}} > 20\,\mathrm{GeV}$ (right) in $H \to WW$ events with pile-up as a function of the number of reconstructed primary vertex candidates

	$H \to WW$		$t\bar{t}$	
	w/o pile-up	with pile-up	w/o pile-up	with pile-up
Reconstruction level:				
Track jet → calo jet:	91.20 ± 0.13	90.63 ± 0.14	86.16 ± 0.09	85.98 ± 0.09
Calo jet → track jet:	77.02 ± 0.19	64.99 ± 0.19	89.08 ± 0.08	83.20 ± 0.09
Truth level:				
Track jet → calo jet:	98.68 ± 0.06	98.68 ± 0.06	97.73 ± 0.04	97.78 ± 0.04
Calo jet → track jet:	91.19 ± 0.14	91.19 ± 0.14	93.15 ± 0.07	93.16 ± 0.07

Table 6.9: Matching efficiencies [%] of track jets to calorimeter jets on the reconstruction and on the truth level.

6.5.3 Track Jet – Calorimeter Jet Matching

Track jets have to be matched to calorimeter jets in order to determine the fraction of the calorimeter jet transverse momentum carried by the track jets. Figure 6.23 and Table 6.9 summarize the matching efficiencies between track and calorimeter jets within $\Delta R < 0.3$. For each reconstructed track jet, a matching calorimeter jet is found with pile-up independent probabilities of 91% and 86% for $H \to WW$ and $t\bar{t}$ events, respectively. On the other hand, significant pile-up dependence and large differences between $H \to WW$ and $t\bar{t}$ events are observed for the matching of calorimeter jets to track jets. The latter are caused by the worse vertex reconstruction efficiency and the significantly larger misidentification rate for calorimeter jets in $H \to WW$ events.

6.5.4 p_{T} Resolution

The ratio of the transverse momenta of the reconstructed and the matching truth track jet is a good measure of the performance of the track jet reconstruction since it is very sensitive to the track selection criteria. As shown in Figure 6.24a, the distribution of the p_{T} ratio peaks at 1 with the enhanced tail towards lower values caused by tracking errors particularly at low-p_{T}. This is also visible in Figure 6.24c which shows the p_{T} ratio as a

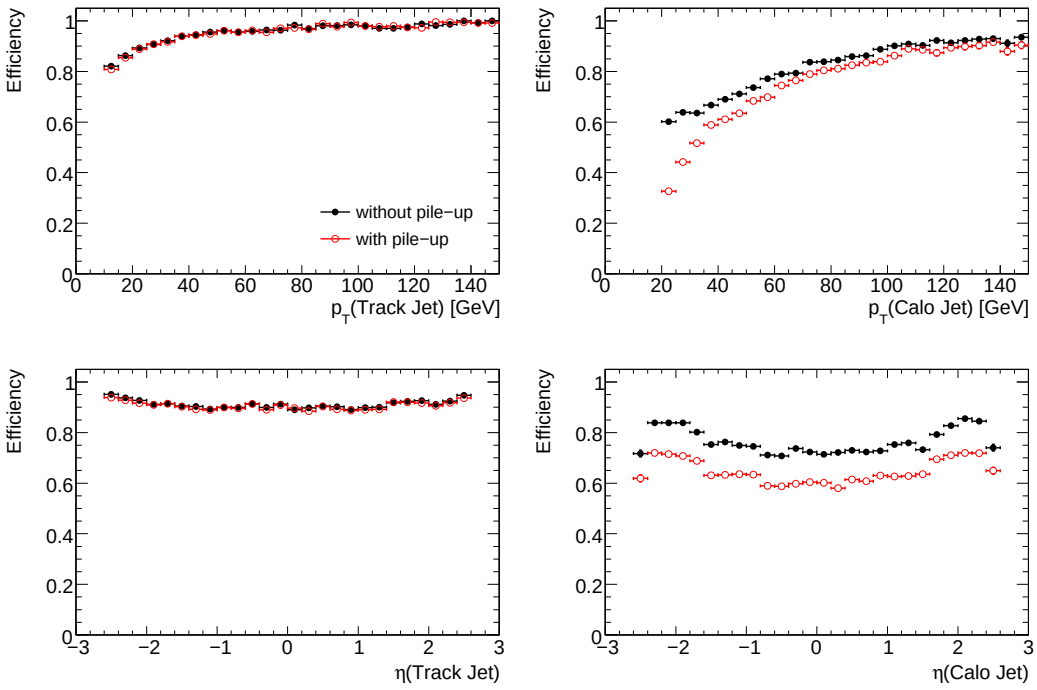

Figure 6.23: Matching efficiencies of track jets to calorimeter jets (left) and of calorimeter jets to track jets (right) in $H \rightarrow WW$ events as a function of p_{T} and η.

function of the transverse momentum of the reconstructed track jets[2]. For low-p_{T} track jets the p_{T} ratio differs significantly from 1.
The p_{T} ratio is independent of η in the range $|\eta| < 2.0$ (Figure 6.24e) but decreases for larger η values due to the deteriorated tracking performance with increased amount inner detector material and the geometrical acceptance of the inner detector being limited to $|\eta| < 2.5$. Thus, track jets with jet axis close to $|\eta| = 2.5$ are reconstructed with low efficiency and, furthermore, suffer from a low p_{T} resolution. Track jets in the region $2.0 < |\eta| < 2.5$ are retained despite the reduced performance since they still allow for an improved rejection of pile-up jets compared to calorimeter jets. In Figure 6.24g, a dependence of the p_{T} ratio on the track multiplicity of the track jets is visible. Low track multiplicities are usually found in low-p_{T} track jets. Thus, the decrease of the p_{T} ratio for low track multiplicities is caused by the tracking inefficiency for low-p_{T} tracks. While the p_{T} ratio for track jets is insensitive to pile-up a clear sensitivity is visible for calorimeter jets, in particular for low transverse momenta.

6.5.5 Comparison of Track Jet and Calorimeter Jet p_{T}

The ratio of the transverse momenta of track and calorimeter jets provides the calibration of track jets relative to calorimeter jets. To first order, it is the fraction of charged energy

[2]In dedicated jet performance studies the jet p_{T} resolution is usually shown as a function of the true jet transverse momentum. Here, the depiction as a function of the reconstructed jet p_{T} has been chosen since it allows for the estimation of the effect of pile-up on the jets deployed in the analysis.

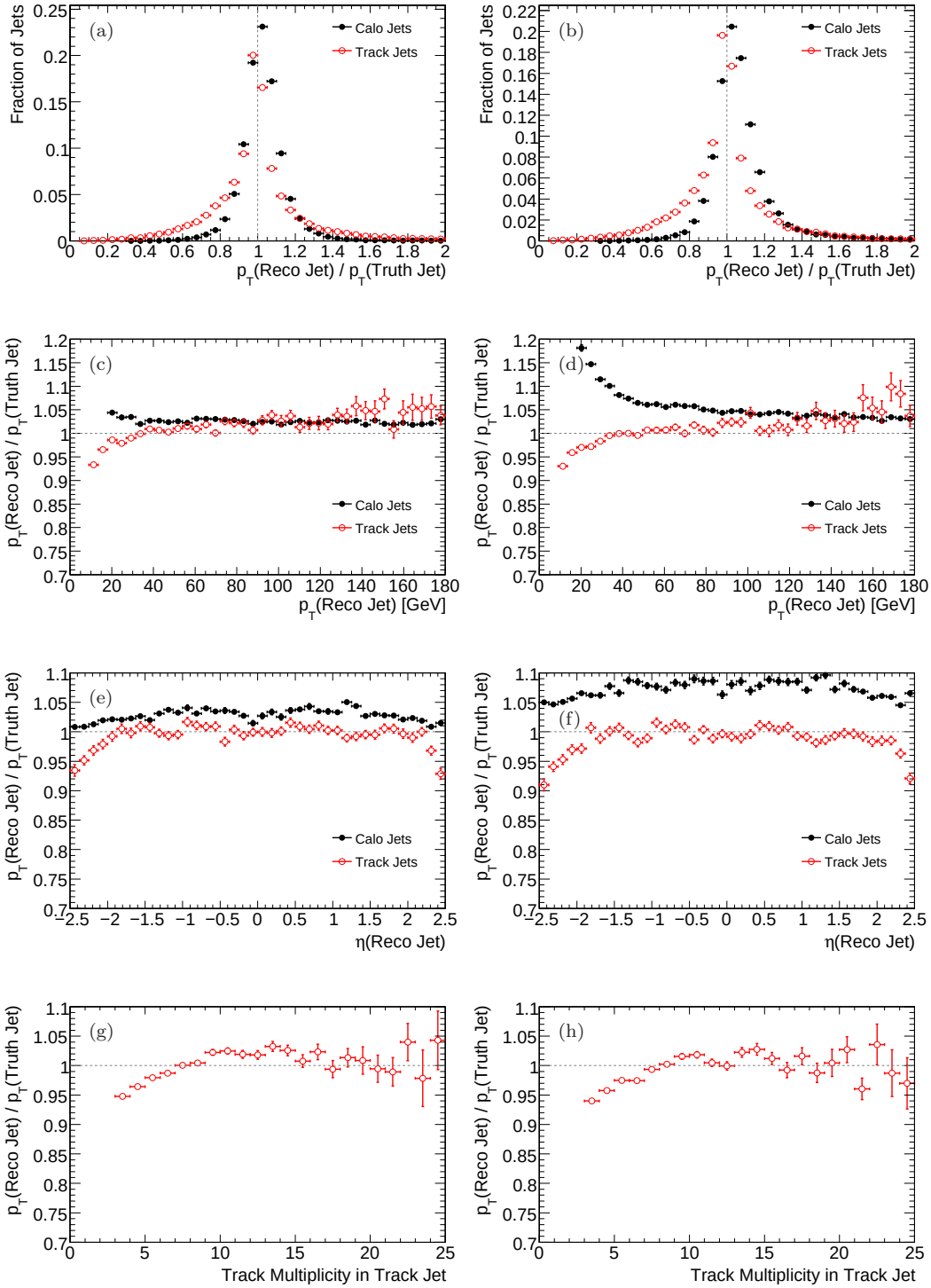

Figure 6.24: Ratio of the transverse momenta of the reconstructed and the matching truth track and calorimeter jets for $H \rightarrow WW$ events without (left) and with pile-up (right). Shown are the distributions of the ratio (a, b), and the dependence on the reconstructed jet p_{T} (c, d) and η (e, f) and on the track multiplicity of the track jets (g, h).

in the jet. Since jets are mainly composed of charged and neutral pions, the ratio is naively expected to be approximately 2/3 based on isospin invariance.

Figure 6.25a shows that the ratio is indeed close to 2/3 for truth jets in $H \to WW$ events. For reconstructed jets slightly lower values are observed due to tracking errors. Small differences on the order of 5% are observed between the events without and with pile-up. The difference between the ratios for truth jets and for reconstructed jets originates from the region $|\eta| > 2.0$ (see Figure 6.25b) where the track jet reconstruction performance is deteriorated (see Section 6.5.4).

In Figures 6.25c and 6.25d, the dependence of the track-to-calorimeter jet p_{T} ratio on the transverse momentum of track and of calorimeter jets is shown. Measuring these distributions with a large data sample of jets is necessary to obtain a calibration of the track jet p_{T} relative to the calorimeter jet p_{T} which is further studied in Section 6.9.

6.6 Performance of the Primary Vertex p_{T} Fraction Cut

Figure 6.26 shows the distributions of the primary vertex p_{T} fraction for calorimeter jets with transverse momenta above 20 GeV in $H \to WW$ and $t\bar{t}$ events without and with pile-up. Separate distributions are shown for the two leading jets within $|\eta| < 4.8$, defined as the tagging jets, and for additional central jets within $|\eta| < 3.0$ after requiring the lepton trigger and at least two reconstructed jets and leptons. As expected, for events without pile-up the distributions peak at 1 whereas for the events with pile-up a significant contribution of jets with small $r_{p_{\mathrm{T}}}$ values is visible. The effect of pile-up on the primary vertex p_{T} fraction of the tagging jets is relatively small while the impact on the central jets is much more pronounced. Thus, in most events the tagging jets can still be correctly identified in the presence of pile-up but additional low-p_{T} jets with $p_{\mathrm{T}} > 20\,\mathrm{GeV}$ are produced. The fraction of jets with small primary vertex p_{T} fraction ($r_{p_{\mathrm{T}}} < 0.5$) is larger for $H \to WW$ than for $t\bar{t}$ events. Hence, due to the lower jet multiplicity, the effect of pile-up on the calorimeter jets is larger in $H \to WW$ events.

In Figure 6.27, $r_{p_{\mathrm{T}}}$ distributions are shown for calorimeter jets within $|\eta| < 2.5$ not identified as tagging jets, which are matched to truth jets and thus are originating from the primary interaction vertex (signal jets), and for calorimeter jets without matching truth jet, which are classified as pile-up jets. The rejection of central jets from pile-up as a function of the selection efficiency of signal jets from the primary interaction is shown in Figure 6.28 for calorimeter jets within $|\eta| < 2.5$ with varying $r_{p_{\mathrm{T}}}$ cut value. Different behavior is observed for $H \to WW$ and $t\bar{t}$ events. The difference at large signal jet selection efficiencies near 100% is caused by the larger number of low-p_{T} signal jets with negative $r_{p_{\mathrm{T}}}$ in $H \to WW$ events (see Figure 6.27) which are not associated to the primary vertex. The higher pile-up jet rejection for $t\bar{t}$ events at low signal jet selection efficiencies is caused by the larger fraction of pile-up jets with $r_{p_{\mathrm{T}}} \approx 1$ in $t\bar{t}$ events ($\sim 14\%$) compared to $H \to WW$ events ($\sim 6\%$) which are misidentified as originating from the primary vertex. This is more likely to happen in $t\bar{t}$ events with larger track multiplicity (see Figure 6.14).

The determination of the $r_{p_{\mathrm{T}}}$ cut value used in order to tag central calorimeter jets as originating from the primary interaction vertex is discussed in Section 6.8.3.

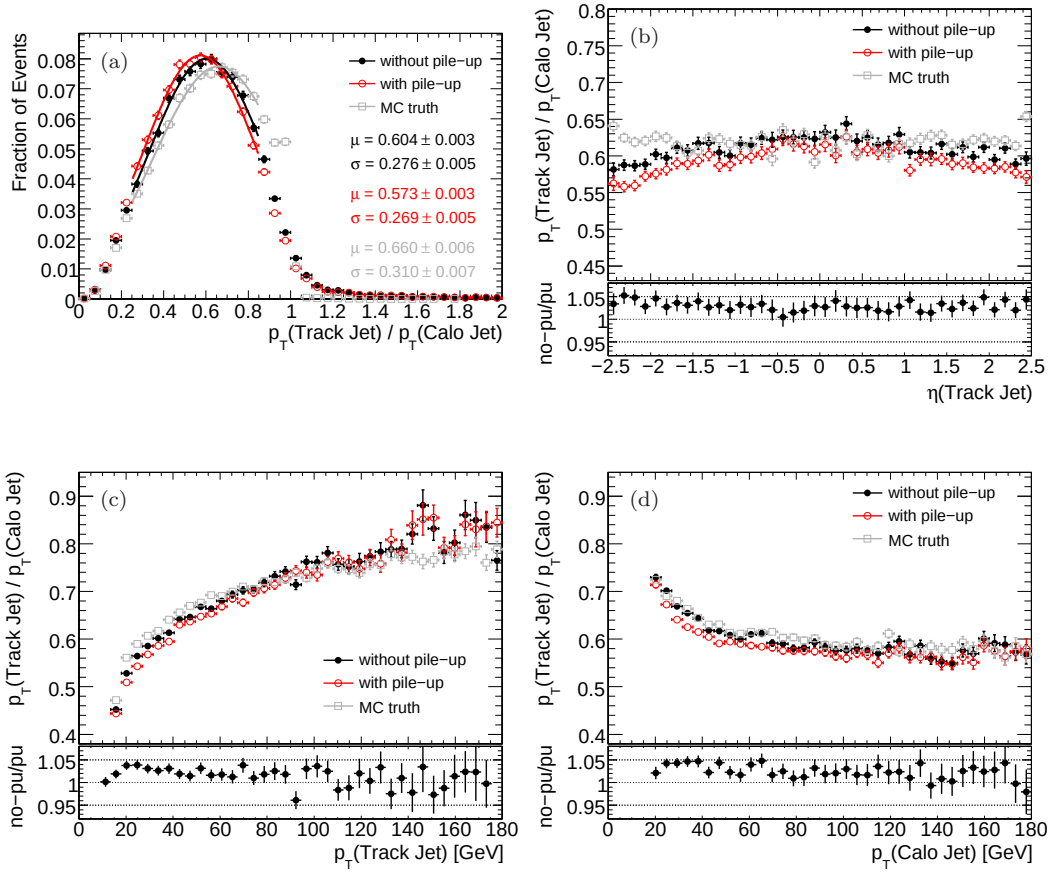

Figure 6.25: Ratio of the transverse momenta of track and matching calorimeter jets for $H \rightarrow WW$ events without (black dots) and with pile-up (red open circles). The p_{T} ratio of truth track jets to corresponding truth calorimeter jets (gray open squares) serves as reference. Shown are the distributions of the ratios (a), and the dependence on η (b) and p_{T} (c) of the track jets and on the calorimeter jet p_{T} (d). The rise of the ratios at low p_{T} in (d) is caused by the transverse momentum cuts of $> 10\,\mathrm{GeV}$ for track jets and $> 20\,\mathrm{GeV}$ for calorimeter jets. The ratios of the distributions of the p_{T} ratios without and with pile-up are shown in the lower parts of Figures (b)-(d).

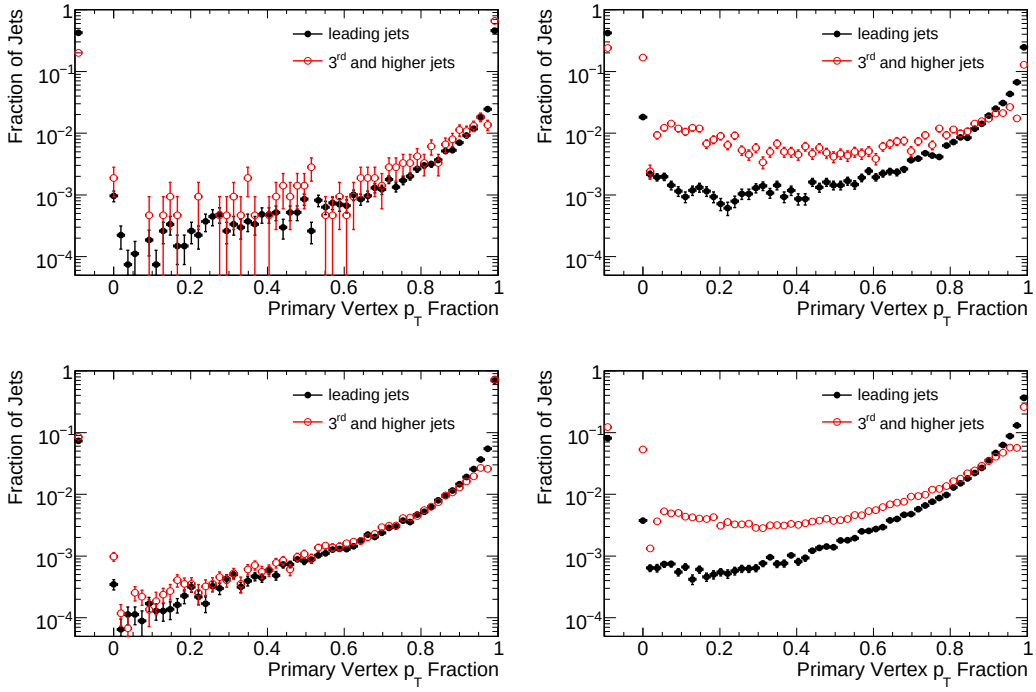

Figure 6.26: Primary vertex p_{T} fraction for $H \to WW$ (top) and $t\bar{t}$ events (bottom) without (left) and with pile-up (right) for calorimeter jets with $p_{\mathrm{T}} > 20\,\mathrm{GeV}$. Separate distributions are shown for the two leading jets within $|\eta| < 4.8$ and for additional central jets within $|\eta| < 3.0$ after requiring the lepton trigger and at least two reconstructed jets and leptons.

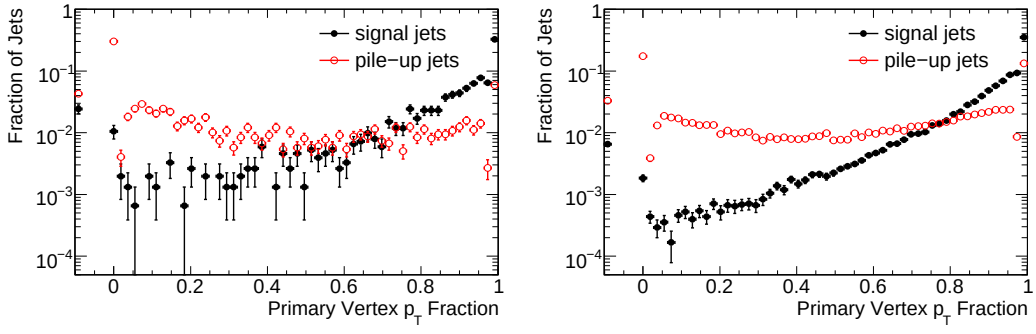

Figure 6.27: Primary vertex p_{T} fraction of calorimeter jets not classified as tagging jets in $H \to WW$ (left) and $t\bar{t}$ events (right) with pile-up. The distributions are shown for calorimeter jets with $p_{\mathrm{T}} > 20\,\mathrm{GeV}$ and $|\eta| < 2.5$ matched to truth jets within $\Delta R < 0.3$, thus originating from the primary interaction vertex (signal jets), and for calorimeter jets without matching truth jet (pile-up jets).

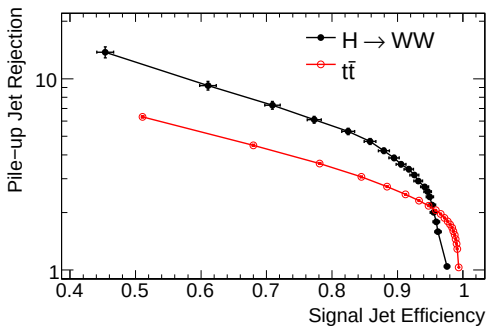

Figure 6.28: Pile-up jet rejection versus signal jet selection efficiency for calorimeter jets within $|\eta| < 2.5$ after the cut on the primary vertex p_{T} fraction for $H \rightarrow WW$ and $t\bar{t}$ events.

	Without pile-up	With pile-up for	
		10^{32} cm^{-2} s^{-1}	10^{33} cm^{-2} s^{-1}
Efficiency:			
Track jets	93.41 ± 0.07	93.01 ± 0.07	93.03 ± 0.07
Calo jets	97.99 ± 0.04	97.79 ± 0.04	97.72 ± 0.04
Misidentification rate:			
Track jets	16.75 ± 0.09	16.93 ± 0.09	17.25 ± 0.10
Calo jets	5.69 ± 0.06	10.20 ± 0.08	12.86 ± 0.08

Table 6.10: Reconstruction efficiencies and misidentification rates [%] for track and calorimeter jets within $|\eta| < 2.5$ in $t\bar{t}$ events with different levels of pile-up.

6.7 Effects of Different Pile-up Levels

Track Jets

In order to demonstrate the insensitivity to different levels of pile-up, the track jet reconstruction has been studied in $t\bar{t}$ events with pile-up corresponding to instantaneous luminosities of $\mathcal{L} = 10^{32}$ cm^{-2} s^{-1} and 10^{33} cm^{-2} s^{-1}, respectively. In contrast to calorimeter jets, the track jet multiplicities are observed to be robust against the different pile-up levels as shown in Figure 6.29. Also the track jet reconstruction efficiency and misidentification rate are insensitive to the level of pile-up as shown in Table 6.10.
Additional distributions are shown in Appendix B, demonstrating the insensitivity of the track multiplicity (Figure B.2), of the reconstructed transverse momentum (Figure B.3) and of the reconstruction efficiency and misidentification rate (Figures B.4 and B.5) of track jets to the different levels of pile-up.

Primary Vertex p_{T} Fraction

The distributions of the primary vertex p_{T} fraction for central jets in $t\bar{t}$ events with different levels of pile-up are shown in Figure 6.30. As expected, the fraction of jets with small $r_{p_{\mathrm{T}}}$ values increases with increasing level of pile-up since more tracks from additional pile-up

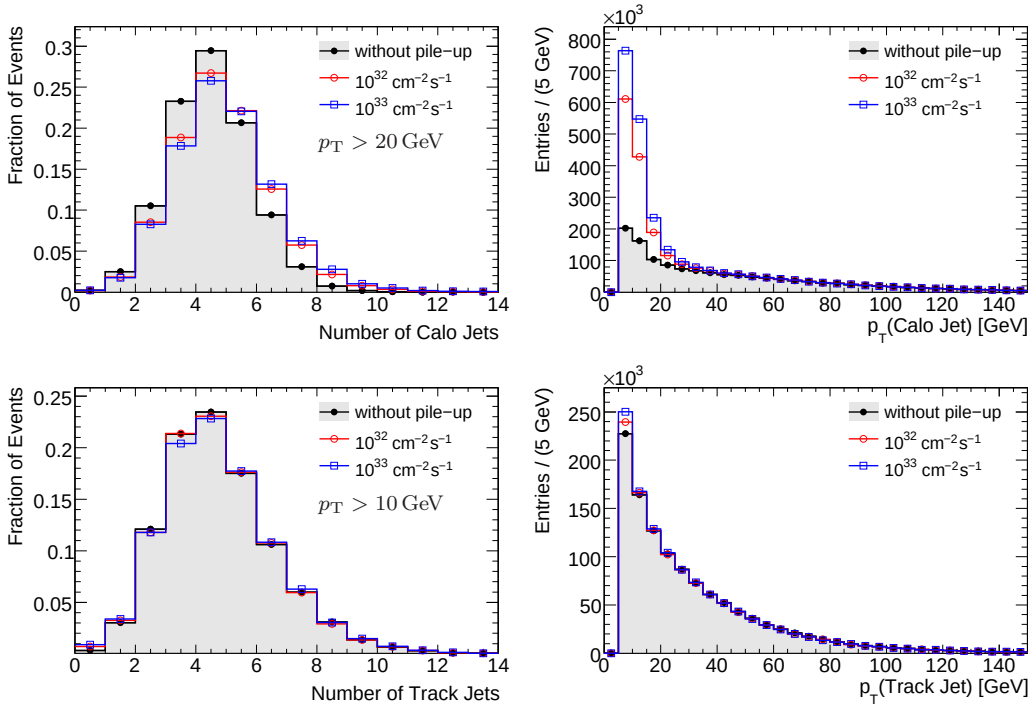

Figure 6.29: Comparison of the jet multiplicities (left) and the p_T distributions (right) for calorimeter jets (top) and for track jets (bottom) within $|\eta| < 2.5$ in $t\bar{t}$ events with different levels of pile-up. The p_T distributions are scaled to $1\,\text{fb}^{-1}$.

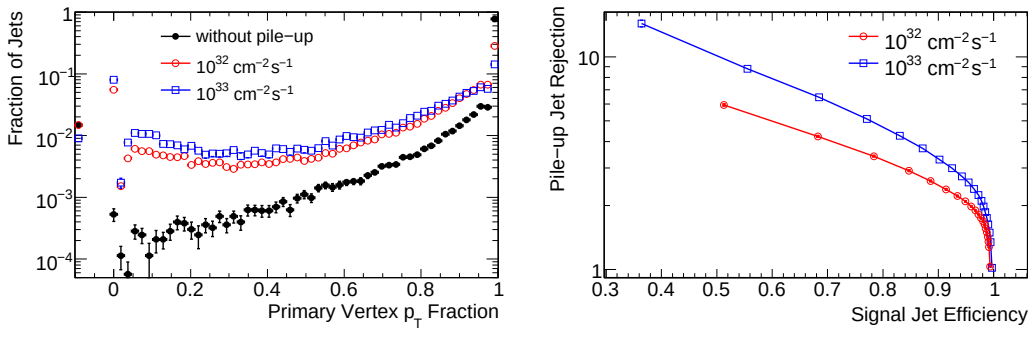

Figure 6.30: Primary vertex p_T fraction for calorimeter jets with $p_T > 20\,\text{GeV}$ and $|\eta| < 2.5$ not classified as tagging jets (left) and pile-up jet rejection versus signal jet selection efficiency (right) for $t\bar{t}$ events with different levels of pile-up.

vertices are associated to the jets. Thus, the pile-up jet rejection as well as the signal jet selection efficiency for a certain $r_{p_{\mathrm{T}}}$ cut depend on the level of pile-up and therefore have to be determined from the data.

6.8 Central Jet Veto Performance

In this section, the pile-up sensitivity of the central jet veto methods exploiting tracking and vertexing information is studied in the region $|\eta| < 2.5$ covered by the inner detector.

6.8.1 Event Selection

In order to study the central jet veto performance for the different methods to reject jets from pile-up events, electrons, muons and calorimeter jets are selected as described in Section 5.4. Track jets are reconstructed as explained in Section 6.4.1.
After applying all event selection criteria described in Section 5.5, only a small number of $t\bar{t}$ Monte Carlo events is retained due to the high rejection rate. In order to derive statistically significant conclusions, only cuts related to the jet selection are applied and cuts exploiting kinematic relations of the leptons are omitted. The following event selection criteria are applied before the central jet veto:

- Single-lepton trigger requirements e10_medium or mu10 (see Section 5.5.1).
- At least two leptons with $p_{\mathrm{T}} > 15\,\mathrm{GeV}$.
- At least two jets with $p_{\mathrm{T}} > 20\,\mathrm{GeV}$.
- The two leading jets within $|\eta| < 3.8$ are classified as the tagging jets by requiring $p_{T,j1} > 40\,\mathrm{GeV}$ and $p_{T,j2} > 20\,\mathrm{GeV}$.
- The two tagging jets are required to point in opposite detector hemispheres ($\eta_{j1} \times \eta_{j2} < 0$), to be well separated in η ($|\Delta\eta_{jj}| > 3.8$) and to have an invariant mass of $m_{jj} > 500\,\mathrm{GeV}$.

As shown in Table 6.7, the fraction of events in which a primary vertex can be reconstructed is considerably lower for $H \to WW$ events ($\sim 90\%$) than for $t\bar{t}$ events ($\sim 100\%$). Events without reconstructed primary vertex are retained in this study. In these events, track jets are reconstructed from all tracks in the event and no cut is applied on the primary vertex p_{T} fraction of calorimeter jets.

6.8.2 Calorimeter Jets

In Figures 6.31a and 6.32a, the performance of the central jet veto based on calorimeter jets within $|\eta| < 2.5$ is shown for $H \to WW$ and $t\bar{t}$ events without and with pile-up as a function of the cut applied on the jet transverse momentum. As expected, in the presence of pile-up a decreased central jet veto efficiency is observed in particular for low p_{T} cut values. The signal-to-background ratio improves with pile-up. However, for a central jet veto using calorimeter jets with $p_{\mathrm{T}} > 20\,\mathrm{GeV}$ lower efficiency of $(82.0 \pm 0.5)\%$ is observed for $H \to WW$ events with pile-up compared to $(93.2 \pm 0.3)\%$ for events without pile-up.

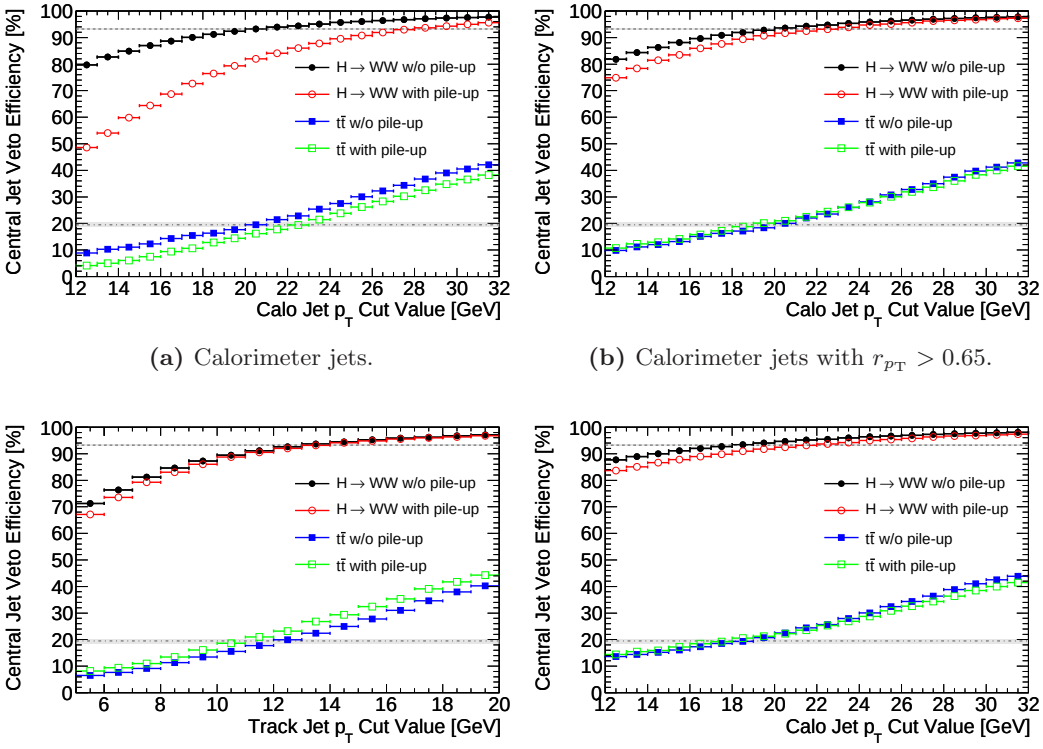

(a) Calorimeter jets.

(b) Calorimeter jets with $r_{p_T} > 0.65$.

(c) Track jets.

(d) Calorimeter jets with matching track jet.

Figure 6.31: Efficiency of the central jet veto for calorimeter and track jets within $|\eta| < 2.5$ for $H \rightarrow WW$ and $t\bar{t}$ events as a function the jet p_T cut. The distributions are shown for calorimeter jets (a), calorimeter jets with $r_{p_T} > 0.65$ (b), track jets (c) and calorimeter jets with matching track jet within $\Delta R < 0.3$ (d). The dashed and dashed-dotted lines represent the efficiencies and their uncertainties for calorimeter jets with $p_T > 20\,\text{GeV}$ in samples without pile-up (a).

Less sensitivity of the veto efficiency to pile-up is observed for higher p_T cut values with the drawback of a significantly decreased signal-to-background ratio.

6.8.3 Calorimeter Jets with Primary Vertex p_T Fraction Cut

The efficiency of the central jet veto and the corresponding signal-to-background ratio for $H \rightarrow WW$ and $t\bar{t}$ events with pile-up are shown in Figure 6.33 for calorimeter jets as a function of the cut on the primary vertex p_T fraction. For both $H \rightarrow WW$ and $t\bar{t}$ events the dependence of the central jet veto efficiency on the cut value is similar. The largest signal-to-background ratio is observed without r_{p_T} cut. In this case, also the lowest veto efficiency of $(82.0 \pm 0.5)\%$ is observed for $H \rightarrow WW$ events. Applying a cut on the primary vertex p_T fraction increases the selection efficiency for $H \rightarrow WW$ by a smaller factor than for $t\bar{t}$ events, leading to a decrease of the signal-to-background ratio. For a cut value of $r_{p_T} > 0.3$, a similar signal-to-background ratio is observed for events with pile-up as for events without pile-up and without cut on the primary vertex p_T fraction. In this case,

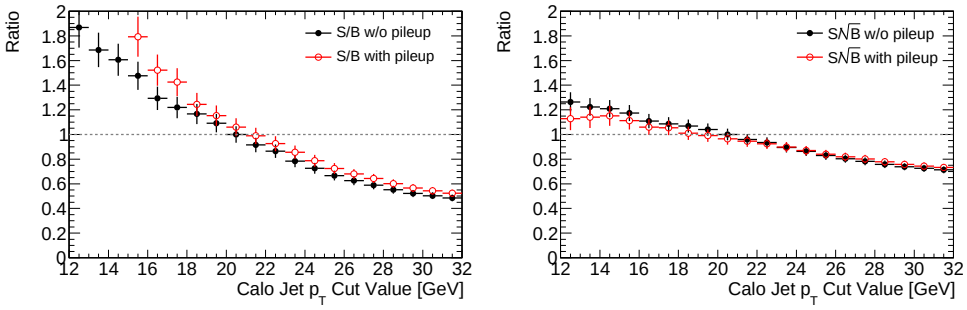

(a) Calorimeter jets.

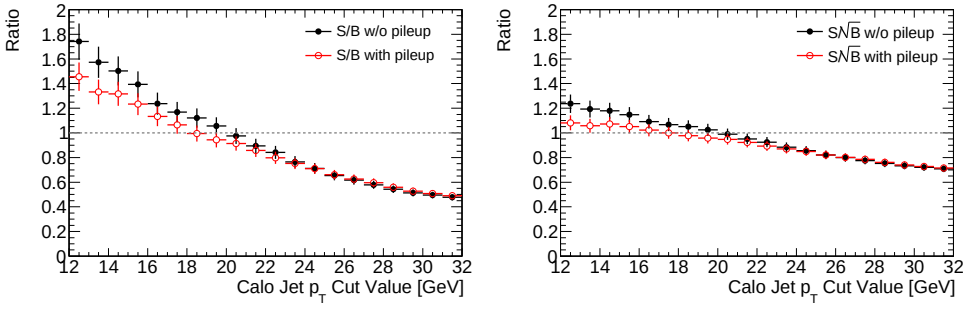

(b) Calorimeter jets with $r_{p_T} > 0.65$.

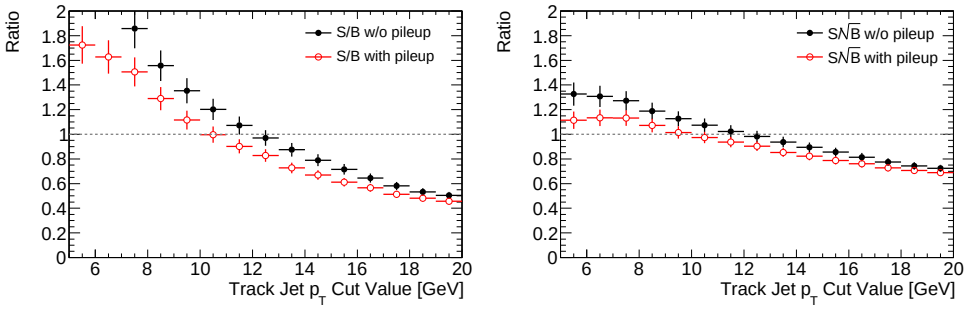

(c) Track jets.

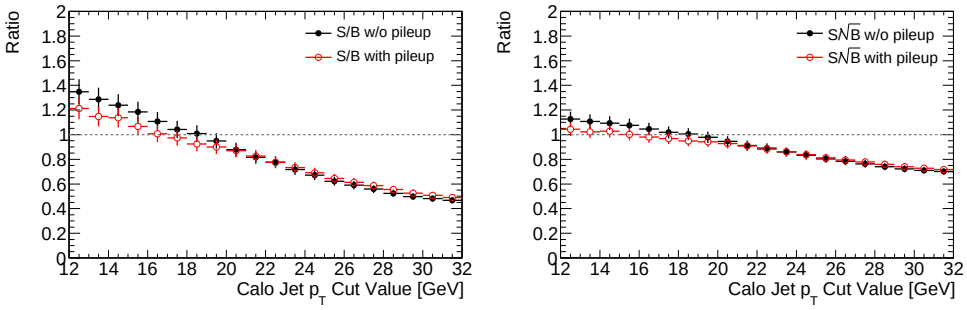

(d) Calorimeter jets with matching track jet within $\Delta R < 0.3$.

Figure 6.32: Signal-to-background ratio (left) and Gaussian signal significance (right) as a function of the jet p_T cut for $H \to WW$ and $t\bar{t}$ events for the different central jet veto methods within $|\eta| < 2.5$. The distributions are normalized to the values for calorimeter jets with $p_T > 20\,\text{GeV}$ in the samples without pile-up (a).

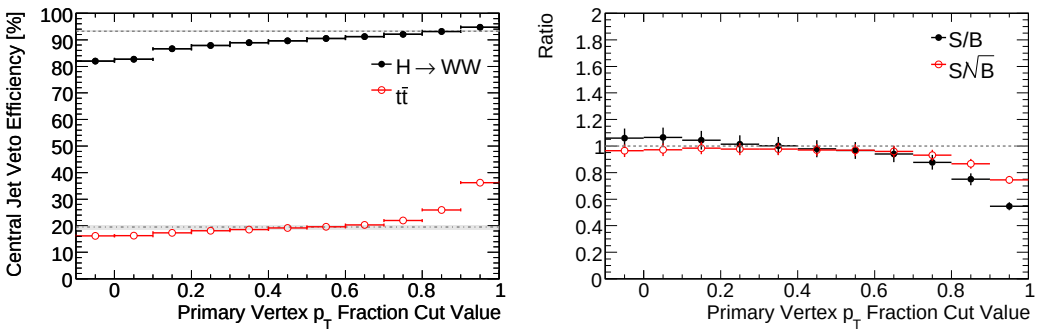

Figure 6.33: Efficiency of the central jet veto using calorimeter jets within $|\eta| < 2.5$ for $H \to WW$ and $t\bar{t}$ events with pile-up as a function of the cut on the primary vertex p_{T} fraction (left). The dashed and dashed-dotted lines represent the efficiencies and their uncertainties in the samples without pile-up for calorimeter jets with $p_{\mathrm{T}} > 20\,\mathrm{GeV}$ and without cut on the primary vertex p_{T} fraction. The figure on the right shows the impact of the $r_{p_{\mathrm{T}}}$ cut on the signal-to-background ratio and on the Gaussian signal significance for the samples with pile-up normalized to the values for calorimeter jets with $p_{\mathrm{T}} > 20\,\mathrm{GeV}$ in samples without pile-up and without $r_{p_{\mathrm{T}}}$ cut.

the veto efficiency for $H \to WW$ events with pile-up decreases by about 6% compared to not applying an $r_{p_{\mathrm{T}}}$ cut for events without pile-up. For cut values above $r_{p_{\mathrm{T}}} = 0.8$ the veto efficiency for $H \to WW$ events becomes insensitive to pile-up with the drawback of a 25% lower signal-to-background ratio. A cut value of $r_{p_{\mathrm{T}}} > 0.65$ has been chosen in order to reject central jets not originating from the primary interaction vertex. In Figures 6.31b and 6.32b, the central jet veto efficiencies and signal-to-background ratios, respectively, are shown as a function of the cut on the transverse momentum for calorimeter jets with $r_{p_{\mathrm{T}}} > 0.65$ in events without and with pile-up. With $r_{p_{\mathrm{T}}}$ cut, significantly less sensitivity of the central jet veto efficiencies to pile-up is observed. However, for low jet transverse momentum cuts, slightly decreased (increased) veto efficiencies are observed for $H \to WW$ ($t\bar{t}$) events with pile-up compared to events without pile-up, which lead to a small degradation of the signal-to-background ratio in the presence of pile-up.

6.8.4 Track Jets

Figures 6.31c and 6.32c show the efficiency and the signal-to-background ratio, respectively, as a function of the track jet p_{T} cut for a central jet veto based on track jets for $H \to WW$ and $t\bar{t}$ events without and with pile-up. In order to achieve comparable signal-to-background ratios for track and calorimeter jets without pile-up, the transverse momentum of the track jets has to be required to be above $p_{\mathrm{T}} = 11.7\,\mathrm{GeV}$. In this p_{T} cut range, the central jet veto efficiency in $H \to WW$ events is insensitive to pile-up while a slightly increased efficiency for $t\bar{t}$ events is observed, which leads to a small degradation of the signal-to-background ratio.

6.8.5 Calorimeter Jets with Matching Track Jet

Instead of directly using track jets for the central jet veto, they can also be used to tag calorimeter jets as originating from the primary interaction by requiring a matching track jet within $\Delta R < 0.3$. This method avoids the systematic uncertainties in the reconstruction efficiency and the calibration of the track jet transverse momentum but requires understanding of the matching efficiency between calorimeter and track jets. As shown in Figures 6.31d and 6.32d, larger veto efficiencies are observed for $H \to WW$ and $t\bar{t}$ events without pile-up due to matching inefficiency in particular at low transverse momenta. However, only little sensitivity of the veto efficiencies and of the signal-to-background ratio to pile-up is observed.

6.8.6 Comparison of the Central Jet Veto Methods

Figures 6.31 and Table 6.11 summarize the central jet veto efficiencies within $|\eta| < 2.5$ for the different methods introduced above. In Figures B.6 and B.7 in Appendix B, the corresponding central jet multiplicities within $|\eta| < 2.5$ are shown for $H \to WW$ and $t\bar{t}$ events without and with pile-up. For all methods exploiting tracking information little sensitivity to pile-up is observed.

The cut on the track jet transverse momentum of $p_{\mathrm{T}} > 11.7\,\mathrm{GeV}$ has been chosen such that the signal-to-background ratio agrees with the one obtained using calorimeter jets on the samples without pile-up. Also the central jet veto efficiencies agree well for using track and calorimeter jets in events without pile-up. While the central jet veto with track jets is insensitive to pile-up for $H \to WW$ events, a small impact is observed for $t\bar{t}$ events. Using calorimeter jets with cut on the primary vertex p_{T} fraction of $r_{p_{\mathrm{T}}} > 0.65$, only minor sensitivity to pile-up is observed for $H \to WW$ events accompanied by a slight decrease of the signal-to-background ratio in the presence of pile-up.

Due to matching inefficiencies, higher veto efficiencies are observed for calorimeter jets matched to a track jet in comparison to calorimeter jets in general. Only small sensitivity of the central jet veto efficiencies to pile-up are observed. In addition, the systematic uncertainties due to the calibration of the track jet transverse momentum can be avoided with this method. All methods presented are insensitive to different levels of pile-up for $t\bar{t}$ events.

In order to apply the central jet veto in the maximum acceptance range $|\eta| < 3.0$, the methods exploiting tracking and vertexing information within the inner detector acceptance $|\eta| < 2.5$ are combined with calorimeter jets in the region $2.5 < |\eta| < 3.0$. As shown in Table 6.11, this introduces a significant sensitivity of the central jet veto to pile-up. Therefore, it is favored to apply the central jet veto only in the region $|\eta| < 2.5$ covered by the inner detector employing the track-based methods introduced in order to reliably reject jets from additional minimum bias events.

The estimation of the central jet veto efficiencies for $t\bar{t}$ events with pile-up corresponding to an instantaneous luminosity of $10^{33}\,\mathrm{cm}^{-2}\,\mathrm{s}^{-1}$ suffers from low Monte Carlo statistics.

All methods studied for the central jet veto exploiting tracking and vertexing information show comparable performance. As shown in Section 6.7, the reconstruction efficiency of track jets is independent of the level of pile-up while the distribution of the primary vertex p_{T} fraction shows a significant sensitivity to the level of pile-up. Hence, the $r_{p_{\mathrm{T}}}$ cut value

for the calorimeter jets has to be determined individually for different levels of pile-up. Still, the pile-up dependence of the central jet veto based on calorimeter jets with $r_{p_{\mathrm{T}}}$ cut is small after applying the other event selection criteria.
For the pile-up levels studied, the central jet veto efficiency is improved by employing calorimeter jets with $r_{p_{\mathrm{T}}} > 0.65$ or track jets with transverse momenta above 11.7 GeV. A decision on which method to use for the data to reject jets from additional minimum bias events can only be made taking into account the systematic uncertainties which have to be determined from data. Prospects for the determination of the systematic uncertainties on the transverse momentum reconstruction and on the reconstruction efficiency for track jets are given in the following section.

6.9 Track Jet Performance Determination from Data

Due to large uncertainties in the modeling of the underlying event and the additional soft pp interactions, a reliable estimation of the systematic uncertainties on the central jet veto requires good understanding of minimum bias events and of the topology of the underlying event from collision data. Furthermore, in order to estimate systematic uncertainties in the track jet reconstruction for the central jet veto, the transverse momentum and the reconstruction efficiency of track jets have to be measured with respect to the values for calorimeter jets with collision data, since they cannot reliably be determined from Monte Carlo data. This section gives the prospects for the determination of the track jet performance from data.
Several processes can be used to measure the calorimeter jet energy scale in the data. For instance, according to Reference [92] the jet energy scale is determined with an expected uncertainty of about 2% with an integrated luminosity of $50\,\mathrm{pb}^{-1}$ using the invariant mass distribution of hadronical W decays in $t\bar{t}$ events. Similar methods can be used to calibrate the track jet transverse momentum relative to calorimeter jets. However, this method requires a reliable and well understood b-tagging in order to suppress combinatorial QCD and $W+\mathrm{jets}$ backgrounds which will not be available for the early data taking phase. Therefore, these methods can only be applied at a later stage when detector effects have been sufficiently understood.
This can be avoided by employing jets from $\gamma/Z+\mathrm{jet}$ or QCD di-jet events where the transverse momenta of the two final-state objects should be exactly balanced. QCD di-jet events have the larger cross-section (above $10^9\,\mathrm{pb}$) but the jets originate predominantly from the hadronization of gluons in contrast to the jets from vector-boson fusion Higgs and $t\bar{t}$ production which are mainly initiated by quarks. Since quarks and gluons have different coupling strengths for gluon emission, gluon jets tend to be broader and their track multiplicity tends to be higher compared to quark jets [90]. Therefore, QCD di-jet events provide only a first step towards the track jet calibration for vector-boson fusion $H \to WW$ and $t\bar{t}$ events[3].
Jets in $\gamma/Z+\mathrm{jet}$ events are predominantly initiated by quarks and allow for a calibration of the jet energy by means of the transverse momentum balance between the jet and the vector boson. However, this method is limited by systematic uncertainties on

[3] A comparison of the track jet reconstruction performance for quark and gluon initiated jets at the CMS experiment is presented in Reference [93].

		$H \to WW$		$t\bar{t}$		
		w/o pile-up	10^{32} cm^{-2} s^{-1}	w/o pile-up	10^{32} cm^{-2} s^{-1}	10^{33} cm^{-2} s^{-1}
Calo jets	$\|\eta\| < 2.5$	93.2 ± 0.3	82.0 ± 0.5	19.5 ± 0.9	16.2 ± 0.8	14.1 ± 1.4
Calo jets ($r_{p_{\mathrm{T}}} > 0.65$)	$\|\eta\| < 2.5$	93.6 ± 0.3	91.7 ± 0.3	20.1 ± 0.9	21.0 ± 0.9	21.2 ± 1.7
Track jets	$\|\eta\| < 2.5$	92.3 ± 0.3	91.6 ± 0.3	19.3 ± 0.9	22.4 ± 0.9	17.5 ± 1.6
Calo jets (track jet match)	$\|\eta\| < 2.5$	94.6 ± 0.3	92.5 ± 0.3	22.5 ± 1.0	22.2 ± 0.9	22.2 ± 1.7
Calo jets	$\|\eta\| < 3.0$	90.5 ± 0.4	76.3 ± 0.5	17.2 ± 0.9	13.2 ± 0.7	12.7 ± 1.4
Calo jets ($r_{p_{\mathrm{T}}} > 0.65$)	$\|\eta\| < 3.0$	90.9 ± 0.4	83.1 ± 0.5	17.7 ± 0.9	16.6 ± 0.8	18.3 ± 1.6
Track jets	$\|\eta\| < 3.0$	89.8 ± 0.4	83.2 ± 0.5	17.1 ± 0.9	17.8 ± 0.8	15.6 ± 1.5
Calo jets (track jet match)	$\|\eta\| < 3.0$	91.9 ± 0.3	83.9 ± 0.5	19.8 ± 0.9	17.7 ± 0.8	19.4 ± 1.6
Calo jets	$2.5 < \|\eta\| < 3.0$	97.0 ± 0.2	90.3 ± 0.4	89.0 ± 0.7	80.0 ± 0.9	85.2 ± 1.5

Table 6.11: Central jet veto efficiencies [%] for the different methods discussed in the text using jets within $|\eta| < 2.5$ (first part). Transverse momenta above 20 GeV and 11.7 GeV are required for calorimeter and track jets, respectively. The values quoted for $|\eta| < 3.0$ (second part) exploit tracking and vertexing information within $|\eta| < 2.5$ combined with a standard calorimeter central jet veto for $2.5 < |\eta| < 3.0$ (last row). The errors quoted are statistical.

MC data sample	p_{T} range [GeV]	Generator	Cross section [pb]	Events	Reco. tag
Di-jet (J1)	17 – 35	Pythia	$8.7 \cdot 10^8$	49 400	r635
Di-jet (J2)	35 – 70	Pythia	$5.6 \cdot 10^7$	49 900	r635
Di-jet (J3)	70 – 140	Pythia	$3.2 \cdot 10^6$	49 900	r635
Di-jet (J4)	140 – 280	Pythia	$1.5 \cdot 10^5$	49 900	r635
γ + jet	> 17	Pythia	$2.9 \cdot 10^5$	50 000	r635

Table 6.12: QCD di-jet and γ + jet Monte Carlo data samples used to study the prospects for the determination of the track jet reconstruction performance with collision data.

the p_{T} balance which are typically on the order of $5 - 10\%$ at 20 GeV and on the percent level at 100 GeV [94]. Leptonic Z-boson decays can be reconstructed with very low background [95] because of the very clean lepton identification in ATLAS. Due to the lower cross section of Z + jet production with $Z \to ee, \mu\mu$ (500 pb) compared to γ + jet production (above $2.6 \cdot 10^5$ pb), a relatively large data sample is needed for a reliable jet calibration with Z + jet events. Reference [94] quotes a statistical uncertainty of 1% on the calorimeter jets energy scale for $p_{\mathrm{T}} < 500$ GeV from Z + jet events corresponding to an integrated luminosity of 300 pb^{-1}. On the other hand, γ + jet events allow for a calibration of calorimeter jets with transverse momenta up to 150 GeV with a statistical uncertainty below 1% already for 10 pb^{-1} [94]. Due to the decreasing cross sections for larger jet transverse momenta, larger statistical uncertainties are expected for the calibration of high-p_{T} jets. In addition, the jet calibration using γ + jet events seriously suffers from the background of QCD jets, in particular at low p_{T}.
The Monte Carlo data samples used for the study of the track jet p_{T} calibration with QCD di-jet and γ + jet events without pile-up are listed in Table 6.12.
Figure 6.34 shows ratio of the transverse momenta of track and calorimeter jets in QCD di-jet and γ + jet events in comparison to vector-boson fusion $H \to WW$ and $t\bar{t}$ events. While the distributions as a function of the calorimeter jet p_{T} agree well between γ + jet, $H \to WW$ and $t\bar{t}$ events, differences are observed for QCD di-jet events for transverse momenta between 20 and 60 GeV, the interesting p_{T} range for this analysis.

6.10 Conclusions

Pile-up of additional inelastic pp collisions will deteriorate the discovery potential of the search for Higgs boson production in association with two jets by deteriorating the jet and $E_{\mathrm{T}}^{\mathrm{miss}}$ reconstruction in the calorimeter. In this chapter, the impact of pile-up on the vector-boson fusion $H \to WW$ analysis has been evaluated for pile-up levels of on average 4.1 and 6.9 events per bunch crossing corresponding to instantaneous luminosities of 10^{32} cm^{-2} s^{-1} and 10^{33} cm^{-2} s^{-1}, respectively.
The impact of pile-up is twofold. First, the higher noise level in the calorimeter results in a degradation of the $E_{\mathrm{T}}^{\mathrm{miss}}$ resolution deteriorating the event selection efficiencies for variables which are calculated based on the missing transverse energy such as the transverse mass m_{T} of the Higgs boson and the total transverse momentum $p_{\mathrm{T}}^{\mathrm{tot}}$. Second, increased jet energies and additional jets from minimum bias events deteriorate the jet selection

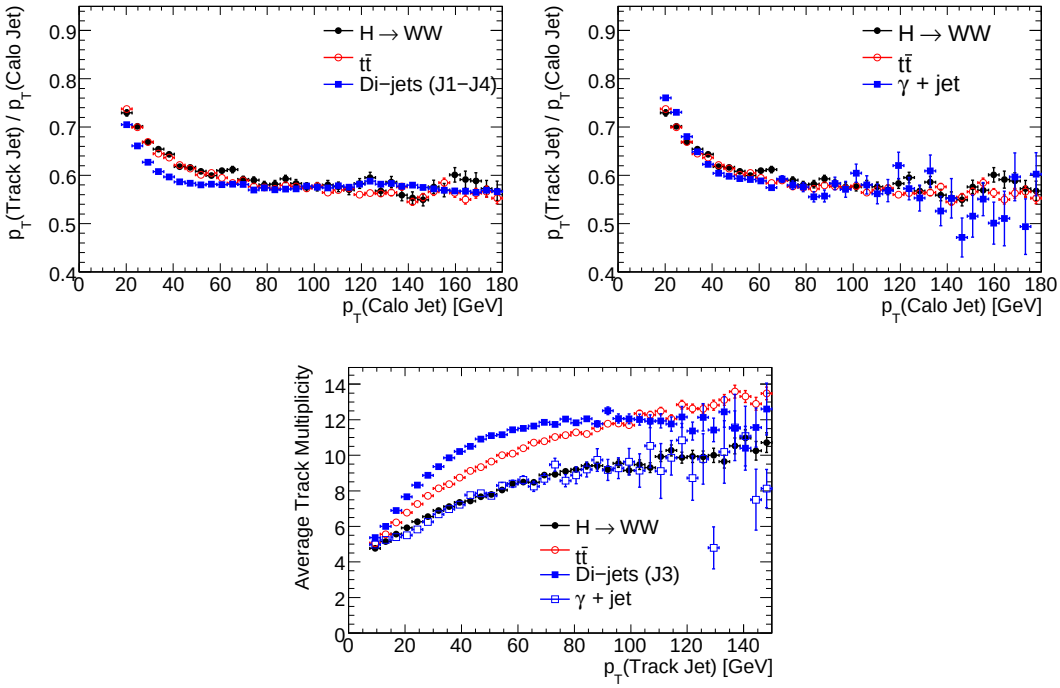

Figure 6.34: Ratio of the transverse momenta of track and matching calorimeter jets as a function of the calorimeter jet p_{T} for QCD di-jet (left) and γ + jet events (right) in comparison to $H \rightarrow WW$ and $t\bar{t}$ events. The lower plot shows the average track multiplicity as a function of the track jet transverse momentum.

performance, in particular the efficiency of the central jet veto.
Exploiting tracking and vertexing information allows for a decreased sensitivity to pile-up effects. Different methods for rejecting jets from additional minimum bias events have been studied: the reconstruction of jets solely from inner detector tracks (track jets) and the association of calorimeter jets to tracks originating from the primary interaction vertex by means of a cut on the primary vertex p_{T} fraction. Finally, track jets can also be employed to tag calorimeter jets as originating from the hard-scattering process. These track-based methods are restricted to jets within the geometrical acceptance of the inner detector $|\eta| < 2.5$.
As shown in this chapter, the different methods show only small sensitivity to pile-up and allow for improved central jet veto efficiencies for jets within $|\eta| < 2.5$. As can be seen in Table 6.13, employing for instance calorimeter jets with matching track jet, almost no differences are observed between the cross section times selection efficiency for $H \rightarrow WW$ events without and with pile-up after the central jet veto while they are larger for $t\bar{t}$ events due to the impact of pile-up on the tagging jet selection. This can partially be avoided by requiring also for the tagging jets within $|\eta| < 2.5$ matching track jets, whereas calorimeter jets alone are used for larger $|\eta|$. The corresponding event selection efficiencies are shown in Table B.1 in Appendix B. Due to matching inefficiencies between calorimeter and track jets, larger central jet veto efficiencies are observed when using calorimeter jets matched to a track jet. Restricting the central jet veto to jets within the acceptance of the inner detector further decreases the rejection power for the $t\bar{t}$ background. This can be avoided by using in addition calorimeter jets in the region $2.5 < |\eta| < 3.0$ for the central jet veto with the drawback of introducing a sensitivity to pile-up.
In comparison to Table 6.6, the insensitivity of the central jet veto efficiency to pile-up shown in Table 6.13 results in a significantly increased dependence of the total transverse momentum $p_{\mathrm{T}}^{\mathrm{tot}}$ on the presence of pile-up, in particular for $H \rightarrow WW$ events. Hence, in order for the event selection to be robust against pile-up, the missing transverse energy reconstruction in the presence of pile-up also has to be improved, for instance by exploiting tracking and vertexing information. In addition to track-based methods, improved calorimeter cluster reconstruction algorithms accounting for the higher noise level in the calorimeter in the presence of pile-up [96] can also reduce the sensitivity of the jet and the $E_{\mathrm{T}}^{\mathrm{miss}}$ reconstruction to pile-up. This is of particular importance in the forward regions of the detector ($|\eta| > 2.5$) beyond the acceptance of the inner detector and, therefore, for the tagging jet selection in $t\bar{t}$ events.
It should be noted that in comparison to the cone algorithm employed for calorimeter jet reconstruction in this study, alternative jet reconstruction algorithms such as the anti-k_T algorithm show reduced sensitivity to pile-up [97]. However, calorimeter jets reconstructed with the anti-k_T algorithm could not be considered here because the available Monte Carlo data samples only contain jets reconstructed with the cone algorithm.

	$H \to WW$		$t\bar{t}$	
	without pile-up	with pile-up	without pile-up	with pile-up
Cross section	74.04	74.04	217 600	217 600
Trigger	67.29 ± 0.11	66.25 ± 0.11	$137\,800 \pm 87$	$134\,000 \pm 86$
$N(e+\mu) \geq 2$	34.17 ± 0.18	32.17 ± 0.18	$9\,982 \pm 38$	$9\,338 \pm 36$
Lepton charge	34.10 ± 0.18	32.11 ± 0.18	$9\,926 \pm 37$	$9\,288 \pm 36$
$N(\text{jets}) \geq 2$	24.86 ± 0.17	25.77 ± 0.18	$9\,115 \pm 36$	$8\,768 \pm 35$
$p_T(\text{jet1}) > 40\,\text{GeV}$	22.85 ± 0.17	23.67 ± 0.17	$8\,668 \pm 35$	$8\,388 \pm 34$
$\eta_{j1} \times \eta_{j2} < 0$	19.70 ± 0.16	19.76 ± 0.16	$3\,924 \pm 24$	$3\,818 \pm 23$
$\lvert\Delta\eta_{jj}\rvert > 3.8$	14.11 ± 0.15	14.29 ± 0.15	403.1 ± 7.7	439.8 ± 8.0
$m_{jj} > 500\,\text{GeV}$	11.76 ± 0.14	12.01 ± 0.14	279.3 ± 6.4	299.0 ± 6.6
Central jet veto	11.13 ± 0.13	11.11 ± 0.13	62.82 ± 3.05	66.43 ± 3.10
$p_{\text{T}}^{\text{tot}} < 30\,\text{GeV}$	10.39 ± 0.13	9.41 ± 0.12	36.30 ± 2.32	31.26 ± 2.13
b-jet veto	9.74 ± 0.13	8.61 ± 0.12	17.19 ± 1.60	15.78 ± 1.51

(a) Cross section times efficiency [fb].

Trigger	90.9 ± 0.1	89.5 ± 0.2	63.3 ± 0.1	61.6 ± 0.1
$N(e+\mu) \geq 2$	50.8 ± 0.3	48.6 ± 0.3	7.2 ± 0.1	7.0 ± 0.1
Lepton charge	99.8 ± 0.1	99.8 ± 0.1	99.4 ± 0.1	99.5 ± 0.1
$N(\text{jets}) \geq 2$	72.9 ± 0.3	80.2 ± 0.3	91.8 ± 0.1	94.4 ± 0.1
$p_T(\text{jet1}) > 40\,\text{GeV}$	91.9 ± 0.2	91.9 ± 0.2	95.1 ± 0.1	95.7 ± 0.1
$\eta_{j1} \times \eta_{j2} < 0$	86.2 ± 0.3	83.5 ± 0.3	45.3 ± 0.2	45.5 ± 0.2
$\lvert\Delta\eta_{jj}\rvert > 3.8$	71.7 ± 0.4	72.3 ± 0.4	10.3 ± 0.2	11.5 ± 0.2
$m_{jj} > 500\,\text{GeV}$	83.3 ± 0.4	84.1 ± 0.4	69.3 ± 0.9	68.0 ± 0.8
Central jet veto	94.6 ± 0.3	92.5 ± 0.3	22.5 ± 1.0	22.2 ± 0.9
$p_{\text{T}}^{\text{tot}} < 30\,\text{GeV}$	93.4 ± 0.3	84.7 ± 0.5	57.8 ± 2.4	47.1 ± 2.3
b-jet veto	93.7 ± 0.3	91.5 ± 0.4	47.3 ± 3.2	50.5 ± 3.4
total	13.1 ± 0.2	11.6 ± 0.2	$(7.9 \pm 0.7) \cdot 10^{-3}$	$(7.3 \pm 0.7) \cdot 10^{-3}$

(b) Relative selection efficiencies [%].

Table 6.13: Evolution of the cross section times selection efficiency and the relative selection efficiencies for events without and with pile-up omitting cuts on the kinematic relations of the leptons. Only calorimeter jets with $p_{\text{T}} > 20\,\text{GeV}$ and $|\eta| < 2.5$ with a matching track jet are employed for the central jet veto.

Chapter 7

Higgs Discovery Potential

In this chapter, the impact of the systematic uncertainties on the event selection efficiencies is studied and the discovery potential of the search for the Standard Model Higgs boson in decays into two W bosons is evaluated. As discussed in the previous chapters, only the Higgs production in association with two jets is considered which is dominated by the vector-boson fusion production with a smaller contribution from gluon fusion production. Section 7.1 introduces the statistical methods employed for the evaluation of the achievable exclusion limit and signal significance. The impact of the theoretical and experimental systematic uncertainties on the event selection efficiencies is discussed in Section 7.2. Section 7.2.3 provides the prospects for the estimation of the different background contributions from data control samples. Finally, in Section 7.3 the expected exclusion limit and signal significance are given taking into account the systematic uncertainties and the impact of pile-up.

7.1 Statistical Methods

In this thesis, the expected exclusion limit and signal significance of the Higgs boson search discussed in the previous chapters are estimated by means of the *profile likelihood ratio* method. The following introduction to the statistical methods employed is based on References [98, 99].

7.1.1 Hypothesis Testing

The statistical interpretation of measurements often involves the test of certain hypotheses. Here, the background-only hypothesis, i. e. assuming the absence of Standard Model Higgs boson production is referred to as H_0 hypothesis while H_1 denotes the hypothesis of Higgs boson production on top of the background (signal + background hypothesis).
The total number of observed events n is assumed to be distributed according to a Poisson distribution with the mean value:

$$E[n] = \mu s + b \quad \text{with} \quad s = \mathcal{L}\varepsilon\sigma\mathcal{B}, \tag{7.1}$$

where $\mathcal{L}$ denotes the integrated luminosity, ε the signal selection efficiency, and σ and $\mathcal{B}$ the production cross section and branching fraction of the Higgs boson, respectively. s

and b are the expected numbers of signal and background events. μ is defined as the signal strength: $\mu = 0$ corresponds to the absence of a signal and $\mu = 1$ to a signal production rate as expected in the Standard Model.
At a fixed Higgs boson mass, the only parameter of interest is the signal strength μ whereas all other free parameters, describing for instance the numbers of events expected from the individual background processes or the shapes of the signal and background distributions of discriminating variables, are referred to as *nuisance parameters*. Since in this analysis the Higgs boson production is studied in vector-boson fusion at low integrated luminosities, only the numbers of expected and observed events are taken into account without exploiting additional information on the shape of discriminating variables. The expected number of background events b represents then the only nuisance parameter. It can either be estimated from background Monte Carlo data or from a control data sample. The number of background events m obtained by such a subsidiary measurement is also assumed to obey the Poisson distribution with mean value $E[m] = \tau b$. The scaling factor τ represents the ratio of the number of background Monte Carlo events or of background events observed in the control data sample to the number of background events expected in the signal region. A likelihood function is then defined as the product of the two Poisson probabilities,

$$L(\mu, b) = \frac{(\mu s + b)^n}{n!} e^{-(\mu s + b)} \frac{(\tau b)^m}{m!} e^{-\tau b}. \tag{7.2}$$

Here, τ is assumed to be exactly known. If different background contributions are estimated in different control regions, the second term becomes a product of the corresponding Poisson probabilities. When the background contribution is estimated by a subsidiary measurement with sufficient statistics, the Poisson probability can be replaced by a Gaussian distribution of the number of background events in the signal region n_b with standard deviation σ_b,

$$L(\mu, b) = \frac{(\mu s + b)^n}{n!} e^{-(\mu s + b)} \frac{1}{\sigma_b \sqrt{2\pi}} e^{-\frac{(n_b - b)^2}{2\sigma_b^2}}. \tag{7.3}$$

This allows for taking into account systematic uncertainties on the predicted number of background events. In order to take into account uncertainties in the estimation of the signal efficiency ε, the likelihood functions specified above are multiplied by a Gaussian probability density function centered at ε with a width corresponding to the uncertainty. A hypothetical value of μ is tested by means of the profile likelihood ratio

$$\lambda(\mu) = \frac{L(\mu, \hat{\hat{b}})}{L(\hat{\mu}, \hat{b})}, \tag{7.4}$$

with $\hat{\mu}$ and $\hat{b}$ representing the maximum likelihood estimators of μ and b. $\hat{\hat{b}}$ denotes the conditional maximum-likelihood estimator of b when maximizing L for a specific value of μ. $\hat{\hat{b}}$ therefore depends on μ. In a more generalized notation, the expected number of background events b is replaced by a vector $\boldsymbol{\theta}$ representing the full set of nuisance parameters taking into account the different background contributions and shape parameters. $\lambda(\mu)$ in Equation 7.4 always fulfills $0 \leq \lambda(\mu) \leq 1$, with $\lambda(\mu) = 1$ implying a good agreement between data and the hypothetical value of μ. The variable

$$q_\mu = -2 \ln \lambda(\mu) \tag{7.5}$$

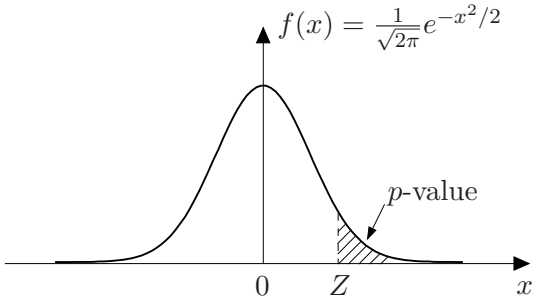

Figure 7.1: Correspondence between the signal significance Z and the p-value for a standard Gaussian probability distribution function.

is used to evaluate the agreement between data and the hypothetical value of μ. q_μ follows a distribution $f(q_\mu|\mu')$ where μ' is the true strength parameter value and μ the hypothetical value. Large (low) values of q_μ imply poor (good) agreement.

7.1.2 Establishing Discovery

A discovery of the Higgs boson is established by rejecting the background-only hypothesis H_0 corresponding to the signal strength $\mu = 0$. A low value of $\lambda(\mu = 0)$ is expected if the data contain signal events.
The discovery potential is estimated by means of the statistical significance Z which is related to the probability of wrongly rejecting the background-only hypothesis although it is true. In the case of negligible systematic uncertainties, this corresponds to the Poisson probability of observing $n' \geq n$ events in the absence of signal events

$$p = \int_n^\infty P(n'|b)dn' \quad \text{with} \quad P(n'|b) = \frac{b^{n'}}{n'!}e^{-b}, \tag{7.6}$$

which is referred to as the p-value. The statistical significance is defined as the number of standard deviations Z corresponding to a one-sided tail-area equal to the p-value for a Gaussian distribution centered at zero with $\sigma = 1$ as illustrated in Figure 7.1. Therefore, the p-value and the statistical significance are related according to

$$p = \int_Z^\infty \frac{1}{\sqrt{2\pi}} e^{-\frac{x^2}{2}} dx = 1 - \Phi(Z) \tag{7.7}$$

with Φ being the cumulative distribution of the normalized Gaussian function. A signal significance of $Z = 5$ corresponding to a p-value of $2.87 \cdot 10^{-7}$ is required in order to claim a discovery.
However, correct treatment of systematic uncertainties is not easily possible in case of a Poissonian distribution. Instead, for this analysis the p-value taking into account systematic uncertainties is determined by means of the profile likelihood ratio $\lambda(\mu)$ and the corresponding q_μ variable (Equation 7.5) according to:

$$p_\mu = \int_{q_{\mu,obs}}^\infty f(q_\mu|\mu)dq_\mu, \tag{7.8}$$

where $f(q_\mu|\mu)$ is the probability distribution function of q_μ. p_μ is a measure of the compatibility between the data with an observed q_μ value of $q_{\mu,obs}$ and the hypothetical value of μ. Hence, the level of agreement between data and the background-only hypothesis is quantified by:

$$p_0 = \int_{q_{0,obs}}^{\infty} f(q_0|0)dq_0, \tag{7.9}$$

where $q_{0,obs}$ refers to the observed value of q_0. Exploiting Equation 7.7, this can approximately be translated into the statistical significance according to

$$Z = \sqrt{q_{0,obs}} = \sqrt{-2\ln\lambda(\mu = 0)}. \tag{7.10}$$

In this thesis, the likelihood ratio is computed taking into account Gaussian systematic uncertainties in the expected number of background events according to Equation 7.3.

7.1.3 Setting Exclusion Limits

Alternatively to establishing a Higgs discovery, exclusion limits are determined by rejecting the signal + background hypothesis H_1 which corresponds to a non-zero signal strength ($\mu > 0$). Exclusion limits are defined by an upper limit on the μ value at a particular confidence level (CL). Typically a confidence level of CL=95% is used. The p-value defined in Equation 7.8 is computed for different values of μ, and the range $[\mu_{low}, \mu_{up}]$ for which p_μ is larger than or equal to 1-CL defines the confidence interval for μ. The upper limit of the Higgs production cross section relative to the Standard Model prediction corresponds to the μ_{up} value with $\mu \leq \mu_{up}$ at 95% CL. For the computation of the exclusion limits the TRolke package [100, 101] provided by the ROOT analysis frame work [102] was employed.

7.2 Systematic Uncertainties

This section summarizes the systematic uncertainties on the expected signal and background cross sections after applying all event selection criteria. The systematic uncertainties to be taken into account in the estimation of the Higgs discovery potential comprise theoretical uncertainties in the predicted signal and background production cross sections and experimental uncertainties in the event selection efficiencies due to the limited Monte Carlo statistics and imperfect knowledge of the detector performance.

7.2.1 Theoretical Uncertainties

The predicted production cross sections for signal and background processes are affected by theoretical uncertainties in the knowledge of the parton distribution functions, in the description of the parton shower and the underlying event, and due to dependence on the renormalization and factorization scales.
The theoretical uncertainties on the production cross sections of the dominant background processes quoted in References [103, 104] range from approximately 4% for the Wt and WW processes to 10% for the W and $t\bar{t}$ processes.
The uncertainties in the next-to-leading order QCD calculations of the vector-boson fusion Higgs production cross section due to renormalization and factorization scale dependence

and due to the uncertainty in the parton distribution functions have been estimated to be 2% and 3.5%, respectively [105]. In addition, a systematic uncertainty of 3% is assigned in order to account for next-to-leading order electroweak corrections [106]. The scale uncertainty on the parton-level central jet veto survival probability is estimated to be 1% [107].
The uncertainties related to the parton-shower, the hadronization and the underlying event, in particular their impact on the central jet veto survival probability, cannot be predicted with comparable accuracy. Monte Carlo simulations of the underlying event are based on extrapolations from the cross sections measured at the Tevatron at a center-of-mass energy of $\sqrt{s} = 1.8\,\text{TeV}$, resulting in large and unknown uncertainties (see Section 2.4). Hence, the underlying event has to be measured with LHC data which allows for tuning of the Monte Carlo simulation to the data. The uncertainty of this procedure is not yet known. It is assumed to be smaller than the systematic errors due to detector effects. Therefore, following Reference [108], a total theoretical uncertainty of 10% is assigned to the vector-boson fusion production cross section.
For gluon fusion Higgs production, the renormalization and factorization scale dependence results in an uncertainty of 10% in the prediction of the cross section [109] while the uncertainties from the parton distribution functions have been calculated to be 5% [1].

7.2.2 Experimental Uncertainties

Uncertainties in the Monte Carlo Simulation

In addition to the theoretical uncertainties, a systematic uncertainty has to be assigned to the event selection efficiencies due to the limited Monte Carlo statistics. The expected cross sections of the signal and dominant background processes as well as the corresponding Monte Carlo statistical errors are quoted in the second column of Table 7.2. As stated in Section 5.6.2, the total contribution of $W+\text{jets}$, $Z+\text{jets}$ and WZ/ZZ processes to the Higgs search at $m_H = 170\,\text{GeV}$ amounts to approximately $(0.37 \pm 0.19)\,\text{fb}$ which has been estimated assuming factorization of the selection criteria. For these background processes, the same dependence on the cut on the transverse mass of the Higgs boson is assumed as determined for the dominant background processes. It should be noted that the contribution of $W+\text{jets}$ events strongly depends on the misidentification rate of jets as leptons which has to be measured with data. Methods to estimate the $W+\text{jets}$ background on real data are currently being developed and are briefly summarized in Section 7.2.3.
As shown in Section 5.6.1, within statistical uncertainties an acceptable agreement between $t\bar{t}$ events from fast and full detector simulation is observed. Thus, no additional systematic uncertainty is assigned because the fast detector simulation has been used.

Uncertainties in the Detector Performance

The prediction of the signal and background event selection efficiencies with Monte Carlo data has to account for the imprecise knowledge of the detector response, for instance due to effects of the misalignment of detector components or additional material within the detector which is not included in the detector simulation. The detector performance can be measured with data with an uncertainty depending on the recorded integrated

Observable	Relative uncertainty
Electron energy scale	$\pm 0.5\,\%$
Electron energy resolution	$\sigma(E_{\mathrm{T}}) \oplus 1.06 \cdot 10^{-2} E_{\mathrm{T}}$
Electron reconstruction efficiency	$-0.5\,\%$
Muon energy scale	$\pm 0.3\,\%$
Muon momentum resolution	$\sigma(1/p_{\mathrm{T}}) \oplus 0.011/p_{\mathrm{T}} \oplus 1.7 \cdot 10^{-4}$
Muon reconstruction efficiency	$-0.3\,\%$
Jet energy scale	$\pm 7.0\,\%$ ($\lvert\eta\rvert < 3.2$)
	$\pm 15.0\,\%$ ($\lvert\eta\rvert > 3.2$)
Jet energy resolution	$\sigma(E) \oplus 0.45\sqrt{E}$ ($\lvert\eta\rvert < 3.2$)
	$\sigma(E) \oplus 0.67\sqrt{E}$ ($\lvert\eta\rvert > 3.2$)
b-tagging efficiency	$\pm 6\%$
b-tagging light-jet rejection	$\pm 10\%$

Table 7.1: Systematic uncertainties in the knowledge of the detector response corresponding to an integrated luminosity of $1\,\mathrm{fb}^{-1}$ according to Reference [110].

luminosity. The systematic uncertainties on the reconstruction efficiency, the energy scale and resolution of physics objects estimated for different integrated luminosities are summarized in Reference [110]. Table 7.1 quotes the systematic uncertainties corresponding to an integrated luminosity of $1\,\mathrm{fb}^{-1}$.

The systematic uncertainties on the event selection efficiencies are obtained by independently varying the reconstruction efficiencies, energy scales and resolutions of electrons, muons and jets. The reconstruction efficiencies are only decreased by randomly rejecting reconstructed objects while the energy resolutions are smeared according to the uncertainties specified in Table 7.1. The measurement of the energy scale is assumed to be systematically biased. For instance for jets, this is taken into account by increasing or decreasing the energy of all jets by 7% for $|\eta| < 3.2$ and by 15% for $|\eta| \geq 3.2$. The assumed systematic uncertainties on the jet energy scale are very conservative for an integrated luminosity of $1\,\mathrm{fb}^{-1}$. The uncertainty on the performance of the b-tagging algorithm is mainly caused by misalignment of the inner detector. The imperfect knowledge of the tagging efficiency of b-jets and of the rejection rate of light jets is taken into account by randomly increasing and decreasing the b-tag weights of the respective jets.

The impact of the systematic uncertainties on the measurement of the missing transverse energy is determined by recalculating the $E_{\mathrm{T}}^{\mathrm{miss}}$ vector after modifying the reconstruction performance of the different physics objects. It is assumed that the $E_{\mathrm{T}}^{\mathrm{miss}}$ scale can be measured with an accuracy of 5%. Thus, the $E_{\mathrm{T}}^{\mathrm{miss}}$ vector is recalculated only with a 5% shift of the jet energy scale. Table 7.2 summarizes the relative systematic changes of the expected cross sections after applying all event selection criteria for the signal process with different Higgs boson masses as well as for the dominant background processes.

The largest impact on the event selection efficiencies for signal and background processes is observed for the systematic uncertainty on the jet energy scale which decreases the event

	Nominal cross section [fb]	Systematic effect [%]																
		Electrons				Muons				Jets			*b*-tagging				Sum	
		$\mathcal{S}-$	$\mathcal{S}+$	$\mathcal{R}$	$\mathcal{E}$	$\mathcal{S}-$	$\mathcal{S}+$	$\mathcal{R}$	$\mathcal{E}$	$\mathcal{S}-$	$\mathcal{S}+$	$\mathcal{R}$	$\mathcal{E}-$	$\mathcal{E}+$	$r-$	$r+$		
H (110 GeV)	0.17 ± 0.02	2.0	0.0	0.7	0.0	0.0	0.0	−2.6	0.0	−22.3	−1.2	−2.0	0.7	0.0	0.0	0.0	−22.6	+ 2.2
H (120 GeV)	0.66 ± 0.04	0.1	0.0	−0.7	−0.1	0.6	0.1	0.9	0.0	−27.3	−5.1	1.1	0.0	0.0	−0.1	0.5	−27.3	+ 1.6
H (130 GeV)	1.78 ± 0.04	−0.1	0.1	0.3	−0.4	0.2	−0.2	−0.6	−0.2	−25.5	−4.0	−1.5	0.1	−0.1	−0.1	0.2	−25.6	+ 0.5
H (140 GeV)	3.39 ± 0.15	−0.1	0.0	0.7	−0.6	−0.1	−0.2	−0.3	−0.8	−29.5	−4.9	−2.7	0.3	0.0	0.0	0.2	−29.7	+ 0.8
H (150 GeV)	4.01 ± 0.29	0.0	0.3	0.9	0.0	0.0	0.0	0.3	−0.6	−26.5	−8.2	−4.2	0.3	0.0	0.0	0.6	−26.8	+ 1.2
H (160 GeV)	7.17 ± 0.47	0.0	0.0	0.2	0.0	0.2	−0.6	−0.4	−0.4	−25.8	−17.3	−4.9	0.0	−0.2	0.0	0.4	−26.3	+ 0.5
H (165 GeV)	8.54 ± 0.19	−0.0	−0.1	0.2	−0.4	0.2	−0.4	−0.1	−0.2	−27.2	−6.0	−0.2	0.1	−0.1	0.0	0.2	−27.3	+ 0.3
H (170 GeV)	8.11 ± 0.16	0.0	−0.1	−0.4	−0.3	0.2	−0.5	−0.5	−0.4	−27.5	−10.4	−2.3	0.1	−0.1	−0.1	0.4	−27.6	+ 0.5
H (180 GeV)	6.91 ± 0.50	0.0	0.0	0.4	−1.5	0.4	−0.6	0.2	−0.4	−21.8	−8.5	−2.3	0.0	0.0	0.0	0.0	−21.9	+ 0.6
H (190 GeV)	3.95 ± 0.31	0.0	0.3	0.0	−0.5	0.3	−0.3	0.0	−0.3	−30.0	4.5	−1.6	0.3	0.0	0.0	0.0	−30.1	+ 4.5
H (200 GeV)	3.55 ± 0.10	0.0	−0.0	0.4	−0.3	0.4	−0.0	0.1	−0.3	−29.3	−6.9	−1.8	0.1	−0.1	−0.0	0.3	−29.4	+ 0.7
WW	1.31 ± 0.31	0.0	0.0	−6.2	0.0	0.2	0.0	3.9	0.0	−26.7	1.4	−9.1	0.0	0.0	0.0	0.0	−28.9	+ 4.2
Wt	0.47 ± 0.18	0.0	0.0	0.0	0.0	0.0	0.0	14.3	0.0	−14.3	−28.6	−14.3	0.0	0.0	0.0	0.0	−31.9	+ 14.3
$t\bar{t}$ (fast sim.)	2.72 ± 0.40	0.0	0.0	0.0	0.0	0.0	2.2	−0.0	2.2	−17.4	2.2	4.3	8.7	−6.5	0.0	0.0	−18.6	+ 10.4

Table 7.2: Impact of the detector-related systematic uncertainties [%] on the cross sections after all event selection cuts for the signal process with different m_H as well as for the dominant background processes. $\mathcal{S}$ and $\mathcal{E}$ denote the effect of the shifts in the energy scale and the modified reconstruction efficiency, respectively. $\mathcal{R}$ denotes the effect of degradation of the energy resolution while r represents the effect of the modified light-jet rejection of the *b*-tagging algorithm. The last column gives the squared sum of the individual systematic uncertainties. The uncertainties on the background contributions are determined for a cut $m_{\mathrm{T}} < 170\,\mathrm{GeV}$ while $m_{\mathrm{T}} < m_H$ is used for the signal process. In case of the Wt background, the detector-related uncertainties are assumed to be negligible compared to the statistical uncertainties (see text).

	VBF $H \to WW$			$t\bar{t}$ (fast sim.)		
	nominal	down	up	nominal	down	up
Trigger	90.9 ± 0.1	90.9 ± 0.1	90.9 ± 0.1	63.8 ± 0.1	63.8 ± 0.1	63.8 ± 0.1
$N(e+\mu) = 2$	50.8 ± 0.3	50.8 ± 0.3	50.8 ± 0.3	7.2 ± 0.1	7.2 ± 0.1	7.2 ± 0.1
Lepton charge	99.8 ± 0.1	99.8 ± 0.1	99.8 ± 0.1	99.4 ± 0.1	99.4 ± 0.1	99.4 ± 0.1
$E_T^{miss} > 30\,\text{GeV}$	88.9 ± 0.2	89.8 ± 0.2	91.2 ± 0.2	85.0 ± 0.1	88.1 ± 0.1	90.6 ± 0.1
$m_{ll} = [15, 70]\,\text{GeV}$	83.4 ± 0.3	83.3 ± 0.3	83.1 ± 0.3	32.5 ± 0.1	31.9 ± 0.1	31.9 ± 0.1
$m_{\text{T}}^{ll\nu} > 30\,\text{GeV}$	95.6 ± 0.2	96.6 ± 0.2	95.8 ± 0.2	89.1 ± 0.1	91.1 ± 0.1	90.8 ± 0.1
$Z \to \tau\tau$ veto	98.7 ± 0.1	99.0 ± 0.1	99.0 ± 0.1	96.5 ± 0.1	97.6 ± 0.1	97.5 ± 0.1
$\lvert\Delta\phi_{ll}\rvert < 1.5$	85.0 ± 0.3	85.3 ± 0.3	85.1 ± 0.3	68.4 ± 0.2	68.0 ± 0.2	67.6 ± 0.2
$\Delta R_{\ell\ell} < 1.8$	97.4 ± 0.2	97.4 ± 0.1	97.4 ± 0.2	92.7 ± 0.2	92.8 ± 0.2	92.7 ± 0.2
$m_{\text{T}} < 170\,\text{GeV}$	93.0 ± 0.2	79.3 ± 0.4	77.9 ± 0.4	83.2 ± 0.2	62.8 ± 0.3	59.2 ± 0.3
$N(\text{jets}) \geq 2$	72.4 ± 0.4	64.8 ± 0.5	73.5 ± 0.5	93.0 ± 0.2	89.3 ± 0.2	93.0 ± 0.2
$p_T(\text{jet1}) > 40\,\text{GeV}$	91.9 ± 0.3	87.4 ± 0.4	92.3 ± 0.3	96.0 ± 0.1	93.3 ± 0.2	96.0 ± 0.2
$\eta_{j1} \times \eta_{j2} < 0$	86.2 ± 0.4	86.6 ± 0.5	86.2 ± 0.5	42.4 ± 0.4	41.2 ± 0.4	41.8 ± 0.4
$\lvert\Delta\eta_{jj}\rvert > 3.8$	71.7 ± 0.6	70.8 ± 0.7	73.1 ± 0.6	9.4 ± 0.3	7.6 ± 0.4	8.9 ± 0.4
Central jet veto	90.6 ± 0.5	93.0 ± 0.5	90.3 ± 0.5	24.0 ± 1.6	33.9 ± 2.3	27.9 ± 2.0
$p_{\text{T}}^{\text{tot}} < 30\,\text{GeV}$	95.7 ± 0.3	92.2 ± 0.5	92.0 ± 0.5	71.1 ± 3.4	68.0 ± 3.8	74.8 ± 3.6
b-jet veto	93.5 ± 0.4	93.5 ± 0.5	94.5 ± 0.4	35.9 ± 4.2	38.0 ± 4.9	42.7 ± 4.7
Cross section [fb]	6.13 ± 0.10	4.47 ± 0.09	5.31 ± 0.10	2.72 ± 0.40	2.25 ± 0.36	2.78 ± 0.41

Table 7.3: Relative event selection efficiencies [%] and cross sections times selection efficiencies after all selection cuts for different jet energy scales. The values are quoted for the nominal jet energy scale as well as for an increase and a decrease by 7% for jets within $|\eta| < 3.2$ and by 15% for jets beyond $|\eta| = 3.2$.

selection efficiencies by up to 30%. As can be seen in Figure 7.2 and 7.3 and Table 7.3, the impact is twofold: On the one hand, decreasing (increasing) the jet energy scale results in a lower (larger) number of reconstructed jets and thus to different central jet veto efficiencies. On the other hand, the modified jet energy scale leads to a significant shift in the missing transverse energy and, therefore, to decreased selection efficiencies for the total transverse momentum $p_{\text{T}}^{\text{tot}}$ and the transverse Higgs mass.
As expected, the uncertainties on the b-tagging performance only affect the selection efficiency of $t\bar{t}$ events which are efficiently rejected by the b-jet veto. Decreasing the b-tagging efficiency by 6% increases the $t\bar{t}$ background by about 10%. Compared to the uncertainties in the jet reconstruction, the uncertainties in the electron and muon reconstruction are almost negligible.
The uncertainty on the Wt background due to the limited Monte Carlo statistics is too large to allow for a reliable estimate of the systematic uncertainties on the event selection efficiency. Therefore, detector-related systematic uncertainties are assumed to be negligible compared to the statistical uncertainty (40%). The impact of detector-related systematic uncertainties on the minor background contributions from $W+\text{jets}$, $Z+\text{jets}$ and WZ/ZZ processes is assumed to be the same as for the dominant background processes.

7.2.3 Background Estimation from Data

With sufficient statistics, the impact of detector-related systematic uncertainties on the expected background cross sections can be reduced by employing methods to determine the

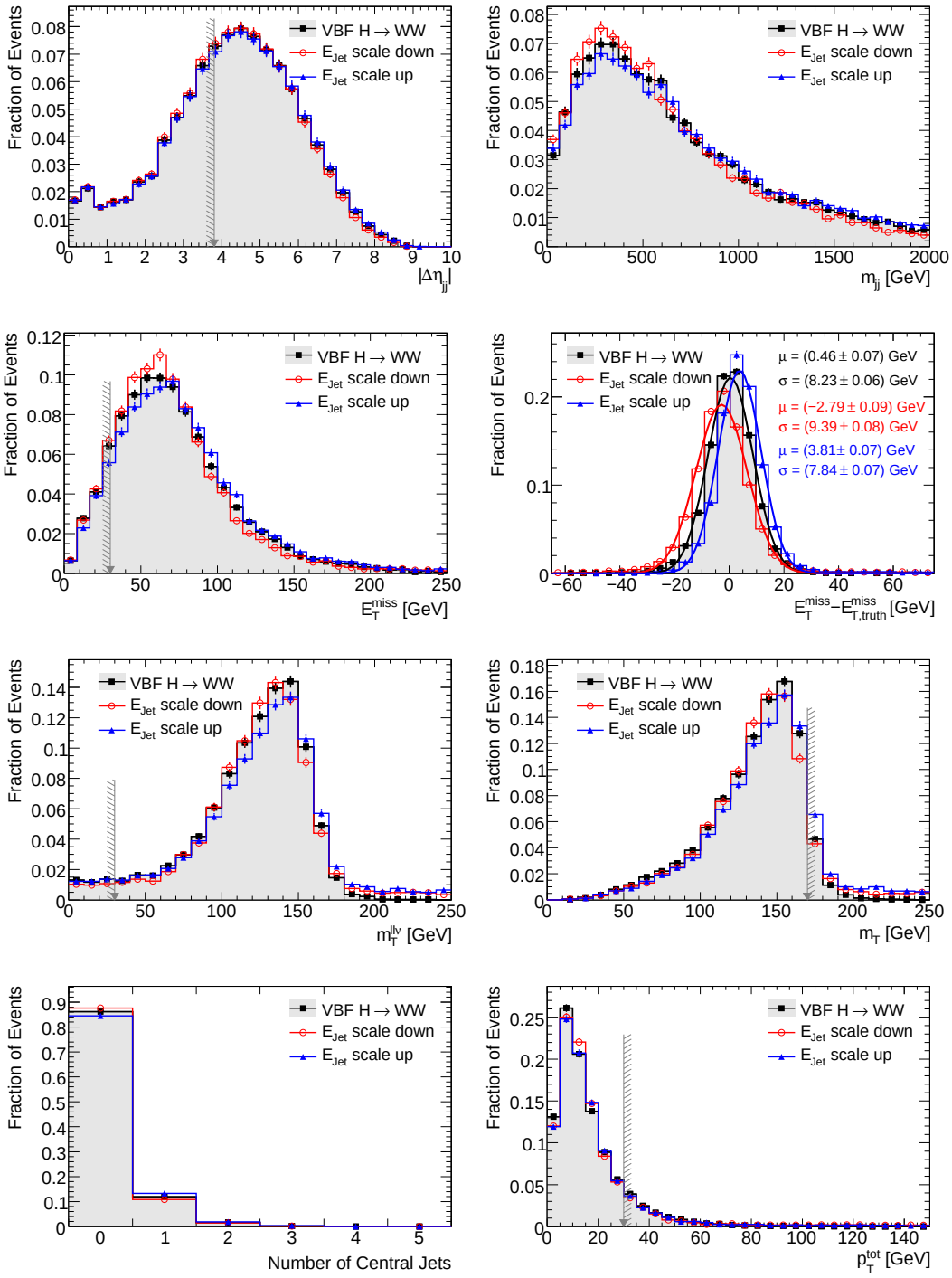

Figure 7.2: Distributions of the most important discriminating variables for vector-boson fusion $H \rightarrow WW$ events for the nominal as well as for modified jet energy scales as in Table 7.3. The gray arrows indicate the cut values.

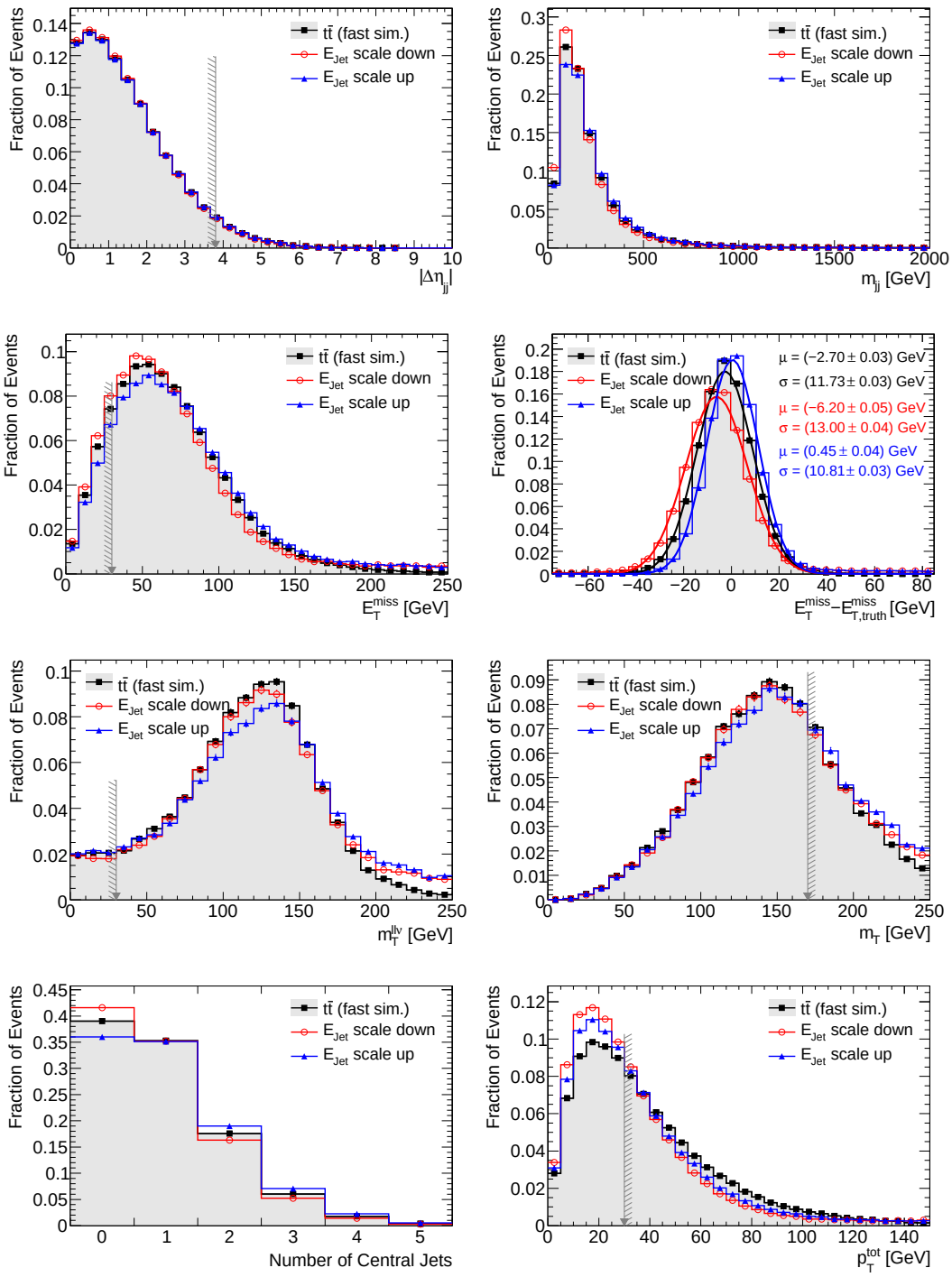

Figure 7.3: Distributions of some of the most important discriminating variables for $t\bar{t}$ events for the nominal as well as for modified jet energy scales as in Table 7.3. The gray arrows indicate the cut values.

background contributions from collision data. Estimating the background contributions by extrapolation from appropriately chosen control regions reduces systematic uncertainties due to the detector response since the impact, for instance, of a modified jet energy scale is largely the same in the signal and the control region. Thus, the ratio of expected events in both regions is less affected by these systematic uncertainties. In addition, estimating the background from data reduces the sensitivity to the accuracy of the predicted background cross sections. Several methods are currently being developed in the ATLAS collaboration [73] which are briefly discussed in the following.

$t\bar{t}$ and Wt Background

Background events containing top-quarks are characterized by the presence of b-jets in the final state. Therefore, requiring one or two tagged b-jets in the event allows for a selection of Wt and $t\bar{t}$ events while efficiently suppressing signal or $W+\text{jets}$ and WW events. Determining the ratio of events without and with two tagged b-jets from Monte Carlo data or another control region (CR′) using collision data allows for the extrapolation of the number of $t\bar{t}$ events from the b-tagged control region ($\text{CR}_{b\text{-tag}}$) to the b-vetoed signal region ($\text{SR}_{b\text{-veto}}$) according to

$$\text{SR}_{b\text{-veto}} = \frac{\text{CR}'_{b\text{-veto}}}{\text{CR}'_{b\text{-tag}}} \text{CR}_{b\text{-tag}}.$$

For instance, the selection of $t\bar{t}$ events with only one lepton but four jets defines a control region which allows for the determination of the ratio $\text{CR}'_{b\text{-veto}}/\text{CR}'_{b\text{-tag}}$. Since Wt and $t\bar{t}$ processes have different numbers of b-jets, both can be estimated with this method by requiring one or two tagged b-jets in the control region, respectively.

WW Background

One of the most efficient selection criteria rejecting the WW background is requiring a the pseudo-rapidity gap between the vector-boson fusion tagging jets (Figure 5.15). Reversing this cut defines a control region with enhanced WW contribution. The contribution of signal events in this region has to be additionally suppressed by reversing the cut on the angular distance $\Delta\phi_{ll}$ (Figure 5.10) and the invariant mass of two leptons m_{ll} (Figure 5.11). Since this control region is also enriched with top events, a reliable estimation of the WW background requires the estimation and subtraction of the top contamination. On the other hand, selecting only events with tagged b-jets, this control region also allows for an estimation of the $t\bar{t}$ and Wt background contributions in the signal region.

$W+\text{jets}$ Background

In contrast to the other signal and background processes which contain real leptons, the $W+\text{jets}$ process only constitutes a background if jets are misidentified as leptons. One approach for a more reliable estimation of the $W+\text{jets}$ background is to measure the lepton misidentification rate in QCD di-jet or $\gamma/Z+\text{jet}$ events with collision data and subsequently estimate the $W+\text{jets}$ contribution from Monte Carlo data by reweighting the events according to the number of jets they contain times the measured lepton misidentification rate.

In order to measure the W + jets contribution entirely from data, a so-called subtraction method has been developed. This method is based on measuring the total cross sections of signal and background depending on the tightness of the electron selection criteria. In addition, the electron selection efficiency has to be measured with data, for instance in $Z \to ee$ events. The cross sections divided by the electron selection efficiency squared are independent of the electron selection criteria for processes with two real electrons. For W + jets events, however, one jet is falsely identified as an electron and, thus, the mentioned ratio decreases with increasing tightness of the electron selection. For sufficiently tight electron selection, the contribution of W + jets events vanishes and the cross sections of the remaining processes can be estimated and subtracted. This allows for the estimation of the W + jets contribution depending on the electron selection criteria.

The small numbers of events expected in the signal and control regions for the search for the Higgs boson with two additional tagging jets (2-jet channel) at an integrated luminosity of $1\,\mathrm{fb}^{-1}$ impose a major challenge on the background estimation with early collision data. The uncertainties of these methods are expected to be still larger or, at most, equal to the uncertainties of a pure Monte Carlo background estimation. The latter is therefore used for the estimation of the discovery potential in the following section. However, for the search for $H \to WW$ decays in gluon fusion production, i. e. the 0-jet channel, significantly larger numbers of events are expected allowing for background estimation from early data with reduced systematic uncertainties. At larger integrated luminosities, these methods will also allow for significantly reduced systematic uncertainties in the 2-jet channel.

7.3 Results

The cross sections times selection efficiencies of the signal and background processes for different Higgs boson masses are shown in Table 5.10 and Figure 5.23. Based on these numbers, the exclusion limits and signal significances are determined for an integrated luminosity of $1\,\mathrm{fb}^{-1}$ by means of the statistical methods introduced above, taking into account the theoretical and experimental systematic uncertainties.
The imperfect knowledge of the detector response has two effects. First, the event selection efficiencies determined with Monte Carlo data are assigned a symmetric positive and negative systematic error given by the maximum of the positive and negative total systematic shifts specified in the last column of Table 7.2. This is in all cases the negative shift which is on the order of 30%. Second, the event selection efficiencies can actually be systematically shifted resulting in lower or larger numbers of expected signal and background events. This is accounted for by determining in addition the exclusion limits and signal significances for the increased and the decreased event selection efficiencies.
Figure 7.4 and Table 7.4a show the expected exclusion limits as a function of the Higgs boson mass taking into account only the theoretical uncertainties and Monte Carlo statistics and with additionally taking into account systematic uncertainties due to the imperfect knowledge of the detector response as given in Table 7.2. For masses close to the threshold $m_H \approx 2m_W$, the Higgs boson decays almost exclusively into two W bosons (see Figure 2.7) and the spin correlation between the two leptons allows for a very efficient suppression of background processes. Therefore, the best exclusion limits are obtained in the range

m_H [GeV]	Without systematics	Theoretical and MC systematics	Detector systematics	With pile-up
120	$6.28^{-0.32}_{+3.18}$	$6.48^{-0.32}_{+3.30}$	$7.43^{-0.40}_{+3.96}$	$10.58^{-0.47}_{-1.05}$
130	$2.09^{+0.79}_{+1.06}$	$2.15^{+0.81}_{+1.08}$	$2.40^{+0.99}_{+1.24}$	$3.48^{-0.14}_{+1.64}$
140	$1.49^{-0.07}_{+0.17}$	$1.53^{-0.07}_{+0.18}$	$1.85^{-0.10}_{+0.16}$	$1.81^{-0.09}_{+1.10}$
150	$1.13^{+0.30}_{+0.63}$	$1.17^{+0.31}_{+0.66}$	$1.34^{+0.41}_{+0.80}$	$2.00^{-0.11}_{+0.13}$
160	$0.69^{+0.15}_{+0.41}$	$0.72^{+0.16}_{+0.42}$	$0.82^{+0.21}_{+0.51}$	$0.91^{+0.29}_{+0.55}$
165	$0.71^{-0.04}_{+0.18}$	$0.73^{-0.04}_{+0.18}$	$0.87^{-0.06}_{+0.21}$	$1.00^{-0.06}_{+0.16}$
170	$0.73^{-0.05}_{+0.19}$	$0.75^{-0.05}_{+0.19}$	$0.89^{-0.06}_{+0.22}$	$1.03^{-0.06}_{+0.17}$
180	$0.80^{+0.14}_{+0.14}$	$0.84^{+0.15}_{+0.15}$	$0.93^{+0.18}_{+0.16}$	$1.10^{-0.07}_{+0.11}$
190	$1.35^{+0.18}_{+0.43}$	$1.41^{+0.19}_{+0.46}$	$1.72^{+0.28}_{+0.55}$	$2.04^{+0.43}_{+0.48}$
200	$1.86^{-0.13}_{+0.06}$	$1.93^{-0.13}_{+0.06}$	$2.38^{-0.18}_{-0.03}$	$2.15^{+0.55}_{+1.50}$

(a) Exclusion limits ($\mu = \sigma/\sigma_{SM}$).

120	$0.22^{+0.00}_{-0.12}$	$0.19^{-0.00}_{-0.10}$	$0.18^{-0.00}_{-0.10}$	$0.11^{-0.00}_{-0.09}$
130	$0.86^{-0.02}_{-0.18}$	$0.80^{-0.02}_{-0.18}$	$0.76^{-0.02}_{-0.17}$	$0.64^{-0.02}_{-0.16}$
140	$1.61^{-0.04}_{-0.36}$	$1.52^{-0.04}_{-0.35}$	$1.46^{-0.04}_{-0.34}$	$1.28^{-0.03}_{-0.31}$
150	$1.76^{-0.03}_{-0.33}$	$1.67^{-0.03}_{-0.32}$	$1.60^{-0.04}_{-0.30}$	$1.40^{-0.03}_{-0.28}$
160	$2.72^{-0.06}_{-0.46}$	$2.55^{-0.06}_{-0.44}$	$2.42^{-0.07}_{-0.40}$	$2.16^{-0.06}_{-0.37}$
165	$3.11^{-0.04}_{-0.55}$	$2.89^{-0.08}_{-0.51}$	$2.73^{-0.08}_{-0.47}$	$2.45^{-0.07}_{-0.43}$
170	$2.90^{-0.02}_{-0.56}$	$2.73^{-0.07}_{-0.50}$	$2.58^{-0.07}_{-0.45}$	$2.30^{-0.06}_{-0.42}$
180	$2.48^{-0.05}_{-0.31}$	$2.30^{-0.06}_{-0.29}$	$2.16^{-0.06}_{-0.26}$	$1.93^{-0.06}_{-0.24}$
190	$1.45^{+0.01}_{-0.36}$	$1.32^{+0.01}_{-0.31}$	$1.23^{+0.01}_{-0.29}$	$1.09^{+0.01}_{-0.26}$
200	$1.25^{-0.04}_{-0.21}$	$1.17^{-0.03}_{-0.27}$	$1.09^{-0.04}_{-0.25}$	$0.95^{-0.03}_{-0.23}$

(b) Signal significances.

Table 7.4: Expected exclusion limits (at 95% CL) and signal significances for different Higgs boson masses and an integrated luminosity of $1\,\text{fb}^{-1}$. The second column in each table gives the values without accounting for systematic uncertainties in the profile likelihood ratio, the third column the values taking into account the theoretical uncertainties and Monte Carlo statistics, the fourth column the values taking into account in addition the uncertainties due to imperfect knowledge of the detector response and the fifth column the values corresponding to the additionally decreased event selection efficiencies due to the presence of pile-up. The superscripts and subscripts represent the impact of the systematic shifts of the detector response (see text).

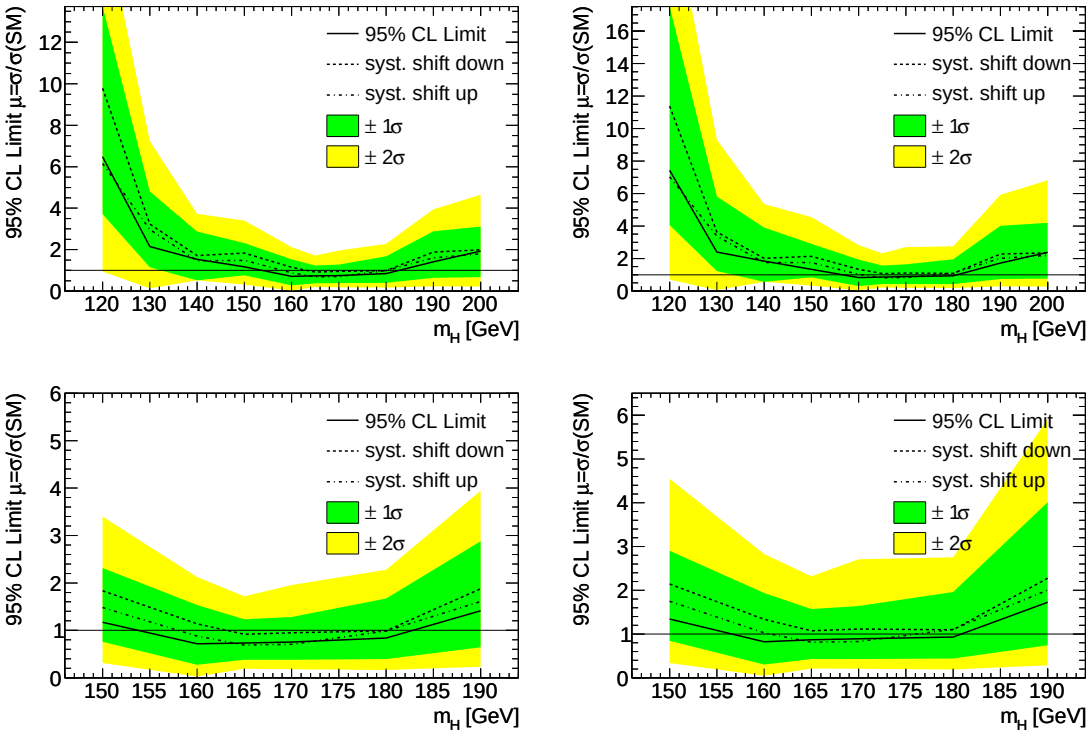

Figure 7.4: Expected exclusion limits relative to the predicted Standard Model cross section as a function of the Higgs boson mass taking into account only the theoretical uncertainties and Monte Carlo statistics (left) and including in addition the uncertainties due to the imperfect knowledge of the detector response (right). The upper figures show the exclusion limits for the whole mass range studied while the lower figures show only the region of the highest sensitivity. The solid line corresponds to the limits for the nominal detector response whereas the dashed lines represent the impact of the systematic shifts of the detector response (see text). The green and yellow bands correspond to the $\pm 1\sigma$ and $\pm 2\sigma$ statistical fluctuations of the number of observed events.

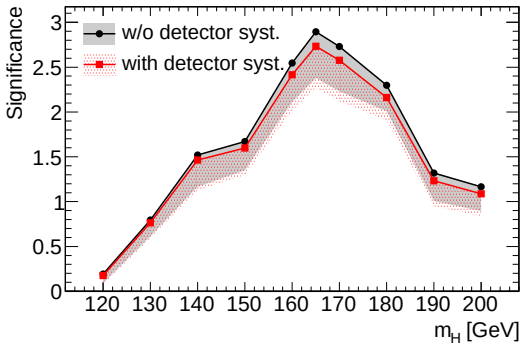

Figure 7.5: Expected signal significances as a function of the Higgs boson mass for an integrated luminosity of $1\,\text{fb}^{-1}$ taking into account only the theoretical uncertainties and Monte Carlo statistics (black dots) and including in addition the systematic uncertainties due to the imperfect knowledge of the detector response (red squares). The solid lines correspond to the significance for the nominal detector response whereas the shaded bands represent the impact of the systematic shifts of the detector response (see text).

$160\,\text{GeV} \leq m_H \leq 180\,\text{GeV}$ where a Higgs boson with the Standard Model production cross section can be excluded at 95% CL including all systematic uncertainties. For Higgs boson masses significantly different from $2m_W$, a degradation of the limits is observed, due to the lower discrimination power of the spin correlation between the leptons, particularly at large Higgs boson masses, and due to the significantly decreased branching ratio for Higgs boson decays into two W bosons. In comparison to the nominal detector performance, slightly worse exclusion limits are expected for the systematically shifted detector response.

For the corresponding signal significances shown in Figure 7.5 and Table 7.4b, a similar behavior as for the exclusion limits is observed. In comparison to only taking the theoretical uncertainties and Monte Carlo statistics into account, slightly worse signal significances are observed when additionally including the uncertainties due to the imperfect knowledge of the detector response. The best discovery potential with a significance of $Z = 2.73$ is expected for a Higgs boson mass of 165 GeV, which significantly decreases for lower and larger m_H.

The impact of pile-up on the expected exclusion limits and signal significances is shown in Figure 7.6 for pile-up of on average 4.1 inelastic pp collisions per bunch crossing corresponding to an integrated luminosity of $10^{32}\,\text{cm}^{-2}\,\text{s}^{-1}$. It is taken into account by multiplying the event selection efficiencies determined from Monte Carlo data without pile-up by the relative impact of pile-up quoted in Table 6.6, assuming for all Higgs boson masses the same effect as for $m_H = 170$. Since Monte Carlo data samples with pile-up are not available for the WW and Wt background processes, the same relative impact of pile-up is assumed as determined for vector-boson fusion $H \to WW$ and $t\bar{t}$ events, respectively, which show similar sensitivity to pile-up. Including pile-up effects, the exclusion limit degrades from $0.9\,\sigma_{SM}$ to $1.0\,\sigma_{SM}$ while the signal significance decreases from $Z = 2.73$ to $Z = 2.45$ for $m_H = 165\,\text{GeV}$.

As stated in Section 6.2, pile-up has two major effects on the event selection efficien-

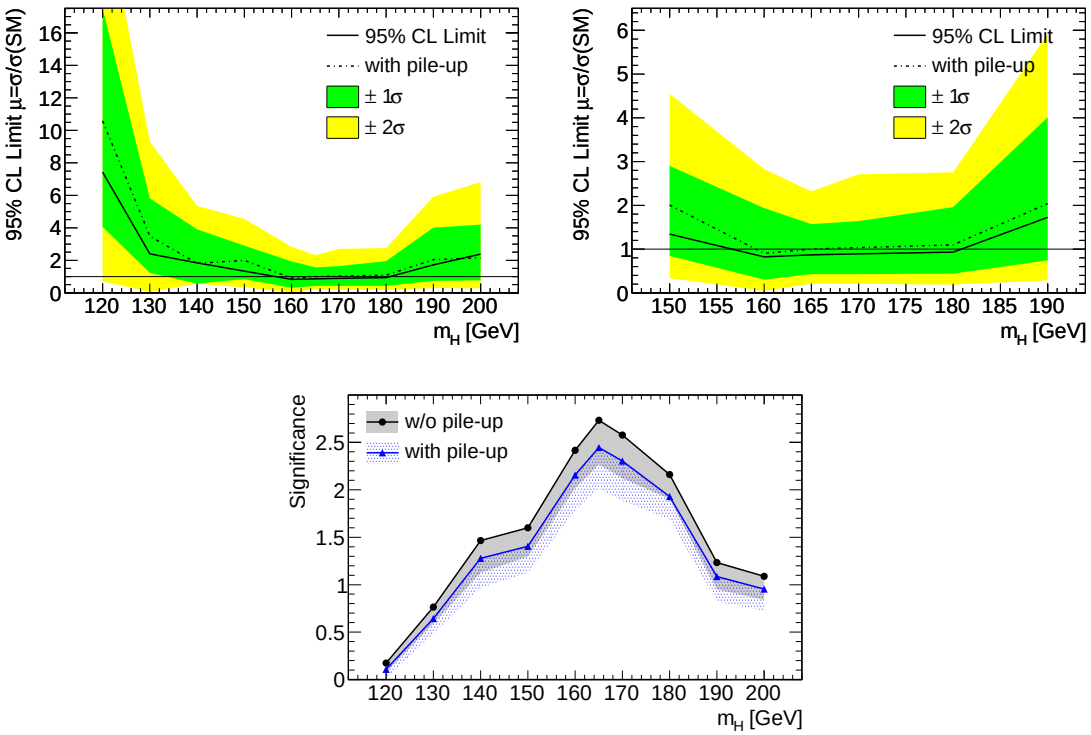

Figure 7.6: Exclusion limits (top) and signal significances (bottom) as a function of the Higgs boson mass for an integrated luminosity of $1\,\mathrm{fb}^{-1}$. The results are compared without and with pile-up effects on the event selection efficiencies where the level of pile-up corresponds to an instantaneous luminosity of $10^{32}\ \mathrm{cm}^{-2}\,\mathrm{s}^{-1}$ and on average 4.1 events per bunch crossing. All theoretical and experimental systematic uncertainties are taken into account.

cies in the vector-boson fusion $H \to WW$ analysis. First, the degradation of the $E_{\mathrm{T}}^{\mathrm{miss}}$ resolution results in broader distributions of variables calculated based on the missing transverse energy such as the transverse mass m_{T} of the Higgs boson and the total transverse momentum $p_{\mathrm{T}}^{\mathrm{tot}}$. Second, additional jets from minimum bias events deteriorate the performance of the central jet veto. The impact of pile-up can be suppressed by exploiting tracks originating from the primary interaction vertex. Employing jets reconstructed from tracks makes the central jet veto less sensitive to pile-up as shown in Section 6.10. In order for the overall event selection efficiencies to be robust against pile-up effects, however, the missing transverse energy reconstruction in the presence of pile-up also has to be improved.

Chapter 8

Conclusions and Outlook

After several years of construction and commissioning, operation of the Large Hadron Collider (LHC) has started providing the first pp collisions at a center-of-mass energy of 900 GeV. ATLAS, one of the two general purpose experiments at the LHC, has been built to probe a broad spectrum of physics processes of the Standard Model of particle physics and beyond.

The ATLAS physics goals require a muon transverse momentum resolution of better than 10% up to transverse momenta of 1 TeV. For this purpose, the relative positions of the precision muon tracking chambers (MDT chambers) have to be determined with an accuracy of about 30 μm in the bending plane of the muon tracks. In addition to the optical alignment monitoring system, track-based alignment is necessary for MDT chambers which are only partially connected to the optical alignment system. A new software framework for inner detector and muon spectrometer alignment has been developed which allows for the implementation of different algorithms as well as for the individual and combined alignment of different detector systems. In this thesis, the performance of a global χ^2 minimization algorithm has been evaluated for the alignment of the small MDT chambers in the barrel part of the muon spectrometer. Monte Carlo data samples corresponding to the number of muon tracks delivered by a dedicated muon calibration stream were employed. Two muon transverse momentum trigger thresholds have been studied: 20 GeV and 6 GeV. While the different MDT chamber triplets within one sector of the barrel muon spectrometer could be aligned with the required precision using muons with transverse momenta of 20 GeV, the increased effect of multiple scattering significantly deteriorates the alignment performance with muons of $p_{\mathrm{T}} = 6\,\mathrm{GeV}$. Further studies are necessary to also achieve the required precision with low-p_{T} muons. In addition, misalignment effects along the muon trajectories to which the global χ^2 algorithm is insensitive (so-called weak modes) have to be better constrained, for instance by using information from the optical alignment system.

The design of the ATLAS detector is driven by requirements for the detection of the Higgs boson, the last undiscovered particle predicted by the Standard Model. Due to its large branching fraction, the decay of the Higgs boson into two W bosons is one of the most promising decay channels for Higgs boson discovery allowing for first exclusion limits on Higgs boson production already with the early ATLAS data. Although suppressed by one order of magnitude with respect to Higgs boson production via gluon fusion, the vector-

boson fusion production mechanism with two characteristic jets in the forward regions of the detector allows for improved background suppression.
In this thesis, the discovery potential for Higgs boson production in vector-boson fusion has been evaluated for an integrated luminosity of $1\,\mathrm{fb}^{-1}$. The highest sensitivity is expected for a Higgs boson mass of 165 GeV with about 8.5 signal and 4.7 background events selected. Contributing about 2.6 events, the $t\bar{t}$ process has been identified as the dominant background. For all Higgs boson masses studied, the uncertainty on the jet energy scale, at approximately 30%, is by far the largest systematic error. Due to the low number of expected events, methods to determine the different background contributions from collisions data in order decrease detector-related systematic uncertainties can probably only be employed at a later stage. Taking the theoretical and experimental systematic uncertainties into account, a signal significance of 2.7σ is expected for $m_H = 165\,\mathrm{GeV}$. In the mass range $160\,\mathrm{GeV} \leq m_H \leq 180\,\mathrm{GeV}$, the Standard Model Higgs boson can be excluded at 95% confidence level.
With increasing instantaneous luminosities, each interesting physics event will be superimposed by several additional inelastic pp collisions (pile-up) decreasing the discovery potential due to the deterioration of the forward tagging jet and the missing transverse energy reconstruction. Two approaches have been studied to associate jets to the primary interaction by exploiting tracking and vertexing information: track-based jet reconstruction (track jets) and the association of calorimeter jets to tracks from the primary vertex. Track jets have been shown to be insensitive to the level of pile-up while a small sensitivity is observed for association of calorimeter jets by means of the primary vertex p_T fraction. Both methods improve the performance of the central jet veto in the presence of pile-up. When using track jets for the central jet veto, their transverse momentum and reconstruction efficiency relative to calorimeter jets have to be measured with collision data. The prospects for the track jet calibration with data have been discussed in this thesis. In order to achieve a pile-up independent discovery potential for the Higgs boson in vector-boson fusion production, the missing transverse energy reconstruction in the presence of pile-up also has to be improved, for instance by exploiting tracking and vertexing information. However, track-based methods can only be employed for the association of physics objects to the primary interaction within the acceptance of the inner detector. Hence, improved algorithms for the reconstruction of calorimeter clusters are currently being developed to improve both the missing transverse energy and the calorimeter jet reconstruction beyond $|\eta| = 2.5$ in the presence of pile-up which is of particular importance for the reliable reconstruction of the tagging jets in the Higgs boson production via vector-boson fusion.

Appendix A

Background Monte Carlo Samples

This appendix provides further details on the background Monte Carlo samples employed for the study of the Higgs boson discovery potential in this thesis (Tables A.1-A.5). Tables A.6-A.8 give the selection efficiencies employed for the estimation of the minor background contributions to the $H \to WW$ analysis assuming factorization of the selection criteria (see Section 5.6.2).

Process	Cross section [pb]	Events	Integrated luminosity [fb^{-1}]
Wt	3.0	44990	15.0
$t\bar{t}$	217.6	1468600	6.8
$t\bar{t}$ (FastSim)	217.6	3680840	16.9

Table A.1: Overview of the top background samples used in this analysis. The next-to-leading order cross sections are given as quoted in Reference [51] together with the numbers of simulated events and the corresponding integrated luminosities. The cross section for the $t\bar{t}$ sample includes the efficiency of the single-lepton filter of 55%. The Wt sample has been generated with the AcerMC program while MC@NLO has been used for the generation of the $t\bar{t}$ sample.

Process	Cross section [fb]	Events	Integrated luminosity [fb^{-1}]
$qq/qg \to WW$ (MC@NLO):			
$\to e\nu e\nu$	845.3	10400	12.3
$\to e\nu\mu\nu$	831.2	17360	20.9
$\to e\nu\tau\nu$	884.6	17210	19.5
$\to \mu\nu e\nu$	831.2	17260	20.8
$\to \mu\nu\mu\nu$	817.3	3430	4.2
$\to \mu\nu\tau\nu$	869.8	17490	20.1
$\to \tau\nu e\nu$	884.6	17340	19.6
$\to \tau\nu\mu\nu$	869.8	17250	19.8
$\to \tau\nu\tau\nu$	925.8	17230	18.6
$gg \to WW$ (GG2WW):			
$\to e\nu e\nu$	30.9	10000	323.2
$\to e\nu\mu\nu$	30.9	10000	323.1
$\to e\nu\tau\nu$	28.7	9950	346.8
$\to \mu\nu e\nu$	30.9	9980	322.6
$\to \mu\nu\mu\nu$	31.0	9960	321.6
$\to \mu\nu\tau\nu$	28.8	10000	347.2
$\to \tau\nu e\nu$	28.7	9960	347.3
$\to \tau\nu\mu\nu$	28.8	9990	346.5
$\to \tau\nu\tau\nu$	10.2	9990	976.5

Table A.2: Overview of the WW background Monte Carlo samples used in this analysis. The next-to-leading order cross sections are reported as quoted in Reference [51] for the $qq/qg \to WW$ process and as obtained with the GG2WW program for the $gg \to WW$ process. The numbers of simulated events and the corresponding integrated luminosities are given.

Process	Cross section [pb]	Events	Integrated luminosity [fb^{-1}]
$W \to e\nu$:			
+ 0 jets	12527.2	1221090	0.10
+ 1 jet	2598.1	262420	0.10
+ 2 jets	831.5	776280	0.93
+ 3 jets	250.1	224070	0.90
+ 4 jets	69.0	58870	0.85
+ $\geq$5 jets	20.4	17490	0.86
$W \to \mu\nu$:			
+ 0 jets	12454.6	1328630	0.11
+ 1 jet	2651.3	248220	0.09
+ 2 jets	839.2	779540	0.93
+ 3 jets	248.5	213090	0.86
+ 4 jets	68.3	58930	0.86
+ $\geq$5 jets	20.0	17480	0.87
$W \to \tau\nu$:			
+ 0 jets	12519.3	1286090	0.10
+ 1 jet	2591.5	246830	0.10
+ 2 jets	827.5	793110	0.96
+ 3 jets	249.3	223160	0.90
+ 4 jets	68.0	58730	0.86
+ $\geq$5 jets	20.9	17410	0.83

Table A.3: Overview of the W background Monte Carlo samples used in this analysis. The next-to-leading order cross sections including a K-factor of 1.23 [103] are given together with the numbers of simulated events and the corresponding integrated luminosities. The samples have been generated with the Alpgen program.

Process	Cross section [pb]	Events	Integrated luminosity [fb^{-1}]
$Z \to ee$:			
+ 0 jets	1104.8	269280	0.2
+ 1 jet	254.1	51770	0.2
+ 2 jets	89.2	216950	2.4
+ 3 jets	25.9	63410	2.5
+ 4 jets	7.4	18310	2.5
+ $\geq$5 jets	2.1	5500	2.8
$Z \to \mu\mu$:			
+ 0 jets	1107.3	270100	0.2
+ 1 jet	252.4	61690	0.2
+ 2 jets	85.3	197370	2.3
+ 3 jets	26.6	64710	2.4
+ 4 jets	7.5	18470	2.5
+ $\geq$5 jets	2.1	5470	2.6
$Z \to \tau\tau$:			
+ 0 jets	1110.3	270650	0.2
+ 1 jet	257.4	62680	0.2
+ 2 jets	86.3	210230	2.4
+ 3 jets	25.9	63430	2.5
+ 4 jets	7.4	18500	2.5
+ $\geq$5 jets	2.1	5480	2.6

Table A.4: Overview of the Z background Monte Carlo samples used in this analysis. The next-to-leading order cross sections including a K-factor of 1.23 [103] are given together with the numbers of simulated events and the corresponding integrated luminosities. The samples have been generated with the Alpgen program.

Process	Cross section [fb]	Events	Integrated luminosity [fb^{-1}]
W^-Z:			
$\rightarrow l\nu ll$	164.1	11260	68.6
$\rightarrow l\nu\tau\tau$	82.2	14600	177.7
$\rightarrow \tau\nu ll$	86.6	14260	164.7
$\rightarrow \tau\nu\tau\tau$	43.4	13900	320.5
$\rightarrow qqll$	520.2	3650	7.0
W^+Z:			
$\rightarrow l\nu ll$	278.7	14560	52.3
$\rightarrow l\nu\tau\tau$	139.6	7140	51.2
$\rightarrow \tau\nu ll$	147.0	14410	98.0
$\rightarrow \tau\nu\tau\tau$	73.6	14630	198.6
$\rightarrow qqll$	883.6	3640	4.1
ZZ:			
$\rightarrow 4l$	43.8	13310	304.2
$\rightarrow 2l2\tau$	43.8	13500	307.9
$\rightarrow 4\tau$	11.0	13460	1226.1
$\rightarrow 2l2\nu$	260.1	13460	51.8

Table A.5: Overview of the WZ and ZZ background Monte Carlo samples used in this analysis. The next-to-leading order cross sections are given as quoted in Reference [51] together with the numbers of simulated events and the corresponding integrated luminosities. The samples have been generated with the MC@NLO program.

	WZ/ZZ	$W+\text{jets}$	$Z \to \ell\ell + \text{jets}$	$Z \to \tau\tau + \text{jets}$
Trigger	84.7 ± 0.1	38.5 ± 0.1	75.6 ± 0.1	18.8 ± 0.1
$N(e+\mu) = 2$	43.4 ± 0.1	0.0 ± 0.1	40.8 ± 0.1	2.9 ± 0.1
Lepton charge	92.5 ± 0.1	69.9 ± 1.9	99.8 ± 0.1	99.7 ± 0.1
$E_T^{miss} > 30\,\text{GeV}$	29.4 ± 0.2	59.5 ± 2.4	0.3 ± 0.1	9.5 ± 0.5
$m_{ll} = [15, 70]\,\text{GeV}$	7.3 ± 0.2	57.7 ± 3.1	3.3 ± 0.3	96.8 ± 0.5
$m_{\text{T}}^{ll\nu} > 30\,\text{GeV}$	89.3 ± 0.7	98.8 ± 1.0	73.9 ± 4.5	24.6 ± 1.3
$Z \to \tau\tau$ veto	96.5 ± 0.5	98.8 ± 1.0	71.0 ± 5.0	39.7 ± 3.4
$\lvert\Delta\phi_{ll}\rvert < 1.5$	63.5 ± 1.2	46.6 ± 4.5	44.4 ± 6.1	2.7 ± 2.0
$\Delta R_{\ell\ell} < 1.8$	91.7 ± 0.9	88.3 ± 3.9	90.9 ± 4.3	100 ± 0
$m_{\text{T}} < 170\,\text{GeV}$	89.7 ± 1.1	99.3 ± 1.1	61.1 ± 7.6	100 ± 0
$N(\text{jets}) \geq 2$	31.8 ± 1.7	13.5 ± 4.5	87.5 ± 6.6	79.5 ± 18.1
$p_T(\text{jet1}) > 40\,\text{GeV}$	88.3 ± 2.1	59.4 ± 11.9	86.5 ± 7.3	100 ± 0
$\eta_{j1} \times \eta_{j2} < 0$	48.7 ± 3.5	40.2 ± 15.5	30.5 ± 10.6	50.0 ± 25.0
$\lvert\Delta\eta_{jj}\rvert > 3.8$	24.7 ± 4.7	25.1 ± 21.7	15.9 ± 14.9	–
Central jet veto	72.9 ± 8.9	100 ± 0	–	–
$p_{\text{T}}^{\text{tot}} < 30\,\text{GeV}$	48.0 ± 12.5	–	–	–
b-jet veto	100 ± 0	–	–	–

Table A.6: Relative selection efficiencies [%] for the minor background contributions. The dash "–" indicates that no Monte Carlo events remain after the respective cut.

	$Z \to \ell\ell + \text{jets}$	$Z \to \tau\tau + \text{jets}$
Cross section	2 965 000	1 489 000
Trigger	$2\,241\,000 \pm 1459$	$279\,700 \pm 921$
$N(e+\mu) \geq 2$	$915\,400 \pm 1538$	$8\,230 \pm 174$
Lepton charge	$913\,500 \pm 1537$	$8\,206 \pm 174$
$E_T^{miss} > 30\,\text{GeV}$	$2\,413 \pm 71$	777.1 ± 41.6
$m_{\text{T}} < 170\,\text{GeV}$	$1\,738 \pm 62$	776.3 ± 41.6
$N(\text{jets}) \geq 2$	906.5 ± 27.8	399.4 ± 18.6
$p_T(\text{jet1}) > 40\,\text{GeV}$	770.5 ± 22.1	377.3 ± 18.3
$\eta_{j1} \times \eta_{j2} < 0$	347.6 ± 14.7	145.4 ± 9.5
$\lvert\Delta\eta_{jj}\rvert > 3.8$	28.75 ± 3.44	19.58 ± 4.8
Central jet veto	10.10 ± 2.06	8.21 ± 1.83
$p_{\text{T}}^{\text{tot}} < 30\,\text{GeV}$	6.26 ± 1.62	6.97 ± 1.69
b-jet veto	5.85 ± 1.56	6.97 ± 1.69

(a) Cross section times efficiency [fb].

$Z \to \ell\ell + \text{jets}$	$Z \to \tau\tau + \text{jets}$
100	100
75.6 ± 0.1	18.8 ± 0.1
40.9 ± 0.1	2.9 ± 0.1
99.8 ± 0.1	99.7 ± 0.1
0.3 ± 0.1	9.5 ± 0.5
72.0 ± 0.8	99.9 ± 0.1
52.2 ± 1.0	51.5 ± 1.5
85.0 ± 0.8	94.5 ± 0.8
45.1 ± 1.2	38.5 ± 1.7
8.3 ± 1.0	13.5 ± 1.9
35.1 ± 5.7	41.9 ± 7.9
62.0 ± 9.9	85.0 ± 8.0
93.5 ± 6.4	100 ± 0

(b) Relative selection efficiencies [%].

Table A.7: Evolution of the cross section times selection efficiency and the relative selection efficiencies for $Z \to \ell\ell + \text{jets}$ and $Z \to \tau\tau + \text{jets}$ events omitting cuts on the kinematic relations of the leptons.

	Cross section times efficiency [fb]	Relative selection efficiency [%]
Cross section	48 855 000	100
Trigger	$18\,797\,000 \pm 9\,300$	38.5 ± 0.1
$N(e+\mu) \geq 2$	$1\,497 \pm 103$	0.0 ± 0.1
Lepton charge	$1\,047 \pm 86$	69.9 ± 1.9
$N(\text{jets}) \geq 2$	121.5 ± 11.7	11.6 ± 1.6
$p_T(\text{jet1}) > 40\,\text{GeV}$	87.95 ± 9.96	72.4 ± 4.3
$\eta_{j1} \times \eta_{j2} < 0$	31.70 ± 5.99	36.0 ± 5.4
$\lvert\Delta\eta_{jj}\rvert > 3.8$	3.43 ± 1.98	10.8 ± 5.9
Central jet veto	2.27 ± 1.61	66.3 ± 27.3
$p_{\text{T}}^{\text{tot}} < 30\,\text{GeV}$	1.12 ± 1.12	49.1 ± 35.3
b-jet veto	1.12 ± 1.12	100 ± 0

Table A.8: Evolution of the cross section times selection efficiency and the relative selection efficiencies for W + jets events omitting cuts on the kinematic relations of the leptons.

Appendix B

Track Jet Distributions

This appendix illustrates the track jet reconstruction performance for $t\bar{t}$ events for different levels of pile-up (Figures B.1-B.5) and provides the central jet multiplicity distributions in $H \to WW$ (Figure B.6) and $t\bar{t}$ events (Figure B.7) for the different central jet veto methods introduced in Section 6.8.
Table B.1 gives the event selection efficiencies for $H \to WW$ and $t\bar{t}$ events without and with pile-up requiring matching of the tagging and central jets with a track jet. These selection efficiencies have to be compared to the efficiencies reported in Table 6.13 where only the central jets are required to have a matching track jet.

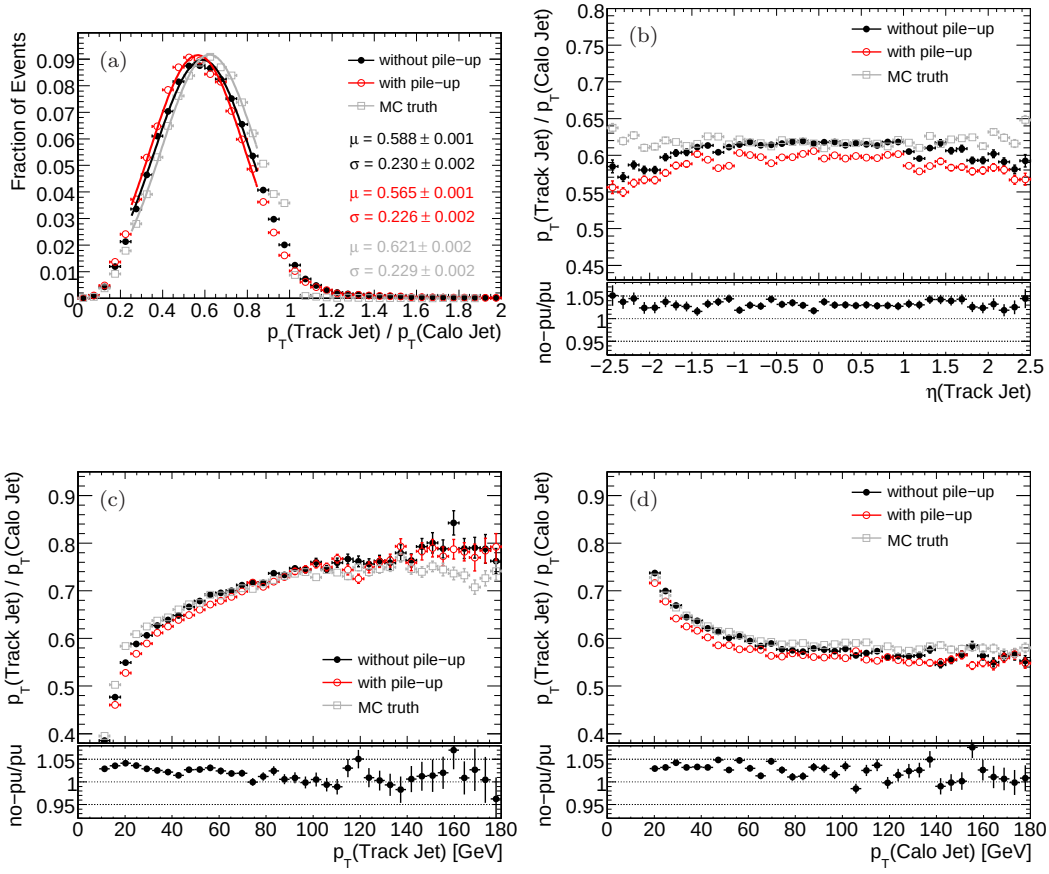

Figure B.1: Ratio of the transverse momenta of track jets and matching calorimeter jets for $t\bar{t}$ events without (black dot) and with pile-up (red open circles). The p_{T} ratio of truth track jets and the corresponding truth calorimeter jets (gray open squares) serve as reference. Shown are the distributions of the ratios (a), and the dependence on η (b) and p_{T} (c) of the track jets and on the calorimeter jet p_{T} (d). The ratios of the distributions of the p_{T} ratios without and with pile-up are shown in the lower parts of Figures (b)-(d).

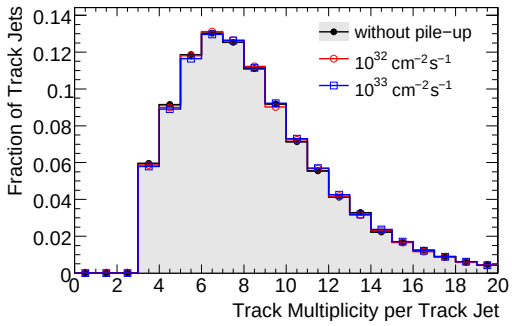

Figure B.2: Track multiplicity per track jet for $t\bar{t}$ events with different levels of pile-up.

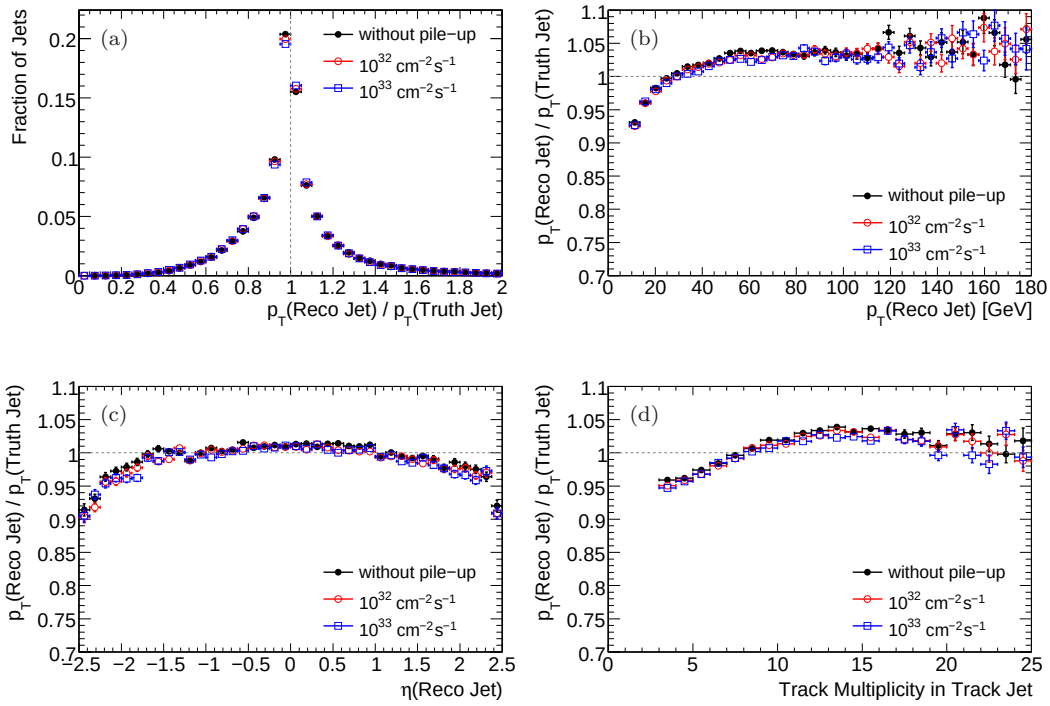

Figure B.3: Ratio of the transverse momenta of the reconstructed and the matching truth track jets for $t\bar{t}$ events with different levels of pile-up. Shown are the distributions of the ratio (a), and its dependence on the reconstructed jet p_{T} (b) and η (c) and on the track multiplicity of the track jets (d).

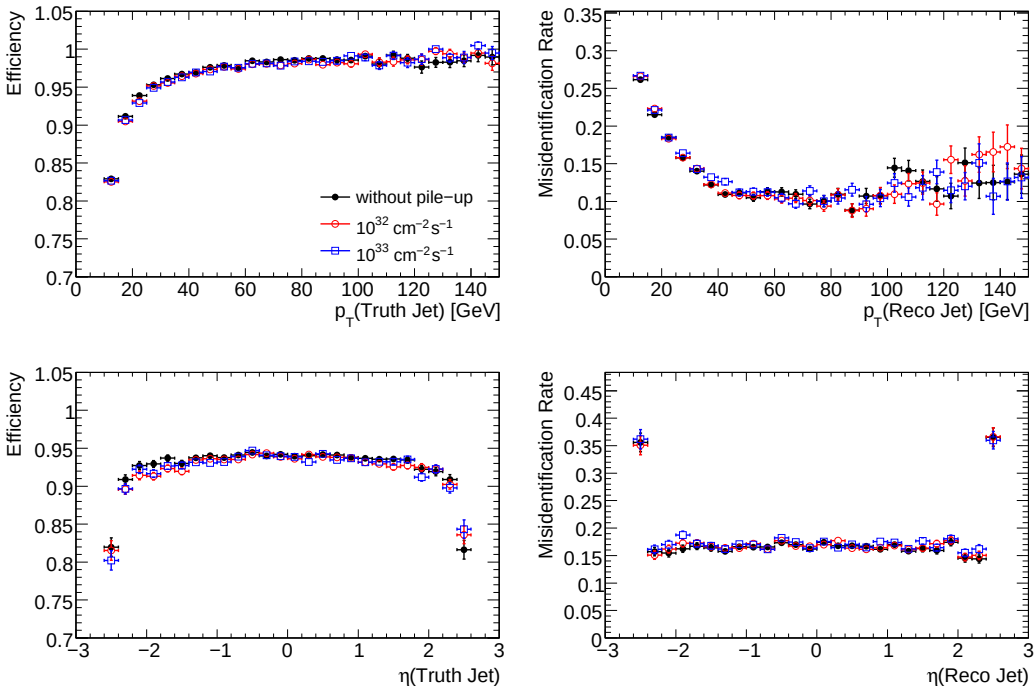

Figure B.4: Track jet reconstruction efficiency and misidentification rate as a function of p_{T} and η in $t\bar{t}$ events with different levels of pile-up.

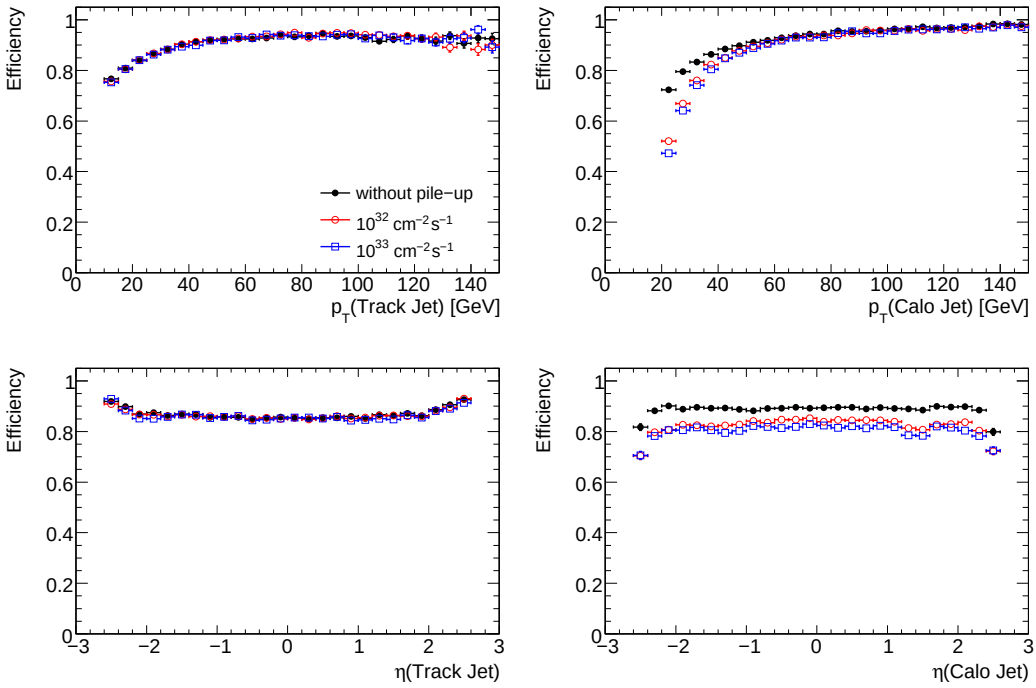

Figure B.5: Matching efficiencies of track jets to calorimeter jets (left) and of calorimeter jets to track jets (right) as a function of p_{T} and η in $t\bar{t}$ events with different levels of pile-up.

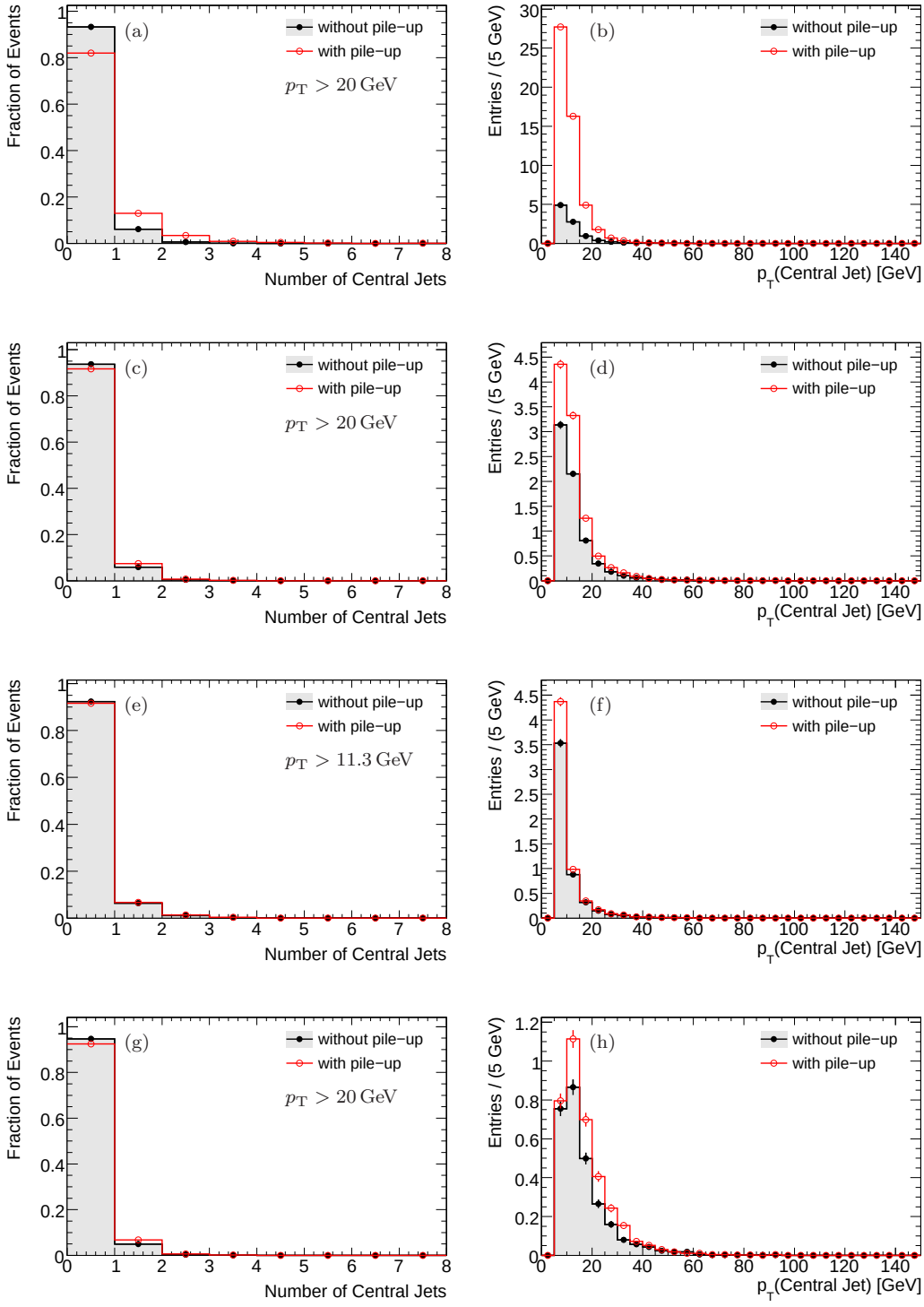

Figure B.6: Central jet multiplicities within $|\eta| < 2.5$ in $H \to WW$ events for calorimeter jets (a), calorimeter jets with $r_{p_T} > 0.65$ (c), track jets (e) and calorimeter jets with matching track jet within $\Delta R < 0.3$ (g). For calorimeter and track jets transverse momenta above 20 GeV and 11.7 GeV, respectively, have been required. The corresponding distributions of the transverse momentum scaled to 1 fb^{-1} are shown in (b), (d), (f) and (h).

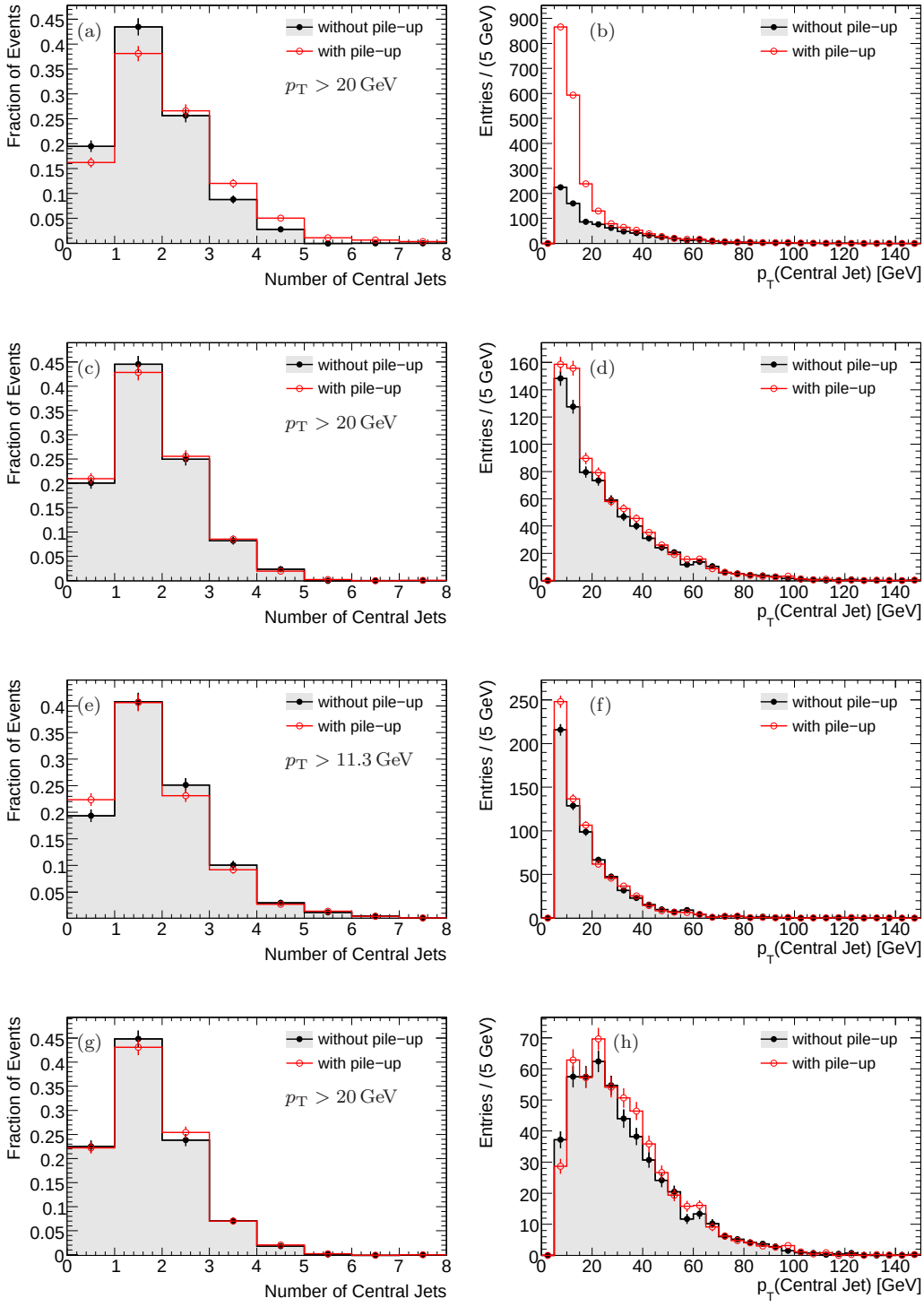

Figure B.7: Central jet multiplicities within $|\eta| < 2.5$ in $t\bar{t}$ events for calorimeter jets (a), calorimeter jets with $r_{p_T} > 0.65$ (c), track jets (e) and calorimeter jets with matching track jet within $\Delta R < 0.3$ (g). For calorimeter and track jets transverse momenta above 20 GeV and 11.7 GeV, respectively, have been required. The corresponding distributions of the transverse momentum scaled to 1 fb^{-1} are shown in (b), (d), (f) and (h).

	$H \to WW$		$t\bar{t}$	
	without pile-up	with pile-up	without pile-up	with pile-up
Cross section	74.04	74.04	217 600	217 600
Trigger	67.29 ± 0.11	66.25 ± 0.11	$137\,800 \pm 87$	$134\,000 \pm 86$
$N(e+\mu) \geq 2$	34.17 ± 0.18	32.17 ± 0.18	$9\,982 \pm 38$	$9\,338 \pm 36$
Lepton charge	34.10 ± 0.18	32.11 ± 0.18	$9\,926 \pm 37$	$9\,288 \pm 36$
$N(\text{jets}) \geq 2$	24.86 ± 0.17	25.77 ± 0.18	$9\,115 \pm 36$	$8\,768 \pm 35$
jet1 – track jet match	23.84 ± 0.17	24.27 ± 0.17	$8\,995 \pm 36$	$8\,614 \pm 35$
jet2 – track jet match	22.16 ± 0.17	21.83 ± 0.17	$8\,673 \pm 35$	$8\,200 \pm 34$
$p_T(\text{jet1}) > 40\,\text{GeV}$	20.51 ± 0.17	20.28 ± 0.17	$8\,291 \pm 34$	$7\,895 \pm 33$
$\eta_{j1} \times \eta_{j2} < 0$	17.76 ± 0.16	17.19 ± 0.16	$3\,757 \pm 23$	$3\,599 \pm 23$
$\lvert\Delta\eta_{jj}\rvert > 3.8$	13.04 ± 0.14	12.73 ± 0.14	390.8 ± 7.6	418.8 ± 7.8
$m_{jj} > 500\,\text{GeV}$	11.08 ± 0.13	10.98 ± 0.13	273.9 ± 6.4	289.0 ± 6.5
Central jet veto	10.50 ± 0.13	10.16 ± 0.13	61.04 ± 3.01	62.81 ± 3.01
$p_{\text{T}}^{\text{tot}} < 30\,\text{GeV}$	9.80 ± 0.13	8.64 ± 0.12	35.11 ± 2.28	29.81 ± 2.08
b-jet veto	9.16 ± 0.12	7.96 ± 0.11	16.30 ± 1.55	15.05 ± 1.48

(a) Cross section times efficiency [fb].

Trigger	90.9 ± 0.1	89.5 ± 0.2	63.3 ± 0.1	61.6 ± 0.1
$N(e+\mu) \geq 2$	50.8 ± 0.3	48.6 ± 0.3	7.2 ± 0.1	7.0 ± 0.1
Lepton charge	99.8 ± 0.1	99.8 ± 0.1	99.4 ± 0.1	99.5 ± 0.1
$N(\text{jets}) \geq 2$	72.9 ± 0.3	80.2 ± 0.3	91.8 ± 0.1	94.4 ± 0.1
jet1 – track jet match	95.9 ± 0.2	94.2 ± 0.2	98.7 ± 0.1	98.2 ± 0.1
jet2 – track jet match	92.9 ± 0.2	89.9 ± 0.3	96.4 ± 0.1	95.2 ± 0.1
$p_T(\text{jet1}) > 40\,\text{GeV}$	92.6 ± 0.2	92.9 ± 0.2	95.6 ± 0.1	96.3 ± 0.1
$\eta_{j1} \times \eta_{j2} < 0$	86.6 ± 0.3	84.7 ± 0.3	45.3 ± 0.2	45.6 ± 0.2
$\lvert\Delta\eta_{jj}\rvert > 3.8$	73.4 ± 0.5	74.1 ± 0.5	10.4 ± 0.2	11.6 ± 0.2
$m_{jj} > 500\,\text{GeV}$	84.9 ± 0.4	86.2 ± 0.4	70.1 ± 0.9	69.0 ± 0.9
Central jet veto	94.8 ± 0.3	92.6 ± 0.3	22.3 ± 1.0	21.7 ± 0.9
$p_{\text{T}}^{\text{tot}} < 30\,\text{GeV}$	93.4 ± 0.3	85.0 ± 0.5	57.5 ± 2.4	47.5 ± 2.4
b-jet veto	93.5 ± 0.3	92.1 ± 0.4	46.4 ± 3.2	50.5 ± 3.5
total	12.4 ± 0.2	10.7 ± 0.2	$(7.5 \pm 0.7) \cdot 10^{-3}$	$(6.9 \pm 0.7) \cdot 10^{-3}$

(b) Relative selection efficiencies [%].

Table B.1: Evolution of the cross section times selection efficiency and the relative selection efficiencies for $H \to WW$ and $t\bar{t}$ events without and with pile-up omitting cuts on the kinematic relations of the leptons. Tagging jets within $|\eta| < 2.5$ are required to have a matching track jet. Only calorimeter jets with $p_{\text{T}} > 20\,\text{GeV}$ and $|\eta| < 2.5$ with matching track jet are employed for the central jet veto.

List of Figures

List of Tables

Bibliography

[1] A. Djouadi, *The Anatomy of electro-weak symmetry breaking. I: The Higgs boson in the standard model*, Phys. Rept. **457** (2008) 1–216, arXiv:hep-ph/0503172.

[2] A. Pich, *The Standard Model of Electroweak Interactions*, arXiv:0705.4264 [hep-ph].

[3] S. L. Glashow, *Partial Symmetries of Weak Interactions*, Nucl. Phys. **22** (1961) 579–588.

[4] S. Weinberg, *A Model of Leptons*, Phys. Rev. Lett. **19** (1967) 1264–1266.

[5] A. Salam, *Weak and Electromagnetic Interactions*, originally printed in "Svartholm: Elementary Particle Theory, Proceedings of the Nobel Symposium held 1968 at Lerum, Sweden", Stockholm 1968, 367-377.

[6] P. W. Higgs, *Broken Symmetries and the Masses of Gauge Bosons*, Phys. Rev. Lett. **13** (1964) 508–509.

[7] F. Englert and R. Brout, *Broken Symmetry and the Mass of Gauge Vector Mesons*, Phys. Rev. Lett. **13** (1964) 321–322.

[8] G. S. Guralnik, C. R. Hagen, and T. W. B. Kibble, *Global Conservation Laws and Massless Particles*, Phys. Rev. Lett. **13** (1964) 585–587.

[9] J. Wess and B. Zumino, *Supergauge Transformations in Four-Dimensions*, Nucl. Phys. **B70** (1974) 39–50.

[10] S. P. Martin, *A Supersymmetry Primer*, arXiv:hep-ph/9709356.

[11] K. Riesselmann, *Limitations of a standard model Higgs boson*, DESY-97-222 (1997), arXiv:hep-ph/9711456.

[12] ALEPH collaboration et al., *Precision Electroweak Measurements and Constraints on the Standard Model*, CERN-PH-EP-2008-020, CERN, Geneva, December 2008. arXiv:0811.4682.

[13] LEP Working Group for Higgs Boson Searches, R. Barate et al., *Search for the standard model Higgs boson at LEP*, Phys. Lett. **B565** (2003) 61–75, arXiv:hep-ex/0306033.

[14] Tevatron New-Phenomena and Higgs working group, G. Bernardi et al., *Combined CDF and D0 Upper Limits on Standard Model Higgs Boson Production at High Mass (155-200 GeV/c^2) with 3 fb^{-1} of data*, FERMILAB-PUB-08-270-E, August 2008. arXiv:0808.0534 [hep-ex].

[15] J. Pumplin et al., *New generation of parton distributions with uncertainties from global QCD analysis*, JHEP **07** (2002) 012, arXiv:hep-ph/0201195.

[16] M. A. Dobbs et al., *Les Houches guidebook to Monte Carlo generators for hadron collider physics*, arXiv:hep-ph/0403045.

[17] A. Moraes, C. Buttar, and I. Dawson, *Prediction for minimum bias and the underlying event at LHC energies*, Eur. Phys. J. **C50** (2007) 435–466.

[18] A. Moraes, *Modeling the underlying event: generating predictions for the LHC*, ATLAS note, ATL-PHYS-PROC-2009-045, CERN, Geneva, March 2009.

[19] L. Evans et al., *LHC Machine*, JINST **3** (2008) S08001.

[20] ATLAS Collaboration, G. Aad et al., *The ATLAS Experiment at the CERN Large Hadron Collider*, JINST **3** (2008) S08003.

[21] CMS Collaboration, R. Adolphi et al., *The CMS experiment at the CERN LHC*, JINST **3** (2008) S08004.

[22] LHCb Collaboration, A. Augusto Alves et al., *The LHCb Detector at the LHC*, JINST **3** (2008) S08005.

[23] ALICE Collaboration, K. Aamodt et al., *The ALICE experiment at the CERN LHC*, JINST **3** (2008) S08002.

[24] CDF Collaboration, F. Abe et al., *Observation of top quark production in $\bar{p}p$ collisions*, Phys. Rev. Lett. **74** (1995) 2626–2631, arXiv:hep-ex/9503002.

[25] D0 Collaboration, S. Abachi et al., *Observation of the top quark*, Phys. Rev. Lett. **74** (1995) 2632–2637, arXiv:hep-ex/9503003.

[26] ATLAS Collaboration, *Prospects for Supersymmetry Discovery Based on Inclusive Searches*, Chapter in [32].

[27] S. Catani, *Aspects of QCD, from the Tevatron to the LHC*, Proceedings of the Workshop Physics at TeV Colliders, Les Houches, France, June 1999. arXiv:hep-ph/0005233.

[28] ATLAS Collaboration, *ATLAS Detector and Physics Performance: Technical Design Report*, CERN/LHCC/99-14, CERN, 1999.

[29] *LCG homepage*, http://lcg.web.cern.ch.

[30] J. Knobloch et al., *LHC Computing Grid: Technical Design Report*, CERN-LHCC-2005-024, Geneva, 2005.

[31] J. v. Loeben, *Test und Kalibrierung der Präzisionsdriftrohrkammern des ATLAS Myonspektrometers*, Diploma thesis, Technische Universität München and Max-Planck-Institut für Physik, December 2006.

[32] ATLAS Collaboration, G. Aad et al., *Expected performance of the ATLAS experiment: detector, trigger and physics*, CERN-OPEN-2008-020, CERN, Geneva, September 2008. arXiv:0901.0512.

[33] J. Schmaler, *Test and Alignment of the ATLAS Precision Muon Chambers*, Diploma thesis, Technische Universität München and Max-Planck-Institut für Physik, March 2007.

[34] R. Avramidou et al., *A summary of the ATLAS MDT Calibration Model*, ATLAS internal note, ATL-MUON-INT-2006-007, CERN, Geneva, September 2005.

[35] J. C. Barriere et al., *The alignment system of the barrel part of the ATLAS muon spectrometer*, ATLAS internal note, ATL-MUON-PUB-2008-007, CERN, Geneva, January 2008.

[36] ATLAS Collaboration, *Trigger for Early Running*, Chapter in [32].

[37] P. Bagnaia et al., *Calibration model for the MDT chambers of the ATLAS Muon Spectrometer*, ATLAS internal note, ATL-COM-MUON-2007-016, CERN, Geneva, December 2007.

[38] I. Potrap et al., *Alignment of the ATLAS muon spectrometer with tracks*, Nucl. Instrum. Meth. A (2009), Article in press.

[39] B. Bittner, *Alignment of the ATLAS Muon Spectrometer Using Muon Tracks*, Diploma thesis, Technische Universität München and Max-Planck-Institut für Physik, 2008.

[40] P. Brückman, A. Hicheur, and S. J. Haywood, *Global chi2 approach to the Alignment of the ATLAS Silicon Tracking Detectors*, ATLAS note, CERN-ATL-INDET-PUB-2005-002, CERN, Geneva, 2005.

[41] A. Bocci and W. Hulsbergen, *TRT Alignment For SR1 Cosmics and Beyond*, ATLAS note, CERN-ATL-COM-INDET-2007-011, CERN, Geneva, June 2007.

[42] R. Härtel, *Iterative local χ^2 alignment approach for the ATLAS SCT detector*, Diploma thesis, Technische Universität München and Max-Planck-Institut für Physik, 2005.

[43] T. Göttfert, *Iterative local χ^2 alignment approach for the ATLAS Pixel detector*, Diploma thesis, Universität Würzburg and Max-Planck-Institut für Physik, 2006.

[44] F. Heinemann and A. Weidberg, *Robust Track Based Alignment of the ATLAS Silicon Detectors and Assessing Parton Distribution Uncertainties in Drell-Yan Processes*. PhD thesis, ETH Zürich, Oxford, 2007.

[45] D. Adams et al., *Track reconstruction in the ATLAS Muon Spectrometer with MOORE 007*, ATLAS internal note, ATL-SOFT-2003-007, CERN, Geneva, May 2003.

[46] T. G. Cornelissen et al., *The global χ^2 track fitter in ATLAS*, J. Phys.: Conf. Ser. **119** (2008) 032013.

[47] Particle Data Group Collaboration, C. Amsler et al., *Review of particle physics*, Phys. Lett. **B667** (2008) 1.

[48] S. Asai et al., *Prospects for the search for a standard model Higgs boson in ATLAS using vector boson fusion*, Eur. Phys. J. **C32S2** (2004) 19–54, arXiv:hep-ph/0402254.

[49] ATLAS Collaboration, *Higgs Boson Searches in Gluon Fusion and Vector Boson Fusion using the $H \to WW$ Decay Mode*, Chapter in [32].

[50] A. J. Barr, B. Gripaios, and C. G. Lester, *Measuring the Higgs boson mass in dileptonic W-boson decays at hadron colliders*, JHEP **07** (2009) 072, arXiv:0902.4864 [hep-ph].

[51] R. Asfandiyarov et al., *Production Cross Section of the Higgs Boson and Other Standard Model Processes in pp Collisions at Different Center-of-Mass Energies*, ATL-COM-PHYS-2009-051, CERN, Geneva, February 2009.

[52] J. M. Campbell and R. K. Ellis, *MCFM homepage*, http://mcfm.fnal.gov.

[53] T. Binoth, M. Ciccolini, N. Kauer, and M. Kramer, *Gluon-induced W-boson pair production at the LHC*, JHEP **12** (2006) 046, arXiv:hep-ph/0611170.

[54] M. Spira, *HIGLU and HDECAY: Programs for Higgs boson production at the LHC and Higgs boson decay widths*, Nucl. Instrum. Meth. **A389** (1997) 357–360.

[55] S. Frixione and B. R. Webber, *Matching NLO QCD computations and parton shower simulations*, JHEP **06** (2002) 029, arXiv:hep-ph/0204244.

[56] G. Corcella et al., *HERWIG 6: An event generator for hadron emission reactions with interfering gluons (including supersymmetric processes)*, JHEP **01** (2001) 010, arXiv:hep-ph/0011363.

[57] M. L. Mangano et al., *ALPGEN, a generator for hard multiparton processes in hadronic collisions*, JHEP **07** (2003) 001, arXiv:hep-ph/0206293.

[58] B. P. Kersevan and E. Richter-Was, *The Monte Carlo event generator AcerMC version 2.0 with interfaces to PYTHIA 6.2 and HERWIG 6.5*, arXiv:hep-ph/0405247.

[59] T. Sjostrand, S. Mrenna, and P. Skands, *PYTHIA 6.4 physics and manual*, JHEP **05** (2006) 026, arXiv:hep-ph/0603175.

[60] J. M. Butterworth, J. R. Forshaw, and M. H. Seymour, *Multiparton interactions in photoproduction at HERA*, Z. Phys. **C72** (1996) 637–646, arXiv:hep-ph/9601371.

[61] GEANT4 Collaboration, S. Agostinelli et al., *GEANT4: A simulation toolkit*, Nucl. Instrum. Meth. **A506** (2003) 250–303.

[62] *ATLAS - ATLFAST II twiki page*, https://twiki.cern.ch/twiki/bin/view/Atlas/AtlfastII.

[63] M. Dührssen, *The fast calorimeter simulation FastCaloSim*, ATLAS internal note, ATL-PHYS-INT-2008-043, CERN, Geneva, July 2008.

[64] ATLAS Collaboration, *Reconstruction and Identification of Electrons*, Chapter in [32].

[65] S. Hassani et al., *A muon identification and combined reconstruction procedure for the ATLAS detector at the LHC using the (MUONBOY, STACO, MuTag) reconstruction packages*, Nucl. Instrum. Meth. **A572** (2007) 77–79.

[66] T. Lagouri et al., *A muon identification and combined reconstruction procedure for the ATLAS detector at the LHC at CERN*, IEEE Trans. Nucl. Sci. **51** (2004) 3030–3033.

[67] W. Lampl et al., *Calorimeter Clustering Algorithms: Description and Performance*, ATLAS note, ATL-LARG-PUB-2008-002, CERN, Geneva, April 2008.

[68] G. C. Blazey et al., *Run II jet physics*, arXiv:hep-ex/0005012.

[69] ATLAS Collaboration, *Jet Reconstruction Performance*, Chapter in [32].

[70] ATLAS Collaboration, *Detector Level Jet Corrections*, Chapter in [32].

[71] M. Cacciari, G. P. Salam, and G. Soyez, *The anti-k_t jet clustering algorithm*, JHEP **04** (2008) 063, arXiv:0802.1189 [hep-ph].

[72] G. P. Salam and G. Soyez, *A Practical Seedless Infrared-Safe Cone jet algorithm*, JHEP **05** (2007) 086, arXiv:0704.0292 [hep-ph].

[73] A. Armbruster et al., *Higgs Boson Searches using the $H \to WW^{(*)} \to l\nu l\nu$ Decay Mode with the ATLAS Detector*, ATLAS internal note, ATL-COM-PHYS-2009-620, CERN, Geneva, November 2009.

[74] ATLAS Collaboration, *Measurement of Missing Transverse Energy*, Chapter in [32].

[75] M. Groh, *Study of the Higgs Boson Discovery Potential in the Process $pp \to Hqq$, $H \to \tau\tau$ with the ATLAS Detector*. PhD thesis, Technische Universität München and Max-Planck-Institut für Physik, 2009.

[76] ATLAS Collaboration, *b-Tagging Performance*, Chapter in [32].

[77] Ames-Bologna-CERN-Dortmund-Heidelberg-Warsaw Collaboration, A. Breakstone et al., *Charged Multiplicity Distribution in pp Interactions at ISR Energies*, Phys. Rev. **D30** (1984) 528.

[78] UA5 Collaboration, G. J. Alner et al., *UA5: A general study of proton-antiproton physics at $\sqrt{s} = 546$-GeV*, Phys. Rept. **154** (1987) 247–383.

[79] ATLAS Collaboration, *A Study of Minimum Bias Events*, Chapter in [32].

[80] E. Bouhova-Thacker et al., *Vertex Reconstruction in the ATLAS Experiment at the LHC*, ATLAS note, ATL-INDET-PUB-2009-001, CERN, Geneva, May 2009.

[81] *ATLAS - Track Missing E_{T} twiki page*, https://twiki.cern.ch/twiki/bin/view/AtlasProtected/TrackMET.

[82] ATLAS Collaboration, *The Expected Performance of the Inner Detector*, Chapter in [32].

[83] T. G. Cornelissen et al., *Updates of the ATLAS Tracking Event Data Model (Release 13)*, ATLAS note, ATL-SOFT-PUB-2007-003, CERN, Geneva, June 2007.

[84] ATLAS Collaboration, *Inner Detector: Technical Design Report*, CERN-LHCC-97-016/017, CERN, Geneva, 1997.

[85] R. Frühwirth and W. Waltenberger, *Adaptive Multi-vertex fitting*, CMS note, CMS-CR-2004-062, CERN, Geneva, September 2004.

[86] C. Ruwiedel, G. Gaycken, and J. Kroseberg, *Study of the Use of Jet-Vertex Association for the Suppression of Pileup Jets in the Central Jet Veto in VBF $H \to \tau^+\tau^- \to lh$*, ATLAS internal note, ATL-COM-PHYS-2009-237, CERN, Geneva, May 2009.

[87] S. Kaiser et al., *Study of Track Jets in VBF $H \to WW$ Production with Pile-up*, ATLAS internal note, ATL-COM-PHYS-2008-019, CERN, Geneva, February 2008.

[88] B. Butler and A. Schwartzman, *Track-Jet Reconstruction and Performance*, ATLAS internal note, ATL-COM-PHYS-2009-193, CERN, Geneva, April 2009.

[89] D. W. Miller, A. Schwartzman, and D. Su, *Jet-Vertex Association Algorithm*, ATLAS internal note, ATL-COM-PHYS-2008-008, CERN, Geneva, January 2008.

[90] CDF Collaboration, D. E. Acosta et al., *Measurement of charged particle multiplicities in gluon and quark jets in $p\bar{p}$ collisions at $\sqrt{s} = 1.8$ TeV*, Phys. Rev. Lett. **94** (2005) 171802.

[91] A. Bhatti et al., *Determination of the jet energy scale at the collider detector at Fermilab*, Nucl. Instrum. Meth. **A566** (2006) 375–412, arXiv:hep-ex/0510047.

[92] ATLAS Collaboration, *Jets from Light Quarks in $t\bar{t}$ Events*, Chapter in [32].

[93] On behalf of the CMS Collaboration, P. Azzurri, *Jet Reconstruction with charged tracks only in CMS*, arXiv:0901.1541 [hep-ex].

[94] ATLAS Collaboration, *Jet Energy Scale: In-situ Calibration Strategies*, Chapter in [32].

[95] ATLAS Collaboration, *Electroweak Boson Cross-Section Measurements*, Chapter in [32].

[96] C. Ruwiedel, J. Kroseberg, and N. Wermes, *Formation of topological clusters in the presence of pileup using asymmetric cuts*, ATLAS internal note, ATL-COM-PHYS-2009-556, CERN, Geneva, October 2009.

[97] L. Asquith et al., *Performance of Jet Algorithms in the ATLAS Detector*, ATLAS note, ATL-COM-PHYS-2009-630, CERN, Geneva, December 2009.

[98] ATLAS Collaboration, *Statistical Combination of Several Important Standard Model Higgs Boson Search Channels*, Chapter in [32].

[99] R. D. Cousins, J. T. Linnemann, and J. Tucker, *Evaluation of three methods for calculating statistical significance when incorporating a systematic uncertainty into a test of the background-only hypothesis for a Poisson process*, Nucl. Instrum. Meth. **A595** (2008) 480–501, arXiv:physics/0702156.

[100] W. A. Rolke, A. M. Lopez, and J. Conrad, *Confidence Intervals with Frequentist Treatment of Statistical and Systematic Uncertainties*, Nucl. Instrum. Meth. **A551** (2005) 493–503, arXiv:physics/0403059.

[101] J. Lundberg, J. Conrad, W. Rolke, and A. Lopez, *Limits, discovery and cut optimization for a Poisson process with uncertainty in background and signal efficiency: TRolke 2.0*, arXiv:0907.3450 [physics.data-an].

[102] R. Brun and F. Rademakers, *ROOT - An Object Oriented Data Analysis Framework, Proceedings AIHENP'96 Workshop, Lausanne, Sep. 1996*, Nucl. Instrum. Meth. in Phys. Res. **A389** (1997) 81–86. http://root.cern.ch/.

[103] S. Asai et al., *Cross sections for Standard Model processes to be used in the ATLAS CSC notes*, ATLAS internal note, ATL-PHYS-INT-2009-003, CERN, Geneva, May 2008.

[104] R. Bonciani et al., *NLL resummation of the heavy-quark hadroproduction cross-section*, Nucl. Phys. **B529** (1998) 424–450, arXiv:hep-ph/9801375.

[105] T. Figy, C. Oleari, and D. Zeppenfeld, *Next-to-leading order jet distributions for Higgs boson production via weak-boson fusion*, Phys. Rev. **D68** (2003) 073005, arXiv:hep-ph/0306109.

[106] M. Ciccolini, A. Denner, and S. Dittmaier, *Strong and electroweak corrections to the production of Higgs+2jets via weak interactions at the LHC*, Phys. Rev. Lett. **99** (2007) 161803, arXiv:0707.0381 [hep-ph].

[107] T. Figy, V. Hankele, and D. Zeppenfeld, *Next-to-leading order QCD corrections to Higgs plus three jet production in vector-boson fusion*, JHEP **02** (2008) 076, arXiv:0710.5621 [hep-ph].

[108] ATLAS Collaboration, *Search for the Standard Model Higgs Boson via Vector Boson Fusion Production Process in the Di-Tau Channels.*, Chapter in [32].

[109] R. Harlander and W. Kilgore, *Scalar and pseudo-scalar Higgs production at hadron colliders*, arXiv:hep-ph/0211380.

[110] ATLAS Collaboration, *Cross-Sections, Monte Carlo Simulations and Systematic Uncertainties*, Chapter in [32].

Acknowledgments

For the past three years I have been given the opportunity to be part of such an interesting environment as the ATLAS collaboration. I want to thank all those who made these years such a valuable experience.
First, I am thankful to Hubert Kroha for giving me the opportunity to prepare my PhD thesis in the MDT group at the Max-Planck-Institute in Munich, for providing me the possibility to attend many interesting physics schools, work shops and conferences and in particular for supporting my extended stay at CERN. I am very grateful to my supervisors Sandra Horvat and Oliver Kortner for their valuable advice, their patience and for wisely guiding me through the various adversities of my PhD endeavor. I am also indebted to Robert Harrington for all the constructive discussions and the help he provided to get the alignment on track.
Of course, I thank all members of the MPI MDT group for the jointly spent hours during many bar visits, the challenging table tennis and squash matches, the mountaineering and the generally very pleasant atmosphere. In particular, I express my gratitude to my office mates at CERN, Alessia d'Orazio and Daniela Rebuzzi, for introducing me to Italian swearing and cooking, and to Manfred Groh, my office mate at MPI, for the Spezi competitions, the shared affection for sweets in the afternoon and for sharpening my awareness for thinking green. I also want to express my gratitude to all those who always found a way to distract me from physics in Munich and especially during my year at CERN. It has been a pleasure!
Zu guter Letzt gebührt der größte Dank meiner Familie, insbesondere meinen Eltern, für den Rückhalt und die wertvolle Unterstützung die sie mir in den letzten Jahren gegeben haben.